

**Soot formation at atmospheric and
diesel engine conditions using 2D
time-resolved laser induced
incandescence**

Lyndon DeLaurey

A thesis submitted in partial fulfilment of the requirements of
the University of Brighton for the degree of Doctor of
Philosophy

2015

Abstract

A novel technique is presented in which two colour, two dimensional, time-resolved Laser induced incandescence (2C-2D-TiRe-LII) is used to produce planar spatially resolved, quantified, soot particle sizing. The technique is applied to a well characterized laboratory flame (Santoro burner) for validation. Accordance with other research efforts of spatial distribution of soot particle size was demonstrated.

Application of a suitably adapted technique, to an optically accessible reciprocating rapid compression machine was performed. This allowed the investigation of the effects of variation of in-cylinder pressure, injection system pressure of a typical diesel fuelled, compression ignition combustion system. A simultaneously performed laser sheet extinction characterization experiment was performed to yield local laser fluence data, necessary for the calculation of primary particle size.

The necessity of addressing the temporal performance of the acquisition equipment is identified and a novel solution presented and utilized within this study.

Depiction of the effects of entrainment wave phenomena upon the spatially resolved data and particle sizing results of the diesel combustion experimentation are presented.

Recommendations for refinement and optimization of the experimental technique and the associated data processing methods are presented.

Keywords: LII, TiRe-LII, 2D-2C-TiRe-LII, PM_{2.5}, PM₁₀, Soot, quantitative, spatially resolved

Contents

Abstract	ii
Contents	iii
List of figures	ix
List of Tables	xviii
Nomenclature	xix
Acknowledgements	xxii
Declaration	xxiii
1 Introduction	1
1.1 Background	1
1.2 Structure of the thesis	9
1.3 Objectives	10
2 Theoretical background and review of literature	11
2.1 Introduction	11
2.2 Soot	11
2.2.1 Morphology	12
2.2.2 Formation and destruction processes	14
2.2.2.1 Pyrolysis	16
2.2.2.2 Nucleation	18
2.2.2.3 Surface growth	18
2.2.2.4 Coalescence	19
2.2.2.5 Agglomeration	19
2.2.2.6 Oxidation	21
2.2.3 Soot characterization	22
2.2.3.1 Particle size distribution	22
2.2.3.2 Soot volume fraction	24
2.2.4 Physical parameters affecting soot production	25
2.2.4.1 Stoichiometry/equivalence ratio	25
2.2.4.2 Temperature	26
2.2.4.3 Pressure	27
2.3 Flame structure	28
2.3.1.1 Premixed flame	28

2.3.1.2	Non-premixed laminar diffusion flame	28
2.4	Diesel combustion	29
2.5	Heat transfer	34
2.5.1	Transport mechanisms	34
2.5.1.1	Radiation	34
2.5.1.1.1	Black-body radiation	34
2.5.1.1.2	Grey-body radiation	36
2.5.1.1.3	Non-vacuum conditions	37
2.5.1.2	Conduction	39
2.5.1.3	Absorption	39
2.5.1.4	Sublimation	40
2.5.1.5	Annealing	41
2.5.1.6	Oxidation	42
2.6	Pyrometry	42
2.6.1	Two colour pyrometry	46
2.7	Laser induced incandescence (LII) of soot	50
2.7.1	Time resolved laser induced incandescence (TiRe-LII) of soot	55
2.7.2	Planar and time-resolved laser-induced incandescence (2D-TiRe-LII) of soot	57
2.7.3	Energy balance for a single spherical, homogenous soot particle	57
2.7.3.1	Knudsen number and model regime	58
2.7.3.2	Internal energy	59
2.7.3.3	Absorption	60
2.7.3.4	Conduction	61
2.7.3.5	Sublimation	62
2.7.3.6	Oxidation	62
2.7.3.7	Annealing	65
2.7.4	High pressure, continuum regime conditions	65
2.7.5	Refractive index of soot	68
2.7.6	Spectral function	69
2.7.7	Emissivity (ϵ_λ)	69
2.7.7.1	The ' α ' model	69
2.7.7.2	The 'E(m)' model	70
2.7.7.3	The 'g' model	70
2.8	Extinction	71

3	Experimental work	75
3.1	Introduction	75
3.2	Experimental subjects	76
3.3	Validation of 2D-2C-TiRe-LII on a laminar diffusion flame at atmospheric conditions	76
3.3.1	Introduction	76
3.3.2	Concept and experimental aims	77
3.3.3	Equipment	77
3.3.3.1	Experimental subject: Santoro burner	77
3.3.3.1.1	Shroud and baffle	80
3.3.3.2	Laser and associated optics	82
3.3.3.2.1	Laser	82
3.3.3.2.1.1	Laser wavelength	83
3.3.3.2.2	Sheet-forming optics	85
3.3.3.2.3	In-line energy monitor	86
3.3.3.2.4	In-line photodiode	86
3.3.3.2.5	Adjustable width slit	88
3.3.3.3	Camera and acquisition optics	90
3.3.3.3.1	Camera/Intensifier	90
3.3.3.3.2	Lens	90
3.3.3.3.3	Image doubler	90
3.3.3.3.4	Spectral Filters	91
3.3.3.3.5	Photomultipliers and associated optics	96
3.3.3.4	Control apparatus	96
3.3.3.4.1	Personal computer	96
3.3.3.4.2	Digital storage oscilloscope	96
3.3.3.4.3	Programmable arbitrary waveform generator	97
3.3.3.4.4	Delay line circuit and line driver	97
3.3.3.4.5	Cables	97
3.3.3.5	Configuration	98
3.3.4	Control/procedure	103
3.3.4.1	Experiment	103
3.3.4.2	Acquisition	104

3.3.5	Sub-frame laser pulse timing	107
3.4	High pressure planar and time resolved laser induced incandescence upon a rapid compression machine	110
3.4.1	Introduction	110
3.4.2	Concept and experimental aims	110
3.4.3	Equipment	111
3.4.3.1	Proteus reciprocation rapid compression machine	111
3.4.3.2	Laser and associated optics	113
3.4.3.2.1	Laser	113
3.4.3.2.2	Sheet forming optics	113
3.4.3.2.3	Adjustable width slit	113
3.4.3.3	Camera and acquisition optics	114
3.4.3.3.1	Camera and intensifier	114
3.4.3.3.2	Lens	115
3.4.3.3.3	Spectral filters	115
3.4.3.4	Extinction apparatus	117
3.4.3.5	Control apparatus	118
3.4.3.6	Configuration	119
3.4.4	Control/ Procedure	121
3.4.4.1	Proteus	121
3.4.4.2	Experiment	122
4	Data processing	125
4.1	Atmospheric conditions	125
4.1.1	Spatial registration	126
4.1.2	Dark field/current characterization and removal	127
4.1.3	Hot pixel characterization and removal	128
4.1.4	Binning	131
4.1.5	Divergence from typical data preparation sequence	132
4.1.6	Camera shutter response	133
4.1.6.1	Characterization of shutter response	135
4.1.6.2	Shutter model	136
4.1.7	Laser fluence	137
4.1.8	Algorithm	139
4.1.8.1	Convergence criteria	141

4.1.8.2	Data ratio weighting	142
4.2	High pressure conditions	143
4.2.1	High pressure regime and models used	143
4.2.2	Laser fluence	143
4.2.3	Algorithm	147
4.2.4	Spatial registration	149
5	Results and discussion	151
5.1	Introduction	151
5.2	Uncertainties	151
5.2.1	Laser fluence	152
5.2.2	Ambient (or flame) temperature	152
5.2.3	Acquisition sensitivity	153
5.2.4	Acquisition temporal jitter	153
5.2.5	High pressure effects	153
5.3	Atmospheric condition experimental results	155
5.3.1	Punctual 2C-TiRe-LII	156
5.3.2	Primary Particle sizing (d_p)	160
5.3.3	2D-2C-TiRe-LII	162
5.3.3.1	LII signal	162
5.3.3.2	No solution regions	169
5.3.3.3	Distribution	170
5.3.4	Comparison of punctual location (2C-TiRe-LII) with planar (2D-2C-TiRe-LII) results	171
5.3.5	Discussion	172
5.4	Application to high pressure diesel combustion	175
5.4.1	Example of experimentally acquired data	175
5.4.1.1	LII data	176
5.4.1.2	Extinction data	177
5.4.1.3	ICP pressure trace and capture event.	178
5.4.2	Ensemble average data set results	179
5.4.2.1	Variation of acquisition timing (T_{Ref}) for ensemble averaged data.	180
5.4.2.2	Variation of fuel injection rail pressure (P_{rail}).	184
5.4.2.3	Variation of in cylinder pressure (ICP)	189
5.4.3	Individual LII data sequence derived results	191

5.4.3.1	Data set 58 (ICP=40 bar, $P_{\text{rail}}=1000$ bar, $T_{\text{Ref}}=1.7$ ms)	191
5.4.3.2	Data set 28 (ICP=40 bar, $P_{\text{rail}}=1300$ bar, $T_{\text{Ref}}=1$ ms)	195
5.4.3.3	Data set 1 (ICP=50 bar, $P_{\text{rail}}=1000$ bar, $T_{\text{Ref}}=1.8$ ms)	197
5.4.3.4	Data set 33 (ICP=40 bar, $P_{\text{rail}}=1600$ bar, $T_{\text{Ref}}=0.66$ ms)	200
5.4.4	Discussion	203
5.4.4.1	10 nm mode	204
6	Conclusion	205
6.1	Validation of the technique at atmospheric conditions	206
6.2	Application of 2D-2C-Tire-LII at high ambient pressures	207
6.3	Future work	208
	References	210

List of figures

Figure 1 The particle deposition upon the pulmonary system versus particle diameter. Adapted (ICRP 1994) & (Price <i>et al.</i> 2002).	2
Figure 2 Equivalence ratio versus temperature operation map, illustrating soot and NO _x islands (adapted from Akihama <i>et al.</i> 2001).	5
Figure 3 TEM images of soot agglomerates imaged using transmission electron microscopy (adapted from Snelling, Liu <i>et al.</i> 2004).	12
Figure 4 TEM image of chain like agglomerates of Diesel soot (adapted from Wentzel <i>et al.</i> 2003).	13
Figure 5 Soot spherule composed of nanocrystalline graphitic carbon and portraying an onion shell type structure.	14
Figure 6 Substructure schematic of carbon particles (Vander Wal <i>et al.</i> 1999).	14
Figure 7 Soot formation scheme (adapted from Tree and Svensson, 2007).	15
Figure 8 HACA mechanism of polycyclic aromatic hydrocarbon formation (adapted from Wang and Frenklach 1997).	16
Figure 9 Direct ring-ring condensate of naphthalene from benzyl and propargyl (Colket <i>et al.</i> 1994).	17
Figure 10 Formation of naphthalene from combination of cyclopentadienyl radicals (oxidized benzene) (Castaldi <i>et al.</i> 1996).	17
Figure 11 Phenanthrene formation by combination of cyclopentadienyl and indenyl (oxidized naphthalene) (Castaldi <i>et al.</i> 1996).	17
Figure 12 Phenanthrene formation by cyclization by acetylene addition, following sequential addition of propargyl radicals to phenyl (D'anna <i>et al.</i> 2000).	17
Figure 13 Number of particles per aggregate as a function of non-dimensional length parameter L/d_p . (Adapted from Koylu <i>et al.</i> 1997).	20
Figure 14 Proposed multi-lognormal soot size distribution (Banerjee, Menkiel <i>et al.</i> 2009).	24
Figure 15 Multiple-hole injector fuel spray pattern captured in an optical access engine from below (left) and in profile (right) using a laser induced fluorescence technique, (adapted from Henle <i>et al.</i> 2005)..	29
Figure 16 Diagrammatic cross section scheme of laminar diffusion flame quasi-steady state combustion typical of a diesel direct injection engine, (D'anna <i>et al.</i> 2000).	30

Figure 17 Combustion phase evolution. (Adapted from Kosaka <i>et al.</i> 2005). _____	33
Figure 18 Spectrally resolved black-body radiation for a range of temperatures [K]. _	36
Figure 19 Variation of refractive index of dry air with temperature and pressure. ___	38
Figure 20 Phase diagram of carbon (Zazula 1997). _____	41
Figure 21 Summary timeline of developments within the field of LII. _____	51
Figure 22 Primary heat transport mechanisms for a single spherical, homogeneous soot particle. _____	57
Figure 23 Santoro burner (left) and cross sectional schematic (right). _____	78
Figure 24 Radial distribution of soot volume fraction for various heights above burner (HAB) (Adapted from Oger 2013). _____	80
Figure 25 Santoro burner with differential air flow entrainment. _____	81
Figure 26 Baffle and cylindrical shroud to facilitate symmetric airflow entrainment paths. _____	82
Figure 27 Normalized LII signal intensity with local laser fluence as recorded by various authors for a laser excitation wavelength of 532 nm. _____	83
Figure 28 Sheet forming optics assembly with cylindrical cover removed and illustrative overlay of laser path and profile. _____	85
Figure 29 (left) Laser beam profile incident upon a pinhole during assembly of experimental setup. _____	86
Figure 30 (right) Laser sheet without clipping in either axis, incident upon a target plate used for spatial calibration. _____	86
Figure 31 In-line energy monitor with associated beam splitting mirror assembly. Note, photodiode fitted via fourth port to junction block, detecting internal stray light. ____	87
Figure 32 Comparison of normalized temporal response of photodiode (solid) and normalized in-line energy monitor (dashed) to a 7 ns FWHM laser pulse. _____	87
Figure 33 Near top hat profile of clipped Gaussian beam/sheet profile. _____	88
Figure 34 Image doubler scheme with overlay depicting optical axes. _____	91
Figure 35 Variation of signal ratio with temperature of radiating body. Note, shallow gradient of blue (488 nm/655 nm) filter is due to broad collection interval (40nm FWHM) of divisor value of ratio. _____	92
Figure 36 Characteristic spectral sensitivity of Specialised Imaging SIM 16 camera. _	93
Figure 37 Spectral sensitivity of Hamamatsu H6780-02 type photomultiplier. _____	93
Figure 38 Qualitative radical emission intensity in the ultraviolet and visible spectrum. Adapted from data presented in (Gaydon 1957). _____	94

Figure 39 Qualitative florescent water molecule emission in the upper visible and infra-red spectrum. Adapted from data in (Gaydon 1957). _____	95
Figure 40 Spectral emissions encompassing ‘Swan bands’ due to C ₂ , CH, CN, and OH excitation. _____	95
Figure 41 Experimental configuration with camera acquisition axes highlighted. _____	98
Figure 42 Experimental configuration with photomultiplier acquisition branch highlighted. _____	99
Figure 43 Illustration of incident angle between acquisition axes for first experimental configuration. _____	100
Figure 44 (left) Typical radial extinction profile for 50mm HAB. (right) plan extinction factor filled contour plot with difference of signal trapping path lengths for a single acquisition channel disposed at angle α . Note the variation of extinction factor K_{ext} along signal trapping paths. _____	101
Figure 45 Second experimental scheme to eradicate differential signal trapping path effect. _____	102
Figure 46 Shot to shot laser fluence variation recorded using a calibrated in-line energy monitor. _____	104
Figure 47 Timing of fixed exposure duration experiment. _____	106
Figure 48 Timing of ramped exposure duration experiment. _____	107
Figure 49 Example timing of laser excitation, radiant emission and shutter opening curves. _____	108
Figure 50 Ratio of intensity of frame 3 to frame 4 versus synchronisation delay time for 488 nm acquisition filtered interval, for a range of primary particle diameters. _____	109
Figure 51 Proteus reciprocating rapid compression machine scheme with sectioned bore and optical chamber detail. Note, optical chamber and accesses depicted by yellow and blue overlay. _____	112
Figure 52 Sectioned view of optical chamber. Approximate fuel spray structure indicated in blue. _____	112
Figure 53 Laser optics and components. (left to right) Beam steering mirror housing, in line energy monitor, sheet forming optics assembly, adjustable width slit. _____	114
Figure 54 Signal magnitude for a range of filter specifications, for 4000 K black-body emission. _____	116
Figure 55 Signal ratio with temperature for 592nm/750nm filter pair. _____	117

Figure 56	Cuvette assembly in which two cuvettes, filled with a solution of Rhodamine 590 in ethanol are mounted. _____	118
Figure 57	Experimental scheme highlighting laser beam/sheet path. _____	120
Figure 58	Experimental scheme highlighting extinction branch apparatus. _____	121
Figure 59	Laser fluence variation across ensemble average LII data sets. _____	123
Figure 60	Timing of high pressure experiment _____	124
Figure 61	Flowchart of registration, dark field data averaging and hot pixel removal/hot pixel map creation. _____	129
Figure 62	Flowchart of LII data averaging, alignment and hot pixel removal. _____	130
Figure 63	Typical variation of signal to noise ratio ($20\log(X/\sigma)$) with binning factor. _____	131
Figure 64	Typical variation of signal to noise ratio ($20\log(X/\sigma)$) with pixel resolution. Note data point enumeration indicates binning factor n, where binned ‘superpixels’ are comprised of n by n pixels. _____	132
Figure 65	Uncaptured opening phase signal (the area $A/(A + B)$ in the figure), as a percentage of total incident signal for varying exposure duration, when photographing a constant emission source. _____	134
Figure 66	Scheme of distinction of transient and linear regions of response for 488nm band-pass filtered, intensified CCD to constant light source for a range of exposure durations. _____	136
Figure 67	Example shutter response curves for 488 nm centred spectral interval model solution algorithm. _____	137
Figure 68	Laser fluence profile across flame at 50mm height above burner (HAB). _____	138
Figure 69	Solution algorithm of D_{mono} particle size map at ambient conditions. _____	140
Figure 70	(left) An example data field for a 750 nm spectrally filtered peak intensity LII emission with, (right) a horizontal profile for row 55. _____	145
Figure 71	(left) shows the accumulation of extinction factor K_{ext} , as the soot plume is traversed, whilst (right) shows the resultant calculated distribution of laser fluence for the same path. _____	146
Figure 72	Solution algorithm of D_{mono} particle size map at high pressure conditions. _____	148
Figure 73	LII signal data, 488 nm spectrally filtered photomultiplier signals _____	156
Figure 74	LII signal data and filtering profiles. Grey data: 488 nm spectrally filtered photomultiplier signal, central black line: median average, upper black line: mean plus two standard deviations, lower black line: mean minus two standard deviations. _____	157
Figure 75	LII signal data, 647 nm spectrally filtered photomultiplier signals. _____	157

Figure 76 LII signal data and filtering profiles. Grey data: 647 nm spectrally filtered photomultiplier signal, central black line: median average, upper black line: mean plus two standard deviations, lower black line: mean minus two standard deviations. ____	158
Figure 77 Normalized ensemble averaged photomultiplier signals due to LII emissions. _____	159
Figure 78 Calculated temperature profile of 50 mm HAB, 2.4mm radius punctual measurement location. _____	159
Figure 79 Fit of modelled temperature change with time (grey curves) compared to measured temperature change through time. _____	160
Figure 80 (Left) Variation of the sum of Chi^2 ($\sum\chi^2$) with successive solution iterations. (Right) Variation of primary particle diameter (d_p) with successive solution iterations _____	161
Figure 81 Variation of (area normalized) multi-log-normal particle size distribution function with successive solution iterations. Black curve denotes the final solution value ($n=4$, $\sigma_1=0.2$ $\sigma_2=0.24$, presented by (Schraml <i>et al.</i> 1999)). _____	161
Figure 82 (Left) LII signal ensemble averaged (107 sets), through 488 nm centre wavelength spectral filter, 295 ns initial delay acquisition strategy _____	164
Figure 83 (Right) LII signal ensemble averaged (104 sets), through 488 nm centre wavelength spectral filter, 300 ns initial delay acquisition strategy _____	164
Figure 84 (Left) LII signal ensemble averaged (107 sets), through 647 nm centre wavelength spectral filter, 295 ns initial delay acquisition strategy. _____	165
Figure 85 (Right) LII signal ensemble averaged (104 sets), through 647 nm centre wavelength spectral filter, 300 ns initial delay acquisition strategy. _____	165
Figure 86 Primary particle diameters plot for (left) 295 ns and (right) 300 ns initial delay acquisition scheme. _____	166
Figure 87 Primary particle diameters plot for (top) 295 ns and (bottom) 300 ns initial delay acquisition scheme data, for height span 49.67 to 50.33 mm HAB. _____	166
Figure 88 Calculated primary particle diameter versus radius for data centred around 50 mm HAB, captured using 295 ns initial delay acquisition scheme. The average (solid line) and median (dashed) data were calculated using a 3 column by 5 row window. The grey envelope bounds indicate the average values \pm one associated standard deviation. _____	167
Figure 89 Calculated primary particle diameter versus radius for data centred around 50 mm HAB, captured using 300 ns initial delay acquisition scheme. The average (solid	

line) and median (dashed) data were calculated using a 3 column by 5 row window. The grey envelope bounds indicate the average values \pm one associated standard deviation. _____ 168

Figure 90 Comparison at 50mm height above burner (HAB) of the variation of primary particle diameter (d_p) with variation of radius from the flame centreline. _____ 172

Figure 91 LII image sequence (images 4 to 16) filtered via 592 nm wavelength centred band-pass filter. _____ 176

Figure 92 LII image sequence (images 4 to 16) filtered via 750 nm wavelength centred band-pass filter. _____ 177

Figure 93 Example florescence emission of Rhodamine 590 dye contained in two mounted cuvettes (left). Example extracted profile of fluorescent intensity excited by extinguished laser sheet (centre-right), and fluorescent intensity excited by unextinguished laser sheet (right). _____ 178

Figure 94 Example in cylinder pressure trace (ICP) resolved by crankshaft angle from TDC. Inset plot shows detail of peak pressure traces for ensemble cycles (grey) with average trace (black). _____ 179

Figure 95 Combustion event and acquisition signal synchronization. Injection driver current pre and main pulses (thin lines) and the corresponding in cylinder pressure trace (smooth continuous line). The trigger pulses $T_{Ref}=1.5$ ms (thick black line) and $T_{Ref}=1.7$ ms (dotted line) respectively place the acquisitions after the diffusion flame combustion phase. _____ 180

Figure 96 Primary particle diameter (d_p) false colour maps for ICP=40 bar, $P_{rail}=1000$ bar, at $T_{Ref}=1.5$ ms (left) and 1.7 ms (right). _____ 182

Figure 97 Peak intensity normalized late LII image. $T_{Ref}=1.5$ ms (left) and 1.7 ms (right).to characterize degree of persistence of LII radiant emission; greater intensity corresponds to larger primary particles, lesser intensity to smaller primary particles. 183

Figure 98 Histograms of primary particle diameter (D_{Mono}) for $T_{Ref}=1.5$ ms (blue) and $T_{Ref}=1.7$ ms (red). _____ 184

Figure 99 Combustion event and acquisition signal synchronization. $P_{rail}=1000$ bar (grey line), $P_{rail}=1300$ bar (black dotted line) and $P_{rail}=1600$ bar (black line), for both injection current driver pre and main pulses. An example fired in-cylinder pressure trace is presented although slight variation with injection timing variation is likely. _____ 185

Figure 100 Primary particle diameter (d_p) false colour maps for ICP=40 bar, at $P_{\text{rail}}=1000$ bar, $T_{\text{Ref}}=1.7$ ms(left), $P_{\text{rail}} =1300$ bar, $T_{\text{Ref}}=1$ ms (centre), and $P_{\text{rail}} =1600$ bar, $T_{\text{Ref}}=0.66$ ms (right).	186
Figure 101 Late LII sequence image 11 normalized by peak LII intensity image 4 to characterize degree of persistence of LII radiant emission; greater intensity corresponds to larger primary particles. $P_{\text{rail}}=1000$ bar $T_{\text{Ref}}=1.7$ ms (left), $P_{\text{rail}} =1300$ bar $T_{\text{Ref}}=1$ ms (centre), and $P_{\text{rail}} =1600$ bar $T_{\text{Ref}}=0.66$ ms (right), all at ICP=40 bar.	187
Figure 102 Histograms of primary particle diameter (D_{Mono}) for $P_{\text{rail}}=1000$ bar, $T_{\text{Ref}}=1.5$ ms (blue), $P_{\text{rail}}=1300$ bar, $T_{\text{Ref}}=1$ ms (green) and $P_{\text{rail}}=1600$ bar, $T_{\text{Ref}}=0.66$ ms (red)	188
Figure 103 Primary particle diameter (d_p) false colour maps for fuel injection rail pressure $P_{\text{rail}}=1000$ bar, at ICP=40 bar at $T_{\text{Ref}}=1.7$ ms (left), and at ICP=50 bar at $T_{\text{Ref}}=1.8$ ms (right).	189
Figure 104 Late LII sequence image 11 normalized by peak LII intensity image 4 to characterize degree of persistence of LII radiant emission; greater intensity corresponds to larger primary particles. $P_{\text{rail}}=1000$ bar with ICP=40 bar, $T_{\text{Ref}}=1.7$ ms (left) and ICP=50 bar, $P_{\text{rail}} =1000$ bar $T_{\text{Ref}}=1.8$ ms (right).	190
Figure 105 Histograms of primary particle diameter (D_{Mono}) for ICP=40 bar, $T_{\text{Ref}}=1.7$ ms (blue) and ICP=50 bar, $T_{\text{Ref}}=1.8$ ms (red).	191
Figure 106 LII radiant emission via 592 nm centre wavelength filter (left) and 750 nm centre wavelength filter (right) for ICP=40 bar, $P_{\text{rail}}=1000$ bar, $T_{\text{Ref}}=1.7$ ms, for data set 58.	192
Figure 107 Primary particle diameter (d_p) false colour map for conditions of ICP=40 bar, $P_{\text{rail}}=1000$ bar, $T_{\text{Ref}}=1.7$ ms for a selected data set 58 (left). Late LII image 11 normalized by image 4 (right) to characterize degree of persistence of LII radiant emission; greater intensity corresponds to larger primary particles.	193
Figure 108 Histograms of primary particle diameter (D_{Mono}) for individual data set 58 (blue) versus ensemble average data (red), at ICP=40 bar, $P_{\text{rail}}=1000$ bar, $T_{\text{Ref}}=1.7$ ms.	194
Figure 109 LII radiant emission via 592 nm centre wavelength filter (left) and 750 nm centre wavelength filter (right) for ICP=40 bar, $P_{\text{rail}}=1300$ bar, $T_{\text{Ref}}=1$ ms, for data set 28.	195

Figure 110 Primary particle diameter false colour map for conditions of ICP=40 bar, RP=1300 bar, TRef=1 ms for data set 28 (left). Late LII image 11 normalized by image 4 (right) to characterize degree of persistence of LII radiant emission; greater intensity corresponds to larger primary particles, lesser intensity to smaller primary particles. 196	196
Figure 111 Histograms of primary particle diameter (D_{Mono}) for individual data set 28 (blue) versus ensemble average data (red), at ICP=40 bar, $P_{\text{rail}}=1300$ bar, TRef=1 ms. _____	197
Figure 112 LII radiant emission via 592 nm centre wavelength filter (left) and 750 nm centre wavelength filter (right) for ICP=50 bar, $P_{\text{rail}}=1000$ bar, TRef=1.8 ms, for data set 1. _____	198
Figure 113 Primary particle diameter false colour map for conditions of ICP=50 bar, RP=1000 bar, TRef=1.8 ms for data set 1 (left). Late LII image 11 normalized by image 4 (right) to characterize degree of persistence of LII radiant emission; greater intensity corresponds to larger primary particles. _____	199
Figure 114 Histograms of primary particle diameter (D_{Mono}) for individual data set 1 (blue) versus ensemble average data (red), at ICP=50 bar, $P_{\text{rail}}=1000$ bar, TRef=1.8 ms. _____	200
Figure 115 LII radiant emission via 592 nm centre wavelength filter (left) and 750 nm centre wavelength filter (right) for ICP=40 bar, $P_{\text{rail}}=1600$ bar, TRef=0.66 ms, for data set 33. _____	201
Figure 116 Primary particle diameter false colour map for conditions of ICP=40 bar, $P_{\text{rail}}=1600$ bar, TRef=0.66 ms for data set 33 (left). Late LII image 11 normalized by image 4 (right) to characterize degree of persistence of LII radiant emission; greater intensity corresponds to larger primary particles. _____	202
Figure 117 Histograms of primary particle diameter (D_{Mono}) for individual data set 33 (blue) versus ensemble average data (red), at ICP=40 bar, $P_{\text{rail}}=1600$ bar, TRef=0.66 ms. _____	203
Figure 118 LII radiant emission via 592 nm (left) and 750 nm (right) filter for TRef=1.5 ms acquisition trigger signal timing (ICP=40 bar, $P_{\text{rail}}=1000$ bar). _____	217
Figure 119 LII radiant emission via 592 nm (left) and 750 nm (right) filter for TRef=1.7 ms acquisition trigger signal timing (ICP=40 bar, $P_{\text{rail}}=1000$ bar). _____	218
Figure 120 LII radiant emission via 592 nm centre wavelength filter (left) and 750 nm centre wavelength filter (right) for $P_{\text{rail}}=1000$ bar, TRef=1.5 ms. _____	219

Figure 121 LII radiant emission via 592 nm centre wavelength filter (left) and 750 nm centre wavelength filter (right) for $P_{\text{rail}}=1300$ bar, $T_{\text{Ref}}=1$ ms, $ICP=40$ bar. _____	220
Figure 122 LII radiant emission via 592 nm centre wavelength filter (left) and 750 nm centre wavelength filter (right) for $P_{\text{rail}}=1600$ bar, $T_{\text{Ref}}=0.66$ ms. _____	221
Figure 123 LII radiant emission via 592 nm centre wavelength filter (left) and 750 nm centre wavelength filter (right) for $ICP=40$ bar, $P_{\text{rail}}=1000$ bar, $T_{\text{Ref}}=1.7$ ms, $ICP=40$ bar. _____	222
Figure 124 LII radiant emission via 592 nm centre wavelength filter (left) and 750 nm centre wavelength filter (right) for $ICP=50$ bar, $P_{\text{rail}}=1000$ bar, $T_{\text{Ref}}=1.8$ ms. _____	223

List of Tables

Table 1 EURO emission standard comparison. _____	3
Table 2 Comparison between author's conduction model regimes, model dependencies and thermal accommodation coefficient α_T . _____	64

Nomenclature

C_{expl}	experimentally-derived calibration constant encompassing all effects of signal collection optics efficiency and geometry, soot emissivity and excitation
C_3	constant of proportionality of LII radiance to extinction
C_{abs}	absorption cross section [m^2]
$C_{abs,recrystallized}$	absorption cross section of recrystallized carbon [m^2]
C_{abs}'	annealing process modified absorption cross section [m^2]
$C_n(t)$	soot particle number density [m^{-3}]
C_p	specific heat of soot at constant pressure [$J.kg^{-1}.K^{-1}$]
C_p^{CO}	specific heat capacity of carbon monoxide [$J.kg^{-1}.K^{-1}$]
C_s	specific heat capacity of solid phase carbon [$J.kg^{-1}.K^{-1}$]
C_v	specific heat of soot at constant volume [$J.kg^{-1}.K^{-1}$]
D_{fr}	fractal dimension
d_p	mean primary particle diameter [m]
E_{LII}	irradiance due to incandescence [$W.sr^{-1}.m^{-2}$]
F	laser fluence [$J.cm^{-2}$]
f	Euchen factor [#] (Chapman <i>et al.</i> 1970)
f_v	soot volume fraction
G	geometric heat transfer factor [#]
I	extinguished laser fluence [$mJ.cm^{-2}$]
i	image sequence frame number
I_0	unextinguished laser fluence [$mJ.cm^{-2}$]
$I_\lambda(T)$	spectral radiance [$J.s^{-1}.m^{-2}.sr^{-1}.m^{-1}$ or $W.m^{-3}.sr^{-1}$]
$I_{\lambda,GB}$	grey body spectral radiance [$J.s^{-1}.m^{-2}.sr^{-1}.m^{-1}$ or $W.m^{-3}.sr^{-1}$]
k_{con}	thermal conductivity [$W.m^{-1}.K^{-1}$]
k	complex component magnitude of refractive index
K_{abs}	absorption coefficient
K_{ext}	extinction coefficient
K_{fr}	fractal prefactor
K_n	Knudsen number [#]
k_{OX}	Oxidation coefficient [$kg.m^{-2}.mol^{-1}.s^{-1}$]
K_{scat}	scattering coefficient
L	optical path-length through emission structure as presented to acquisition [m]
L_{kn}	system characteristic length [m]

m	complex refractive index
$m_{\text{constituent}}$	mass of constituent [kg]
N	number of incident photons
$\frac{dN_{\text{photon}}}{dx}$	rate of absorption along an incidental path [m^{-1}]
n_{mol}	number of molecules per unit volume [m^{-3}]
n	real component of refractive index
n_{dist}	count of log normal distributions
N	particle number
N_d	particle number per unit volume [m^{-3}]
N_p	number of primary particles per unit volume [m^{-3}]
N_{photon}	number of incident photons
$(n-1)S$	increase of refractive index of air at standard temperature and pressure, relative to refractive index of free space
$(n-1)tp$	increase of refractive index in dry air relative to refractive index in free space
p	pressure [Pa]
$P(r)$	probability density function
$p(r)_N$	normalized size distribution/probability density function
P^*	reference pressure for soot vaporization temperature, T^* . [Pa]
P_0	ambient pressure [Pa]
$q(t)$	temporal laser intensity profile [$\text{J}\cdot\text{s}^{-1}\cdot\text{cm}^{-2}$]
\vec{q}	heat flux [$\text{W}\cdot\text{m}^{-2}$]
q_{exp}	experimental temporal profile of laser fluence [$\text{J}\cdot\text{s}^{-1}\cdot\text{cm}^{-2}$]
q_x	heat flux parallel to the heat flux parallel to the spatial dimension [$\text{W}\cdot\text{m}^{-2}$]
r	particle radius [m]
R_g	radius of gyration [m]
$r_{i,\text{cmd_multi}}$	count median radius [m]
r_{mode}	modal particle radius, [m]
S_{LII}	temporally integrated, temporally gated LII signal [Counts]
T	temperature of the black-body [K]
$\frac{dT}{dx}$	temperature gradient parallel to the spatial dimension [$\text{K}\cdot\text{m}^{-1}$]
∇T	temperature gradient [$\text{K}\cdot\text{m}^{-1}$]
T^*	Soot vaporisation temperature [K]
T_0	ambient temperature [K]
T_a	apparent temperature [K]
T_c	is temperature [C]
t_{centre}	is the time at which the laser intensity is at its peak value
U_{sub}	rate of sublimation [$\text{Kg}\cdot\text{s}^{-1}$]

U_v	vapour phase velocity [m.s^{-1}]
v	is the phase velocity [m.s^{-1}]
V_{measure}	is the volume of measurement [m^3]
$W(t)$	signal windowing function
W_s	molar mass of sublimated carbon [kg.mol^{-1}]
W_s	molecular weight of carbon solid [g.mol^{-1}]
W_v	molar mass of carbon vapour [g.mol^{-1}]
X_{ann}	recrystallized carbon mass ratio
$X_{\lambda,i}$	LII data pixel value for spectral interval centre wavelength λ
α	wavelength variant empirically derived factor [-]
α_T	thermal accommodation coefficient
α_λ	monochromatic absorptivity
γ	heat capacity ratio [#]
ΔH_{OX}	enthalpy of oxidation [J.kg^{-1}]
ΔH_{sub}	heat of vaporization of carbon = $7.78 \times 10^5 \text{ J.mol}^{-1}$
Δh_{sub}	sublimation enthalpy [J.Kg^{-1}]
ΔH_v	enthalpy of vaporisation [J.mol^{-1}]
ε	statistical variation
ε_λ	monochromatic emissivity
λ_{em}	acquisition wavelength [nm]
ρ_s	density of solid phase carbon [kg.m^{-3}]
ρ_v	density of vapour phase carbon [kg.m^{-3}]
σ	absorption cross section [m^2]
σ_0	(zero order) probability distribution width.
σ_A	mean molecular cross section of surrounding gas
$\sigma_{g,i}$	geometric standard deviation
σ_i	distribution width parameter
σ_{sb}	density of solid carbon in grams per centimetre cubed, 2.26 [g.cm^{-3}]

Acknowledgements

In addition to faultless academic support, Dr Cyril Crua demonstrated patience, understanding and kindness throughout my Ph.D study period. I am grateful to an extent that defies communication. Professor Morgan Heikal's encouragement and incisive provision of guidance at key moments has been highly appreciated. I am fortunate to have met Dr Beniot Oger; simultaneously technically competent, generous, and enjoyable to work with. I hope to do so again one day.

Mr Ken Maris, Mr Brian Maggs, and in the later years, Mr Peter Rayner, made my experimental work possible by excelling in their respective technical roles. It is my long held belief that each could have ably performed my work, whereas my skills deficit would have become apparent for the reciprocal arrangement. What will the world be like when all the authentically capable individuals retire, I wonder?

I would like to express my gratitude to members of staff from the University of Brighton Doctoral College. Mrs Ursula O'Toole, Dr Susan Sandeman, and Professor Neil Ravenscroft; I thank you all for your support. However, it is my sense of indebtedness to Miss Alice Parks that is most distinct and whose efforts on my behalf have been numerous. I thank you most sincerely.

Dr Ana Maria Denis Bacelar, whom I met at the University of Brighton, and shall with her consent, be with hereafter, has been unrelentingly supportive and has served as a much needed reference point of sanity throughout. Nobody should doubt your significance to me.

Four VIP's, Ross, Lenny, Berty and Keri, have all uniquely provided me with support and encouragement; they constitute the otherwise undocumented positive forces acting upon my life.

In the time that I have undertaken this study, I have lost two friends to cancer. Katrina Colburn was a kind hearted and witty veterinary nurse whose life was far too short and all too incomplete of experiences. Austin Clarke was an electrical engineer and programmer. His awareness of nuance and detail occasionally seemed incongruous with his often ebullient manner, but was manifest in both his work and the incisiveness of his humour. I miss them both and will remember them vividly.

Declaration

I declare that the research contained in this thesis, unless otherwise formally indicated within the text, is the original work of the author. The thesis has not been previously submitted to this or any other university for a degree, and does not incorporate any material already submitted for a degree.

Signed

Dated

1 Introduction

1.1 Background

Diesel engine tailpipe emissions are comprised of both gaseous and solid phase materials. Of the gaseous phase materials, oxides of carbon (CO_x), nitrogen (NO_x) and sulphur are amongst those of interest. Carbon dioxide (CO_2) is produced in direct proportion to the quantity of fuel consumed in complete stoichiometric combustion, whereas carbon monoxide (CO), sulphur dioxide (SO_2) and the various oxides of nitrogen constitute the undesirable products of incomplete non-stoichiometric combustion.

For complete diesel combustion, each gram of fuel burnt produces approximately 3.14 grams of CO_2 . Reduction of carbon dioxide therefore necessarily relates to the reduction in the quantity of fuel used for a given motive purpose; the appetite for ever more efficient diesel combustion systems persists and any improvements in terms of the reduction of other emission types must be weighed against any decrease in overall efficiency.

Whilst all the gaseous phase emissions are undesirable in that they contribute towards the effect upon the environment, termed climate change, it is the solid particulate emissions about which concern as to their harmful effects has recently become elevated. Solid phase particulate matter (PM) emissions are soot particulates that contain carcinogens, mutagens and toxins and have a detrimental effect upon the pulmonary system (Inagaki *et al.* 1998, Fann *et al.* 2012), cardiovascular and nervous system (Politis *et al.* 2008) of living mammalian organisms. Soot is principally agglomerated carbon spherules that contain small proportions of metals from engine wear, Sulphur, and hydrocarbon compounds from incompletely combust fuel. Soot particle toxicity is principally due to the presence of hydrocarbon compounds, sulphur and metallic ashes.

Particles of 10 μm diameter and less (PM_{10}) are considered capable of respiratory system ingress. In particular, particles of diameter of 2.5 μm and less ($\text{PM}_{2.5}$) exhibit a degree of buoyancy that prolongs their suspension in the atmosphere, increasing the likelihood of inhalation. Once inhaled, incursion as far as the alveoli within the lungs may occur for the smallest particles (Oberdörster 2000) where expulsion by the host, from what is a region of delicate cells, does not readily occur; typically, mucociliary transport and

coughing remove particles larger than 5 μm only (Kreyling *et al.* 2006). In humans, respiratory problems ranging from the stimulation of pre-existing conditions such as asthma, to cell mutations promoting lung carcinomas and other cancers, can occur as a result of the production, transportation and subsequent inhalation of soot particulates. Figure 1 illustrates the deposition of a range of small particle diameters within the human pulmonary system. A significant proportion of the smallest particles (10 to 100 nm diameters) deposit in the most sensitive cellular region (alveoli).

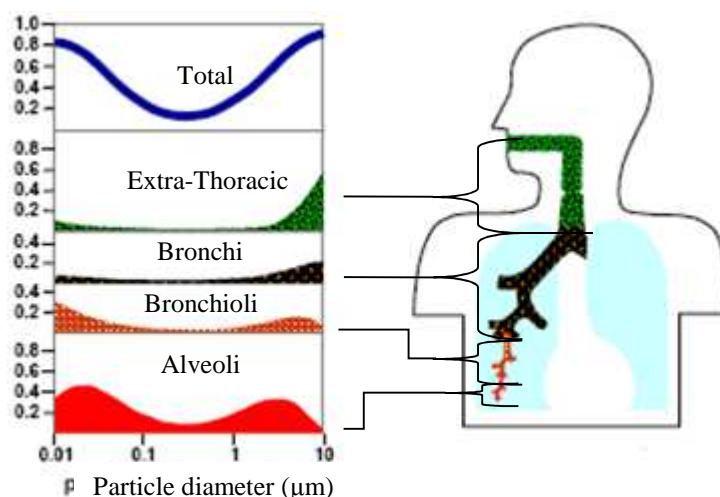


Figure 1 The particle deposition upon the pulmonary system versus particle diameter. Adapted (ICRP 1994) & (Price *et al.* 2002).

More recently, studies have concluded that both the size range and composition are of relevance when attempting to characterize the burden upon human health of airborne particulate materials (Limbach *et al.* 2007). Notably, $\text{PM}_{2.5}$ size range particles produced through incomplete hydrocarbon combustion are considered most hazardous due to their combination of uninhibited ingress into the body as well as their chemical composition and possible catalytic agency. (Janssen *et al.* 2011), suggests black carbon content as an additional indicator of adverse health effects. This suggests a strong correlation between the degree of hazardousness to human health and the compositional similarity of particulate matter to that produced by incomplete combustion of diesel fuel.

The automotive industrial sector is therefore quite correctly charged with contributing to these emissions and there exists considerable will, both from within and externally, to

reduce emission levels. Legislation in the territories in which manufacturers wish to sell vehicles defines the permissible levels of emission of various tailpipe constituents. For example, for the United States of America, the Environmental Protection Agency (EPA) defines nationally applicable standards, termed ‘Tier’ that are divided into numerous sub-categories, termed ‘Bins’, that differ between vehicle size, type and cargo capacity, and specify limits of permissible emission levels of CO, NO_x, PM, non-methane organic gases and non-methane hydrocarbons. Tier 1 was introduced between 1994 and 1999 and was superseded by Tier 2, introduced between 2003 and 2009. Tier 2 additionally restricts the sulphur content of both gasoline and diesel fuels such that widespread adoption of (sulphur intolerant) exhaust after-treatment apparatus including particulate filters and selective catalytic converters is possible. As of 2009, it would seem that the more stringent Low Emission Vehicle II standards defined by the California Air Resources Board (CARB) are in future to be adopted nationwide.

Emissions standard (introduced)	Diesel			Gasoline		
	Particulate Matter (PM) [mg.km ⁻¹]	Oxides of nitrogen (NO _x) [mg.km ⁻¹]	Hydrocarbons (HC) [mg.km ⁻¹]	Particulate Matter (PM) [mg.km ⁻¹]	Oxides of nitrogen (NO _x) [mg.km ⁻¹]	Hydrocarbons (HC) [mg.km ⁻¹]
Euro 1 (1992)	140	970		-	970	
Euro 2 (1996)	100	700		-	500	
Euro 3 (2000)	50	500	-	-	150	200
Euro 4 (2005)	25	250	-	-	80	100
Euro 5 (2009)	5	180	-	5	60	100
Euro 6 (2014)	5	80	-	5	60	100

Table 1 EURO emission standard comparison.

European legislation upon vehicle emissions has been in effect for the past two decades and has dictated a steady reduction in emissions of all vehicles sold and operated within Europe. Of note, and depicted in Table 1, is the universal limit of 5 mg per kilometre of

particulate matter, introduced as of Euro 5. This limitation is maintained for the Euro 6 standard, but associated with a further decrease of NO_x for diesel fuel powered vehicles. No legislation as to the particulate matter population, in particular the particle size distribution, is currently enacted allowing the implementation of operating strategies (typically higher injection pressures) to reduce particle sizes as a means of total particle population mass reduction. Yet, ever greater focus upon the effects and concentrations of PM_{2.5} and ultra-fine particles (UFP) (Limbach *et al.* 2007), particularly in heavily populated areas, will no doubt lead to a more widespread appreciation of the hazards they pose and codification (perhaps within Euro 6) of appropriate constraint upon their emission into the atmosphere. As of 2009, the World Health Organisation (WHO) estimated that 373,000 premature deaths occurred for the year 2005, or 830 per million inhabitants, that can be attributed to anthropogenic emissions of primary PM and PM precursors (Fiala *et al.* 2009). For the year 2000, the average life span of a European inhabitant (EU-25) was reduced 8.1 months (2005).

The so called ‘NO_x-Soot trade-off’ encapsulates the idea that either combustion by-product can be reduced but at the cost of an increase in the formation of the other. Whilst it is possible to filter out these undesirable elements with exhaust ‘after-treatment’ apparatus such as a Diesel Particulate Filter (DPF) and Lean NO_x Trap (LNT), it is less costly and more efficient to abate their production due to the combustion process. Additionally, given that CO₂ emissions are not legislated for, but are reported for each vehicle within the retail arena, pressure is indirectly exerted upon the automotive industry to produce ever-lower CO₂ emission vehicles, whilst simultaneously adhering to the Euro legislation. It is therefore no longer an option to trade lower overall diesel powertrain efficiency against simultaneously meeting both NO_x and soot (PM) limits.

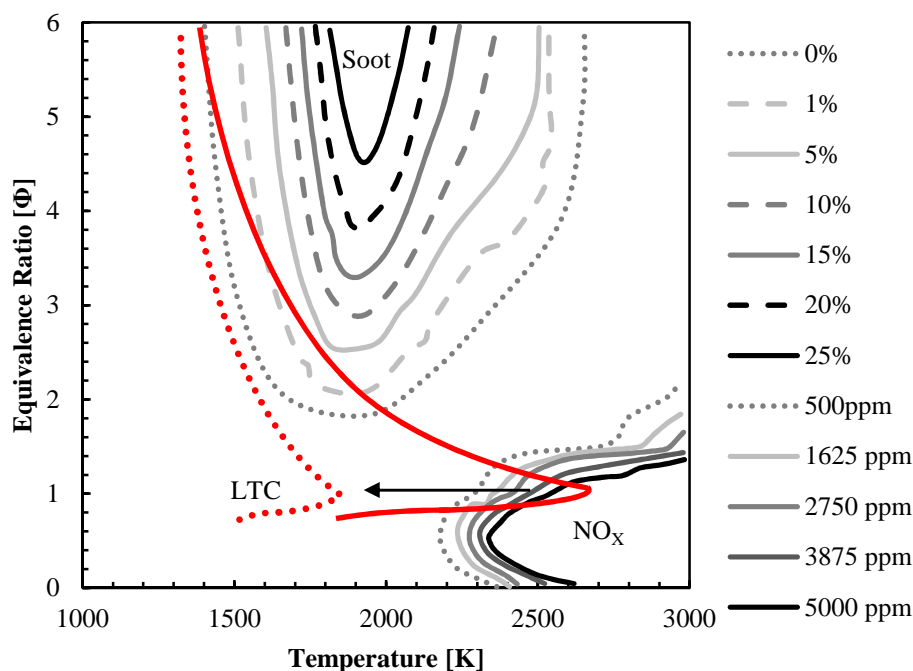


Figure 2 Equivalence ratio versus temperature operation map, illustrating soot and NO_x islands (adapted from Akihama *et al.* 2001).

So called ‘low temperature combustion’ (LTC) strategies in which a comparatively low in-cylinder temperature is achieved through the employment of low compression ratios more typical of gasoline engines, or through the extensive use of exhaust gas recirculation (EGR), result in reduced NO_x formation without increasing soot emissions. Figure 2 shows typical diesel engine characteristic soot and NO_x island regions upon a temperature versus equivalence ratio graph ($T-\Phi$). The dotted red curve illustrates an operating point contour for a LTC strategy, distinct from a more typical (solid red) combustion strategy contour. LTC strategies, evidently have more impact upon NO_x than soot production, however research upon the effect of EGR upon the local oxygen concentration and therefore completeness of combustion and soot production is the subject of many research efforts (Gao *et al.* 2001, Alriksson *et al.* 2005, Idicheria *et al.* 2005, Idicheria *et al.* 2007, Al-Qurashi *et al.* 2011). However, overall combustion efficiency is reduced and the undesirable effect of the increase of unburnt hydrocarbon emissions is manifest for low temperature combustion regimes due to the effects of ‘over-mixing’ (Koylu *et al.* 1997).

It is therefore preferable to seek to optimize the combustion process to simultaneously meet these conflicting requirements. In order to do this, a detailed model of soot formation, in terms of all the parameters that affect it is the aim of considerable research efforts. The subsequent aim is to more fully understand and characterize the effects of all aspects of the design and geometry of an engine, and the combustion strategy employed, upon the formation, destruction and emission of soot particles. Furthermore, to quantify the effects upon the specific characteristics of the produced soot population; specifically, the particle size range and the quantity of particles of each size produced.

The competing formation and destruction mechanisms that occur for soot production within the combustion cycle and the effects upon these mechanisms due to the variation of the fuel injection event and the condition of the induced air are therefore the foci of numerous research efforts. Tailpipe sampling for exhaust constituents disregards the spatial and temporal distributions within the combustion chamber during the combustion event and accordingly offers limited insight into soot formation and destruction processes. Also, the soot particle population will have changed considerably by the time it has completed the journey from combustion chamber to atmosphere due to the different and changing conditions experienced along the extent of the exhaust apparatus and the different parameter dependencies of the various formation and destruction mechanisms occurring throughout. In summary, a complex scheme in which the conditions experienced throughout the entire lifespan of the soot particles must be considered as contributory factors to the development of the resultant particulate population discharged to the atmosphere.

Optical investigative techniques however, have several inherent advantages. They allow spatially and temporally varying phenomena to be measured. They allow sensitive and often delicate measurement equipment to be situated at some practical distance from that which is to be measured, and when comprising a purely passive detection technique, do not perturb that which is to be measured. For the investigation of the in-cylinder formation and destruction processes of soot, laser induced incandescence (LII), whilst necessarily affecting that which is of interest by imparting energy to it, can constitute a powerful diagnostic technique provided care is taken to understand and minimize the perturbing effects upon the subject.

At present, LII is an emergent technique for soot diagnostics. Many authors and experimentalists have sought to improve upon and refine both the theoretical foundations and the experimental application of the technique. A transition in this developmental path of particular note is that of moving from a qualitative technique to a fully quantitative technique. This is far from straightforward and many aspects that were previously disregarded are necessarily reconsidered. For a qualitative technique, an acceptable outcome may be the successful capture of an incandescence signal that illustrates the presence of some unknown quantity and population distribution of soot particles. This is an appropriate formative step in the development of the technique. A 'relative' quantitative or fully quantitative measurement technique is however possible through the employment of simultaneous measurements or expanding the LII measurement domain to encompass temporal variation of radiated energy.

LII is not of itself a technique; it is the process of elevating a soot particles internal energy until radiated electromagnetic spectral emissions occur. If a sufficiently intense laser beam is incidental with a soot population, a region encompassed by the beam profile will absorb energy at a high enough rate that the temperature of the soot particles will increase rapidly. As the temperature increases, the heat transfer mechanisms of radiation, conduction and sublimation impart energy from the particles to the surrounding medium. The radiated emission is very nearly in proportion to the volume of particles and the fifth power of temperature.

A qualitative measurement of a single data value at a point location offers limited insight into the nature of the subject. More typically, a planar measurement may be made using a sheet profile laser for excitation and a monochrome camera, positioned normally to both laser propagation axis and sheet profile major axis. Referred to as two dimensional laser induced incandescence (2D-LII), the scheme allows the capture of the emission signal accumulation that occurred for the span of the image exposure time duration at each pixel location. This near planar incandescence signal image will depict the presence of soot and spatial resolve the relative signal intensity. If radiant emissions are simultaneously captured over two spectrally filtered intervals, the two signals may be used to establish the spatially resolved average particle temperatures in the imaged plane at each location.

This technique has been used in conjunction with simultaneous capture of the planar resolved elastic light scattering (ELS) signal. A ratio of LII and ELS signal yields the relative primary particle diameter at each pixel location.

Time-resolved laser-induced incandescence (TiRe-LII) is a significantly different utilisation of the radiated emission signal whereby the temporally changing signal is recorded and used to calculate the primary particle diameter. This, almost universally, has been conducted using photomultipliers to measure the radiated emission at a point location within an incandescing soot structure. TiRe-LII is based upon the principle that a particles rate of cooling is dependent upon its diameter. The temperature history of an incandescing particle may be calculated by capturing two discrete spectral intervals of radiation and applying the principle of two colour pyrometry. The primary particle diameter is not directly calculable. An indirect problem is established whereby the temporal evolution of temperature and particle diameter is simultaneously modelled. An iterative algorithm adjusts the model primary particle diameter until a best fit of temperature history is achieved.

For all variants of LII, laser fluence is important in that it can affect the composition and structure of the soot agglomerates with which it is incident. A suitably low rate of energy transfer is necessary such that the soot particles internal energy, and therefore temperature, does not rise too much. Elevation of temperature beyond the vaporisation threshold of carbon, approximately 3900 K at typical atmospheric pressure, likely changes the nature of the soot population; the smallest particles are completely vaporized whilst larger particles are reduced in diameter.

The technique cannot be considered truly non-invasive since it perturbs that which it is attempting to measure. To establish the soot volume fraction or any other convenient soot concentration measurement, an absolute signal intensity calibration must be performed. This allows the absolute quantity of particles of each size (within the previously established size distribution interval) to be calculated. The sum of the particles volumes within the measurement volume is the soot volume fraction at that location.

Both approaches, temporal or spatial, provide insight into a particular aspect of the subject of interest; an absolute punctual measurement or a relative quantitative planar resolved measurement. With regards to gaining insight into the nature of the soot produced in

internal combustion engines, the usefulness of a technique that may produce planar, spatially resolved measurements of absolute primary particle diameter, should be self-evident. The range of soot particle sizes present, the number of each particle size, and their location relative to other parts of the combustion system such as chamber and piston crown geometry and fuel spray structure, are fundamental to the understanding and refinement of a holistic combustion system model.

This thesis is focused upon refining and applying a quantitative, spatially and temporally resolved technique at both atmospheric and subsequently elevated pressures that constitute realistic operating conditions, through the use of ultra-high-speed imaging equipment.

1.2 Structure of the thesis

The theoretical background to this work is presented in chapter two. The findings of a literature survey upon the subjects soot, heat transfer, the various forms of LII, both theoretical and experimentally applied, are presented therein.

Chapter three addresses the experimental work of both the atmospheric condition, validation experiment and the diesel engine conditions, technique application experiment. Apparatus design and configuration is presented in addition to the experimental procedures employed.

Chapter four addresses various aspects of the data processing and solution algorithms used to generate the results data that is presented in chapter five.

Chapter five presents the processed results of both validation and application experiments as well as a discussion upon efficacy of the technique with a view to informing future research efforts utilizing the working principles of the experimental technique and associated data processing routines.

Chapter six concludes the work presented herein, presenting a summary of the successes and framing the outstanding challenges for future work upon the subject.

1.3 Objectives

The principle objective of the work presented in this thesis is to present a new form of an optical diagnostic technique that enables new insight into the nature of the solid matter products of direct injection combustion, particularly those formed in diesel internal combustion engines.

Specific initial objectives were:

- To have developed the acquisition technique such that data of sufficient quality to enable analysis, is recorded.
- To develop a technique this is effective when applied to the soot structures produced in high pressure combustion events.
- To develop and apply data pre-processing routines of sufficient subtlety to maintain captured signal whilst removing obfuscating signal content from necessarily low signal to noise ratio data.
- To develop and apply a heat transfer expression derived model for extracting particle primary diameter.
- To extend and apply the primary particle diameter yielding model to that of a particle size distribution interval.

2 Theoretical background and review of literature

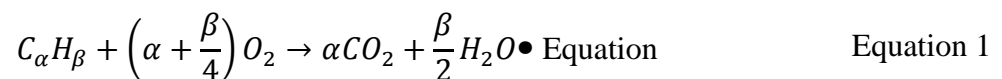
2.1 Introduction

The progression of the consensus of understanding and conceptualization regarding the nature of soot and the methods employed to study it, warrants a summary of foundation concepts and working principles. The nature of soot particles and the characteristics of soot particle populations produced during combustion events are addressed. The evolution of the nature of both individual soot particles and soot particle populations are addressed in terms of the competitive formative and destructive mechanisms that occur. In particular, the effect of the environmental parameters upon those processes and the resultant soot population distribution and agglomerated structures, are characterized. Pertinent concepts pertaining to the physics of optics, the mechanisms of heat transfer, the nature of flame structures, diesel combustion, pyrometry and laser induced incandescence are addressed thereafter.

2.2 Soot

Soot is the name given to carbonaceous agglomerates that are produced during the combustion of hydrocarbon fuels. Whilst regarded as not well defined (Svensson 2005), it is suggested that it is a solid insoluble substance composed of roughly eight carbon atoms and a single hydrogen atom C_8H (Melton 1984). A representative particle molecular composition was produced (Idicheria *et al.* 2005) in which 88.3% comprised carbon, 1.2% metals, with the remainder consisting of Oxygen (4.9%), Nitrogen (0.5%), Hydrogen (2.6%) and Sulphur (2.5%).

Theoretically perfect combustion occurs when a stoichiometric mixture of oxidant and fuel are presented to the combustion region. Such a reaction can be described by the reaction path equation:



Carbon dioxide and water are produced, in addition to the desired release of energy. However, when a localized region has an excess of fuel relative to oxidant, incomplete combustion occurs in which some proportion may be left unburnt or partially burnt but where the reaction pathway in which CO is produced, is dominant (Equation 2). For the unburnt or partially burnt fuel, a pyrolytic reduction to more simple molecules may also occur, yielding an excess of carbon atoms that unless consumed by a subsequent reaction, contribute to the formation of soot precursors. Other hydrocarbons or available molecules can be absorbed or condensed onto the resulting carbon solid.



Typically, particulate matter is regarded as the insoluble constituent soot and other particles such as unburnt and partially burnt hydrocarbons and lubrication oil, bound water, wear metals and sulphate.

2.2.1 Morphology

Throughout the formation processes, soot or its precursors assume structures that are difficult to define to a completely satisfactory extent. Agglomeration of primary particles into clusters of between 10^5 and 10^6 carbon atoms occurs. Agglomerated soot particles can be composed of up to 4000 spherule-like particles and may form structures that are from 10 to 1000 nm long.

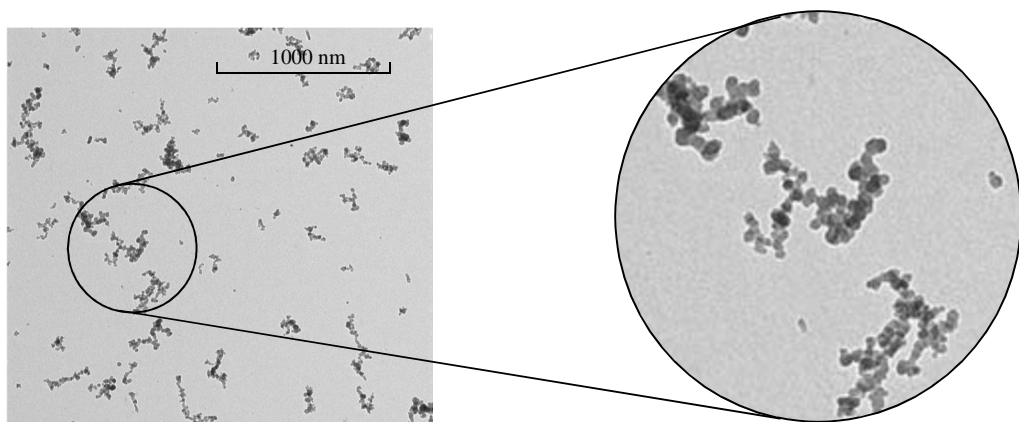


Figure 3 TEM images of soot agglomerates imaged using transmission electron microscopy (adapted from Snelling, Liu *et al.* 2004).

Whilst the particle diameter range may span between 10 and 80 nm, the majority are between 15 to 30 nm in size (Amann *et al.* 1981). A tailpipe sampling probe and laser elastic scattering based size measurement technique has yielded a size range of 30 to 70 nm (Bruce *et al.* 1991). In-cylinder laser elastic scattering experiments in diesel engines have resulted in 30-50 nm (Tree *et al.* 1994) and 40-65 nm (Pinson *et al.* 1994) range of particle sizes. The agglomerated soot particles that are formed by the end of the combustion process have been determined to be in the order of 100 nm to 2 μm in size (Ladommatos *et al.* 1994, Vander Wal *et al.* 1999, Desantes *et al.* 2005).

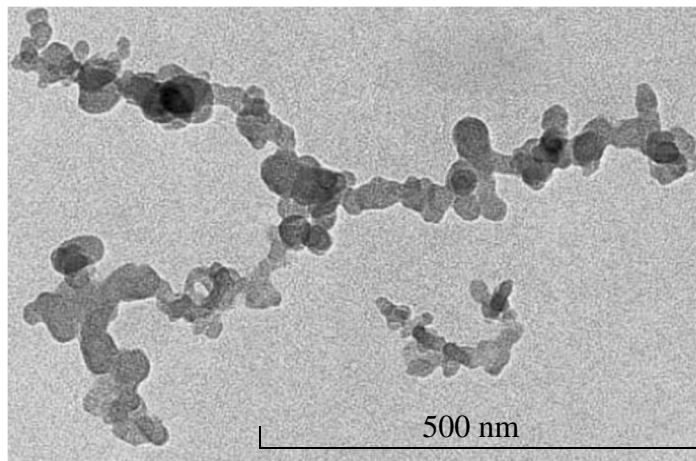


Figure 4 TEM image of chain like agglomerates of Diesel soot (adapted from Wentzel *et al.* 2003).

Figure 5 shows the turbostratic structure within a soot spherule. It has widely been likened to an ‘onion’ structure in that it is composed of thousands of unordered shells or layers of smaller crystallite structures.

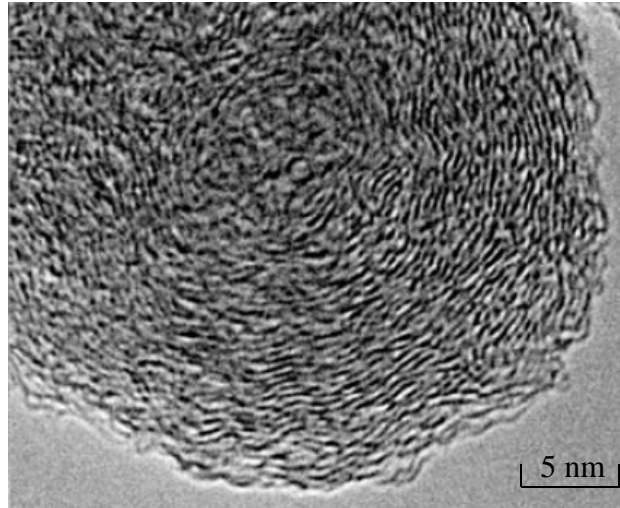


Figure 5 Soot spherule composed of nanocrystalline graphitic carbon and portraying an onion shell type structure.

Crystallite structures are themselves composed of between two and five platelets which are hexagonally face centred plane arrays of carbon atoms illustrated in Figure 6. Though physically and chemically distinct from soot (Watson *et al.* 2001), and particularly soot produced through diesel combustion (Clague *et al.* 1999), carbon black has typically been used as an experimental analogue. For carbon black, platelet separation is typically between 0.35 and 0.36 nm.

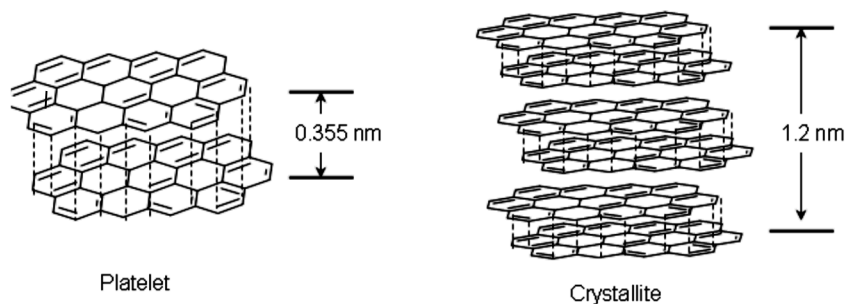


Figure 6 Substructure schematic of carbon particles (Vander Wal *et al.* 1999).

2.2.2 Formation and destruction processes

Soot formation is still regarded as only partially understood; a model that comprises of six distinct and commonly identified processes have been presented by several authors

(Haynes *et al.* 1981, Smith 1981, Melton 1984, Kock *et al.* 2003) and recently reviewed (Michelsen *et al.* 2003, Tree *et al.* 2007). Soot formation processes and the rivalling destructive oxidation process are notably complex and as such no simple parameter or few parameters will allow the calculation of soot yield per unit of fuel consumed (Melton 1984). The complexity is due to the various steps of the formation and oxidative processes being dependent on the local temperatures, pressures and chemical compositions, material phases and their numerous physical parameters present at and immediately adjacent to the region of consideration.

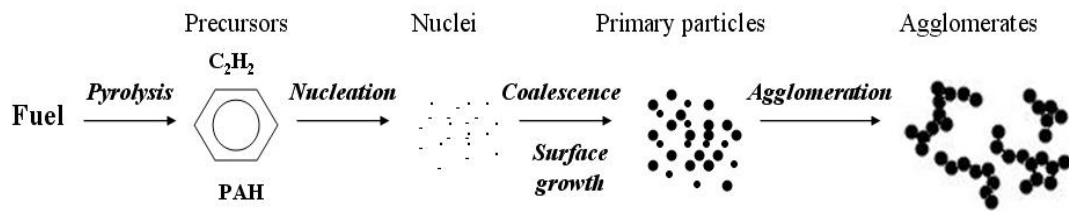


Figure 7 Soot formation scheme (adapted from Tree and Svensson, 2007).

The broadly accepted soot formation model consists of five processes, pyrolysis, nucleation, surface growth, coalescence and agglomeration. These processes occur approximately sequentially at a given location, triggered by temperature and pressure conditions as well as the population of the substances produced by the preceding process. However, at different locations at the same point in time, different regions may be undergoing different processes, something of significance when considering the possibility for transportation of substance between adjacent regions and therefore between different processes.

The destructive process of oxidation occurs simultaneous to some of those of formation. The competition between these rival processes defines the soot population at each moment in time. As the local ambient temperature decreases, such as after a combustion event, a threshold is exceeded, below which all formation and destruction processes cease; the soot population ceases to change.

2.2.2.1 Pyrolysis

Pyrolysis of fuel is the thermo-chemical decomposition whereby unburnt liquid fuel is broken down into more simple molecules such as aliphatic hydrocarbons – alkanes, alkenes, and alkynes. Despite the likely presence of oxidant, pyrolysis is primarily caused by high temperatures, is endothermic in nature and accordingly the rate of pyrolysis is highly dependent upon the temperature (Smith 1981). It is considered that fuel pyrolysis is the most important factor of sooting tendency in non-premixed laminar diffusion flame structures (Ladommatos *et al.* 1996). The rate of pyrolysis is also dependent upon local fuel concentration. The molecules produced by the pyrolysis of pure fuel are described as soot precursors and typically consist of polycyclic aromatic hydrocarbons (PAH), unsaturated hydrocarbons, acetylene and polyacetylenes. It is reported (Haynes *et al.* 1981) that typical pyrolysis products in a non-premixed laminar diffusion flame structure are C_2H_2 , C_2H_4 , CH_4 , C_3H_6 as well as Benzene, C_6H_6 . Polycyclic aromatic hydrocarbons are typically formed from monocyclic hydrocarbons by one of two rivalling mechanisms: hydrogen-abstraction-acetylene-addition (HACA) (Wang *et al.* 1997) in schemes where acetylene concentration is at least equal to that of benzene (Figure 8), or direct ring-ring condensation (Figure 9) where aromatics concentration is sufficiently high (Wang *et al.* 1997). Other kinetic formation pathways are proposed (D'anna *et al.* 2000) as producing Naphthalene, through radical addition (Figure 10), Phenanthrene through radical combination (Figure 11) and cyclization of bi-phenyl by acetylene addition (Figure 12)

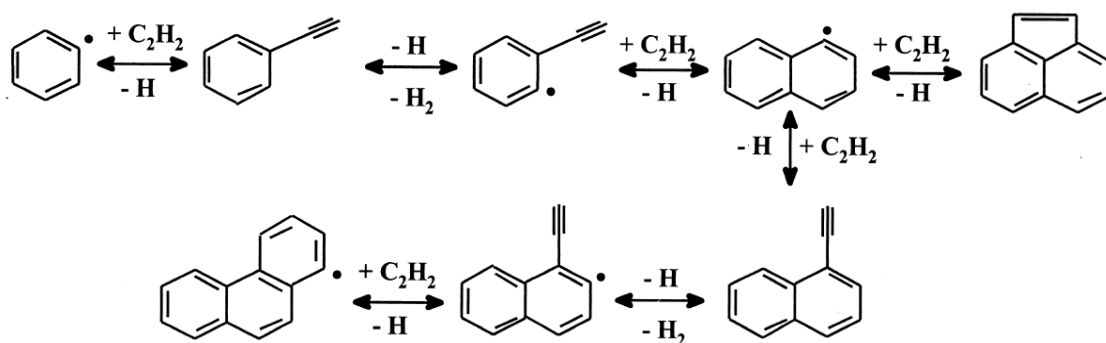


Figure 8 HACA mechanism of polycyclic aromatic hydrocarbon formation (adapted from Wang and Frenklach 1997).

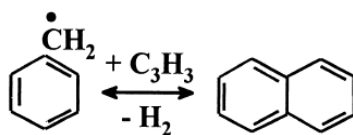


Figure 9 Direct ring-ring condensate of naphthalene from benzyl and propargyl (Colket *et al.* 1994).

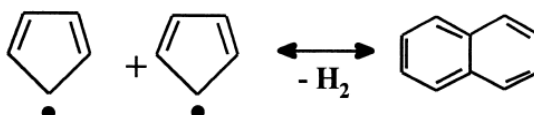


Figure 10 Formation of naphthalene from combination of cyclopentadienyl radicals (oxidized benzene) (Castaldi *et al.* 1996).

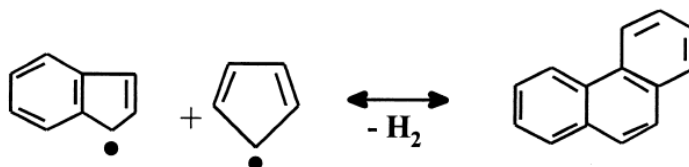


Figure 11 Phenanthrene formation by combination of cyclopentadienyl and indenyl (oxidized naphthalene) (Castaldi *et al.* 1996).

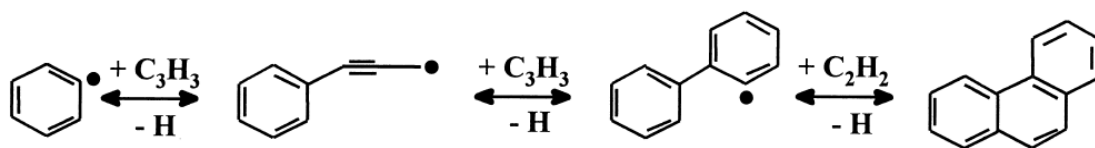


Figure 12 Phenanthrene formation by cyclization by acetylene addition, following sequential addition of propargyl radicals to phenyl (D'anna *et al.* 2000).

In premixed flame structures where an abundance of oxidative species such as the hydroxyl radical OH occurs, the pyrolysis and oxidation compete in their creation and

destruction of soot precursors. In non-premixed flame structures, typical of direct injection diesel engines, minimal oxidative species are locally present and so almost no oxidation of precursors occurs. Both oxidation and pyrolysis processes rates increase with temperature. However, the rate of oxidation increases more quickly, a consequence of which is that premixed flames decrease in soot production by mass more quickly than non-premixed flames as temperature increases.

Pyrolysis occurs through a free radical mechanism so the diffusion of radicals (H, HO, O, O₂) into fuel rich zones in diffusion flames increases the rate of pyrolysis (Smith 1981, Glassman 1996). Radicals are also produced due to pyrolysis, which may contribute to the rival process of oxidation.

2.2.2.2 Nucleation

The initial formation of the smallest incipient particles (in the order of 1 nm diameter) from gas-phase reactants occurs through nucleation. Nucleation is an irreversible process that occurs near the primary reaction zone, characterized as a region within which the highest temperatures as well as radical and ion concentrations occur for both premixed and diffusion flames (Bartok *et al.* 1991). Particle inception occurs when local temperature is approximately 1300 to 1600K, whereby small aliphatic hydrocarbons undergoing radical addition form soot precursors as well as polycyclic aromatic hydrocarbons (PAH). Also, a process of radical addition of small, probably aliphatic, hydrocarbons to larger aromatic molecules may occur (Melton 1984). Nucleation, of itself does not directly contribute significantly to the total mass of soot. It is however, highly significant regarding the overall production of soot in that it provides sites for the surface growth mechanism to subsequently occur.

2.2.2.3 Surface growth

Whilst no clear division between the end of nucleation and the beginning of surface growth is apparent, they are distinct, separate mechanisms. Surface growth is principally a process of mass increase of the soot nuclei and occurs when the hot surface accepts principally gas phase acetylene. As soot particles are transported away from the primary reaction zone to cooler and therefore less reactive regions, surface growth is still

observed, even where hydrocarbon concentration is less than the soot inception limit (Haynes *et al.* 1981). Surface growth is the dominant mechanism with regard to increase of soot particle size and mass and accordingly has a significant effect upon the final soot mass and volume fraction. Bartok *et al.* (1991) noted that smaller young particles exhibit higher growth rates than older, similarly sized particles due to a higher number of available radical sites.

Acetylene and other aromatic species more effectively promote surface growth than species aliphatic species. It has been demonstrated that the rate of surface growth is higher for larger molecules (Haynes *et al.* 1981). Due to this preferential addition of larger molecules, the hydrogen to carbon ratio of the soot particle decreases throughout the surface growth process. This is an indication that the polyacetylenes added have a very high molecular weight or that dehydrogenation takes place concurrently. As the soot particles grow, they lose their affinity for polyacetylenes (Smith, 1981).

2.2.2.4 Coalescence

Coalescence, also referred to as coagulation, is the process by which the soot particles that have previously undergone surface growth, join together to form larger spherule-like particles in the order of 30 to 70 nm diameter (Tree *et al.* 2007). Overall particle mass is conserved and therefore soot volume fraction remains unchanged. The soot particles count is therefore reduced by coalescence.

2.2.2.5 Agglomeration

Agglomeration is a process by which particles become attached to other particles. The possibility exists for infinite variation of agglomerated particle structure, though typically chain like structures occur with some clumping (Figure 3 and Figure 4). When considering a soot population, the number of particles becomes reduced as they agglomerate into the larger, fractal like geometry particles. Since agglomeration constitutes a rearrangement of material, no change of mass or soot volume fraction occurs. The resultant size of, and the amount of particles agglomerated together is dependent upon the duration of the agglomeration process, which in turn is dependent upon the residence time within the flame structure (Xu *et al.* 2001).

The agglomerated soot structures formed can be characterized by the mass fractal concept, using the fractal dimension, D_{fr} (Koylu *et al.* 1995, Koylu *et al.* 1997). Figure 13 supports the validity of Equation 3, the relationship between the number of primary particles N_p , and the non-dimensional ratio of radius of gyration, R_g , to mean particle diameter, d_p :

$$N_p = K_{fr} \left(\frac{2R_g}{d_p} \right)^{D_{fr}} \quad \text{Equation 3}$$

N_p number of primary particles per unit volume [m^{-3}]

K_{fr} fractal prefactor

R_g radius of gyration [m], equivalent to half of the projected maximum diameter of the aggregate (L)

d_p mean primary particle diameter [m]

D_{fr} fractal dimension

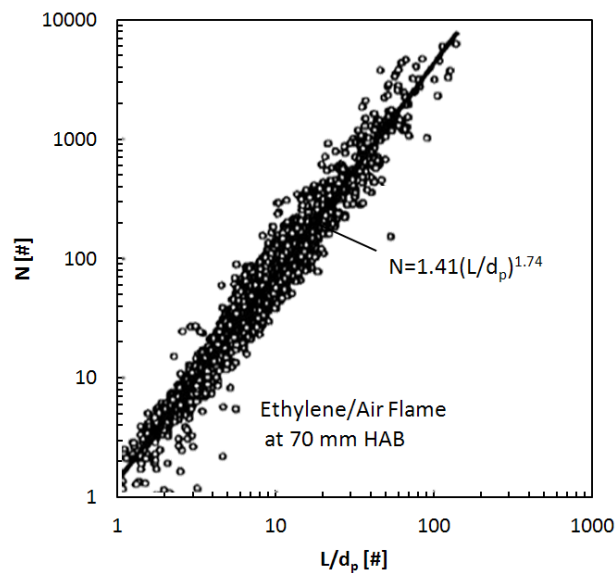


Figure 13 Number of particles per aggregate as a function of non-dimensional length parameter L/d_p . (Adapted from Koylu *et al.* 1997).

2.2.2.6 Oxidation

Oxidation is the process by which soot, or soot precursors are broken down to form combustion products. Significant oxidation of soot occurs at temperatures in excess of 1300 K (Melton 1984). All products from the sequence of formation mechanisms are susceptible to being oxidized and in fact the soot products progress through the formation steps may be curtailed at any point. Carbon atoms oxidized from the hydrocarbon fuel molecules will not contribute to soot formation even if they are subsequently presented to a high temperature fuel rich region of the combustion structure. Oxidation is responsible for the production of O_2 , O, OH, CO_2 and H_2O .

The process of oxidation for soot precursors occurs when oxygen atoms attach to the surface of the molecules (absorption) and then separate (desorption), taking the atom(s) to which the oxygen bonded from the surface (Glassman 1998). For locally fuel rich conditions, the OH radical itself a product of oxidation, is responsible for the majority of soot and soot precursor oxidation. For locally fuel lean conditions however, both the OH radical and the O_2 molecule constitute the dominant oxidative species (Bartok *et al.* 1991). It is estimated that 10-20% of all OH collisions with soot particles result in a gasification of a carbon atom (Watson *et al.* 2001).

As the soot particles increase in size and agglomerate, so the surface area to volume ratio is decreased resulting in an increased resistance to oxidation (Smith 1981). The soot production is highly dependent on the oxidation process Comparison of methane/air and methane/oxygen flames (Lee *et al.* 2000) demonstrated that although a methane/oxygen flame produces a far more rapid combustion with a higher rate of heat release, the anticipated higher rate of soot formation was at least matched by the higher rate of oxidation. Also, the soot volume fraction and primary particle diameter were found both to be lower in the case of the methane/oxygen flame, this being attributed to the increased rate of oxidation but also the shorter residence time within the flame structure reducing the surface growth formation process.

2.2.3 Soot characterization

2.2.3.1 Particle size distribution

Time resolved optical techniques have been applied to sooting flames at ambient conditions (Dec 1992, Schraml *et al.* 2000), and to optical diesel engines (Matsui *et al.* 1980, Flower 1985, Kock *et al.* 2002, Boiarciuc *et al.* 2005, Ryser *et al.* 2009) to characterize the soot particles produced within hydrocarbon fuelled flame structures. The spectral emissions measured are compared to modelled emissions and indirectly yield data as to the nature of the emission source. Such processing routines and the data yielded are dependent upon the assumptions of the models employed.

For laser induced incandescence spectral emissions, the temporally decaying incandescence emission has typically, as a first approximation, been assumed to have emanated from a population of single sized particles of radius r_{mono} corresponding to a mono-dispersed size distribution function. The effect upon the calculated incandescence signal is equated to the total contribution from a distribution of soot particle sizes. Melton (2005) used a normalized probability density function $p(r)$ of particle radius within expressions for the radiative heat transfer mechanism that constitutes the LII emission. As an approximate soot particle size distribution, Melton used a zero order lognormal (ZOLN) distribution:

$$p(r) = \frac{e^{\left(\frac{(\log(r) - \log(r_{mode}))^2}{2\sigma_0^2}\right)}}{(2\pi)^{0.5} r_{mode} \sigma_0 e^{\left(\frac{\sigma_0^2}{2}\right)}} \quad \text{Equation 4}$$

Where:

r_{mode} modal particle radius that, [m].

σ_0 (zero order) probability distribution width.

Subsequently, it has been proposed that the time-resolve laser induced incandescence signal is composed of the contribution of a lognormal distribution of particle sizes

(Dankers *et al.* 2004). Most recently, a multi-lognormal distribution has been proposed; the modelled temporal decay of LII signals incorporating this distribution have been demonstrated to more closely agree with experimentally measured data (Schraml *et al.* 1999) than those calculated using either lognormal or mono-dispersed particle size distribution characterizations. The proposed distribution, expressed as a series:

$$p(r) = \sum_{i=1}^{n_{dist}} \frac{e\left(\frac{(\ln(r) - \ln(r_{i,cmd_multi}))^2}{2\sigma_i^2}\right)}{(2\pi)^{0.5} r \cdot \sigma_i} \quad \text{Equation 5}$$

Where:

n_{dist} count of log normal distributions

For the *ith* series:

$$\sigma_{i=ln}(\sigma_{g,i}) \quad \text{Equation 6}$$

$\sigma_{g,i}$ geometric standard deviation

σ_i distribution width parameter

r_{i,cmd_multi} count median radius [m]

Their published works suggest a multi log normal distribution of order n=4 produces a fit that more closely matches distributions obtained experimentally (Figure 14).

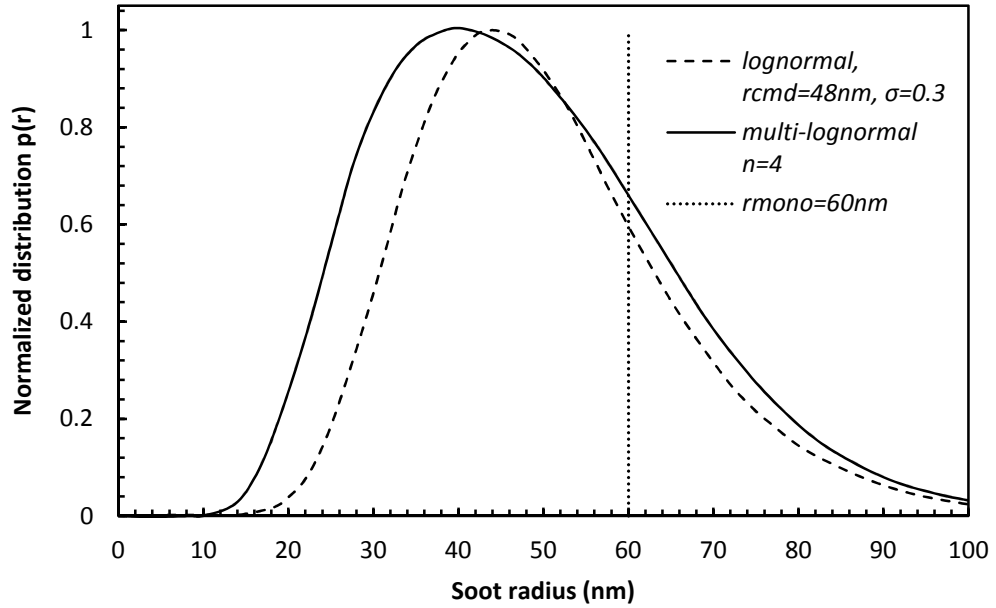


Figure 14 Proposed multi-lognormal soot size distribution (Banerjee, Menkiel *et al.* 2009).

Typical primary particle diameters were obtained experimentally and were in the 20 to 50 nm diameter range, with a mean diameter measuring approximately 30 nm (Lee *et al.* 2001).

2.2.3.2 Soot volume fraction

To characterize the concentration of soot in a measurement region, the soot volume fraction, f_v is commonly used. This is a convenient measure in that it is dimensionless and expresses the quantity of soot in terms of volume-to-volume fraction (rather than mass or mole fraction). Since optical techniques detect radiant emissions that correspond with the geometry of particles, it is appropriate to utilize a measure that is also related to geometry.

For a mono-disperse particle size characterization, the soot volume fraction may be defined as:

$$f_v = \frac{1}{6} \pi N_d d_p^3 \quad \text{Equation 7}$$

Where:

f_v	soot volume fraction
N_d	particle number per unit volume [m^{-3}]
d_p	mean particle diameter [m]

For a distributed particle size population, an expression that encompasses the distribution characterization function $p(r)$ must be used (whose unbounded integral with respect to r , is equal to 1):

$$f_v = \frac{\frac{4}{3}\pi \int_{r=0}^{\infty} p(r)_N \cdot N \cdot r^3 \cdot dr}{V_{measure}} \quad \text{Equation 8}$$

Where:

$p(r)_N$	normalized size distribution/probability density function
N	particle number
r	particle radius[m]
$V_{measure}$	volume of measurement [m^3]

2.2.4 Physical parameters affecting soot production

2.2.4.1 Stoichiometry/equivalence ratio

The oxidant to accelerant ratio, typically referred to as the air-fuel ratio, can be more usefully characterized as to how closely it adheres to the stoichiometric ratio; a ratio of constituents that promote complete combustion in which all of the accelerant is used in

such a way that maximum energy is released. For hydrocarbon fuels, carbon dioxide and water are the by-products (Equation 1) of complete combustion.

The (fuel air) equivalence ratio, Φ is defined as:

$$\Phi = \frac{\left(\frac{m_{fuel}}{m_{oxidant}}\right)_{mixture}}{\left(\frac{m_{fuel}}{m_{oxidant}}\right)_{stoichiometric\ mixture}} \quad \text{Equation 9}$$

Where:

$m_{constituent}$ mass of constituent [kg]

Equivalence ratio (Equation 9) is a useful concept in that a value of one indicates a stoichiometric mixture that will promote complete combustion. Less than one indicates excess oxidant, and greater than one, excess fuel.

2.2.4.2 Temperature

The temperature occurring during combustion affects the reaction rates of each of the soot formation mechanisms. Temperature also affects the oxidation process and consequently, whilst a monotonic increase in the formation of soot with temperature increase occurs for diffusion flames, the rival oxidation mechanism increases at a greater rate such that a non-linear characteristic of soot yield to temperature is realized. (Tree *et al.* 2007) suggests premixed flames demonstrate a peak soot yield temperature but that diffusion flames continue to increase soot yield with temperature. This is inconsistent with the work presented by (Akihama *et al.* 2001). Figure 2 shows the soot island within the equivalence ratio temperature map. Soot inception is reported to begin at 1400 K (Glassman 1989). For a constant, excess fuel equivalence ratio ($\phi > 1$), the overall soot yield increases with temperature up to the point where the oxidation becomes dominant. Peak soot formation in a well stirred reactor, occurring between 1500 and 1700 K is reported (Sato *et al.* 1990). However, Figure 2 (Akihama *et al.* 2001) suggests a peak soot yield between 1800 and 1950 K for diesel combustion with high equivalence ratios. High combustion

temperatures reduce the overall particulate emission, even in fuel rich combustion conditions (Kamimoto *et al.* 1989).

2.2.4.3 Pressure

The effect of variation of pressure upon soot formation is difficult to isolate and is therefore difficult to characterize in a satisfactory manner. A change in pressure within a combustion chamber will typically be as a result of a change in intake charge density, and a change of temperature, thermal diffusivity and fluid transport of species, results in a change of flame structure. For premixed combustion, an increase of soot formation with pressure is reported (Haynes *et al.* 1981). A pressure squared dependence of final soot volume fraction for premixed C₂H₄ and C₆H₆ flames has been reported for flames above 1650 K with carbon to oxygen ratios between 0.65 and 0.75 and pressure in the 0.1 to 0.5 MPa interval (Böhm *et al.* 1989). Overall mass burn rate also increases with pressure (Glassman 1989).

Diffusion flame structures are affected by pressure whilst thermal diffusivity varies inversely with pressure. Soot volume fraction (f_v) of an ethylene diffusion flame at pressures from 0.1 to 0.25 MPa demonstrate a pressure square dependence (Flower 1985). Subsequently, measurement by laser extinction upon an axisymmetric turbulent ethylene diffusion flame at pressures (P) between 0.1 and 0.5 MPa demonstrated an $f_v \propto P^{1.4}$ relationship when constrained to a fixed residence time and flame tip Reynolds number (Flower 1989). Elevation of pressure increases density such that volumetric measures are proportionally increased. For a constant rate of conversion of carbon to soot, a higher pressure condition will therefore yield larger agglomerated particles and a greater number density. Beyond 0.8 MPa, soot formation rate reduces with increase of residence time. This may be attributable to suppression of local temperature due to increased radiation losses. A speculative consensus that soot formation rate may be as high as $f_v \propto P^2$, and is suggested to be consistent with an intuitive appraisal of the affect of increased collision rates, concentration of soot precursors, and consequential reaction rates (Tree *et al.* 2007).

2.3 Flame structure

To study the formation of soot, it is desirable to classify flame structures by characteristics that have distinct consequences upon the formation and destruction processes of soot. At each location within a flame structure, the nature of the presented constituents and ambient conditions will affect soot production. The local degree of mixing of fuel and oxidant will affect the resultant degree of homogeneity in the region. This affects both the stoichiometric ratio of the point of interest within the combustion zone and its spatial variation in the local region. The spatially resolved gradients of property imposed upon a combustion region will affect the continuation of the combustion reaction and local temperature, the chemical kinetics of soot production and the degree of completeness of combustion. A distinction between premixed and non-premixed, laminar diffusion flames encompasses the principle difference of how the fuel and oxidant is presented to the combustion zone.

2.3.1.1 Premixed flame

Premixed flame structures occur when the fuel and oxidative species have undergone some degree of mixing prior to being presented to the combustion zone or when they are introduced to a region in which mixing occurs and then combustion is initiated.

This latter definition is typical of the effect of pilot injection strategies typically employed in (common rail) direct injection diesel combustion systems. An injection of a comparatively (to that of the main injection) small quantity of fuel into the combustion chamber before the main injection event, is principally employed to control the rate of pressure rise of the main combustion event, thus reducing the noise associated with the mode of combustion as well as the spike of in-cylinder pressure at an unfavourable crank-arm geometry for extraction of mechanical work. The rate of combustion for a premixed flame structure is dictated by the chemical kinetics of interaction between the species.

2.3.1.2 Non-premixed laminar diffusion flame

A non-premixed laminar diffusion flame is one that occurs due to conditions in which fuel and oxidative species are fed to the combustion zone, typically an interface between

the two species, where a stoichiometric ratio that is conducive to combustion occurs. The scheme therefore constrains the propagation of the combustion zone to the region that can support combustion. Combustion however, occurs in the regions that deviate from stoichiometric conditions also; the fuel scarce region towards the exterior of the flame structure, and the fuel abundant, oxidative species scarce interior regions both support incomplete combustion. Since pyrolysis, the first step in the formation sequence of soot, is highly dependent on both temperature and fuel concentration, initial formation commences in the interior region of laminar diffusion flames.

2.4 Diesel combustion

Non-premixed, laminar diffusion flame is an appropriate characterization of the flame structure that occurs during the main injection event within a direct injection diesel engine.

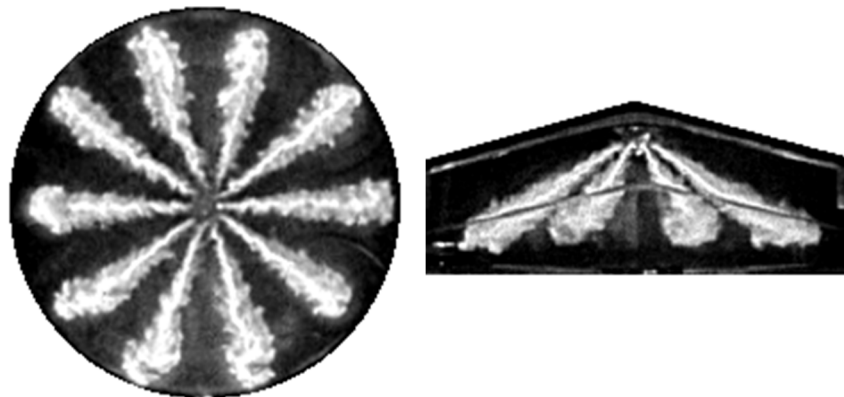


Figure 15 Multiple-hole injector fuel spray pattern captured in an optical access engine from below (left) and in profile (right) using a laser induced fluorescence technique, (adapted from Henle *et al.* 2005)..

Typically an injector will be vertically disposed and of a multiple-hole design, producing multiple, inclined and radial disposed fuel plumes (Figure 15). For the purpose of studying fundamental aspects of the soot formation mechanisms within a combusting diesel fuel injection plume, a single nozzle design is preferred; optical excitation and

acquisition pathways do not therefore intersect multiple fuel plumes, combustion regions, and soot structures.

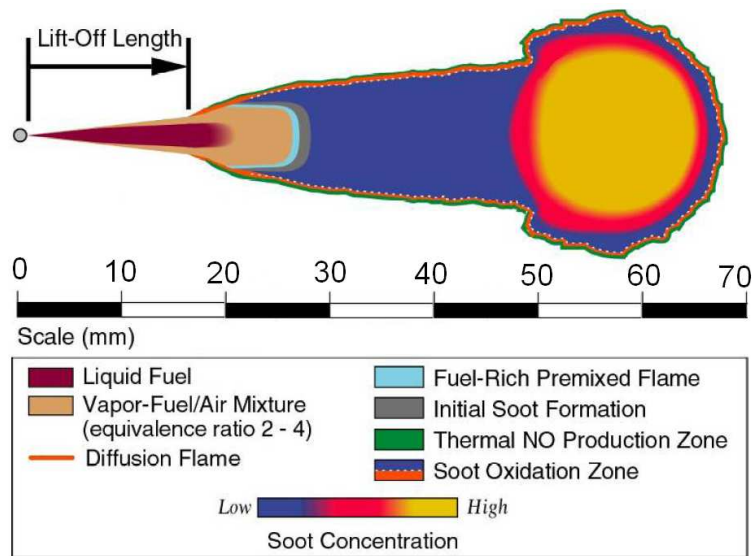


Figure 16 Diagrammatic cross section scheme of laminar diffusion flame quasi-steady state combustion typical of a diesel direct injection engine, (D'anna *et al.* 2000).

The widely accepted conceptual model of the fuel plume combustion (Figure 16), was first realized at the Sandia laboratory and presented, (Dec 1997). Subsequently, insight gained by a research collective has built upon the model with quantitative empirical models for the reacting jets through studies focusing upon aspects of ignition (Higgins *et al.* 2000), penetration (Siebers 1999), and lift off length (Higgins *et al.* 2001).

The model represents a quasi-steady state combustion condition and is valid for sprays that do not impinge upon chamber geometry and do not interact with other spray plumes. Experimentation underpinning the model was conducted at typical direct injection conditions in which measurements were obtained at TDC with an in-cylinder temperature of 1000 K and injection at 12° BTDC at 860 bar fuel rail pressure.

The spray scheme portrayed in Figure 16 has a liquid fuel core structure that begins immediately after the nozzle and penetrates into the overall plume, its extent termed the 'liquid length'. Due to sufficiently high injection pressure and accordingly fine atomization, entrainment of the surrounding hot gases imparts energy at a rate that dictates the evaporation rate of the liquid fuel. A vaporized fuel and air mixture region

grows at the surface of the liquid fuel core. The entrainment of hot combustion chamber gasses elevates the local temperature such that the entire liquid fuel core evaporates at some distance from the nozzle, for the modelled conditions, approximately 20 mm.

A diffusion flame envelopes the entire fuel plume, burning at the perimeter surface where a stoichiometric or near stoichiometric mixture is presented. The flame does not reach upstream to the nozzle since the velocity of the fuel spray in conjunction with the time required for the fuel and air mixture to react is such that favourable combustion conditions are not present until sometime after, and therefore distance from the nozzle. The distance is termed 'lift-off length' and is considered critical to overall soot formation in direct injection combustion systems (Siebers *et al.* 2001).

The region within this diffusion flame envelope comprises of a fuel rich, soot formation promoting volume. A fuel rich mixture is partially burnt, increasing temperature of the constituents as they propagate axially and diffuse radially. This, in conjunction with the scarcity of local oxidative species (the diffusion flame consumes the majority of oxygen before significant ingress can occur) yields the highest rate of soot production within the flame structure. The high local temperature significantly increases the rate of pyrolysis of the fuel into soot precursors and initiates the sequence of soot formation mechanisms.

Combustion is maintained at the diffusion flame front by diffusion of fuel-air mixture towards it from within. Simultaneously, oxygen is consumed from outside the diffusion flame front by molecular diffusion and a steep gradient of equivalence ratio is established; immediately outside of the diffusion flame front is fuel scarce, oxidative species abundant, immediately inside the spray/flame structure, fuel is abundant and oxidative species scarce. As the whole fuel/flame structure propagates away from the nozzle, the mixing layer increases in thickness, tending towards a more homogeneous distribution. The rate of combustion by diffusion flame is controlled by the mass diffusion rate of fuel towards the diffusion flame at the stoichiometric contour.

Figure 17 depicts a temporally resolved model of direct injection diesel spray plume combustion, adapted from that first presented (Kosaka *et al.* 2005). This model illustrates the fuel plume prior to the initial premixed combustion phase in which favourable conditions for combustion occur within a region within the head of the plume. The core region presents a fuel vapour and air mixture with an equivalence ratio $\Phi > 1$, surrounded

by a region where $\Phi < 1$. Subject to increasing internal energy (due to a temperature and pressure increase produced during the compression stroke), localized combustion occurs within the core of the plume. The exterior region of the plume head is unable to support combustion, however (comparatively) low temperature oxidation leading to formaldehyde formation initially occurs. After the premixed combustion phase has consumed the premixed constituents, a transition to mass diffusion rate controlled combustion scheme occurs. The transition point fuel plume combustion scheme depicts the head region as containing a large core in which PAH's are formed due to the combination of elevated temperature and the continuous supply of fuel vapour from upstream. As the laminar diffusion flame becomes established, the dynamics of kinetic motion and chemical kinetics of combustion dominate the model scheme. The core axis serves as a supply pathway for fuel vapours that go on to form PAH's. The PAH's nucleate into young soot, and coalesce into larger particles all within the core of the combustion plume and notable subject to little oxidation. A head vortex transports the soot back towards the flanks of the plume, simultaneously entraining oxygen from the surrounding gasses, to a region where the high temperature of the laminar diffusion flame surface drives the oxidation process.

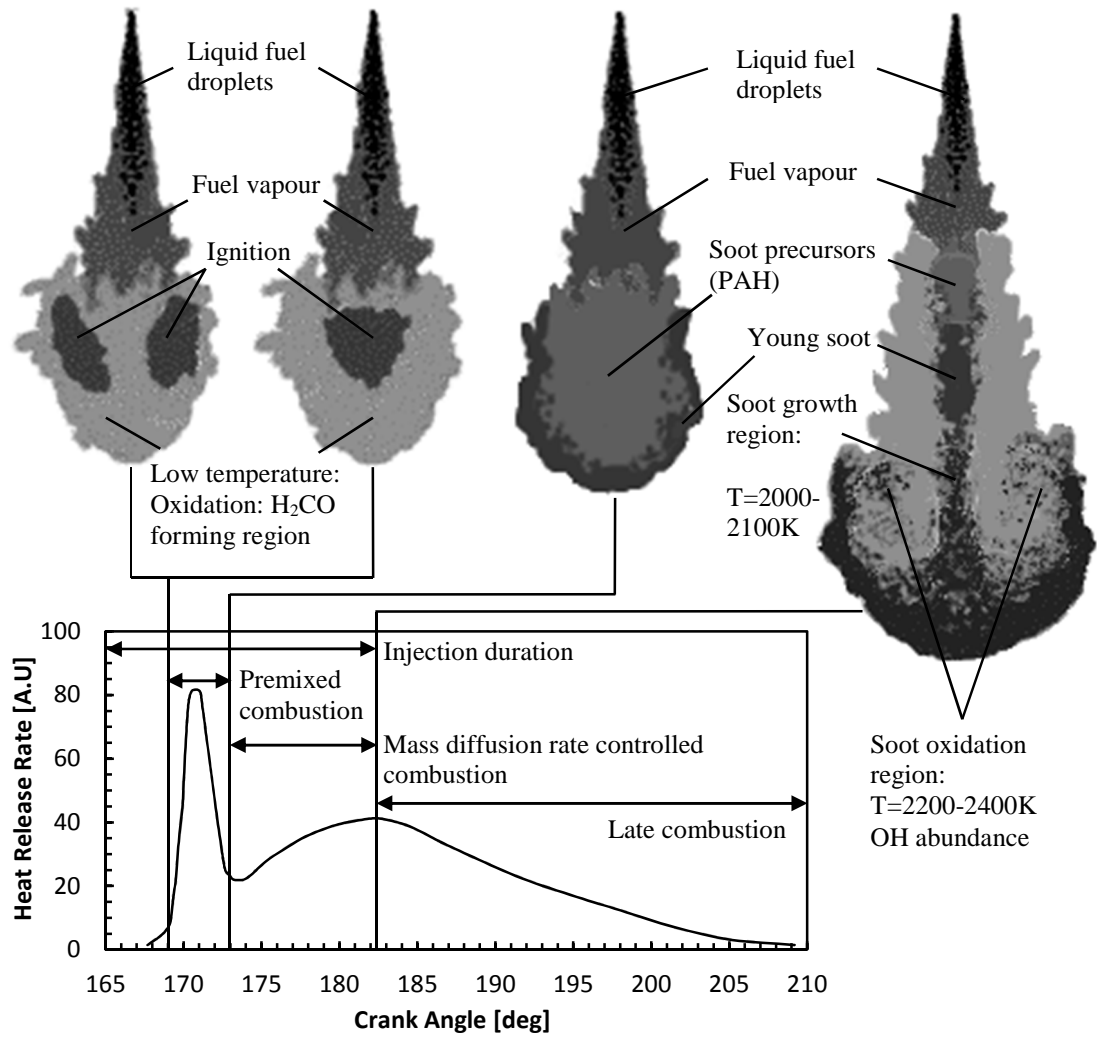


Figure 17 Combustion phase evolution. (Adapted from Kosaka *et al.* 2005).

2.5 Heat transfer

2.5.1 Transport mechanisms

Descriptions of conceptual heat transport mechanisms in the most general sense are outlined herein. Subsequently, specific formulations are presented for each of the heat transfer mechanisms of the LII model used in this study.

2.5.1.1 Radiation

A body at some temperature above zero degrees Kelvin emits electromagnetic radiation, the spectral characteristics of which vary with the temperature difference of that body relative to that of its environment, as well as its emissivity, which is in itself a wavelength and material property dependent characteristic of the body that will be discussed subsequently.

Gustav Kirchhoff proposed three laws of spectroscopy, the first of which stated that a hot solid object produces light of a continuous spectrum. In 1859 he went on to propose what we now regard as Kirchhoff's law of thermal radiation which states that if at thermal equilibrium, the emissivity of a body must equal its absorptivity in order to not violate the second law of thermodynamics.

$$\alpha_{\lambda} = \varepsilon_{\lambda} \quad \text{Equation 10}$$

Where:

α_{λ} monochromatic absorptivity

ε_{λ} monochromatic emissivity

2.5.1.1.1 Black-body radiation

Gustav Kirchhoff used the term black-body to describe an ideal material behaviour where all electromagnetic energy incident upon the body is absorbed. By definition the absorptivity property must be unity. In order that thermal equilibrium, and therefore internal energy, is maintained, the black-body must simultaneously emit the same quantity of energy, hence it must also have a unity value emissivity property.

When a black-body is heated by some means to a non-zero temperature, it will cease to be in thermal equilibrium with its environment, and will emit electromagnetic energy. The spectral distribution of this energy was described by Wilhelm Wien's empirically derived 'distribution law' in 1896, and can be written:

$$I_{\lambda}(T) = \frac{2hc^2}{\lambda^5} e^{\frac{-hc}{\lambda kT}} \quad \text{Equation 11}$$

Where:

$I_{\lambda}(T)$	spectral radiance defined as the amount of energy per unit surface area, per unit time, per unit solid angle, per unit wavelength emitted at wavelength λ [$\text{Js}^{-1}\text{m}^{-2}\text{sr}^{-1}\text{m}^{-1}$ or $\text{Wm}^{-3}\text{sr}^{-1}$]
T	temperature of the black-body [K]
h	Planck's constant, 6.626068×10^{-34} [$\text{m}^2.\text{kg}.\text{s}^{-1}$]
c	speed of light in vacuum, 299792458 [$\text{m}.\text{s}^{-1}$]
k	Boltzmann's constant, $1.3806504 \times 10^{-23}$ [$\text{J}.\text{K}^{-1}$]

Subsequently, it became apparent that whilst this law satisfactorily described the electromagnetic spectral emissions at high wavelengths, it diverged from true, experimentally verifiable behaviour at short wavelengths, producing the so called 'ultraviolet catastrophe' of infinite intensity as wavelength tends to zero. Max Planck derived his law of black-body radiation from electromagnetic and thermodynamic theory, as they then existed. The spectral distribution of radiant energy for a range of temperatures of a black-body emitter are illustrated in Figure 18.

$$I_{\lambda}(T) = \frac{2hc^2}{\lambda^5} \frac{1}{e^{\frac{hc}{\lambda kT}} - 1} \quad \text{Equation 12}$$

An alternative formulation combines $2hc^2$ into a single constant C_1 , and $\frac{hc}{k}$ into C_2 :

$$I_\lambda(T) = \frac{C_1}{\lambda^5 \left[e^{\left(\frac{C_2}{\lambda T}\right)} - 1 \right]} \quad \text{Equation 13}$$

C_1 first spectral radiation constant, 3.7418×10^{-16} [W.m²]

C_2 second spectral radiation constant, 1.4388×10^{-2} [m.K]

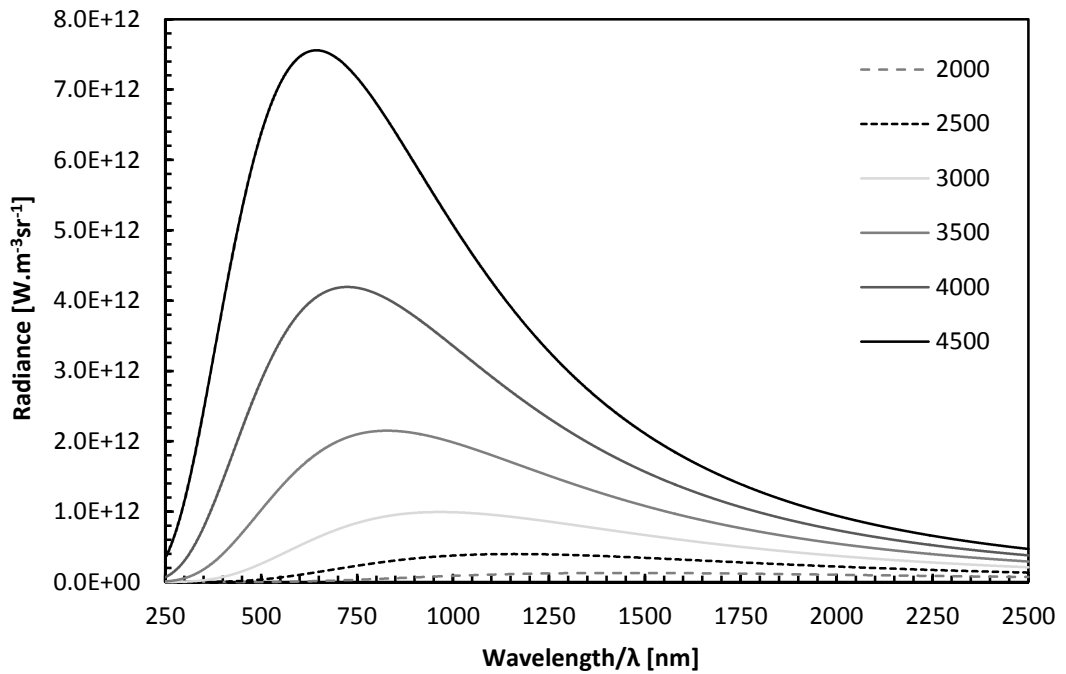


Figure 18 Spectrally resolved black-body radiation for a range of temperatures [K].

2.5.1.1.2 Grey-body radiation

A grey-body is a material state with behaviour similar to that of a black-body, but has an emissivity (and absorptivity) value that is less than unity. It does not absorb or re-emit all the incidental energy that falls upon it. Of the absorbed incidental energy, a quantity is emitted as governed by the black-body emission multiplied by the emissivity value, itself a function of wavelength.

$$I_{\lambda,GB}(T) = \frac{2hc^2}{\lambda^5} \frac{1}{e^{\frac{hc}{\lambda kT}} - 1} \cdot \varepsilon(\lambda) \quad \text{Equation 14}$$

Where:

$I_{\lambda,GB}$ grey body spectral radiance [$\text{J}\cdot\text{s}^{-1}\cdot\text{m}^{-2}\cdot\text{sr}^{-1}\cdot\text{m}^{-1}$ or $\text{W}\cdot\text{m}^{-3}\cdot\text{sr}^{-1}$]

2.5.1.1.3 Non-vacuum conditions

The speed of light through a medium such as air differs from the speed of light in vacuum c , according to the phase velocity equation:

$$n = \frac{c}{v} \quad \text{Equation 15}$$

Where:

n refractive index of the medium

v phase velocity [$\text{m}\cdot\text{s}^{-1}$]

The phase velocity therefore represents the speed of propagation through the medium and should be used instead of c , the speed of light in the calculation of radiation energy levels.

As noted by (Blevin 1972), non-vacuum experimental conditions introduce a calculable error is knowingly introduced into any calculation that involves the speed of light in that medium when the refractive index of that medium is neglected.

At elevated pressures within a combustion chamber of perhaps 8 MPa and temperatures potentially several hundred degrees above atmospheric, the refractive index of the air medium will be affected. An expression for the refractive index in terms of air's state variables and the wavelength of interest was proposed (Edlen 1966) and subsequently revised as more accurate experimentally derived data was realized (Birch *et al.* 1993), yielding:

$$(n-1)_{tp} = \frac{(p/Pa)(n-1)_s}{96095.43} \times \frac{[1 + 10^{-8}(0.601 - 0.00972T_c)p/Pa]}{(1 + 0.003661T_c)} \quad \text{Equation 16}$$

Where:

$(n-1)_{tp}$ increase of refractive index in dry air relative to refractive index in free space

p pressure [Pa]

$(n-1)_s$ represents the increase of refractive index of air at standard temperature and pressure, relative to refractive index of free space

T_c temperature [C]

For conditions where both temperature and pressure are elevated to those typical of a diesel combustion chamber, the effects upon the refractive index of air can be disregarded as illustrated in Figure 19.

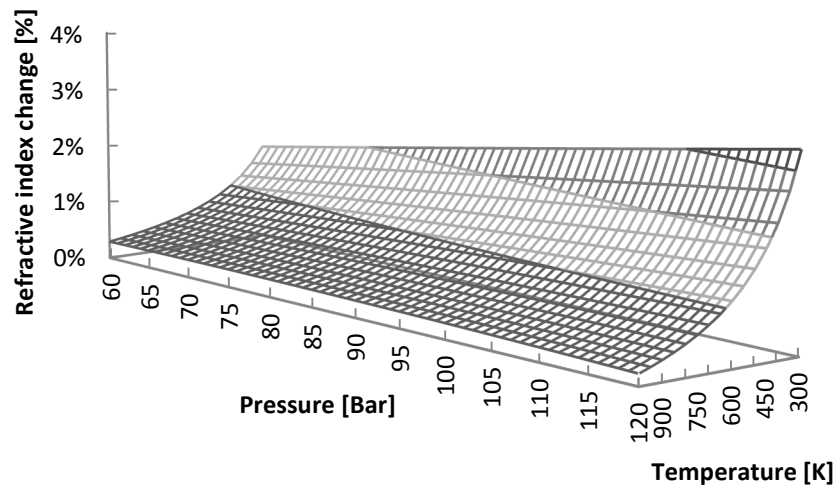


Figure 19 Variation of refractive index of dry air with temperature and pressure.

2.5.1.2 Conduction

The rate of flow of energy between two adjacent bodies is in proportion to the degree of imbalance that exists within a system and may be conceived of as a thermal gradient. This is captured in Fourier's law of conduction which states:

$$\vec{q} = -k\nabla T \quad \text{Equation 17}$$

Where:

\vec{q} heat flux [$\text{W}\cdot\text{m}^{-2}$]

k thermal conductivity [$\text{W}\cdot\text{m}^{-1}\cdot\text{K}^{-1}$]

∇T temperature gradient [$\text{K}\cdot\text{m}^{-1}$]

Expressed in differential form for a single spatial dimension, x:

$$q_x = -k \frac{dT}{dx} \quad \text{Equation 18}$$

Where:

q_x heat flux parallel to the spatial dimension, x [$\text{W}\cdot\text{m}^{-2}$]

$\frac{dT}{dx}$ temperature gradient parallel to the spatial dimension, x [$\text{K}\cdot\text{m}^{-1}$]

2.5.1.3 Absorption

Absorptive heat transfer occurs when an energy flux is incidental with a subject and produces an increase of internal energy of the subject (disregarding other transport mechanisms). When considering a flux of electromagnetic energy, there exists a statistical likelihood of interaction depending upon the frequency of incidence between photons and molecules. Absorption cross section, σ , is a probability coefficient that characterizes the likelihood of interaction between incident photons and molecules. The rate of absorption

is therefore dependent upon absorption cross section, σ , the concentration of molecules along a path of propagation, n , and the number of photons traversing the path, N .

$$\frac{dN_{\text{photon}}}{dx} = -N_{\text{photon}} \cdot n_{\text{mol}} \cdot \sigma \quad \text{Equation 19}$$

Where:

$\frac{dN_{\text{photon}}}{dx}$ rate of absorption along an incidental spatial dimension, x [m^{-1}]

N_{photon} number of incident photons

n_{mol} number of molecules per unit volume [m^{-3}]

σ absorption cross section [m^2]

2.5.1.4 Sublimation

Sublimation is the term used to describe a phase transition of a material directly from solid to gas. Carbon in solid phase and at low pressures can change directly from solid to gas (carbon vapour) at a temperature of approximately 3900K, often referred to as the vaporisation temperature of carbon. Figure 20 depicts a phase diagram for carbon over a wide range of pressures and temperatures. A transition directly from solid to gas phase is possible from ambient pressure up to approximately 10^7 Pa. When considering sublimation as a mechanism of energy transfer, the energy used to drive the sublimation process is the aspect of interest and is related to the material property of heat of vaporisation per mole of solid material, the molecular weight of the material and the rate of change of the material mass.

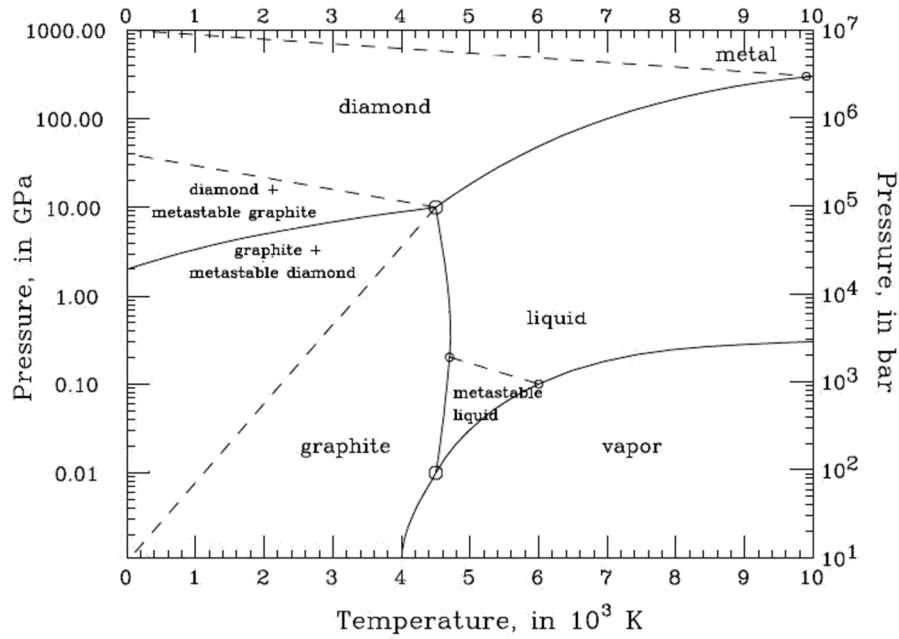


Figure 20 Phase diagram of carbon (Zazula 1997).

$$\dot{Q}_{sub} = U_{sub} \cdot \Delta h_{sub} \quad \text{Equation 20}$$

Where:

\dot{Q}_{sub} rate of change of energy due to sublimation [$\text{J} \cdot \text{s}^{-1}$]

U_{sub} rate of sublimation [$\text{Kg} \cdot \text{s}^{-1}$]

Δh_{sub} sublimation enthalpy [$\text{J} \cdot \text{Kg}^{-1}$]

2.5.1.5 Annealing

Annealing refers to the process where the internal structure of a material is afforded mobility, typically through raised temperature, such that intermolecular forces tend to a local minimum. Since this internal rearrangement of matter does not yield a measureable flow of energy across any chosen boundary, the effects of annealing cannot be readily quantified.

The effect of annealing may account for some amount of energy reduction of the system, specifically, the energy consumption associated with the redistribution of material within a particle. As such, annealing constitutes a parameter that can reasonably be neglected in terms of its direct contribution to heat transfer within the system of carbonaceous particles. However, the change of particle cross section to mass ratio may have a significant effect upon other heat transfer mechanisms such as absorption, that are dependent upon the particle(s) cross section(s).

2.5.1.6 Oxidation

The rate of oxidation is dependent upon the degree of the energized state (temperature) of the system and the nature of and proportion of the oxidizing species, which can be expressed as the mean free path length to oxidizing molecules, within the system being considered.

Oxidation is a term used to describe the interaction of oxidative agent and donor species where a simultaneous respective decrease and increase of oxidation number occurs. For the simple case of a so called 'redox pair', the transfer of electrons from a donor species to the oxidizing agent occurs due to the oxidizing agent being highly electronegative and gaining the sought electrons from adjacent species and in particular from any local electropositive species that will freely donate electrons. The donor species, having been oxidized will accordingly reduce in population.

2.6 Pyrometry

Pyrometry is the measurement of temperature by measuring the intensity of radiated electromagnetic spectral emissions from a body of interest. The remote nature of the technique finds favour with experimentalists who aim to measure hostile subjects or measure in hostile environments or who wish to avoid perturbing that which they are measuring. The measurement of flame temperature tends to constitute several of these aspects; a physical probe often introduces a perturbation error by disrupting the flame structure to be measured. Additionally, soot particulates tend to be deposited upon a probes surface distorting the measurement data further and necessitating frequent removal

for cleaning. This may be unsuitable due to interrupting the operation of the equipment which may take a period of operating time to settle to steady state behaviour. A probe must also be robust to elevated temperatures and high thermal gradients. For temporal measurements, the rate at which thermal equilibrium is reached between a probe and the medium into which it is placed is also important such that any lag in the measured temperature relative to the actual temperature at that time can be removed during post processing of the data.

During diesel fuel combustion both solid soot particulates and gaseous combustion products are present. The spectral emission that occurs during diesel combustion is dominated by the intense radiation from the soot particles. The measurement of flame temperature through pyrometry is indirect in that it is in fact the measurement of the luminous radiated emission from the heated soot particles within the structure rather than a measurement of the gas temperature. The temperature difference between soot particles and gaseous constituents is negligible ($<1\text{K}$) when the gas and soot particles have attained thermal equilibrium, this can be attained in about 10^{-5} to 10^{-6} seconds within the cylinder (Baker *et al.* 1961, Beyer *et al.* 2006) In the absence of surface reactions on the soot particles, it can be shown that the soot particles can faithfully follow the surrounding gases' temperature as they change with time (Baker *et al.* 1961). It can therefore be assumed that soot particle temperature and combustion gas temperature are the same.

The calculation of temperature is possible due to the adherence to a known spectral distribution of emitted electromagnetic energy. For a true black-body, an emission measurement at a single known wavelength, with known collection optics efficiency and geometry, allows temperature of the black-body to be calculated from Planck's black-body distribution law equation, but for a grey-body, the emissivity at that wavelength must also be known.

The monochromatic emissivity can be defined by the relationship between the spectral emission of a (grey-body) object at a temperature and the spectral emission of a true black-body at the same temperature, by:

$$\varepsilon_{\lambda} = \frac{I_{\lambda}(T)}{I_{b,\lambda}(T)} \quad \text{Equation 21}$$

Where:

$I_\lambda(T)$ monochromatic emission power of a non-black-body at temperature T

$$I_\lambda(T) = \varepsilon_\lambda I_{b,\lambda}(T) \quad \text{Equation 22}$$

ε_λ will always have a value less than 1 such that non-black-body emission is less than that of a black-body of the same temperature.

Apparent temperature T_a or ‘brightness’ is the temperature for a black-body that will emit the same monochromatic radiation power as a non-black-body at temperature T , and is related to T by:

$$I_\lambda(T) = I_{b,\lambda}(T_a) \quad \text{Equation 23}$$

T_a will always be a lower value than T , since a non-black-body will emit less energy than a black-body at the same temperature. This expression provides a relationship between an unknown behaviour, non-black-body function $I_\lambda(T)$, and the well-defined black-body function $I_{b,\lambda}(T_a)$.

Combined, the two expressions relate the radiation power associated with the ‘true’ temperature T to the radiation power associated with the apparent temperature T_a of a black-body:

$$I_{b,\lambda}(T)\varepsilon_\lambda = I_{b,\lambda}(T_a) \quad \text{Equation 24}$$

Rearranged such that the once again monochromatic emissivity is the subject:

$$\varepsilon_\lambda = \frac{I_{b,\lambda}(T_a)}{I_{b,\lambda}(T)} \quad \text{Equation 25}$$

This relationship is of interest because it allows the measurement of the spectral radiated power of a non-black-body at a temperature to be measured and expressed, in conjunction

with the spectral monochromatic emissivity value as a spectral radiated power of a black-body, and subsequently its true temperature. The true temperature value is therefore dependent upon the value of the spectrally variant monochromatic emissivity term.

The substitution of black-body characteristic behaviour terms allows the substitution of Max Planck's equation for black-body spectral emission because we have two expressions that are both true black-body terms and it relates the measurable quantity of an emission signal of the apparent temperature T_a , to an expression that is a function of true temperature T , the quantity of interest.

The convenience lies in the fact that we can measure a radiated emission at a known wavelength and calculate an apparent temperature as though the emission was that of a true black-body. We can then convert this to a true temperature for the non-black-body emitting subject of interest.

Combined with Planck's equation:

$$\varepsilon_\lambda = \frac{e^{\left(\frac{C_2}{\lambda T}\right)} - 1}{e^{\left(\frac{C_2}{\lambda T_a}\right)} - 1} \quad \text{Equation 26}$$

Hottel and Broughton developed an empirical correlation between spectral emissivity and optical path length through the emission structure (L) and the optical characteristic of absorption coefficient (K):

$$\varepsilon_\lambda = 1 - e^{\left(\frac{-KL}{\lambda^\alpha}\right)} \quad \text{Equation 27}$$

Where:

K absorption coefficient [-]

L optical path-length through emission structure as presented to acquisition apparatus in metres [m]

α wavelength variant empirically derived factor [-]

Combining and rearranging to make KL the subject:

$$KL = -\lambda^\alpha \ln \left[1 - \frac{\left(e^{\left(\frac{C_2}{\lambda T} \right)} - 1 \right)}{\left(e^{\left(\frac{C_2}{\lambda T_a} \right)} - 1 \right)} \right] \quad \text{Equation 28}$$

It is therefore possible to establish the true temperature of a non-black-body source of emission from its spectral emission if two additional parameters, one geometric (L) and one optical (K), are known. Since it is neither convenient nor useful to establish either of the variable values independent of the other, KL is typically treated as a composite parameter and referred to as the ‘optical thickness’.

2.6.1 Two colour pyrometry

Remote optical temperature measurement in the form of two wavelength pyrometry, often referred to as two colour pyrometry, has been extensively applied to ambient condition experimental setups (Hottel *et al.* 1932, Choi *et al.* 1994, De Iuliis *et al.* 1998, Jenkins *et al.* 2001, Snelling *et al.* 2002); typically upon either a pre-mixed burner or non-premixed laminar burner. This technique can yield quantitative measurement of temperature of the soot particulates and, by extension, of the flame (Schack 1925, Baker *et al.* 1961). A small region within a flame structure may be measured using a single point measurement system such as focusing optics and a photomultiplier. Whole flame structure images may be used to digitize intensity levels, typically through the application of intensified ‘charge coupled device’ (CCD) cameras where the number of data points corresponds to the pixel count of the imaging array. Calibration of the signal intensity occurs through use of a known emitter such as a calibrated tungsten filament lamp.

Further work carried out in diesel engines (Yan *et al.* 1988, Beatrice *et al.* 1995, Zhao *et al.* 1998, Payri *et al.* 2007) has tended to use modified production engines, where optical access was gained through modified unused cylinder head ports or dedicated added optical apertures. The use of optical linkages or fibre optic bundles to transport the signal to the measuring equipment has been employed, albeit to the detriment of signal strength or resolution. Alternatively, experimental arrangements limited to lower in-cylinder and

injection pressures have been used, but offer limited insight into the behaviour at operating conditions more typical of modern production diesel engines.

The values of absorption coefficient K , and optical path length L , are physical parameters of the material from which the emission occurs. They are difficult to quantify with satisfactory exactness and certainty and may vary through time. The absorption coefficient K , also represents an average value across the extent of the optical path length L , and as such is a geometric average. They are however wavelength independent quantities and so allow the expression for two different acquisition wavelengths to be equated, for which the KL terms cancel.

$$KL = \left[1 - \left(\frac{e^{\left(\frac{C_2}{\lambda_1 T}\right)} - 1}{e^{\left(\frac{C_2}{\lambda_1 T_{a1}}\right)} - 1} \right) \right]^{\lambda_1^{\alpha_1}} = \left[1 - \left(\frac{e^{\left(\frac{C_2}{\lambda_2 T}\right)} - 1}{e^{\left(\frac{C_2}{\lambda_2 T_{a2}}\right)} - 1} \right) \right]^{\lambda_2^{\alpha_2}} \quad \text{Equation 29}$$

Another formulation of this equation equates the two measured signals (I_1, I_2) directly:

$$KL = \left[1 - \left(\frac{I_1(\lambda_1)\lambda_1^5 \left(e^{\left(\frac{C_2}{\lambda_1 T}\right)} - 1 \right)}{C_1} \right) \right]^{\lambda_1^{\alpha_1}} = \left[1 - \left(\frac{I_2(\lambda_2)\lambda_2^5 \left(e^{\left(\frac{C_2}{\lambda_2 T}\right)} - 1 \right)}{C_1} \right) \right]^{\lambda_2^{\alpha_2}} \quad \text{Equation 30}$$

These formulations do not permit a convenient direct solution of T and an appropriate iterative method is typically employed. Also, the second formulation is expressed in terms of the spectral radiance $I_1(\lambda_1)$ and $I_2(\lambda_2)$. Utilization of this formulation necessitates the substitution of measured quantities $E_1(\lambda_1)$ and $E_2(\lambda_2)$, the spectral irradiance, since this is the quantity that is measured by typically either a camera or photomultiplier.

An alternative and practically more immediately utilizable formulation can be derived if the experimental setup is treated as a ‘black box’ system: the effect of each of the optical

components in the transmission path between emission source and detection apparatus is considered only in total. This yields a single ratio of the sensitivity of the two acquisition wavelengths that incorporates their respective optical geometry, their compound spectral transmissivities and detection sensitivity values.

This experimental detection sensitivity ratio can itself be derived through capturing the emission of a well characterized black-body radiating source such as a calibrated emission tungsten filament lamp. The calibration data allows the temperature of the filament to be directly inferred through the application of Wien's displacement law. The ratio of measured signal will likely differ from the expected ratio of signal from the black-body at its known temperature, by some factor. This factor represents the compounded calibration coefficient for the experimental detection system and comprises the effect of the collection optic geometry, the spectral transmissivities of the sequence of optical components (including the selected spectral filters) in the detection path, and the spectrally variant response of the detection apparatus.

$$\frac{E_{\lambda_1}}{E_{\lambda_2}} = \frac{\varepsilon_1 \text{Cal}_1 I_1}{\varepsilon_2 \text{Cal}_2 I_2} \quad \text{Equation 31}$$

For detection wavelengths that are both in the optical wavelength range, the emissivity of soot is considered sufficiently invariant that it may be incorporated into the calibration factors Cal_1 and Cal_2 .

$$\frac{E_1}{E_2} = \frac{\text{Cal}_1 \lambda_2^5}{\text{Cal}_2 \lambda_1^5} \left(\frac{e^{\left(\frac{C_2}{\lambda_2 T}\right)} - 1}{e^{\left(\frac{C_2}{\lambda_1 T}\right)} - 1} \right) \quad \text{Equation 32}$$

Therefore, a known light source may be used to find a value of the ratio $\text{Cal}_1/\text{Cal}_2$ since all other terms in the expression are either known or measured. Once the overall calibration of the system is established, a relationship between signal ratio and temperature is defined. As with previous formulations, temperature (T) is not directly calculated.

A convenient method to relate temperature (T) to the signal ratio is to graphically plot a signal ratio versus temperature curve. If this curve is manipulated such that temperature versus signal ratio is fitted with some polynomial curve fit, an expression that yields temperature directly from the measured signal ratio may be produced.

2.7 Laser induced incandescence (LII) of soot

When a laser beam of sufficient intensity is incident with particulate matter, energy is imparted such that the internal energy and therefore temperature of the particle(s) increase(s). If the rate of absorption is sufficiently high, the particle(s) will reach incandescent temperatures (2500-4500K for soot) and produce photonic emissions that exhibit a near black-body spectral characteristic, termed grey-body emission. This effect was first documented (Dec *et al.* 1991), when the unwanted interference of soot incandescence upon an anti-Stokes Raman scattering experiment was observed. Subsequent authors have demonstrated the radiation intensity to be very nearly proportional to the soot volume fraction (Smallwood *et al.* 2002, Snelling *et al.* 2005). The technique has found favour with experimentalists due to the ease of obtaining a signal through application of a high powered laser and the broadband spectral emission characteristic that enables the employment of a wide range of collection strategies. Accordingly, LII has been extensively applied to well characterized laboratory burner flames as a means of validating and refining the technique (Bladh *et al.* , Flower 1989, Schraml *et al.* 1999, Siebers 1999, Higgins *et al.* 2000, Snelling *et al.* 2000, Higgins *et al.* 2001, Smallwood *et al.* 2002, Hofmann *et al.* 2003, Bladh *et al.* 2004, Bladh *et al.* 2006, Pickett *et al.* 2006).

The application of LII to optically accessible diesel engines and rapid compression machines to investigate in-cylinder soot formation has been the focus of many successful research initiatives (Flower 1985, Böhm *et al.* 1989, Kamimoto *et al.* 1989, Sato *et al.* 1990, Dec 1992, Alatas *et al.* 1993, Marinov *et al.* 1999, Schraml *et al.* 1999, Kock *et al.* 2002, Henle *et al.* 2005, Miles *et al.* 2007, Blanquart *et al.* 2009).

Previous authors have been successful in qualitatively characterising the spatial soot distribution (Böhm *et al.* 1989, Dec *et al.* 1991, Smallwood *et al.* 2002, Henle *et al.* 2005, Miles *et al.* 2007) through the use of planar LII (2D-LII) in which a sheet formed laser is incident with a soot population of interest. A suitably excited planar region within a soot structure will produce spatially distributed LII emissions, from which, spatially resolved relative soot concentration data may be realized.

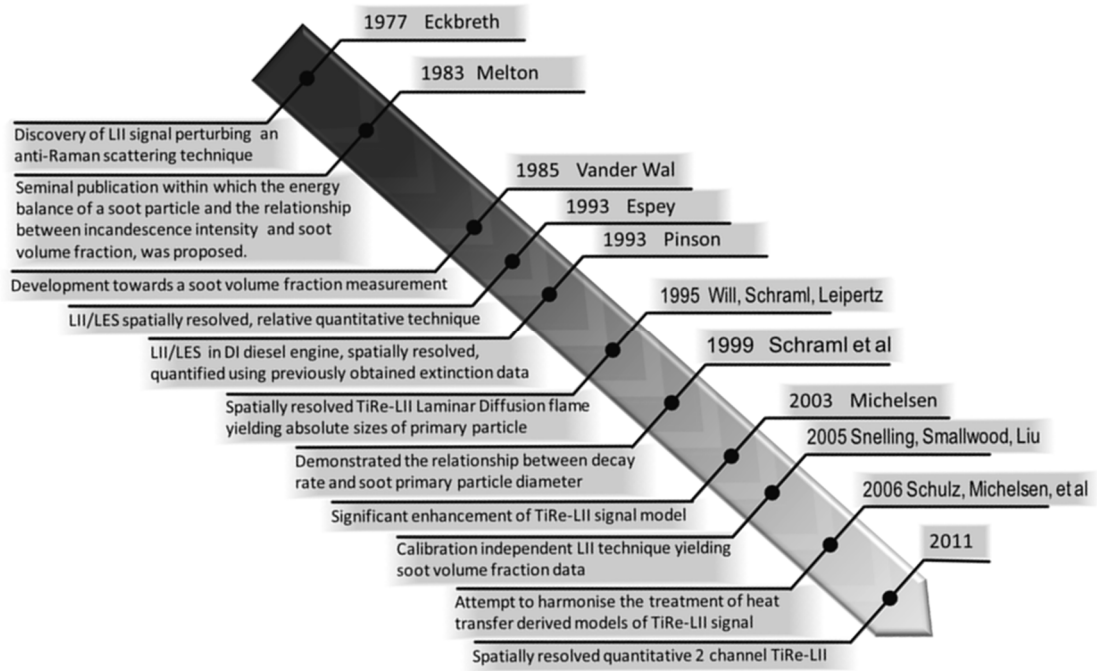


Figure 21 Summary timeline of developments within the field of LII.

The pioneering experimentalists regarding the LII technique were, quite appropriately concerned with achieving the measurement of the incandescing soot's radiant signal and were less concerned about affecting the soot population constituents; the notion that if a sufficiently intense laser heating event occurred, a vaporisation of carbon temperature threshold would be exceeded, the unvaporized soot particles would all have approximately the same temperature. This allowed Melton (2005) to propose that radiation intensity is very nearly proportional to the soot volume fraction:

$$E_{LII} = C_{exp1} \int_{\lambda_{em}=0}^{\infty} \int_{r=0}^{\infty} N_p P(r) r^{(3+0.154\lambda_{em}^{-1})} dr \cdot d\lambda \quad \text{Equation 33}$$

Where:

E_{LII} irradiance due to incandescence [$\text{W} \cdot \text{sr}^{-1} \cdot \text{m}^{-2}$]

C_{exp1}	experimentally-derived calibration constant encompassing all effects of signal collection optics efficiency and geometry, soot emissivity and excitation
N_p	number of primary particles per unit volume [m^{-3}]
$P(r)$	probability density function
r	particle radius [m]
λ_{em}	acquisition wavelength [nm]

Since:

$$f_v = \frac{\frac{4}{3}\pi \int_{r=0}^{\infty} p(r) N \cdot N \cdot r^3 \cdot dr}{V_{measure}} \quad \text{Equation 34}$$

See Equation 8 in Section 2.2.3.2 for variable description.

The radiated LII signal is in proportion to particle radius raised to the power $(3+154\lambda_{em}-1)$, which for visible light wavelengths takes the value between 3.2 and 3.4:

$$r^{(3+0.154\lambda_{em}^{-1})} \cong r^3 \quad \text{Equation 35}$$

Therefore:

$$E_{LII} \propto f_v \quad \text{Equation 36}$$

This is dependent upon a set of assumptions:

- The laser fluence propagating through the measurement volume is considered homogeneous. A measurement volume is typically defined as the volume described by the edge(s) of an incident laser beam or sheet with the bounds of the normally disposed measurement area, typically a circular section for pinhole constricted photomultiplier tube optical schemes, or a rectangular section defined by the dimensions of a camera pixel (multiplied by the total optical path magnification factor).

- The entire soot population must reach very nearly the same peak temperature, approaching or exceeding the sublimation temperature of soot.
- The absorption coefficient, K_{abs} , of the soot is considered equal to the soot extinction coefficient, K_{ext} ; therefore the scattering coefficient, K_{scat} , must necessarily be insignificant, since:

$$K_{ext} = K_{scat} + K_{abs} \quad \text{Equation 37}$$

Where:

K_{ext} Extinction coefficient

K_{scat} Scattering coefficient

K_{abs} Absorption coefficient

For application to LII experimentation, both planar and punctually resolved, a temporal integration across an acquisition window of radiance due to incandescence can be expressed as:

$$S_{LII} = C_1 \int_{t=0}^{\tau} C_n(t) \cdot W(t) \int_{\lambda_{em}=0}^{\infty} \int_{r=0}^{\infty} N_p P(r) r^{(3+154\lambda_{em}^{-1})} dr \cdot d\lambda \cdot dt \quad \text{Equation 38}$$

Where:

S_{LII} temporally integrated, temporally gated LII signal [Counts]

$C_n(t)$ soot particle number density [m^{-3}]

$W(t)$ signal windowing function

Considering the implications of a formulation that equates a recorded LII signal, S_{LII} , with an expression that is a product of a windowing function, $W(t)$, then it is apparent that the recorded signal constitutes the sum of the temporally variant LII signal captured throughout the time span in which $W(t) \neq 0$. The $W(t)$ function may be thought of as a camera exposure function, or as the temporal summation interval of a signal captured by a photomultiplier.

Planar resolved laser induced incandescence (2D-LII) yields a spatially resolved LII emission. Though not temporally resolved, the captured signal must necessarily constitute the summation of radiant emission signal across the ($W(t) \neq 0$) sampling duration of the acquisition apparatus. Typically an intensified charged coupled device (ICCD) camera will be used and the sampling duration will therefore be the exposure duration. In order to capture an LII emission that may then be equated to the soot volume fraction, a 'prompt' acquisition strategy may be employed; the camera exposure is timed to capture the peak emission that occurs shortly after ($\sim 2-3$ ns) the laser pulse peak intensity point. Prompt acquisition precludes the capture of signal that varies in intensity due to differential cooling of different size particles.

LII has several aspects that are conceptually and practically challenging, yet it suggests itself to be an insightful diagnostic tool for the study of soot particles within flames. Previous experimentalists have undertaken LII measurements upon diesel engines at elevated pressures, experiencing difficulties owing to the weak emitted signal. Typically, low soot concentration soot plumes (low equivalence ratio) are employed to reduce laser beam or sheet extinction and attenuation of signal through signal trapping. Signal trapping occurs when the soot structure between the measurement volume and the detection optics attenuates the radiant emission signal. Deviation from a typical diesel engine condition soot plume structure is balanced against the necessity of producing a sufficiently intense emission signal. The necessarily modest soot yield and associated emission intensity (relative to that of a laboratory burner at atmospheric conditions), as well as the comparatively rapidly rate of decay of the LII emission at elevated pressures, present challenging experimental conditions. Additionally, compromises associated with the application of optical detection apparatus to modified engines (Boiarciuc *et al.* 2005), versus the deviation from typical engine geometry of dedicated optical access research engines and rapid compression machines, must be appropriately considered.

2.7.1 Time resolved laser induced incandescence (TiRe-LII) of soot

Time-resolved laser-induced incandescence (TiRe-LII) is a technique in which the temporal variation of radiant emission due to incandescence is used as a means of characterising the cooling of the soot particulate population within the measurement volume and subsequently to calculate primary particle diameter

TiRe-LII exploits the dependence of particle cooling upon surface area and internal energy capacity upon particle volume. The ratio of surface area to volume is greater for a small particle than for a large particle. Consequently, the rate of cooling is more rapid for a small particle relative to that of a large particle.

A relationship between a temporally resolved, spectrally filtered, radiance emission and particle temperature may be established by means of an absolute intensity calibration. This typically, would be performed utilizing the radiance from a tungsten filament

calibration lamp, the associated calibration data and knowledge of the optical collection geometry.

A model of particle energy and mass conservation in terms of particle diameter, (encompassing the significant heat transfer and mass transport mechanisms) is manipulated to yield a pair of coupled simultaneous differential equations for particle temperature and mass. Solution of these yield temporally resolved particle temperature and diameter data.

The expressions are dependent upon input parameters, amongst which is initial particle diameter. By employing an indirect solution search algorithm, the modelled temperature variation of the particles can be adjusted such that the difference between the modelled and measured data is minimized, yielding the input parameter value of initial particle diameter.

TiRe-LII has been and remains the pursuit of much research (Will *et al.* 1995, Appel *et al.* 1996, Will *et al.* 1998, Schraml *et al.* 1999, Allouis *et al.* 2000, Axelsson *et al.* 2000, Snelling *et al.* 2000, Axelsson *et al.* 2001, Kock *et al.* 2002, Snelling *et al.* 2005)

Two-colour time-resolved laser-induced incandescence (2C-TiRe-LII) is a technique that employs the principles of TiRe-LII except radiant emissions are captured across two different discrete spectral intervals such that temperature may be calculated utilizing the two-colour pyrometry principle. This has the advantage that absolute intensity calibration is not necessary since the ratio of signals (for both modelled and measured data) is used to calculate temperature (2.6.1).

Model expressions for the heat transfer mechanisms of soot are the subject of considerable research efforts (Filippov *et al.* 2000, Bladh *et al.* 2004, Kock *et al.* 2005, Schulz *et al.* 2006, Liu *et al.* 2007, Michelsen *et al.* 2007). Several models have been proposed and successively refined or expanded upon, and although not entirely in agreement, an overarching consensus as to the significant parameters is apparent amongst the research community. Excellent work has been conducted to date in an attempt to harmonize the research field in terms of standardizing aspects of experimental studies to aid comparison between proposed models (Schulz *et al.* 2006, Michelsen *et al.* 2007).

2.7.2 Planar and time-resolved laser-induced incandescence (2D-TiRe-LII) of soot

Simultaneous spatial and temporal resolution of LII radiant emission from a planar region within a soot plume presents the possibility of spatially resolving soot primary particle size. In this study, a multi-framing camera unit is employed to capture a sequence of discrete exposure duration images. The sequence of images may then be processed to obtain information about the temporal evolution of the LII signal at each pixel location within the field of view.

Such an approach differs from punctually calibrated planar LII in which a simultaneous TiRe-LII punctual experimental branch is utilized (Boiarciuc *et al.* 2006). This typically, will be through the use of camera capturing the emitted signal from a planar region of excited particles and two spectrally filtered photomultipliers capturing the temporally varying emission at a known location within the field of capture of the camera.

2.7.3 Energy balance for a single spherical, homogenous soot particle

An energy balance, arranged such that all rate of heat transfer terms are summed together, must necessarily equal the change of internal energy of a system. For this study, a single spherical, homogeneous particle whose properties are consistent with that of graphitic carbon, serves as the base premise of the model of heat transfer mechanisms of LII and is illustrated in Figure 22.

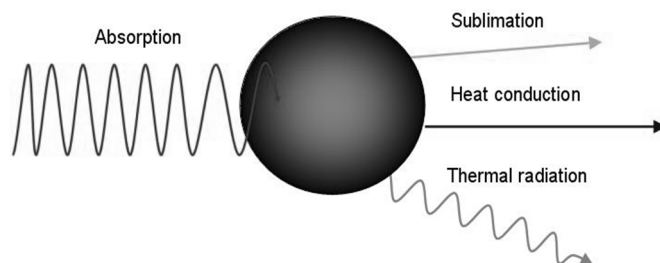


Figure 22 Primary heat transport mechanisms for a single spherical, homogeneous soot particle.

This constriction of the conceptual scheme affords the simplicity of regular geometric expressions of surface area, cross sectional area and volume. The absolute value of internal energy is an inconvenient quantity since at its broadest interpretation it involves many terms that are unknown, problematic to define, and do not change across any process described herein. The rate of change of internal energy is however equal to the rate of change of the thermal transport mechanisms. The differential relationship may be rearranged to equate to zero thus illustrating the necessary adherence to conservation of energy:

$$\dot{Q}_{int} - \dot{Q}_{abs} - \dot{Q}_{con} - \dot{Q}_{rad} - \dot{Q}_{sub} - \dot{Q}_{ann} - \dot{Q}_{oxi} = 0 \quad \text{Equation 39}$$

An energy balance equation, valid for non-aggregated particles at atmospheric conditions as framed by Melton (Snelling *et al.* 2005) and sighting expressions of efficiency proposed by Eckbreth (Dec *et al.* 1991, Allouis *et al.* 2000) is presented:

$$C_{abs}(r)\pi r^2 q(t) - \frac{K_r (T - T_0)(4\pi r^2)}{r (1 - GK_n)} + \frac{\Delta H_v dM}{W_s dt} - \sigma_{sb}(T^4 - T_0^4)(4\pi r^2) - \frac{4}{3}\pi r^3 \rho_s C_s \frac{dT}{dt} = 0 \quad \text{Equation 40}$$

2.7.3.1 Knudsen number and model regime

The Knudsen number is a non-dimensional value that quantifies the distinction between continuum, transition and molecular regimes. If the ratio of the mean free path length (λ_{kn}) to system characteristic length (L_{kn}) in which pressures are sufficiently high then a statistical mechanics derived molecular model of interaction between particles is warranted. When the pressures are sufficiently high that the spacing between adjacent molecules is more nearly immediate, a continuum regime is more representative of their interactive behaviour. An intermediate condition where neither of these approaches is satisfactory is considered to constitute a transition regime within which contributions of both model types may be used in appropriate proportion.

K_n Knudsen number [#], defined as:

$$k_n = \frac{\lambda_{kn}}{L_{kn}} \quad \text{Equation 41}$$

Where:

L_{kn} system characteristic length defined as:

The condition of the Knudsen regime is verified if $L \gg$ radius of the particle

$$L_{kn} = \frac{k_p \cdot T_0}{\sqrt{2} \cdot \sigma_A \cdot P_0} \quad \text{Equation 42}$$

Where:

σ_A mean molecular cross section of surrounding gas

K_p Boltzmann constant in effective pressure units

T_0 ambient temperature [K]

P_0 ambient pressure [Pa]

2.7.3.2 Internal energy

The change of internal energy of the particle is dependent upon the mass and specific heat capacity.

$$\dot{Q}_{int} = \frac{4}{3} \pi r^3 \rho_s C_s \frac{dT}{dt} \quad \text{Equation 43}$$

Where:

ρ_s density of solid phase carbon [$\text{kg} \cdot \text{m}^{-3}$]

C_s specific heat capacity of solid phase carbon [$\text{J} \cdot \text{kg}^{-1} \cdot \text{K}^{-1}$]

2.7.3.3 Absorption

The rate of energy absorbed from the incident laser, \dot{Q}_{abs} is:

$$\dot{Q}_{abs} = C_{abs}(r)\pi r^2 q(t) \quad \text{Equation 44}$$

Where:

C_{abs} absorption cross section [m^2] and may be expressed as:

$$C_{abs} = \frac{\pi^2 8r^3 E(m)}{\lambda} \quad \text{Equation 45}$$

$q(t)$ temporal function of laser intensity [$J.s^{-1}.cm^{-2}$]

$$q(t) = \frac{F q_{exp}(t)}{\int_0^{60ns} q_{exp}(t') dt'} \quad \text{Equation 46}$$

Where:

F laser fluence [$J.cm^{-2}$]

q_{exp} experimentally realized laser

For the laser apparatus used in this study, the temporal profile is considered Gaussian:

$$q_{exp} = \frac{1}{\sigma\sqrt{2\pi}} \int_a^b e^{\left(-\frac{(t-t_{centre})^2}{2\sigma^2}\right)} \quad \text{Equation 47}$$

$$\sigma = \frac{\Delta t}{2} \quad \text{Equation 48}$$

All evaluated for:

$$t \leq t_{centre} - 4\sigma \quad \text{and} \quad t \geq t_{centre} + 4\sigma \quad q_{exp}=0$$

Where:

t_{centre} is the time at which the laser intensity is at its peak value

2.7.3.4 Conduction

The rate of heat transferred to the medium (in this formulation defined as air at ambient temperature T_0) is:

$$\dot{Q}_{con} = \frac{K_r (T - T_0)(4\pi r^2)}{r (1 - GK_n)} \quad \text{Equation 49}$$

Where (Kock *et al.* 2002) defined for air:

$$K_r = 5.83 \times 10^{-5} \left(\frac{T}{273} \right)^{0.82} \quad \text{Equation 50}$$

T_0 Ambient/surrounding gas temperature [K]

G Geometric heat transfer factor [#], defined as:

$$G = \frac{8f}{\alpha} (\gamma + 1) \quad \text{Equation 51}$$

Where:

f Euchen factor [#] (Chapman *et al.* 1970)

γ Heat capacity ratio [#], defined as:

$$\gamma = \frac{C_p}{C_v} \quad \text{Equation 52}$$

Where:

C_p specific heat of soot at constant pressure [$\text{J.kg}^{-1}.\text{K}^{-1}$]

C_v specific heat of soot at constant volume [$\text{J.kg}^{-1}.\text{K}^{-1}$]

2.7.3.5 Sublimation

The energy expended in vaporizing the carbon is:

$$\dot{Q}_{sub} = \frac{\Delta H_v}{W_s} \frac{dM}{dt} \quad \text{Equation 53}$$

Where:

ΔH_v Enthalpy of vaporisation [J.mol^{-1}]

W_s molar mass of sublimated carbon [kg.mol^{-1}]

2.7.3.6 Oxidation

Oxidation is disregarded in this study, as is typical when modelling the heat transfer phenomena of LII. The overall heat transfer contribution is small enough to disregard having weighed the additional complexity and computational cost. For completeness, a formulation (Michelsen 2003) that considers CO production from a surface reaction of oxygen and carbon is presented:

$$\dot{Q}_{oxi} = (-\Delta H_{ox} - 2\alpha_T C_p^{CO} T) \frac{4\pi r^2 k_{OX}}{N_A} \quad \text{Equation 54}$$

Where:

ΔH_{OX}	Enthalpy of oxidation [J.kg ⁻¹]
α_T	Thermal accommodation coefficient
C_p^{CO}	Specific heat capacity of Carbon monoxide [J.kg ⁻¹ .K ⁻¹]
k_{OX}	Oxidation coefficient [kg.m ⁻² .mol ⁻¹ .s ⁻¹]
N_A	Avagadro number, 6.02214179x10 ²³ [mol ⁻¹]

Author(s)	Regime	α_T
Bladh-Bengtsson	Transition regime	0.3
Boiarciuc	Transition at low pressure	0.26
Boiarciuc	Continuum at high pressure	
Dreir-Bockhorn	Free molecular Flow	0.2
Dreier-Roth	Free molecular Flow	1
Dreier-Roth	Transition	1
Dreier-Roth	Continuum	1
Dreir-Schittkowski	Transition	0.9
Hadef	Free molecular Flow at low pressure	0.3
Hadef	Transition at high pressure	
Kock-Roth	Free molecular at low pressure	<1
Kock-Roth	Transition at intermediate pressure	<1
Kock-Roth	Continuum at high pressure	
Liu	Transition	0.37
Michelsen	Free molecular at low pressure	0.26
Michelsen	Transition at high pressure	

Table 2 Comparison between author's conduction model regimes, model dependencies and thermal accommodation coefficient α_T .

As illustrated in Table 2, absolute consensus on the correct value of thermal accommodation coefficient, α_T , in any (Knudsen) regime, is not achieved at present. For this study, atmospheric conditions constitute a free molecular regime, utilizing a value of $\alpha_T = 0.3$. High pressure, diesel engine conditions, constitute a continuum condition in which $\alpha_T = 1$.

2.7.3.7 Annealing

Though disregarded in this study, an effect of annealing may be the rearrangement of solid phase material within the carbon spherules of soot, such that inhomogeneous shell like structures are resultant. Since annealing does not reduce the amount of material, an increase of externally presented surface area, and therefore particle cross section must occur. An expression of the cross section in terms of the proportion of recrystallized and non-recrystallized carbon constituents was presented (Michelsen 2003).

$$C_{abs'} = (1 - X_{ann})C_{abs} + X_{ann}C_{abs,recrystallized} \quad \text{Equation 55}$$

Where:

$C_{abs'}$ annealing process modified absorption cross section [m^2]

$C_{abs,recrystallized}$ absorption cross section of recrystallized carbon [m^2]

X_{ann} recrystallized carbon mass ratio

2.7.4 High pressure, continuum regime conditions

High-pressure conditions, as occur in an engine combustion chamber, reduce the distance between adjacent molecules to such an extent that the statistical mechanics derived expression for the conduction heat transfer mechanism ceases to be valid. A continuum regime model is utilized throughout the high pressure experimental data processing, and is expressed as:

$$\dot{Q}_{con} = \frac{K_r (T - T_0)(4\pi r^2)}{r (1 - GK_n)} \cdot f_h \quad \text{Equation 56}$$

Where f_h is an empirical relationship defined by (Williams *et al.* 1991):

$$f_h = \frac{1}{\left(1 + \frac{K_n(1.923.R_{HF} + 1.3026)}{1.9243.K_n + 1}\right)} \quad \text{Equation 57}$$

Within which, R_{HF} , the ratio of heat fluxes is defined as:

$$R_{HF} = 5 \cdot \frac{\sqrt{\pi}}{\alpha_T} \cdot \frac{(\gamma - 1)}{(\gamma + 1)} \cdot K_n \quad \text{Equation 58}$$

The rate of energy loss by black-body radiation is:

$$\dot{Q}_{rad} = \sigma_{sb}(T^4 - T_0^4)(4\pi r^2) \quad \text{Equation 59}$$

σ_{sb} Density of solid carbon in grams per centimetre cubed [gcm^{-3}]=2.26

(Allouis *et al.* 2000)

The rate of internal energy rise is defined as:

$$\dot{Q}_{int} = \frac{4}{3}\pi r^3 \rho_s C_s \frac{dT}{dt} \quad \text{Equation 60}$$

Continuity equation (mass balance)

$$-\rho_s \frac{dr}{dt} = \rho_v U_v \quad \text{Equation 61}$$

Where:

ρ_s density of solid phase carbon [kg.m^{-3}]

ρ_v density of vapour phase carbon [kg.m^{-3}]

U_v vapour phase velocity [m.s⁻¹]

The rate of energy loss of energy due to sublimation is:

$$\dot{Q}_{sub} = -\frac{\Delta H_{sub}}{W_s} 4\pi \cdot r^2 \cdot P^* \cdot e^{\left[\frac{\Delta H_{sub} \cdot (T - T^*)}{R \cdot T \cdot T^*}\right]} \frac{1}{R_p} \left(\frac{W_v \cdot R_m}{2\pi}\right)^{1/2} \cdot T^{-1/2} \quad \text{Equation 62}$$

Where:

W_s Molecular weight of carbon solid [g.mol⁻¹]

T^* Soot vaporisation temperature [K]

P^* Reference pressure for soot vaporization temperature, T^* . [Pa]

R_p Gas constant, effective pressure units [atm.cm³.mol⁻¹.K⁻¹]

W_v Molar mass of carbon vapour [g.mol⁻¹]

R_m Gas constant, effective mass units [atm.cm².mol⁻¹.K⁻¹.s⁻¹]

Relating sublimation to mass change:

$$\dot{Q}_{sub} = \frac{1}{W_s} \left(\frac{dM}{dt}\right) \Delta H_{sub} \quad \text{Equation 63}$$

Relating particle mass change to particle vapour phase velocity:

$$\frac{\rho_s}{2} \frac{dD}{dt} = -\rho_v U_v \quad \text{Equation 64}$$

Relating vapour phase velocity to pressure and temperature:

$$\frac{\rho_s dD}{2 dt} = - \left(\frac{P \cdot W_v}{R_p \cdot T} \right) \cdot \left(\frac{R_m \cdot T}{2\pi \cdot W_v} \right)^{1/2} \quad \text{Equation 65}$$

Expressing pressure utilizing the Clayperon equation:

$$P = P^* \cdot e^{\left[\frac{\Delta H_{Sub} \cdot (T - T^*)}{R \cdot T \cdot T^*} \right]} \quad \text{Equation 66}$$

Where:

ΔH_{Sub} Heat of vaporization of carbon = $7.78 \times 10^5 \text{ J} \cdot \text{mol}^{-1}$

2.7.5 Refractive index of soot

The propagation of electromagnetic waves through carbonaceous soot particles incurs losses associated with the internal dispersion of energy during transit. This is expressed in the following form:

$$m = n - ik \quad \text{Equation 67}$$

Where:

m is the complex refractive index

n is the real component of refraction

k is the complex component of refractive index or extinction coefficient

Several authors have conducted studies upon the complex refractive index of soot (Habib *et al.* 1988, Stagg *et al.* 1993, Smyth *et al.* 1996) and whilst no universal concurrence has been achieved, values of $n=1.57$ and $k=-0.56$ are generally considered suitable for analysis of the interaction with electromagnetic waves in the visible spectrum. Accordingly, these values are used in this study.

2.7.6 Spectral function

The spectral function is a function of the refractive index of soot and characterizes the spectrally variant soot absorption, defined as:

$$E(m) = \frac{6nk}{(n^2 - k^2 + 2)^2 + 4n^2k^2} \quad \text{Equation 68}$$

Which may also be expressed as:

$$E(m) = -Im \left(\frac{m^2 - 1}{m^2 + 2} \right) \quad \text{Equation 69}$$

2.7.7 Emissivity (ϵ_λ)

The variation of the emissivity value of soot with emission wavelength and other parameters of the soot necessitates the use of an expression that captures this information. No definitive, universally accepted expression has been adopted; several approaches both empirical and theoretically derived, have been proposed (Hottel *et al.* 1932, Siddal *et al.* 1962, Lee *et al.* 1981, Wahiduzzaman *et al.* 1987) and are closely related to either the empirical quantity α or the spectral function $E(m)$.

2.7.7.1 The ' α ' model

An empirically derived expression was proposed (Hottel *et al.* 1932) following experiments with a series of luminous flames and an optical pyrometer. They proposed that the emission could be equated to that of the absorption of a diathermanous of a medium and that the absorption coefficient (k_{abs}) could, for a limited wavelength range, be equated to an extinction coefficient (K_{ext}) divided by wavelength to the power of an empirically derived and wavelength dependent constant α . This yielded the expression that has endured and under certain circumstances, produces the most accurate values for emissivity of soot of the expressions that have so far been proposed.

$$\epsilon_\lambda = 1 - e^{\left(\frac{-KL}{\lambda^\alpha}\right)} \quad \text{Equation 70}$$

2.7.7.2 The 'E(m)' model

An alternative expression for the emissivity of soot was proposed (Siddal *et al.* 1962, Lee *et al.* 1981) using spectral function $E(m)$, based upon complex refractive index of soot and the soot volume fraction, f_v . The spectral function equates to an absorption coefficient for the soot related to the complex refractive index and is invariant with wavelength of the incident radiation.

$$\varepsilon_\lambda = 1 - e^{\left(\frac{-36\pi E(m)f_v}{\lambda}\right)} \quad \text{Equation 71}$$

2.7.7.3 The 'g' model

A third model was proposed (Wahiduzzaman *et al.* 1987) that attempts to ignore the refractive index of the soot and therefore the spectral function $E(m)$. The refractive index of soot is in itself the subject of extensive study (Smyth *et al.* 1996) and presents difficulties to the experimentalist in determining its value with sufficient certainty. An additional constant g , is introduced and following subsequent work (Gray *et al.* 1974), its value was reappraised to be 6.3.

$$\varepsilon_\lambda = 1 - e^{\left(\frac{-g f_v L}{\lambda^\alpha}\right)} \quad \text{Equation 72}$$

Selection of a suitable value of α depends on the wavelength of light being measured, the soot particle size and the refractive index of soot. It is also reported that fuel type may also have an influence on the value of α (Gaydon 1957).

In the visible region of the electromagnetic spectrum, the calculated value for true flame temperature demonstrate invariance with that of α . Conversely, the effect of α upon the calculated temperature when employing wavelengths in the infra-red region is significant.

A similar effect of α on the calculation of KL is observed, in the visible range, the effect upon KL value is negligible, yet in the infra-red region the effect is to alter the calculated value by several orders of magnitude.

A recommendation for a value of 1.39 when measuring at visible wavelengths is made. For the infra-red region, the choice of α value is far less clear, though a fixed value close

to unity (0.77 to 1.25, typically around 0.96) appears to be most appropriate for diesel flames from 800 nm to 7000 nm.

2.8 Extinction

Extinction refers to the ray-wise attenuation of laser fluence incident with an absorptive medium. The working principle is to measure the fluence before and after the absorptive region, such that the ray-wise integrated, or summed, reduction in laser fluence is measured and therefore the ray-wise average extinction coefficient, K_{ext} , is calculable:

$$\frac{I}{I_0} = e^{-f_v \int_0^L K_{ext} dL} \quad \text{Equation 73}$$

Where:

I Extinguished laser fluence [$\text{mJ}\cdot\text{cm}^{-2}$]

I_0 Unextinguished laser fluence [$\text{mJ}\cdot\text{cm}^{-2}$]

Since the extinction medium is typically, spatially distributed, and potentially non-homogeneously distributed, more information is required to define the local laser fluence profile along the ray path. For an axisymmetric burner flame, the spatial distribution of the extinction medium, the soot, can be inferred from the radial soot volume fraction distribution f_v , at the same height above burner as the laser ray path. From this data and that of the ray-wise integrated extinction through the flame and soot structure, the distribution of extinction, the local KL optical thickness value, may be calculated and used to construct a spatially distributed laser fluence map.

For an irregular extinction medium distribution, such as that produced in the combustion chamber of a diesel engine, LII data in addition to that of ray-wise integrated extinction data is utilized to calculate a spatially distributed laser fluence map.

The theoretical association between the distribution of the LII radiant emission signal and the extinction constituents at each location within the field of data can be explained by starting from an expression for the radiant LII signal S_{LII} , which is in terms of a practically established calibration factor C_{cal} , a particle size distribution or PDF function, a particle number density C_n , and a laser excitation temporal function, all integrated across the detection spectral interval, constituent particle size population and through time:

$$S_{LII} = C_1 \int_{t=0}^{\tau} C_n(t) \cdot W(t) \int_{\lambda_{em}=0}^{\infty} \int_{r=0}^{\infty} N_p P(r) r^{(3+154\lambda_{em}^{-1})} dr \cdot d\lambda \cdot dt \quad \text{Equation 74}$$

Spectrally filtered, disregarding windowing function since we are considering the emissions within a single frame that is therefore consistent with itself, disregarding the temporal evolution of soot particle number density since the acquisition duration is short and change due to sublimation of soot being minimized by selection of a suitably non-perturbing laser fluence level:

$$S_{LII} = C_1 C_n r^{(3+154\lambda_{em}^{-1})} \int_{r=0}^{\infty} N_p dr \quad \text{Equation 75}$$

Where:

$C_n = N_d$ number density [m^{-3}]

$$\int_{r=0}^{\infty} N_p dr = 1 \quad \text{Equation 76}$$

Since the integral of a normalized probability density function is by definition equal to the value one:

$$S_{LII} \propto r^{(3+154\lambda_{em}^{-1})} \cdot N_d \quad \text{Equation 77}$$

$$S_{LII} \propto r^{3.2} \cdot N_d \quad \text{Equation 78}$$

$$f_v = \frac{\pi N_d}{6} D^3 = \frac{8\pi N_d}{6} r^3 \quad \text{Equation 79}$$

$$f_v \propto r^{3.2} \cdot N_d \propto S_{LII} \quad \text{Equation 80}$$

$$S_{LII} = C_2 \cdot f_v \quad \text{Equation 81}$$

So soot volume fraction, f_v , is demonstrated to be very nearly in proportion to measured LII signal, S_{LII} . This allows the substitution into:

$$\frac{I}{I_0} = \exp\left(-\frac{k_e \cdot S_{LII} \cdot C_2 \cdot L}{\lambda}\right) \quad \text{Equation 82}$$

$$S_{LII} = -\frac{\lambda}{k_e C_2 L} \ln\left(\frac{I}{I_0}\right) \quad \text{Equation 83}$$

Where:

C_3 constant of proportionality of LII radiance to extinction is defined as:

$$C_3 = -\frac{\lambda}{k_e C_2 L} \quad \text{Equation 84}$$

Yielding the relationship between LII signal intensity and attenuation through extinction at each location along the path of propagation of the laser:

$$S_{LII} = C_3 \ln\left(\frac{I}{I_0}\right) \quad \text{Equation 85}$$

The LII emission within the field of view presents a non-homogeneous distribution of soot and therefore a non-homogeneous distribution of laser fluence must occur as the soot structure is traversed. The bulk extinction from the cuvette data for each ray-wise path was divided by the sum LII emission along that path. This provided an extinction factor per unit of LII emission that was then multiplied by the 'LII emission intensity at each location along the ray-wise path. The resultant overall extinction was therefore consistent with the observed ray-wise integrated extinction data and demonstrated a distribution in relation to the soot location within the chamber (see section 4.2.2). A laser fluence map was then produced where the successive steps of attenuation along the laser ray path were calculated and mapped onto the spatial grid of the LII data.

3 Experimental work

3.1 Introduction

Two variations of a technique validation experiment and an application experiment are described in this chapter. The technique of planar, two-colour and time-resolved laser-induced incandescence (2D-2C-TiRe-LII) can be thought of as an extension of punctual TiRe-LII across a two dimensional plane. Rather than using a photomultiplier to measure a single radiant spectral emission value emanating from a single point location, a framing camera was used to capture a sequence of images. The camera resolution provides a matrix of point location measurements constituting the accumulated signal across the duration of the image exposures.

For an experimental technique with some element of novelty in its design or operation, it must be validated by measuring a known phenomenon or by performing the same measurements by a previously validated technique. The validation of the 2D-2C-TiRe-LII technique employed in this study was conducted upon a well-characterized laminar diffusion flame laboratory burner. The laboratory Santoro type burner was constructed and operated at the same conditions used by numerous other LII experimentalists. The measurements were performed at a location that encompassed the point locations where numerous concurring studies have mapped the nature of the soot particulates, specifically the primary particle size and soot volume fraction measurements. By applying the measurement technique to a subject of known parameter values, the efficacy and validity of the technique is itself examined.

The final experimental step is to employ the validated technique upon a subject of interest. For this work, that constitutes the soot population structure produced within a direct injection diesel engine; the notable differences being the elevated pressures and temperatures encountered. In order to realize these conditions, a reciprocating rapid compression machine (RCM) was used that provided optical access to the combustion chamber in which temperatures and pressures typical of diesel engines were produced. The effect upon the LII radiant emission was countenanced through the adjustment and optimisation of the acquisition apparatus and strategy of the experimental setup.

3.2 Experimental subjects

For development and validation of the 2D-2C-TiRe-LII technique, a laboratory burner that operates at ambient pressure was used. The challenging aspects of working upon an optical access diesel engine or reciprocating rapid compression machine relate to the limitations in terms of the optical access, the optical access window fouling, the cycle-to-cycle variation of the combustion event and therefore the cycle-to-cycle variation of flame structure, the finite duration of the flame/soot structure and the flame structure irregularity of form. These aspects are circumvented by the use of a laboratory laminar burner that produces an axially symmetric, temporally invariant flame and corresponding soot structure suitable for refining challenging techniques upon with reasonable certainty as to the reality of what is being measured.

The laminar diffusion flame and associated high sooting region is similar to that found in the flame structure produced in a diesel injection combustion event within an engine. The flame structure is of course continuous and without external disturbance, and is broadly invariant in terms of both geometry and structure. Accordingly, the carbonaceous particles produced within it are also consistent and repeatable in terms of both particle size and spatial distribution within the overall structure. This is highly beneficial when developing a measurement technique because the value of the measurement of a parameter at each location within the flame is approximately constant. This enables the verification of recorded values across multiple measurements as well as the meaningful application of ensemble averaging of data within which low standard deviation occurs.

3.3 Validation of 2D-2C-TiRe-LII on a laminar diffusion flame at atmospheric conditions

3.3.1 Introduction

For this experiment, a measurement technique is applied to a laboratory laminar diffusion flame burner of known performance. Further, the acquisition of data that yields insight into the performance of the experimental setup is also important to the development and refinement of the processing and modelling that is subsequently

employed to calculate the parameters of interest: soot primary particle diameter and soot size distribution.

3.3.2 Concept and experimental aims

A near planar region of soot particles within the burner flame structure was heated rapidly by an incidental sheet formed laser pulse, causing the particles to incandesce. The temporal decay of radiated LII emission was recorded using a calibrated camera capable of capturing a rapid sequence of images and in doing so resolving an entire planar region. This discrete, time integrated series of data point values for each pixel location may then be processed to extract the temporal signal.

The radiant emissions filtered over two spectral intervals allowed the average temperature at each location to be established through the application of two colour pyrometry theory. The application of a heat transfer mechanism derived differential equation model yielded the primary particle diameter at each location. An extension of this technique can quantify a size distribution of particles that constitutes a more likely solution for the soot population from which the radiant emission emanates.

This experimental technique aims to resolve across a spatial plane and through time, the laser induced incandescence emission. By achieving this, the spatial distribution of soot population and its size distribution at each location can be determined.

3.3.3 Equipment

3.3.3.1 Experimental subject: Santoro burner

The Santoro burner (Figure 23) has formed the basis of many studies and as such, its behaviour and its soot production are well characterized elsewhere (International Commission on Radiological 1994, Liu *et al.* 2005, Mansurov 2005, Wang 2011).

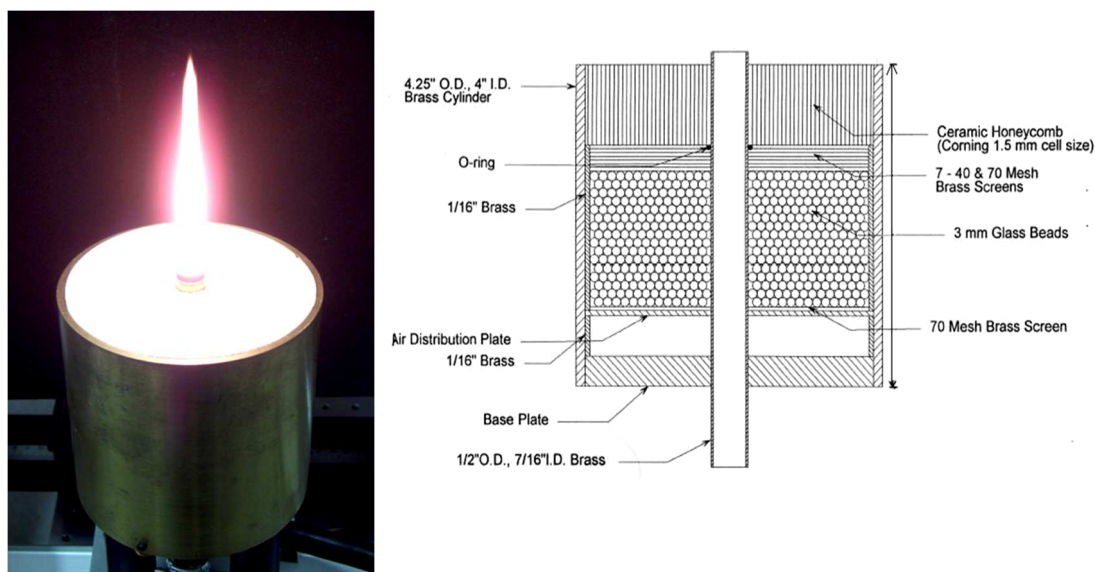


Figure 23 Santoro burner (left) and cross sectional schematic (right).

The Santoro burner produces a quasi-static laminar diffusion flame such that the combustion at the region of mixing air and fuel is at a fixed location. This affords experimentation upon it a favourable degree of repeatability such that individual data values do not significantly deviate from those obtained through ensemble averaging of multiple data points; a low standard deviation value for data possible. The co-flow serves two purposes, to provide a consistent and quantifiable supply of air (flow field direction, velocity, mass flow rate) and to act as an air curtain to the flame, notionally decoupling it from perturbing air movement fluctuations within the room in which the experiment is situated. For experimental arrangements in which even slight deviation of the flame structure from a vertical, rotationally symmetric axis is unacceptable, an arrangement of baffle and shroud elements can be added to the burner assembly to further decouple the effects of room ambient air motion.

A convenient aspect is that of the operation of the burner at ambient conditions. TiRe-LII, be it punctual or two dimensionally resolved, relies upon the principle of recording the temporally decreasing radiation from the heated soot particles and using this to calculate the nature of the soot population from which it came. The heat transport mechanism of conduction is dependent upon the pressure of the surrounding medium; at low (ambient ~ 0.1 MPa) pressure, less frequent interaction with surrounding medium molecules occurs and so the rate of conduction is lower than if the pressure was high

(typical motored in-cylinder peak pressure 8MPa) and the molecular interaction accordingly more likely. The effect of this is to slow the rate of cooling such that radiant signal changes less rapidly; at realistic engine conditions, radiant emission from laser heated soot (above that of natural flame luminosity) may last 100 ns, at ambient pressures this same decaying signal may last 1.5-2 μ s. The experimental technique developed and applied in this work uses a camera to capture a sequence of images. Each image capture has a finite exposure duration during which time incident radiant emission is incident upon the camera's sensor. The lower the rate of change of the radiant emission, the more nearly representative the captured discrete, time integrated emission is. This in turn allows a more direct use of the captured data which is beneficial in that the underlying model fit algorithm can be directly applied and accordingly particle diameter information calculated.

For the experimental work addressed here, flow rates of ethylene at 0.231 SLM (standard litres per minute) and air co-flow at 43 SLM are employed to replicate those used by other authors when characterizing the burner behaviour and soot formation. Since the burner is manufactured at the institution in which the experimentation occurs, rather than by the designer of the burner, there exists the possibility of different performance than that of the original, even where the design specification is adhered to. By operating the burner with the same fuel type, fuel and co-flow flow rates, it is possible to validate the performance of the burner itself through the application of a well understood technique of laser extinction. Data from subsequent experimentation utilizing other techniques can then be validated against the known values of the burner's properties.

An Omega FMA5400 mass flow rate regulator, calibrated for ethylene was used to meter the ethylene supply. A manufacturer-supplied calibration coefficient allowed the conversion from voltage to flow rate such that the value displayed upon a multimeter unit provided confirmation of the mass flow rate.

The co-flow of air supplied to the burner was provided by the facility compressed air supply. This was metered using an air specific GAP Meter rotimeter. A generic adjustable flow regulator was situated between the air supply and the rotimeter. The facility air supply pressure fluctuated between 6.8 and 10.0 bar due to dissipation of the reservoir content, a pressure threshold triggered compressor recharged the system

activating at 6.8 bar. The variation of supply pressure presented to the regulator caused a variation of flow rate, dropping from the target flow rate of 43 SLM to 30 SLM at the lowest supply pressure.

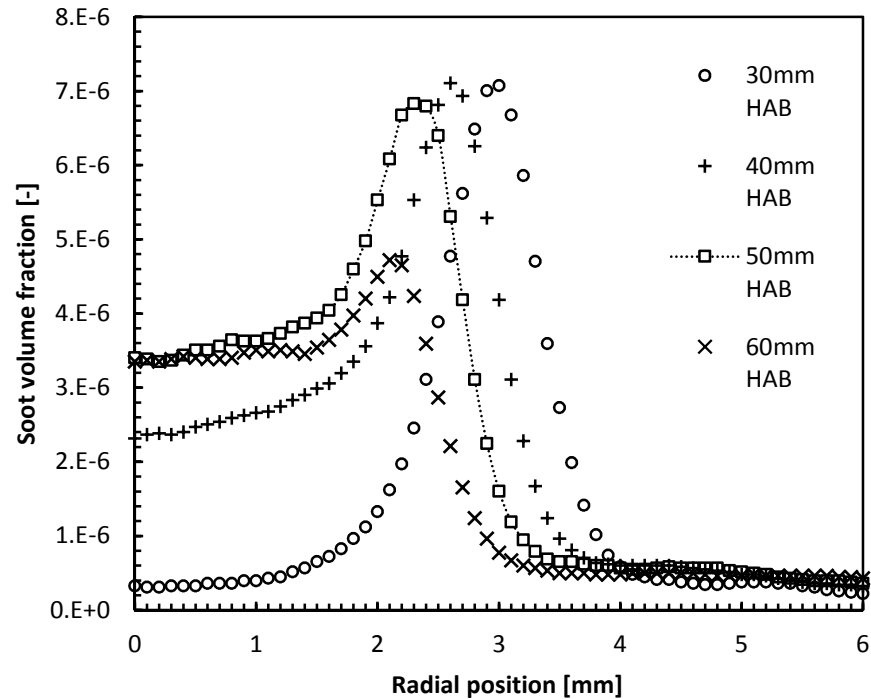


Figure 24 Radial distribution of soot volume fraction for various heights above burner (HAB) (Adapted from Oger 2013).

Figure 24 illustrates the soot volume fraction radial distribution for a range of heights above burner as obtained by (Oger 2013). This is consistent with experimentally obtained data (Santoro *et al.* 1983). A measurement region centred upon the 50 mm height above burner region was selected due to the numerous sources of data obtained by several experimentalists as well as portraying a region in which high radiant signal intensity should occur.

3.3.3.1.1 Shroud and baffle

A shroud with optical apertures was used to aid stability of the flame structure and in doing so, maintain a steady spatial distribution of soot incandescence and scattering

signals. This reduced the necessity of filtering out anomalous spatial distributions of signal data. A horizontal baffle was fitted around the base of the cylindrical main section of the burner body. This had the effect of presenting a near quiescent region of air for entrainment in the flow regime driven by the burner co-flow air and convection due to the heating of air by the flame. It was noted that illustrations of experimental arrangements conducted elsewhere often featured the burner situated upon an extensive horizontal surface and in doing so, presented more nearly similar conditions for the air that travels through the shroud, to be sourced from. The experimental arrangement employed in this work necessitated the burner be positioned at the near edge of an optical table (Figure 25). This presented a significantly different air flow to the base of the shroud and in turn affected the airflow through the shroud.

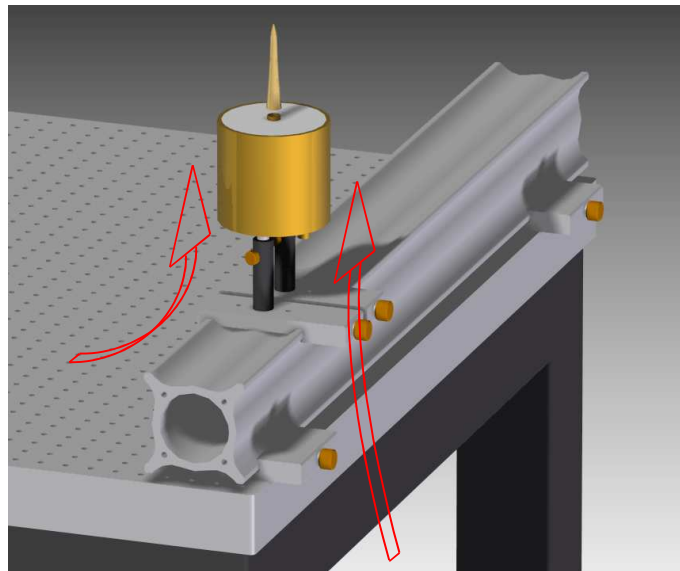


Figure 25 Santoro burner with differential air flow entrainment.

A horizontal plane baffle was fitted at the base edge of the burner. The baffle featured cut-outs to accommodate the table mounted optical components of the experimental configuration. A qualitatively more steady flame was realized. The shroud decoupled the flame from fluctuations of the air flow field within the room, whilst the baffle ensured a more nearly symmetric convective flow entrainment (Figure 26).

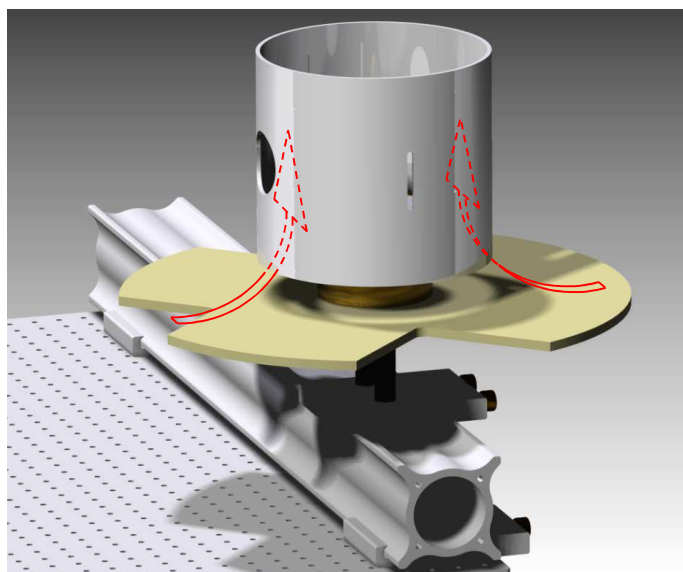


Figure 26 Baffle and cylindrical shroud to facilitate symmetric airflow entrainment paths.

3.3.3.2 Laser and associated optics

3.3.3.2.1 Laser

A frequency-doubled Quanta-Ray® GCR 150 by Spectra-Physics, Nd:YAG (Neodymium Yttrium Aluminium Garnet) laser produced a beam of coherent light 8.7mm in diameter (Figure 29) and of 532 nm wavelength. A repetition rate of between 9.4 and 10.6 Hz could be produced, however the optimum for the unit is 10Hz at which rate it can produce pulses up to 300 mJ energy. For this experiment the laser fluence was carefully selected to address a fundamental trade-off; that of maximizing incandescent radiant emission, whilst minimizing the sublimation of soot particles being measured. Figure 27 illustrates the onset of sublimation reducing the intensity of radiant emission. In addressing both the necessity to harvest a sufficiently intense signal, with that of minimizing the sublimation of the soot population, a target interval of laser fluence between 150 and 180 mJ.cm⁻² was defined. The precise fluence value produced by each laser pulse varied from one pulse to the next, necessitating online measurement for subsequent comparison and verification of the modelled value utilized in particle diameter modelling.

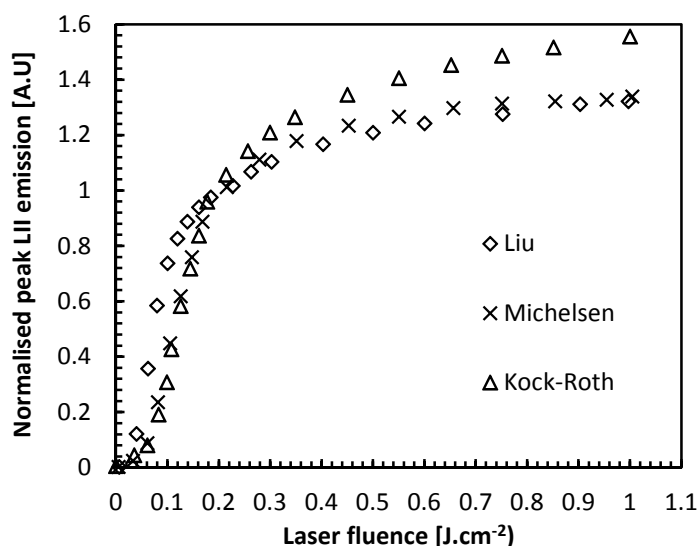


Figure 27 Normalized LII signal intensity with local laser fluence as recorded by various authors for a laser excitation wavelength of 532 nm.

3.3.3.2.1.1 Laser wavelength

The utilization throughout this study of a frequency doubled Nd:YAG laser was as a result of considering and weighing appropriately, aspects of experimentation, both practical and theoretical. Previous studies within the experimental facility had been undertaken utilizing a 532 nm wavelength laser excitation and so many of the available optical elements demonstrated suitable behaviour across the visible spectrum.

Whilst the experimental schemes were designed and the required elements obtained prior to their undertaking, extensive reconfiguration and adjustments were necessary to optimize their performance. As such, working with a visible spectrum emission was both informative and expedient. It also minimized the jeopardy posed to the people in the laboratory, for example by aiding the detection and attenuation of stray emissions.

The principle reservation regarding the utilization of 532 nm wavelength laser excitation is that of stimulating unwanted obfuscating emissions from PAH's, and molecular (H_2O , CO , CO_2 , C_2) and radical fluorescence (OH , NO , CH , HCO , NH , NH_2 , CN). Laser excitation at 532 nm wavelength of a hydrocarbon fuelled, sooting flame structure will impart energy indiscriminately to all constituents that demonstrate sufficient absorption efficiency at that wavelength.

Characterizing the fluorescence lifetimes of the various constituents is complicated by the effect of the conditions to which they are subjected. For example, the theoretical fluorescence lifetime of NO, often exploited for LIF imaging, is 700 ns, but when considering the effect of predissociation or collisional quenching, has been found to demonstrate a lifetimes of between 2 ns (Ketterle *et al.* 1992) and 0.1 ns (Arnold *et al.* 1990) for various deactivation pathways. The experimental fluorescence lifetime of PAH at atmospheric conditions has been reported at around 40 ns (Therssen *et al.* 2007). OH radical fluorescence lifetime at atmospheric conditions is reported to be in the order of 2 ns (Schwarzwald *et al.* 1987). It should be noted also that experimentation upon the same optical access rapid compression machine as used in this study, that a LIF technique study reported an absence of NO fluorescence emission from the centre of the combusting fuel plume, postulating the susceptibility to attenuation by the flame front. Where NO was present, it was situated at the tip of the fuel spray plume for high injection pressures (1600 bar) and to have stagnated at the sides of the plume for lower injection pressures (600 bar) (Demory 2007). High OH density and high soot density were found to not coexist spatially (Demory 2007).

The utilization of a prompt acquisition strategy, either encompassing or starting immediately after a 532 nm wavelength laser pulse, will likely stimulate fluorescent emissions that may manifest in the acquisition spectral interval(s) at the point of acquisition. This study therefore effectively utilized a delayed acquisition strategy. The sequence of captured images encompassed the time interval that contained the laser pulse and the consequential emissions such as fluorescence, however the data processing utilized sequences that commenced after the erroneous emissions contributions had ceased or were attenuated sufficiently such that LII signal dominated.

In the period of time through which this study was conducted, a broadening of consensus amongst experimentalists occurred regarding the superiority of 1064 nm wavelength laser excitation; principally regarding the avoidance of stimulation of fluorescence emissions. Informed by this and the challenge of, and degree of success achieved in mitigating, the effects of fluorescence, that 1064 nm represents a more suitable wavelength of excitation for such an experimental scheme in which the desire to measure only incandescence radiation is fundamental.

3.3.3.2.2 Sheet-forming optics

A series of four lenses mounted in a cylindrical housing (Figure 28) alter the beam shape from a round section into a thin and very nearly flat ‘sheet’ form (Figure 30). Each of the four lenses performs a different manipulation of the incident beam profile: the first diverges the incident beam in one axis producing a high aspect ratio oval section, the second compresses the output from the first lens into a thin sheet, the third lens collimates the still diverging sheet output from the second lens parallel to the oval profiles major axis, the fourth lens collimates across the minor axis of the oval sheet form. The composite effect of the optical scheme within the sheet forming optics is to expand the round profile in one axis normal to the axis of propagation and compress it in the other axis normal to propagation. This yields a sheet that maintains an approximately Gaussian energy distribution albeit scaled to the dimensions of the sheet.



Figure 28 Sheet forming optics assembly with cylindrical cover removed and illustrative overlay of laser path and profile.

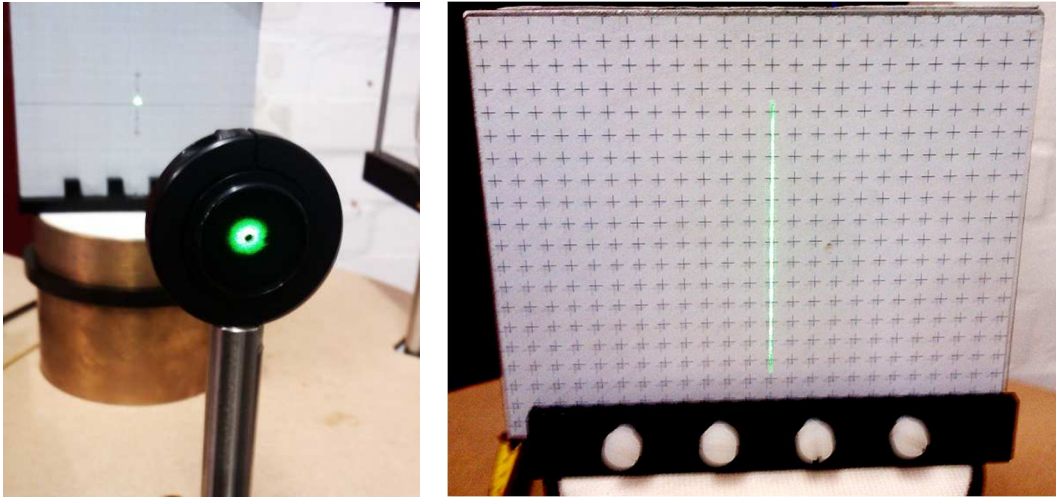


Figure 29 (left) Laser beam profile incident upon a pinhole during assembly of experimental setup.

Figure 30 (right) Laser sheet without clipping in either axis, incident upon a target plate used for spatial calibration.

3.3.3.2.3 In-line energy monitor

A LaVision manufactured in-line energy monitor was situated prior to the sheet forming optics such that the intensity of each laser pulse could be captured. An optical beam splitter assembly splits the beam in the ratio of 10% to 90%. The lower intensity beam was directed via a series of attenuating filters and an adjustable aperture to a photodiode sensor (Figure 31). The generated signal was fed into a digital storage oscilloscope. The temporal response of the energy monitor was insufficient to faithfully illustrate the point in time that the laser pulse occurred, taking several microseconds to portray a peak accumulated value (Figure 32).

3.3.3.2.4 In-line photodiode

A photodiode was employed in an appropriate impedance matching circuit such that the temporal occurrence of the laser pulse could be measured and recorded. The circuit configuration allowed the photodiode's maximum rate of response to be realized; a slew rate in the order of $5 \text{ V}\cdot\text{ns}^{-1}$. The photodiode was incorporated into the in-line energy monitor's optical assembly (Figure 31) and was suitably sensitive to detecting just the stray, internally reflected light within the housing. This yielded a signal in the order of a

few volts peak magnitude, qualitatively adhering to the expected temporal intensity profile of the laser. The magnitude of the signal in conjunction with the slew rate gave confidence of a faithful temporal representation of the laser pulse (Figure 32).

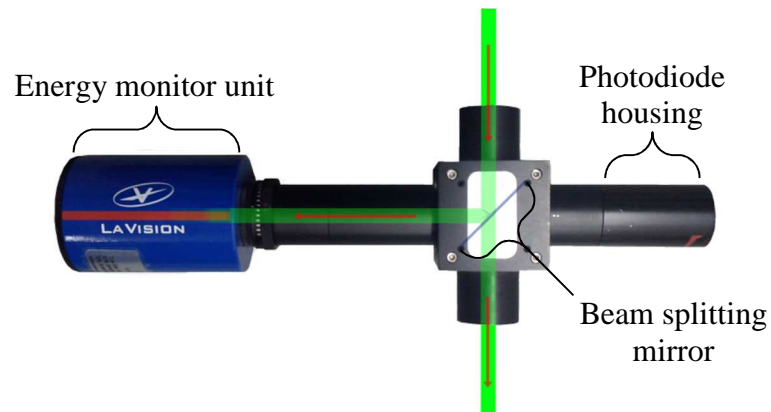


Figure 31 In-line energy monitor with associated beam splitting mirror assembly. Note, photodiode fitted via fourth port to junction block, detecting internal stray light.

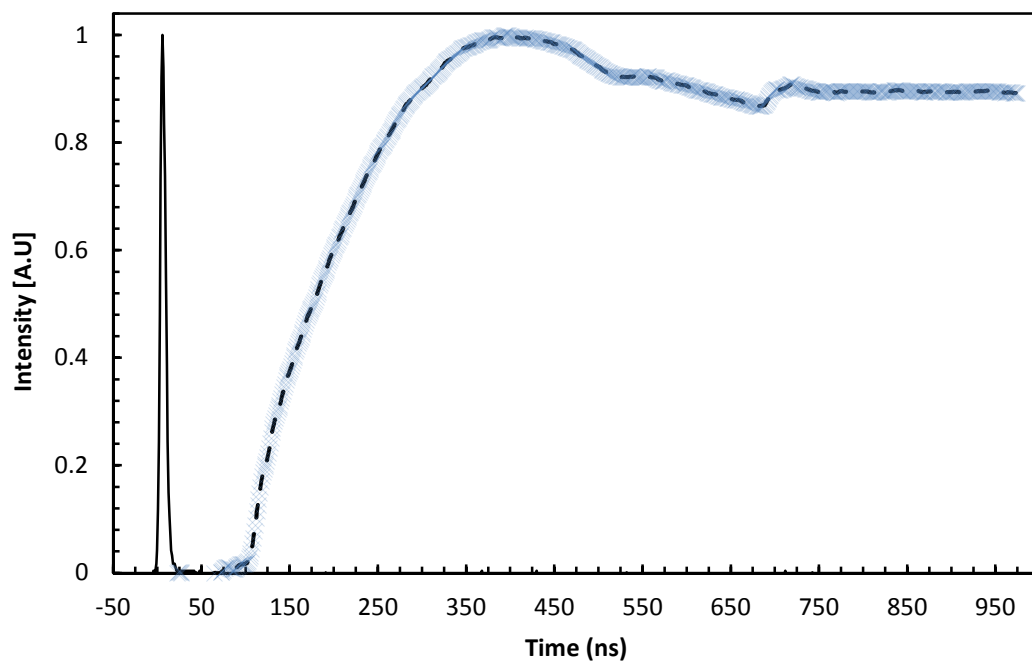


Figure 32 Comparison of normalized temporal response of photodiode (solid) and normalized in-line energy monitor (dashed) to a 7 ns FWHM laser pulse.

3.3.3.2.5 Adjustable width slit

The adjustable width slit assembly consisted of two knife edges precisely articulated to remain parallel whilst allowing fine adjustment. The laser sheet was clipped down to 0.50 mm in width immediately adjacent to the sheet forming optics assembly. The purpose of doing so was to select the central section of the notionally Gaussian distribution of intensity, thus more nearly approximating a top-hat profile, illustrated in Figure 33.

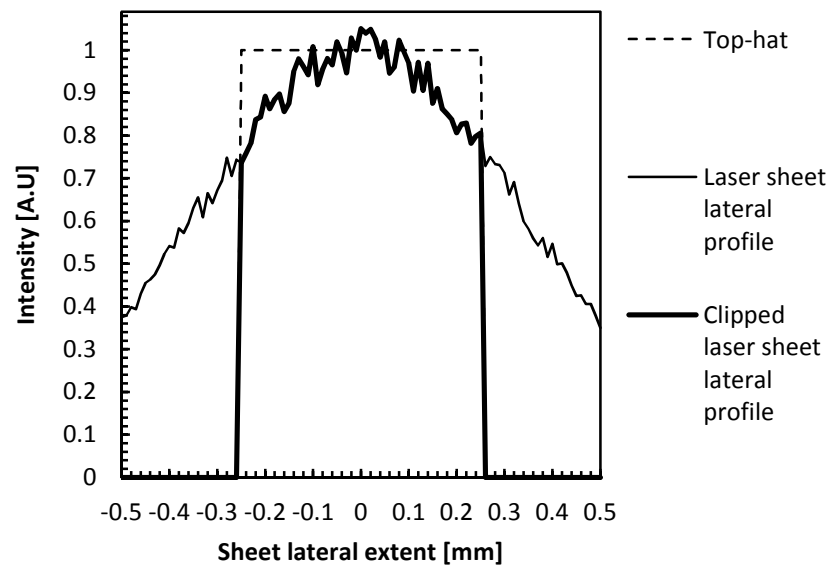


Figure 33 Near top-hat profile of clipped Gaussian beam/sheet profile.

It is desirable to have homogeneous laser fluence due to the effect upon the resulting incandescence emission. A measurement volume has finite extent along the acquisition axis defined by the excitation region thickness, be it in beam or sheet form. The incandescence emission is the sum of the radiation from all the soot particles within the measurement volume. It can conveniently be thought of as the radiation being the integration of the signal contributions across the beam or sheet thickness. If a Gaussian fluence distribution beam profile or unclipped sheet is used to excite the resident soot particles, two distinct emission schemes may occur.

Firstly, if the laser fluence is low enough such that all particles across the beam/sheet are not sublimated, then all soot particles of all sizes will be heated to approximately a temperature that is a function of the incident local fluence. If some undetermined size

distribution of particles and volume fraction are consistent across the depth of the measurement volume, then the average temperature at each location across the measurement volume extent will adhere to a Gaussian profile. Since the radiant emission intensity from each particle is dependent upon temperature to a fifth power, the radiant emission contribution will vary significantly through the depth of the measurement volume. Since these contributions are integrated along the measurement volume extent of the acquisition axis, a total emission value affected by the lower temperature outer regions of the measurement volume will be captured. Consequently, a very small underestimation of the initial temperature will occur. The fundamental challenge is that the temperature decay and according radiant emissions will be significantly different for the central and outer regions. The outer regions begin cooling from a lower initial temperature than that of the centre region. They do so more slowly since radiation and conduction heat transfer mechanisms are dependent upon temperature and temperature difference to the surrounding medium, respectively. The resulting measured temporal radiant emission will be composed of the contributions of a particle size interval population, cooling from different temperatures and will therefore be almost impossible to meaningfully interpret the contributions with the purpose of establishing constituent particle size and size distribution.

Secondly, if the laser fluence is sufficiently intense that the peak local fluence at the centre of the beam or sheet sublimates the local soot particles, then a scheme in which the central region soot population and its contribution to the sum radiant emission, occurs. Sublimation reduces the mass of all particles as a function of their temperature. Particles at the smaller end of the population size interval are therefore eradicated sooner than larger particles. For a finite period of time in which some degree of sublimation is occurring upon a population size interval of soot, the biasing of the size distribution towards smaller particles will occur. If the rate of sublimation is sufficiently high, then the entire central region soot population may be eradicated. The overall effect of a scheme in which some sublimation in the central region occurs is to significantly alter the sum radiant emission. The outer regions are likely to be at a sufficiently high temperature and to dominate the radiant emission signal. If particles do persist in the central region, then they will serve only to bias the calculated size distribution at the corresponding location in the measurement field. The technique is no longer non-invasive and the subject of interest, the nature of the soot population, is perturbed by the attempt to measure it.

3.3.3.3 Camera and acquisition optics

3.3.3.3.1 Camera/Intensifier

The Specialised Imaging SIM16 camera consists of sixteen intensified charge coupled device (CCD) sensors arranged such that notionally all have the same optical signal incident upon them. Each CCD sensor has 1280 by 960 pixel resolution and resolves incident light to a 12 bit luminescence depth (4096 discrete values). The intensifiers' gain values can be individually set for each image capture. A control system that automates their operation such that a series of shots or images are recorded, each with specified exposure duration, delay duration, and intensifier gain value, enables acquisition of sequences of consecutive images spanning potentially a very short period of time (sixteen sequential images of 5 ns exposure duration with no inter-frame delay equates to 80 ns).

3.3.3.3.2 Lens

A Tamron SP 90mm lens was selected primarily due to featuring a wide aperture ($F=2.5$) to maximize the solid angle of radiation passing into the camera inner optics, intensifier and camera CCD sensor assemblies.

3.3.3.3.3 Image doubler

The image doubler is an optical apparatus that splits the optical path between a camera and subject to be imaged, into two steerable paths, imaged side by side upon the camera objective lens. Care must be taken when adjusting the acquisition axes to ensure minimal rotation and shear type spatial distortion are introduced into the acquisition pathway. Figure 34 illustrates the working principle of the image doubler assembly and in particular the scheme of the elliptical profile, steerable, plane mirrors mounted upon adjustable platforms.

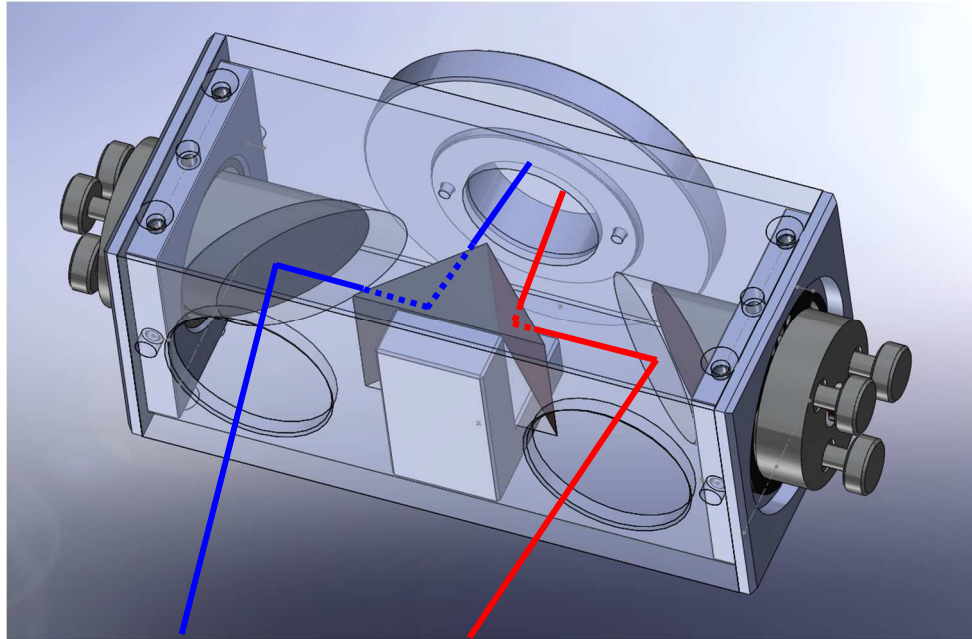


Figure 34 Image doubler scheme with overlay depicting optical axes.

3.3.3.3.4 Spectral Filters

For this study, two filters, both with 10 ± 2 nm full width at half maximum (FWHM) were selected, centred at 488 nm with a peak transmissivity of 85% (Edmund Optics part #65-147) and 647 nm with a transmissivity of 70% (Thorlabs part FL647.1-10). Both fall within the spectral interval of the camera that is 90% or greater (Figure 36) of maximum sensitivity and avoid significant perturbing radical emissions, as detailed herein.

For this technique the radiant spectral emission must be captured at two separated spectral intervals such that their ratio perceptibly changes with change of temperature of the radiating black (or grey) body, allowing calculation of the temperature of the body through application of the two colour pyrometry calculation.

The sensitivity of the two colour pyrometry technique to temperature change of the emitting object is dependent upon the two radiant emission signals differing in their rate of change with temperature. The ratio of the intensity of the two radiant emission signals can be related to the temperature of the body from which they were emitted. If a single acquisition interval were used, then an absolute intensity calibration would be required to relate intensity of signal to temperature. Prior additional knowledge of the subject would also be necessary; particle size distribution and overall concentration

from which the emission radiated would allow the specific radiation to be calculated and related to temperature.

Inspection of Figure 35 illustrates the effect of filter pair selection on the signal ratio. The two filter pair ratio curves demonstrate a significant difference in gradient, although both are monotonic, the steeper the gradient, the greater the certainty of the calculated temperature value for a given uncertainty of signal magnitudes.

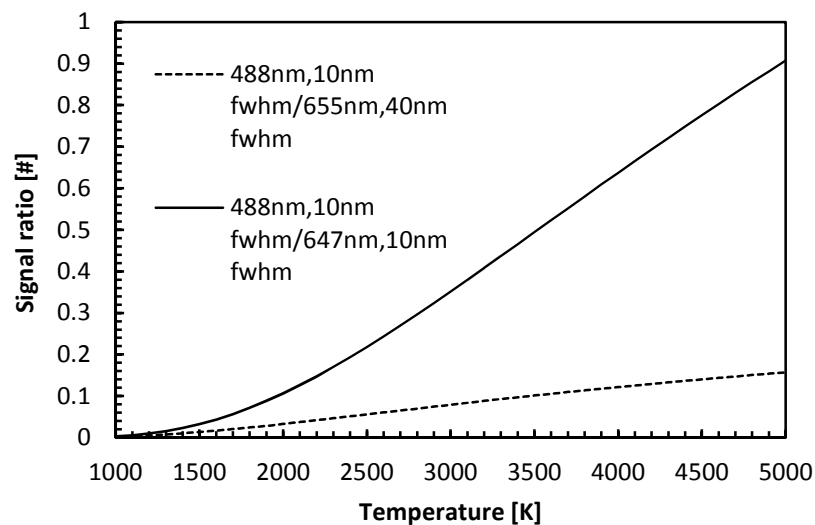


Figure 35 Variation of signal ratio with temperature of radiating body. Note, shallow gradient of blue (488 nm/655 nm) filter is due to broad collection interval (40nm FWHM) of divisor value of ratio.

Since a punctual measurement utilizing photomultipliers was to be made simultaneously for experimental scheme validation purposes, the additional constraint of selecting a filter pair that also fell within the acceptably sensitive spectral interval for the utilized photomultipliers was also necessary (Figure 37). The selection of a pair of wavelength intervals that yields a high ratio of signal, suggests a wide spectral separation between the two band-pass intervals. However, it was necessary to select filter specifications within the spectral interval in which both camera and photomultipliers demonstrated acceptable sensitivity. The desire to maximize sensitivity of the apparatus whilst maximizing variation of signal ratio with temperature change, represents a compromise of conflicting requirements.

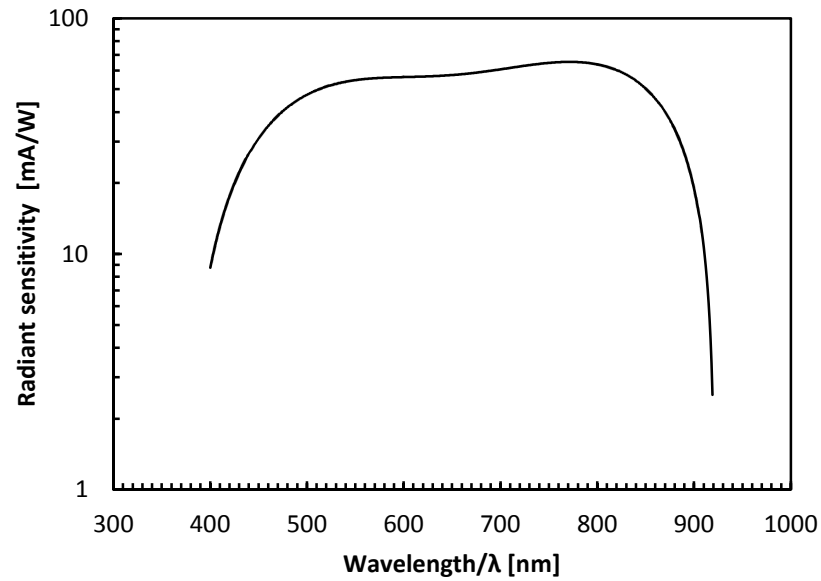


Figure 36 Characteristic spectral sensitivity of Specialised Imaging SIM 16 camera.

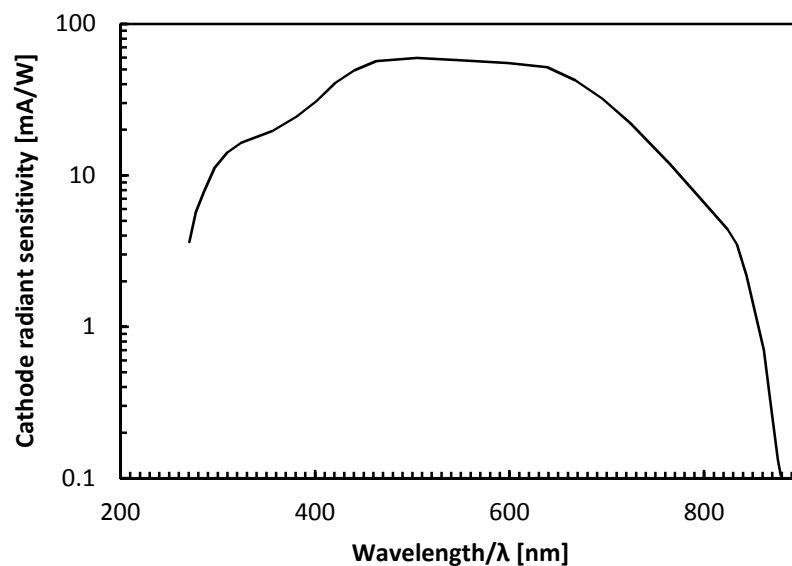


Figure 37 Spectral sensitivity of Hamamatsu H6780-02 type photomultiplier.

Another aspect to consider is the spectral variation of emissivity of soot. For the formulation used in this work, the emissivity of soot is related to the empirically derived, spectrally variant constant $\alpha(\lambda)$ by:

$$\varepsilon_{\lambda} = 1 - e^{\left(\frac{-KL}{\lambda^{\alpha(\lambda)}}\right)} \quad \text{Equation 62}$$

Whilst no widespread agreement upon the most correct value to use exists, several experimentalists have reported success from working with both wavelength intervals within the visible wavelength range (Matsui *et al.* 1980, Yan *et al.* 1988) and adopting a value of $\alpha=1.38$ to 1.39.

Radical, or more specifically termed ‘free radical’ molecules, are produced during combustion. Radical spectral emissions occur due to their inherent instability, afforded by their unpaired electrons. Since the nature of combustion can vary significantly, definitive quantitative data as to the emission intensities for the various molecular radicals is not readily available. However, qualitative intensity scale data has been published and is presented below in Figure 38 for radical emission and Figure 39 for water molecule emission.

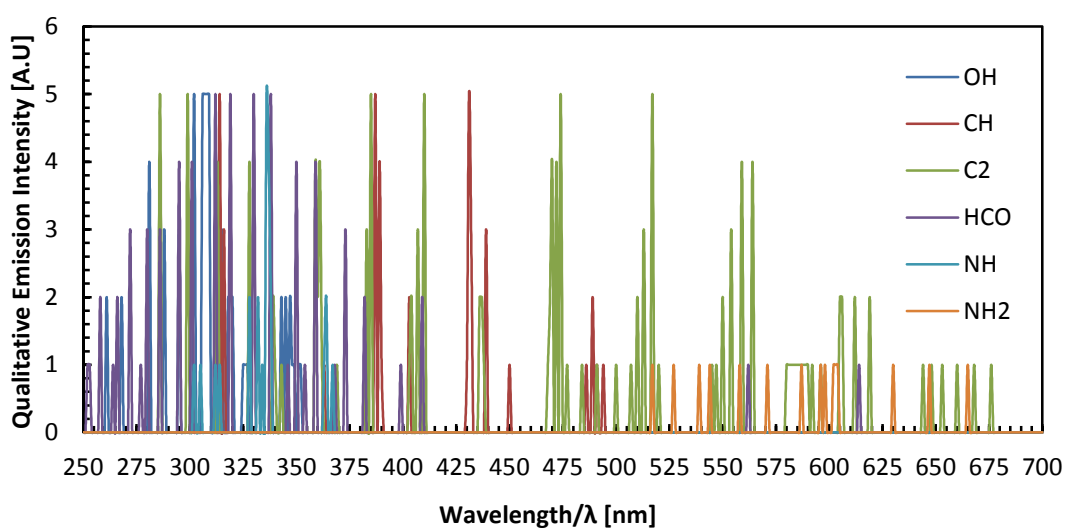


Figure 38 Qualitative radical emission intensity in the ultraviolet and visible spectrum. Adapted from data presented in (Gaydon 1957).

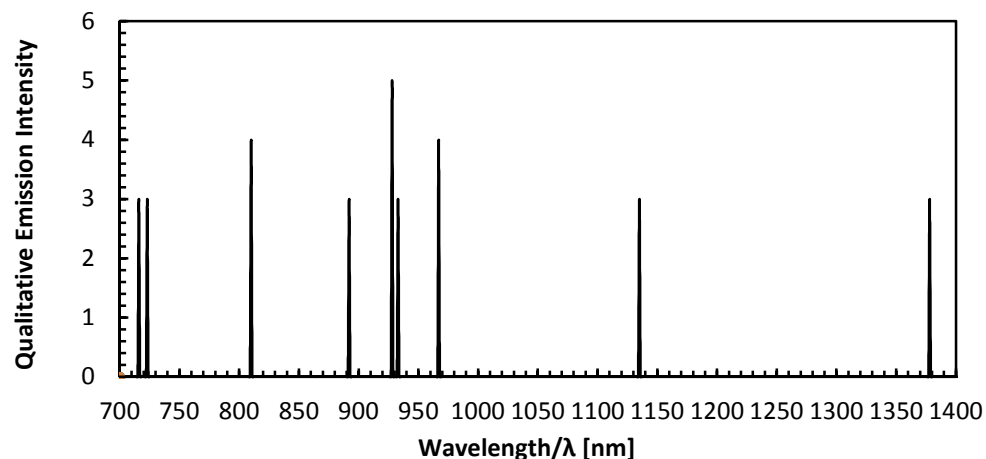


Figure 39 Qualitative fluorescent water molecule emission in the upper visible and infra-red spectrum. Adapted from data in (Gaydon 1957).

Figure 40 depicts the spectrally resolved emission bands, referred to as ‘Swan bands’. These emissions are particularly intense in the 500-520 nm interval; acquisition wavelengths that are not coincident must be selected in order to avoid significant erroneous signal acquisition.

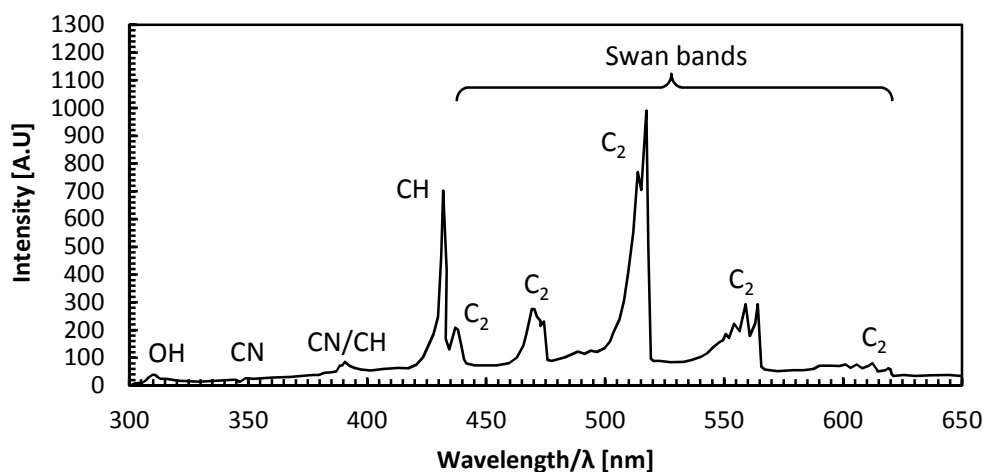


Figure 40 Spectral emissions encompassing ‘Swan bands’ due to C_2 , CH, CN, and OH excitation.

3.3.3.3.5 Photomultipliers and associated optics

A punctual measurement at a known location within the soot structure was simultaneously performed through a second branch of optical acquisition. Two Hamamatsu H6780-20 VCD photomultipliers were housed in an assembly within which a common 1mm diameter pinhole optical path was split in equal proportion via a prism and incident upon the photomultipliers. A pair of spectral filters matching those fitted to the SIM16 camera was inserted prior to each photomultiplier, thus allowing direct comparison between the two instruments. The photomultipliers produce a continuous signal and have a rise time of 0.78 ns; the signals captured are for the purposes of this study, a faithful depiction of the temporal decay of the LII emission radiated from the measurement volume.

Hamamatsu manufactured power supplies were used. Variation of response with control voltage was investigated prior to fixing upon a conservative value of 0.600 volts. The magnitude of the signal was observed to increase in scale with increasing control voltage, but temporal response was not noticeably decreased. Since sufficient sensitivity to the radiated signal was obtained with a modest control voltage value, this was used throughout. A benefit of a low sensitivity configuration is that the signal floor remains at a negligible level despite the incident flame luminescence.

3.3.3.4 Control apparatus

3.3.3.4.1 Personal computer

The camera unit is configurable and operable by a software interface upon a personal computer. The software allows configuration of each individual camera exposure and intensifier gain value. Also, the configuration to accept external triggering or a combination of internal and external trigger criteria may be set such that the camera may be synchronized to the occurrence of other events within the experimental scheme.

3.3.3.4.2 Digital storage oscilloscope

A Wavesurfer 422 from LeCroy™, was used for setup diagnostics, particularly addressing the synchronisation of equipment actuation. The experimental purpose of the oscilloscope was to capture and store the signals produced by the in line energy monitor,

the photodiode, and the photomultiplier pair. The oscilloscope had a maximum sample rate of 2×10^9 samples per second, which allowed sub nanosecond resolution and faithful capture of the rapidly changing output signals from the photomultipliers and photodiode.

3.3.3.4.3 Programmable arbitrary waveform generator

A programmable arbitrary waveform generator was used to generate two simultaneous pulse trains to enable external control of the laser. This was necessary to allow synchronization between the lasing of the soot and commencement of the acquisition process. The laser control system has facility for a synchronisation pulse to be transmitted with each q-switch event, however the camera required a minimum of 105 ns between receiving an external trigger and commencing the sequence of shutter events.

A continuous pulse train of 100 μ s duration pulses at a 100 ms interval was used to externally drive the laser flash lamps at the optimum rate of 10 Hz. A single 100 μ s pulse at 1 Hz repetition rate was used to drive the q-switch via the delay line circuit, described below.

3.3.3.4.4 Delay line circuit and line driver

A trigger delay generator was built using a sequence of four ‘hex invertors’ chained together such that the output signal was delayed relative to the input by 120 ns. A ‘line driver’ output stage was required since the load to which it was connected (the laser control unit) presented a 50 Ohms impedance. The laser unit utilizes a 50 Ohms impedance to facilitate impedance matching across the exclusively BNC (Bayonet Neill-Concelman) connection terminated wires.

3.3.3.4.5 Cables

Maintenance of signal integrity between apparatus was addressed by the use of 50 Ohm impedance BNC connector terminated co-axial cabling, used throughout the experiment control and acquisition systems for all two conductor wire type connections. Where possible, matching terminal impedance was specified. Matched impedance across a

network of conductors ensures that no significant degradation, typically temporal ‘smearing’, of the signal occurs through reflection at non-matching impedance interfaces. This is particularly important where square wave pulses are used for communicating logical states i.e., switch on or switch off and where the signal is being employed to synchronize the operation of different equipment.

3.3.3.5 Configuration

Figure 41 illustrates the experimental configuration in which the laser sheet propagation and conditioning prior to the flame is apparent. The camera acquisition axes, incident with the region of interest in the flame structure are indicated as passing through an optical aperture in the shroud.

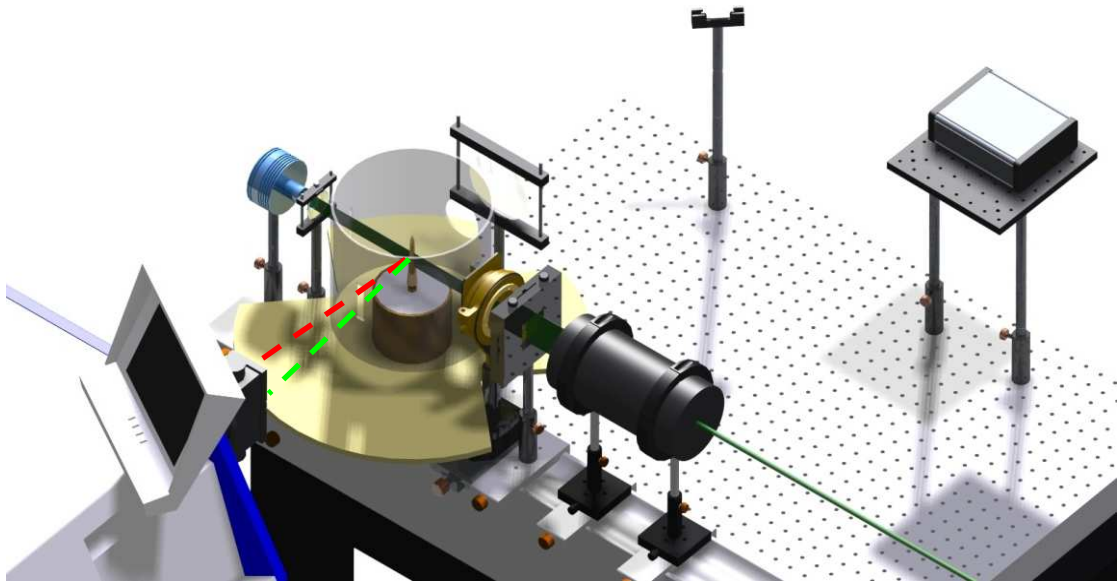


Figure 41 Experimental configuration with camera acquisition axes highlighted.

Figure 42 illustrates the punctual measurement acquisition path. A wide collection solid angle necessitated a large optical aperture in the shroud.

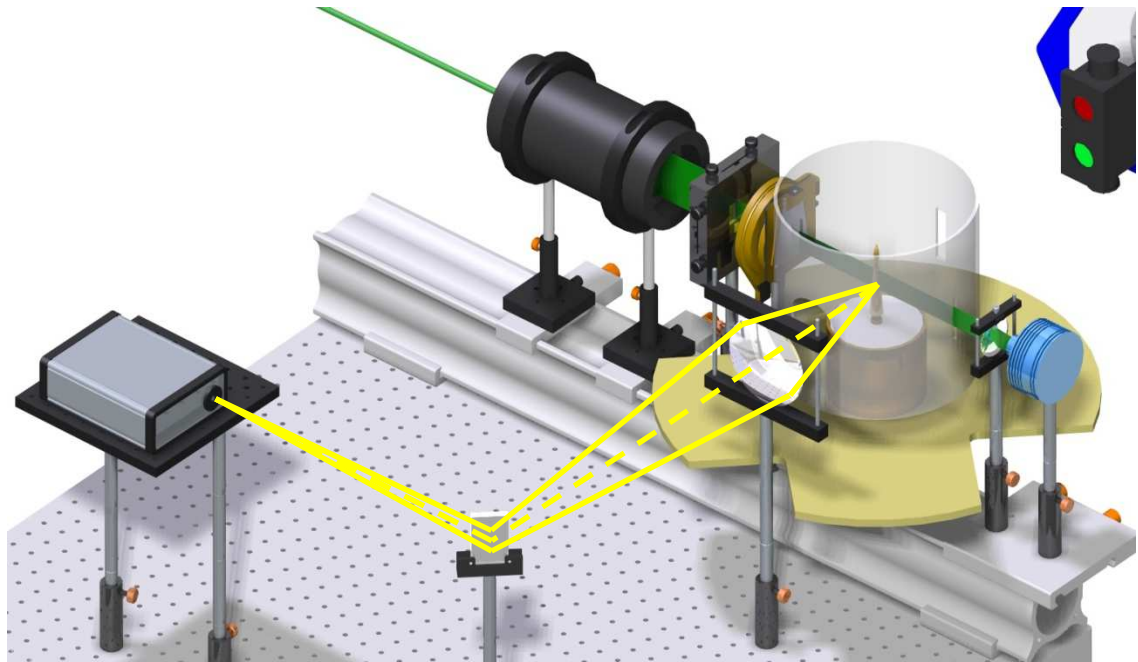


Figure 42 Experimental configuration with photomultiplier acquisition branch highlighted.

The laser beam was orientated horizontally to be incident with the central plane of the burner flame structure. Prior to reaching the burner it traversed the sheet forming optics unit. This produced a vertically orientated sheet like beam profile that continued on to traverse the central vertical plane of the flame structure. The sheet forming optics assembly incorporated adjustment of the proximity of the lenses such that the focus in the major and minor axes could be adjusted separately. The sheet width/minor axis was set to focus at approximately the point when passing through the flame structure, a focal length of 450 mm. The major axis/vertical focus was set to produce minimal divergence. The centre of the vertical span of the sheet was set to coincide with the 50 mm height above burner point. An adjustable width slit was employed after the sheet forming optics assembly to clip the sheet width to 0.50 mm. An adjustable knife edge unit was used to clip the major axis of the sheet such that its span and the affected soot region was entirely captured within the field of view of the camera acquisition and equated to between 42 mm to 59 mm height above burner tip.

The camera was situated horizontally normal to the laser sheet axis such that the acquisition axis was incident at approximately 50 mm height above burner. Upon completion of final alignment of the acquisition optics, the direct acquisition axis was 51 mm height above burner. The camera body lens aperture to laser sheet plane was

500 mm. The lens F-stop was set to its minimum value of 2.5. An image doubler unit was fitted to the camera lens such that two near parallel optical paths to the measurement plane were subtended. Adjustment within the image doubler assembly allowed the same location to be centred upon for both paths. The effect of this was to present two images to each of the camera sensors. Each path was fitted with a spectral band-pass filter in two spectral ranges as specified in section 3.3.3.3.4.

This experiment was performed twice due to the first configuration yielding data that whilst valid, portrayed an undesirable effect due to the slight difference in optical acquisition paths from the image doubler to the measurement plane (Figure 43). The axis-symmetric structure of the soot produced a signal trapping effect that attenuated the radiant emission differentially due to differing extinction path lengths and local soot extinction factor (Figure 44).

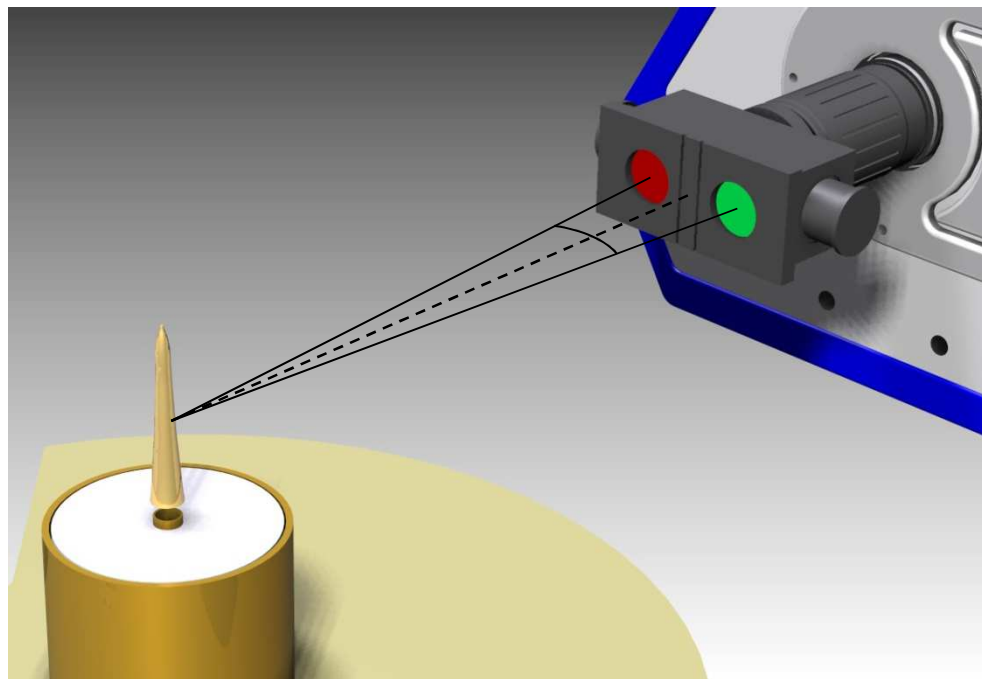


Figure 43 Illustration of incident angle between acquisition axes for first experimental configuration.

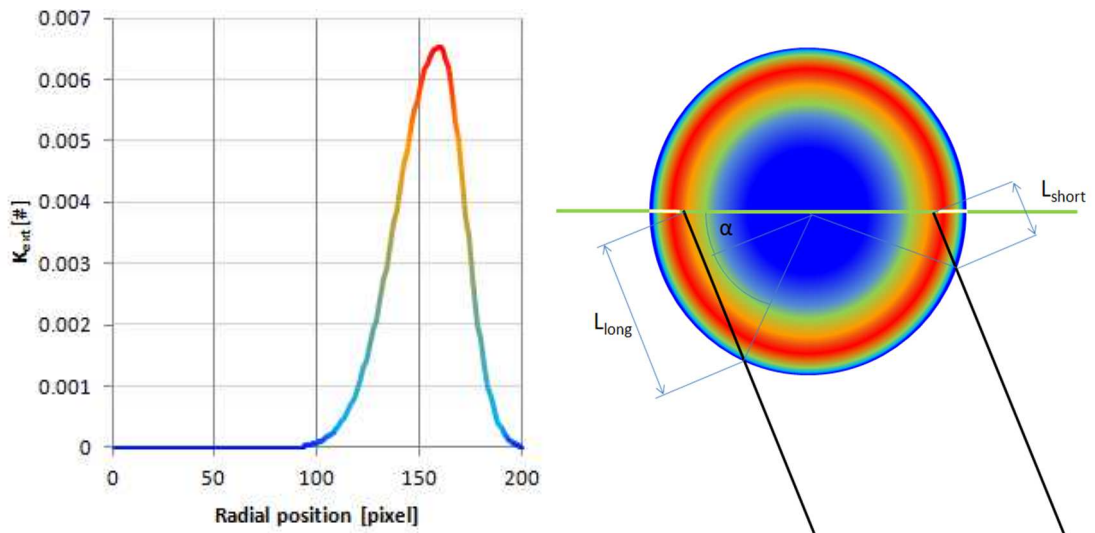


Figure 44 (left) Typical radial extinction profile for 50mm HAB. (right) plan extinction factor filled contour plot with difference of signal trapping path lengths for a single acquisition channel disposed at angle α . Note the variation of extinction factor K_{ext} along signal trapping paths.

The second undertaking of this experiment eradicated the effect by reorientation of the image doubler (Figure 45) such that whilst the optical axes remained non-parallel, their paths to the measurement plane traversed a near identical extinction path and corresponding signal attenuation. This was an acceptable solution due to the ratio of signals being the primary utilisation of the emission signals.

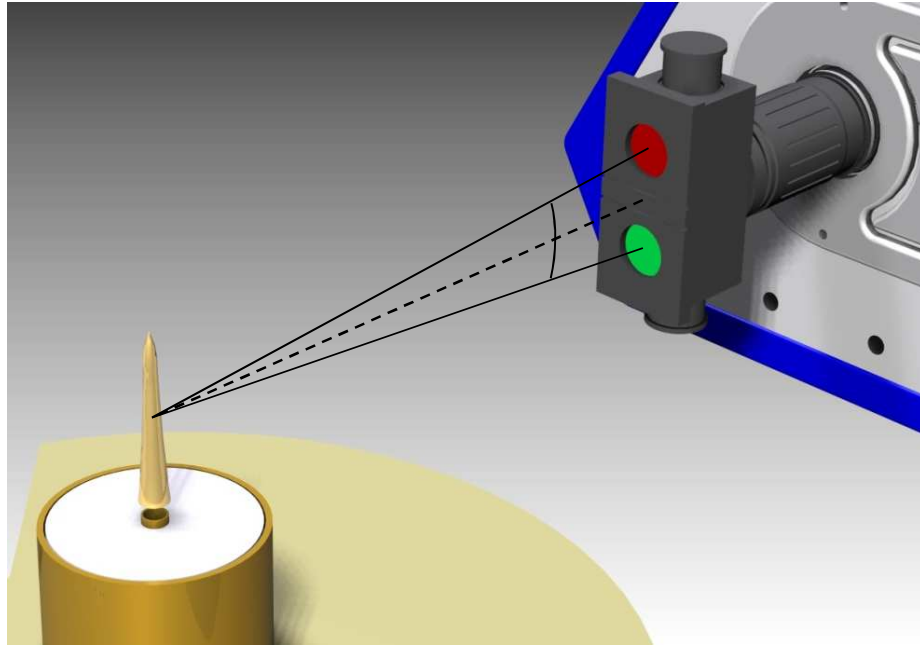


Figure 45 Second experimental scheme to eradicate differential signal trapping path effect.

A punctual measurement at a known location within the soot structure was simultaneously performed by the photomultipliers through a second branch of optical acquisition. This was performed to allow a point location comparison between the well-established photomultiplier utilizing TiRe-LII technique and the data captured via the camera at the same location for the 2D-2C-TiRe-LII technique. The second optical branch constituted an acquisition axis horizontal and normal to the laser sheet plane as with the camera acquisition axis, but on the opposite side of flame. Since the flame and associated soot structure is axis-symmetric, any occurrence of radiated emission attenuation was the same for both acquisition paths. A bi-convex lens of 90 mm diameter and focal length of 150 mm was situated 17 cm from the laser sheet plane. A path length (turned midway by a mirror of near constant spectral reflective performance) of 120 mm produced a focused and magnified image of the flame structure upon the pinhole of the photomultiplier housing. The magnification factor of 7.07 and the pinhole diameter of 1 mm yielded a sample diameter of 0.14 mm and was centred at 2.4 mm radius, 50 mm height above burner (a location on the inner face of the high sooting region).

3.3.4 Control/procedure

The control aspect of the experiment can be most conveniently divided into operation of the experiment and acquisition. The bridge between the two aspects is through the necessity to synchronize the laser event and subsequent soot incandescence emission with the triggering of the acquisition equipment.

3.3.4.1 Experiment

The operation of the Santoro burner operating point was set in terms of the target ethylene flow rate and the air co-flow rate, defined previously. The experimental procedure adopted was to light the burner and allow a period of time to pass such that the flame visibly stabilized. A fluctuation in flame height was apparent as the ethylene flow rate control system initially oscillated above and below the set-point, before stabilizing. Since the air-flow control system was not automatic in its regulation of the flow rate, it was necessary to check and adjust it prior to each data acquisition process.

The laser system was triggered by an externally produced trigger pulse. A programmable waveform generator was used as a master clock; providing synchronisation between the triggering of the laser's Q-switch and the initiation of the camera acquisition sequence. The pulse used to trigger the laser was sent via a delay line circuit to allow advanced actuation of the camera. The process of setting the laser fluence was performed at several points during the collection of multiple datasets to monitor any significant drift in laser fluence. This was achieved by situating a laser power meter after the burner but incident with the laser sheet. A planar-convex lens produced convergence of the laser sheet to a form that was entirely encompassed by the detection area of the power meter head. Characterization of the relationship between the in-line energy monitor measurement and that of laser power meter was performed without the flame. This allowed monitoring of both laser fluence and provided a qualitative measure of the consistency of the laser fluence extinction due to the laser sheet's traversal of the sooting flame. Data sets for which atypically high or low extinction occurred (attributable to flame movement) were noted for exclusion from subsequently processed ensemble average data. Data sets produced utilizing unusually high or low laser fluence were also disregarded. Figure 46 illustrates the variation of laser fluence measured by the in-line energy monitor. The target

range of 150 to 180 $\text{mJ}\cdot\text{cm}^{-2}$ was satisfactorily adhered to despite the apparent drift towards the upper limit value.

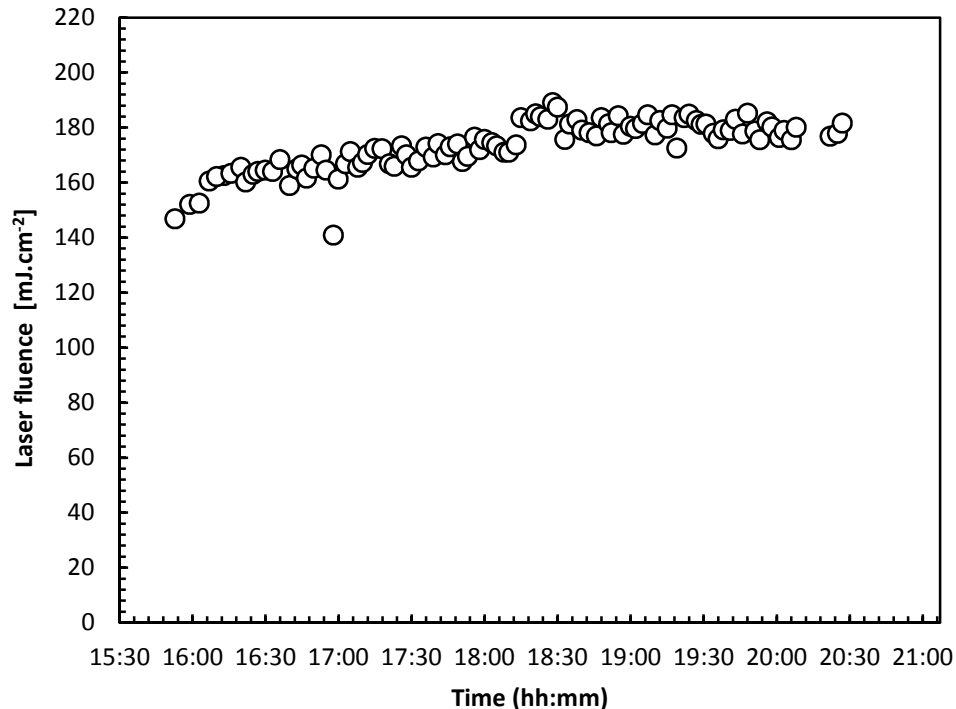


Figure 46 Shot to shot laser fluence variation recorded using a calibrated in-line energy monitor.

3.3.4.2 Acquisition

The experiment was performed with two different camera acquisition strategies. The first, featured all camera images being of equal exposure duration of 20 ns with no inter-frame delay. This scheme (Figure 47) allowed fine resolution of the rapid decay of the LII signal, but the limited number of frames prevented the capture of the full decay. The second acquisition strategy addressed this limitation by using an increasing frame exposure duration sequence (Figure 48). The first four images were of 20 ns duration, images five to eight of 40 ns, images nine to twelve of 80 ns, and images thirteen to sixteen of 160 ns. This strategy allowed the initial frames to capture the rapidly changing initial phase of the LII signal with sufficiently fine temporal resolution. As the signal decayed to a lower intensity, the frame exposure durations were increased to compensate the significant drop

in signal-to-noise ratio that would otherwise occur. The entire decay of the incandescence emission signal was suitably encompassed by the variable exposure strategy. Combining and comparing data from both acquisition schemes may represent an enhancement of the overall measurements in terms of overall span and fineness of temporal resolution.

The photomultiplier acquisition branch was triggered by the configurable output pulse of the camera. The photodiode pulse could also have been used to locate the laser pulse event and trigger the oscilloscope waveform capture; however the initial setup used a configurable output pulse from the camera. The initial idea was that this configuration allowed an advanced trigger signal to be used. Advancement of the trigger was not necessary, the photomultiplier waveforms as well as the in-line energy monitor and photodiode signals were all captured and automatically stored by the oscilloscope. The trigger linked to the camera was retained because the system worked, but also a common timing reference was maintained across all elements of the experiment.

The acquisition of the camera was set to capture the peak incandescence signal in the third image. The rationale for this was that in order to not miss the start of the signal, the first image should appear completely blank. The exposure duration for the first four images for both acquisition configurations was 20 ns, so the rise period (~5 ns) and the initial sublimation dominated radiance curve, fitted within a single image exposure duration. In order to locate the precise start of the incandescence signal, a processing routine that compared the contribution in adjacent images was developed.

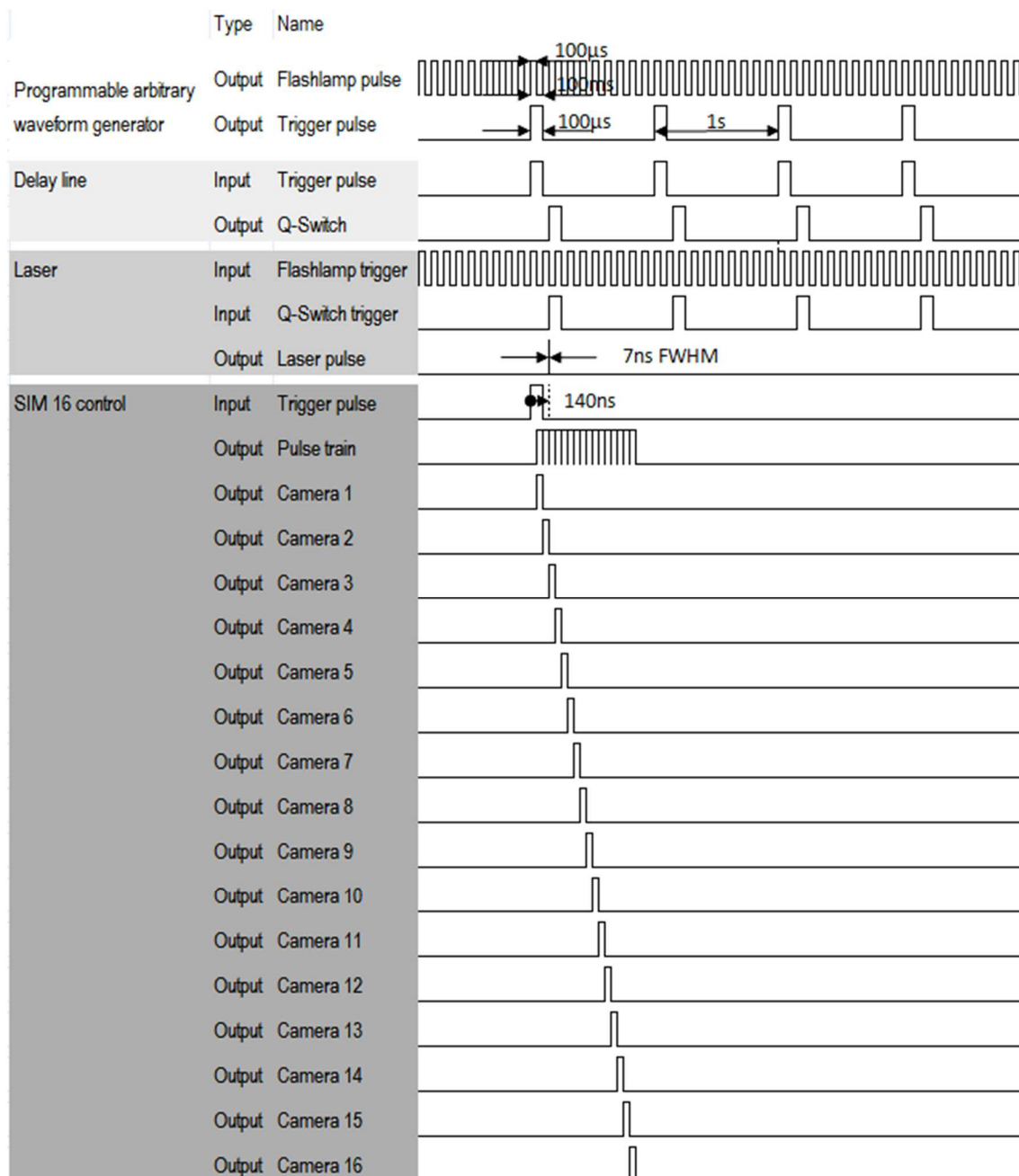


Figure 47 Timing of fixed exposure duration experiment.

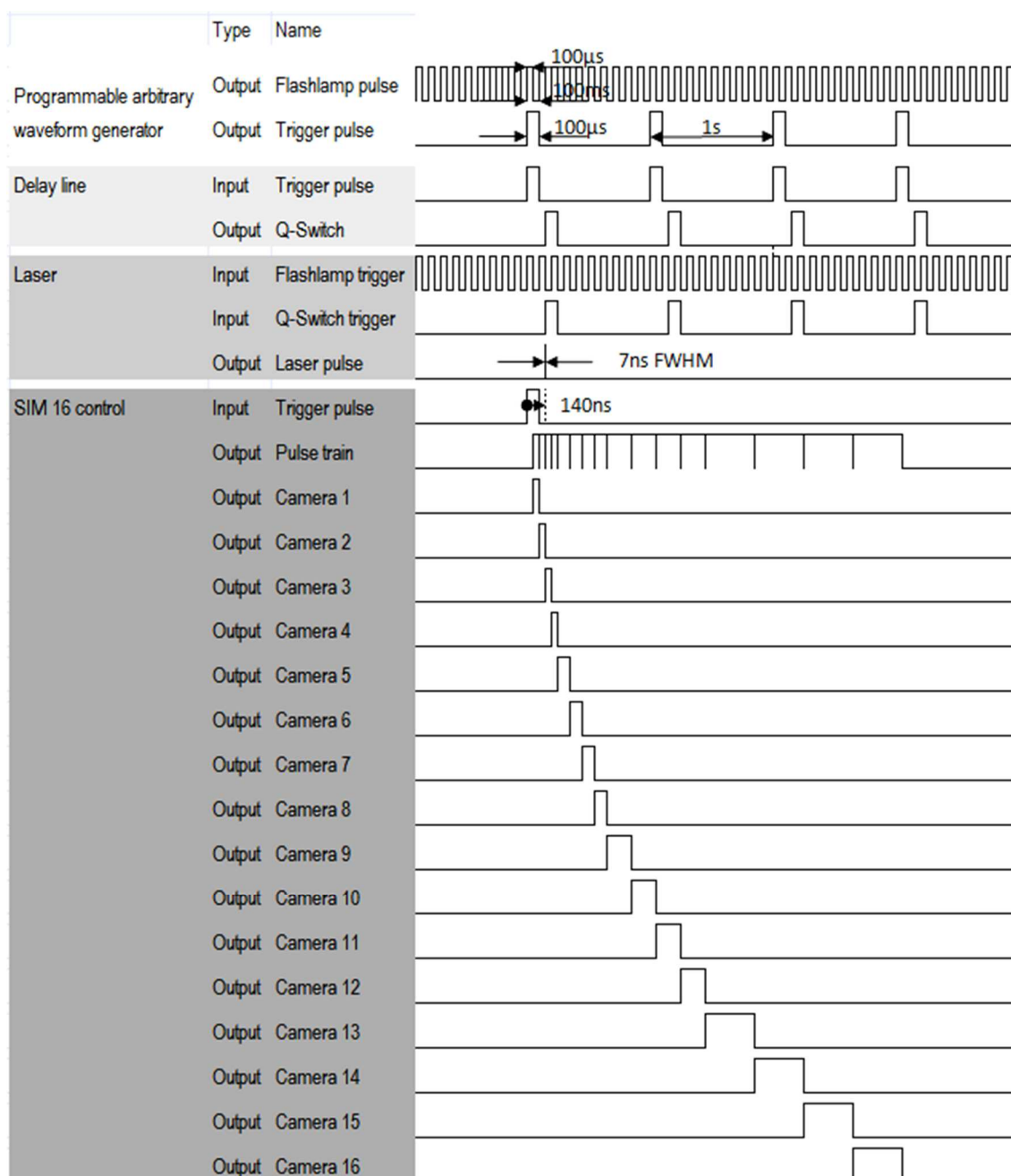


Figure 48 Timing of ramped exposure duration experiment.

3.3.5 Sub-frame laser pulse timing

Since the exposure duration (or gating) of the exposures of the acquisition sequence were short (20 ns) compared to that of the laser pulse (7 ns FWHM), the precise timing of the acquisition sequence relative to the LII signal decay affected the distribution of the radiant emission into the sequence of images (Figure 49).

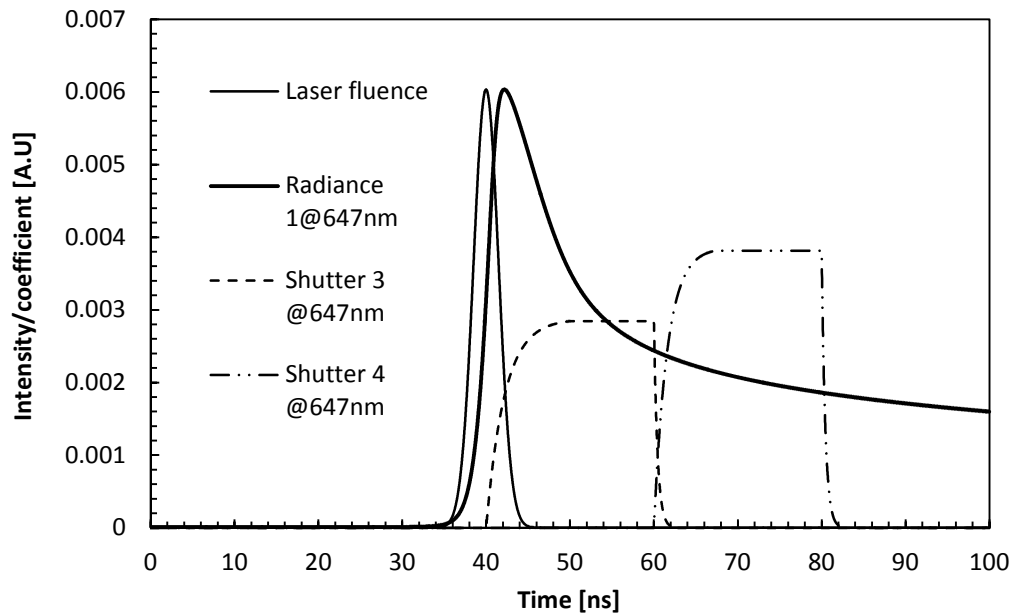


Figure 49 Example timing of laser excitation, radiant emission and shutter opening curves.

An analysis was conducted in which the sensitivity to variation of the timing of the acquisition shutter model exposures sequence relative to that of the laser pulse and corresponding radiant emission. Figure 50 shows the variation of ratio for the first two frames in which radiant emission was captured (frames 3 and 4) versus the timing offset of the laser event. This allowed the experimental sub-frame timing to be established by matching the emission ratio to that of the model. The modelled radiant emission signal is dependent upon the primary particle diameter. However, the peak emission point, occurring shortly after the peak of fluence of the laser pulse excitation, provides an initial radiation temporal profile that is broadly independent of primary particle size. As synchronisation delay is increased past 20 ns, the first acquisition image (frame 3) is convolved with a progressively smaller signal contribution from the radiant emission curve, such that a plateau of frame 3 to frame 4 signal ratio occurs before sharply dropping off with increase of synchronisation delay.

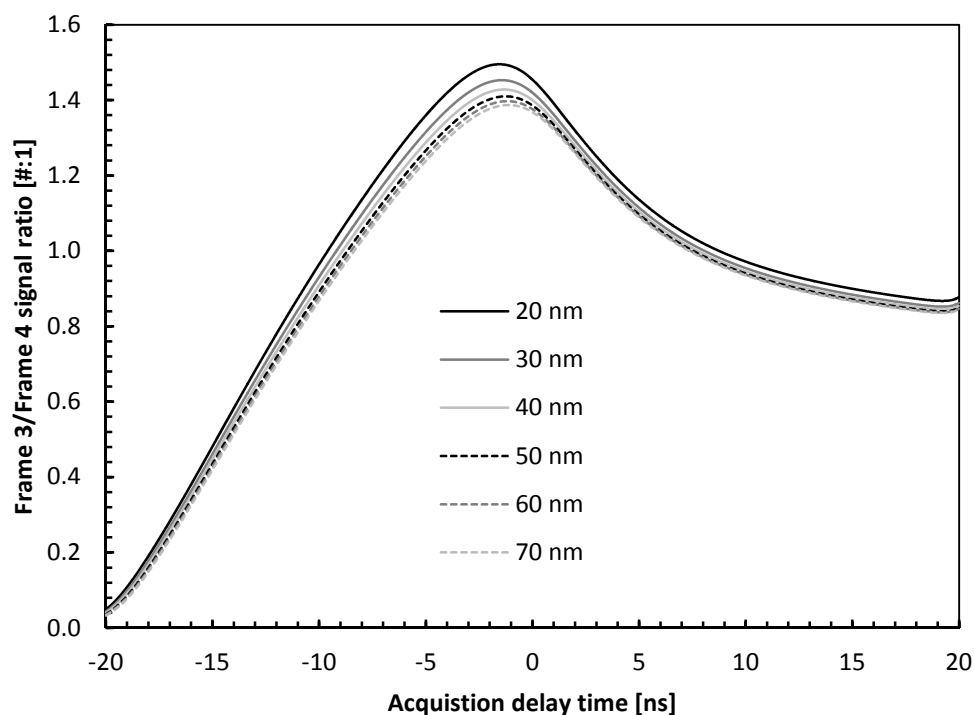


Figure 50 Ratio of intensity of frame 3 to frame 4 versus synchronisation delay time for 488 nm acquisition filtered interval, for a range of primary particle diameters.

As shown in Figure 50, the variation of the ratio of signal captured by frame 3 divided by that captured by frame 4 demonstrate peaks that are very nearly temporally invariant for a range of modelled primary particle diameters. Adjustment of the experimental timing such that a peak of ratio was realized, allowed the sub-frame laser to acquisition synchronisation to be ascertained and accordingly matched in the subsequent numerical modelling of signal acquisition.

3.4 High pressure planar and time resolved laser induced incandescence upon a rapid compression machine

3.4.1 Introduction

The previously designed and validated planar and time resolved LII technique was applied to an optically accessible reciprocating Rapid Compression Machine (RCM) as described in Section 3.4.3.1. Adaptation of the experimental configuration was necessary due to the physical constraints of the optical accesses, the conditions in which combustion was occurring and the corresponding effect upon the radiated emission signal. In addition to the application of the LII experimental scheme to the RCM, a laser extinction experiment was simultaneously performed as a means of allowing the calculation of spatially resolved, localized laser fluence; necessary for calculation of particle size.

3.4.2 Concept and experimental aims

A near planar region of soot particles within the diesel spray laminar diffusion flame structure was heated rapidly by an incidental sheet formed laser pulse, causing the particles to incandesce. The optical accesses of the Proteus rapid compression machine allowed acquisition of the radiated laser induced incandescence emission to be captured normal to the laser sheet such that a planar region of soot was measured.

The ensemble averaging of widely varying spatially resolved data will not provide the precise soot properties at a specific location for a specific combustion event as may be achieved through individual cycle analysis. For this experiment, the aim was to demonstrate the viability of the technique being applied to realistic engine condition combustion events, but also to capture data of sufficient quality to allow both an individual cycle and ensemble average data analysis to be undertaken. Previously, ensemble averaged relative soot concentration data was presented (Miles *et al.* 2007); similarly processed data from this study could be compared to ascertain similarity of the soot location and structure.

3.4.3 Equipment

Much of the experimental apparatus and scheme used in this experiment were the same as that used for the validation experiment, described in detail in section 3.3.3. Only information as to changes of configuration or components will be detailed herein.

3.4.3.1 Proteus reciprocation rapid compression machine

The Ricardo Proteus RCM (Miles *et al.* 2007) features an unusually large displacement for a research single cylinder engine. A bore of 135mm and stroke of 150mm equate to a swept volume of 2.2 litres. The operating speed is 500 crankshaft revolutions per minute; the large reciprocating mass (~13 kg for the piston and wrist pin) and absence of balancer shafts in the design necessitating the lower than typical diesel engine speed limit. The modification from single cylinder engine to optically accessible rapid compression machine was through the fitment of the optical access chamber where the cylinder head top plate formerly attached. A piston with conical crown section matches the geometry of the cylinder head presented to the chambers main extent (Figure 51). A cylindrical region 50 mm in diameter and 80 mm extent is vertically orientated with four access ports than can be fitted with optical access windows, blanking plates, injector mounting assemblies or in cylinder pressure transducer mounts. The top plate of the optical chamber has provision for the fitment of a fuel injector with an angle of inclination such that the spray from a single hole, research specific injector may be vertically orientated in the centre of the optical chamber.

The design of the optical chamber shape and orientation, the position of the cylinder wall ports and the piston crown and head geometry were all optimized towards the goal of producing a quiescent region into which the liquid fuel is injected. The purpose therefore of the optical Proteus RCM is not to replicate exactly the conditions found in a typical diesel engine (particularly regarding turbulence introduced through piston squish band to cylinder head proximity), but to allow a fundamental study of fuel sprays and the combustion that results.

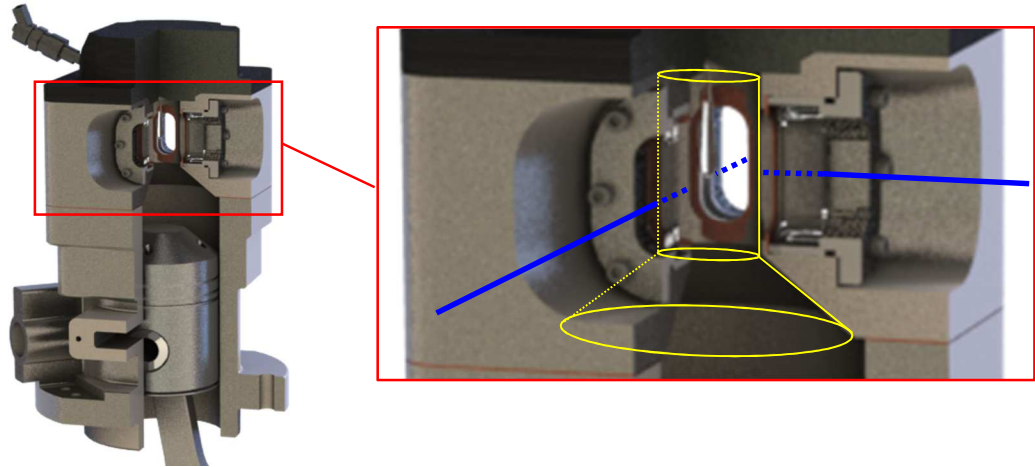


Figure 51 Proteus reciprocating rapid compression machine scheme with sectioned bore and optical chamber detail. Note, optical chamber and accesses depicted by yellow and blue overlay.

A Bosch CR2 injector with single 0.2 mm diameter valve-closed-orifice (VCO) nozzle was used with the spray axis orientated to be incident with the vertical symmetric axis of the optical chamber as depicted in Figure 52.

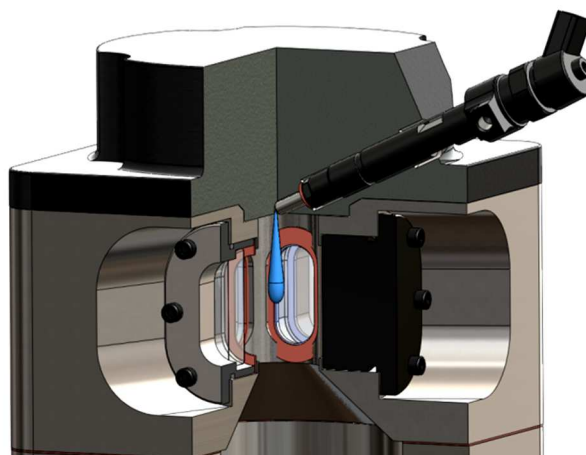


Figure 52 Sectioned view of optical chamber. Approximate fuel spray structure indicated in blue.

3.4.3.2 Laser and associated optics

The components and elements of the laser excitation branch of this experiment were identical to those of the validation experiment; only aspects that differ are detailed in this section.

3.4.3.2.1 Laser

For this experiment the acceptable operating range of laser pulse repetition rate between 9.4 and 10.6 Hz was utilized due to the pulses being externally triggered and timed to occur at a particular point in the Proteus's combustion event. The slight fluctuation of engine speed that is the typical behaviour of any mechanical inertial system being modulated by a feedback loop control meant the actual repetition rate continuously varied within a small frequency band, satisfactorily encompassed by the laser units operating range.

3.4.3.2.2 Sheet forming optics

The (minor axis) width of the sheet was focused upon a vertical, normal target plate incident with the symmetric axis of the optical chamber. The height of the sheet was adjusted to be very nearly non-divergent and positioned to allow as much of the soot plume to be excited as constrained by the chamber optical access.

3.4.3.2.3 Adjustable width slit

The adjustable width slit was situated immediately after the sheet forming optics assembly. For the compact installation as shown in Figure 53, a base that enabled rotation about a vertical axis whilst minimally altering the lateral displacement of the slit was used. A slight angle of the adjustable width slit assembly helped to avoid alignment of back reflections propagating back to the laser head.

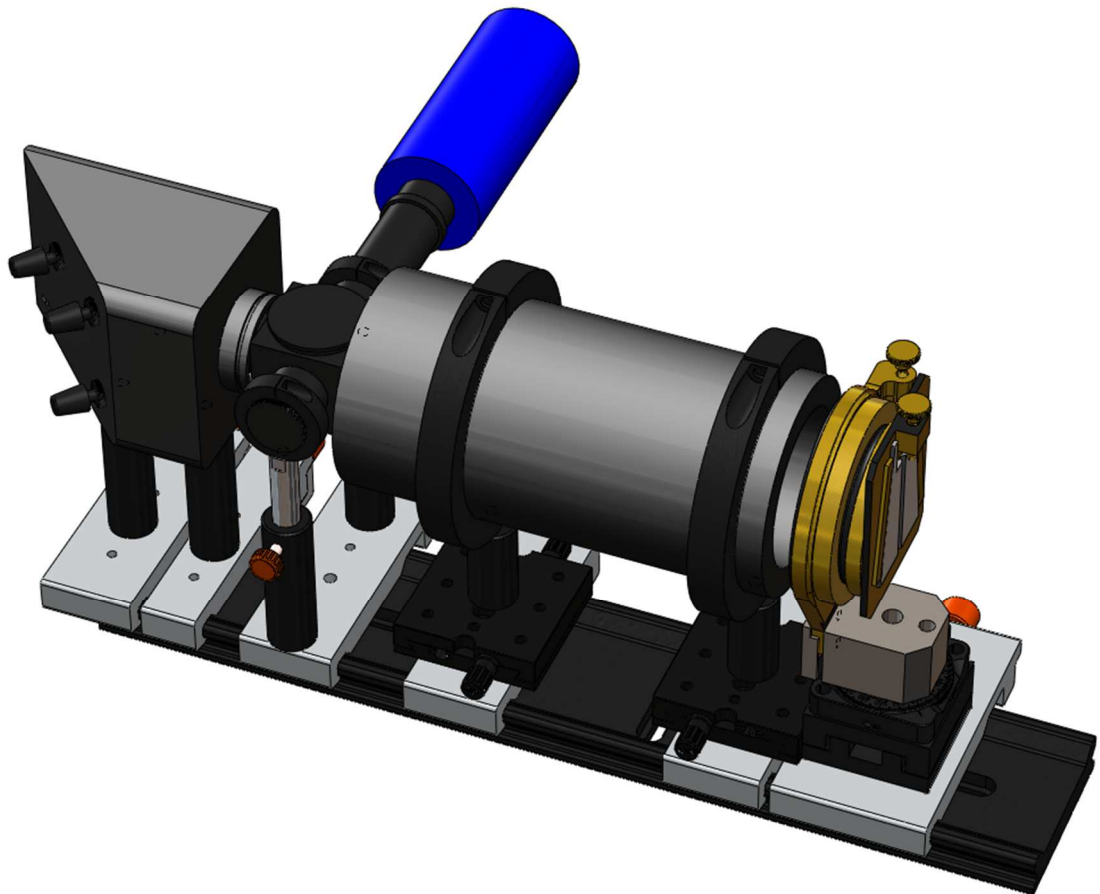


Figure 53 Laser optics and components. (left to right) Beam steering mirror housing, in line energy monitor, sheet forming optics assembly, adjustable width slit.

3.4.3.3 Camera and acquisition optics

3.4.3.3.1 Camera and intensifier

The Specialised Imaging SIM-16 camera was used for this experiment. Due to concern that the low frequency, large amplitude vibration caused by the operation of the Proteus would move the camera, it was mounted upon an optical table using purpose-built low density polyethylene clamping rails. The table bed was partially isolated from vibration through the employment of high acoustic loss material pads fitted between table bed and leg structure.

A second aspect also addressed by the more remote position of the camera was to minimize the incident angle between the two optical acquisition axes emanating from the image doubler. Since the irregular and certainly non axis-symmetric soot structures

anticipated within the optical chamber would present different signal extinction for different optical axes, it was desirable to minimize the difference between the two paths. The scale factor for the high pressure experiment LII images was measured as 15.7 pixels/mm.

3.4.3.3.2 Lens

A Vivitar 70-210 mm macro focussing zoom lens was used for this experiment. It features a reasonably wide aperture (minimum $f/4.5$) to maximize the collected solid angle of light, but also a variable magnification. This was necessary due to situating the camera at a distance of 350 mm from the laser propagation axis and the desire to fill as much of the field of view with the optical access (dimension of 55 mm by 25 mm). The image doubler described in section 3.3.3.3.3 was fitted on the lens to allow recording of the incandescence signals at two different wavelengths. It was orientated horizontally; both optical acquisition axes were horizontal. The incident angle between acquisition axes was reduced relative to the validation experiment due to the increased distance between camera and optics and the measurement plane.

3.4.3.3.3 Spectral filters

Filter selection for the high pressure experiment was a compromise between addressing several aspects intrinsic to the high pressure conditions. The increased rate of heat transfer by conduction between soot particles and surrounding molecules relative to ambient conditions, causes a far more rapid decay of particle temperature and corresponding incandescence signal. Shorter duration exposures were necessary to portray the temporal evolution of the signal. The camera was capable of operating with exposures of just 5 ns duration thus allowing the capture of the rapid signal decay (<80 ns). However, this represented a short period of time to accumulate signal. The experience of the validation experiment had demonstrated the magnitude of the filtered signals as being quite low (~ 200 - 300 counts peak pixel value equating to a signal to noise ratio of just 16 to 20 decibels) for 20 ns duration exposures. Since shorter exposure durations were necessary, the compromise of using wider interference filters for both wavelengths was made. For both filters, a specification of the highest available transmissivity value was sought. In

Figure 54, the signal intensities resulting from irradiance of a black-body at 4000 K for a selection of filters is shown. A significant increase of signal intensity by employing broader interference filters is illustrated. The two filter wavelengths still had to be within the 450 to 800 nm wavelength band to utilize the camera's peak sensitivity range and so that the assumption of a spectrally invariant emissivity factor could be employed in pyrometry temperature calculations.

The next consideration was that of the interfering emissions from free radicals, and fluorescence from molecules and polycyclic aromatic hydrocarbons. An interval between 560 and 610 nm was considered to be minimally populated by radical emissions (Gaydon 1957). Therefore, a filter of 592 nm wavelength, 43 ± 2 nm FWHM value with a transmissivity of 93% was selected (Edmund Optics NT67-034).

The second filter wavelength was chosen to be of 750 ± 8 nm wavelength, 40 ± 2 nm FWHM, with a transmissivity of 75% (Thorlabs FB750-40).

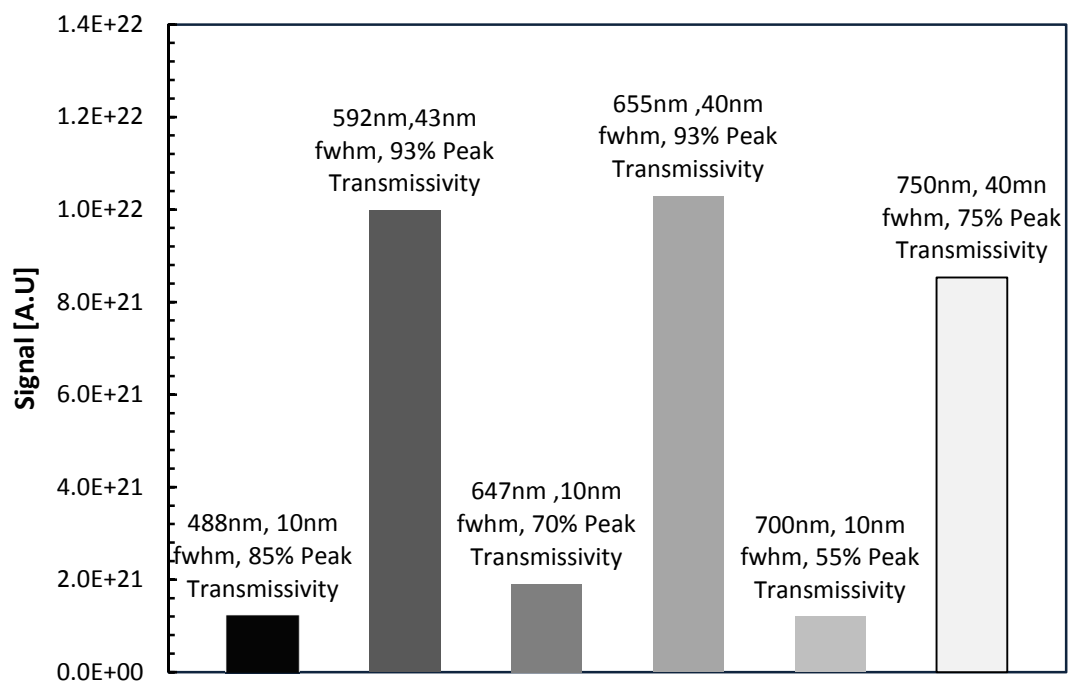


Figure 54 Signal magnitude for a range of filter specifications, for 4000 K black-body emission.

The signal ratio versus temperature curve (Figure 55) is monotonic and has a suitably high rate of change, minimizing uncertainty in subsequently calculated temperature values.

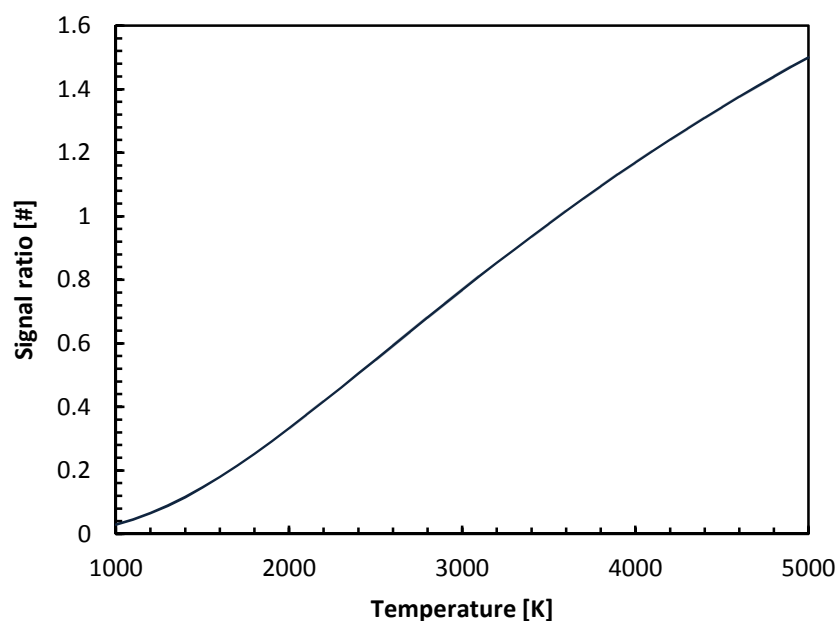


Figure 55 Signal ratio with temperature for 592nm/750nm filter pair.

3.4.3.4 Extinction apparatus

A beam splitting mirror (Melles Griot BS1-532-10-2037-45-UNP) was inserted between the output of the conditioned laser sheet and the RCM. The transmission to reflection ratio of 9:1 allowed an unextinguished laser sheet profile to be presented, via a series of laser mirrors (Qioptiq G340064000) to a cuvette. The high transmission characteristic was selected to ensure the laser sheet fluence was sufficiently high to induce incandescence whilst remaining suitably within the laser units working power range. The extinguished laser sheet, due to traversing the RCM combustion chamber soot plume, was incident with a second cuvette (Figure 56).

The matching cuvettes were filled with a solution of Ethanol and Rhodamine 590 of a concentration of $6.785 \times 10^{-5} \text{ mol.l}^{-1}$. The concentration was successively diluted until an acceptable balance between the propagation of the laser into the cuvette and the intensity of emission was observed.

The cuvettes were mounted into a housing that allowed both to sit adjacent and in-line with the laser sheet post RCM, and such that a single camera, normally disposed could capture both luminous emission profiles. The central region of the mount between the cuvettes features a ‘beam dump’ arrangement consisting of a low specularity surface finish applied to angled faces such that reflection back into the respective cuvettes, of incident laser sheets, was minimized.

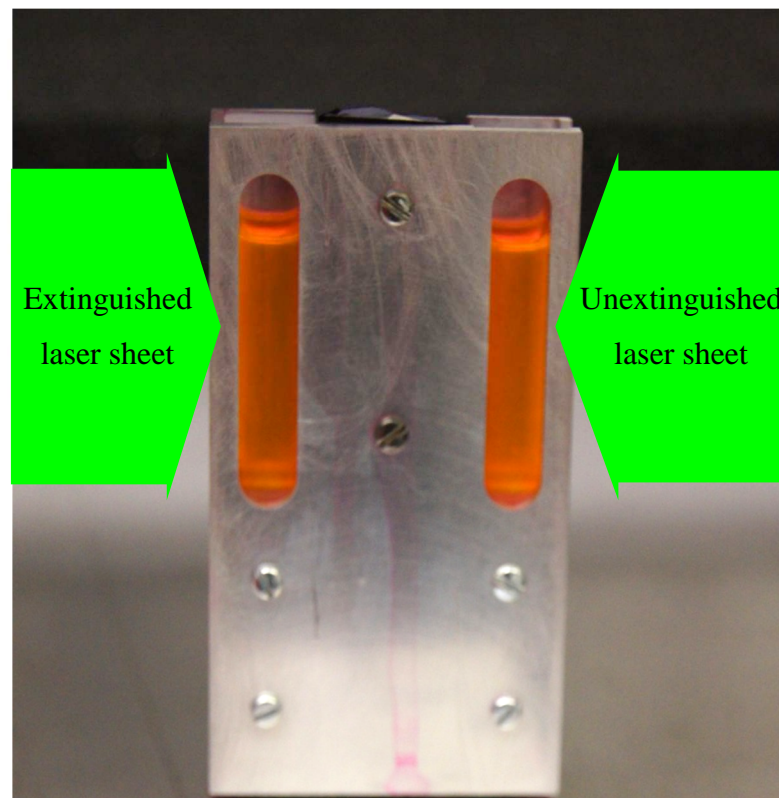


Figure 56 Cuvette assembly in which two cuvettes, filled with a solution of Rhodamine 590 in ethanol are mounted.

3.4.3.5 Control apparatus

A personal computer was used to interface with the Proteus control dedicated hardware. An interface for the remote operation of the lubrication, cooling and air supply pressure and temperature was used alongside an interface for the injection system hardware. These two interfaces provide the test cell operator with full authority over the operation of the Proteus and its parameters. A further interface to an AVL Indiset data acquisition unit

was used to enable the capture and storage of mechanical and thermodynamic operating parameters whilst running the Proteus RCM.

A personal computer with LaVision timing control hardware fitted, was used to coordinate the laser pulse event with the desired crankshaft rotation position. A second programmable timing card enabled triggers for the in-line energy monitor and the camera acquisition to be produced. The in-line energy monitor's output data values were also captured and stored on the same computer.

A personal computer to operate the SIM16 camera unit was used as with the previous experiment. A trigger pulse was provided from the LaVision timing card that was calculated to precede the pulse for the Laser unit by 145 ns, such that the camera's internal delay between actuation and capture of images was negated.

3.4.3.6 Configuration

The laser unit and the laser beam conditioning optics were mounted upon the same structure. Care was taken to ensure the operation of the RCM did not perturb either the acquisition apparatus or laser conditioning optics by the low frequency vibration modes generated. The laser sheet was orientated to horizontally propagate through the central plane of the optical chamber. The laser sheet profile was positioned such that the major axis was set vertical, and intersected the central vertical plane of the optical chamber. The sheet was clipped by the adjustable width slit assembly immediately after the sheet forming optics assembly, to be 0.50 mm across the minor axis.

The camera was situated horizontally and normal to the optical access of the Proteus. The optical access was itself normal to the axis of propagation of the laser sheet through the chamber, such that a planar region was presented, normally disposed and within the camera's field of view. The lens aperture was set to its maximum size (f/4.5). Figure 57 illustrates a plan projection of the experimental scheme.

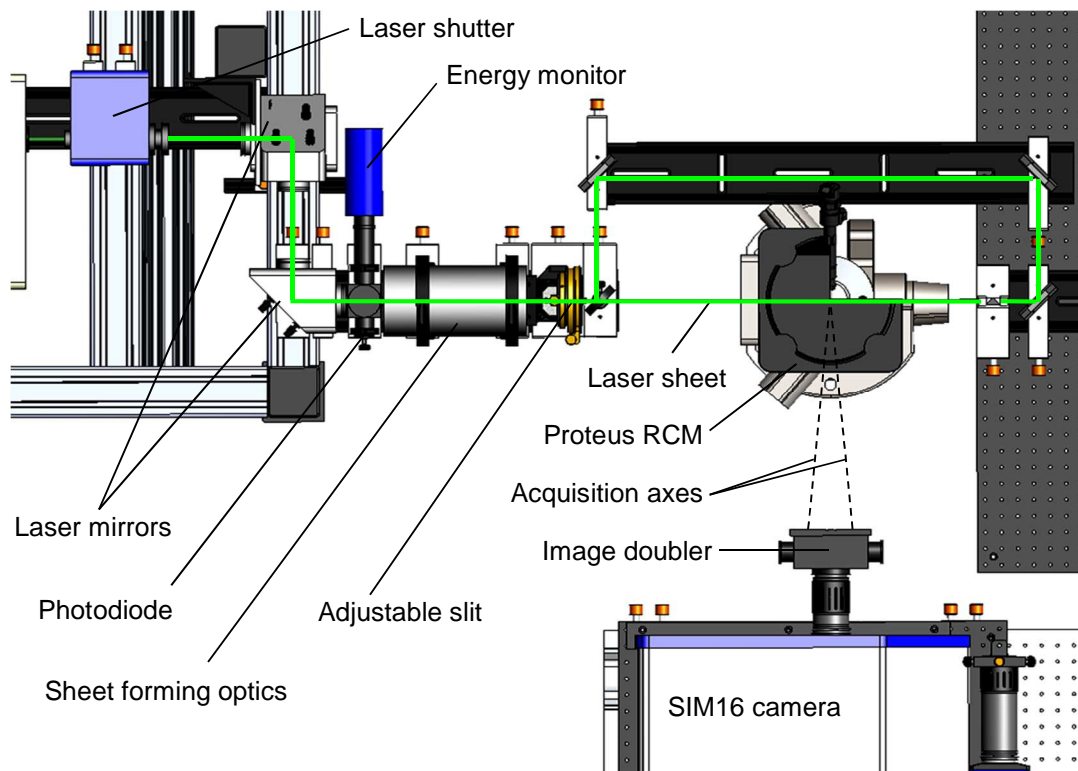


Figure 57 Experimental scheme highlighting laser beam/sheet path.

The laser beam emission from the laser unit (leftmost), passed through a (fail to safe) shutter unit before being reflected vertically by a laser mirror. The vertical beam was reflected horizontally but approximately normally to the intended path of propagation. The third laser mirror reflected the beam to be horizontal and incident with the optical chamber. Prior to reaching the RCM, the beam passed through the in-line energy monitor, sheet forming optics assembly, the adjustable width slit assembly, and finally the beam splitting mirror (Figure 58). The unextinguished laser sheet profile was guided to the right cuvette, the extinguished (via the RCM combustion chamber) laser sheet to left cuvette.

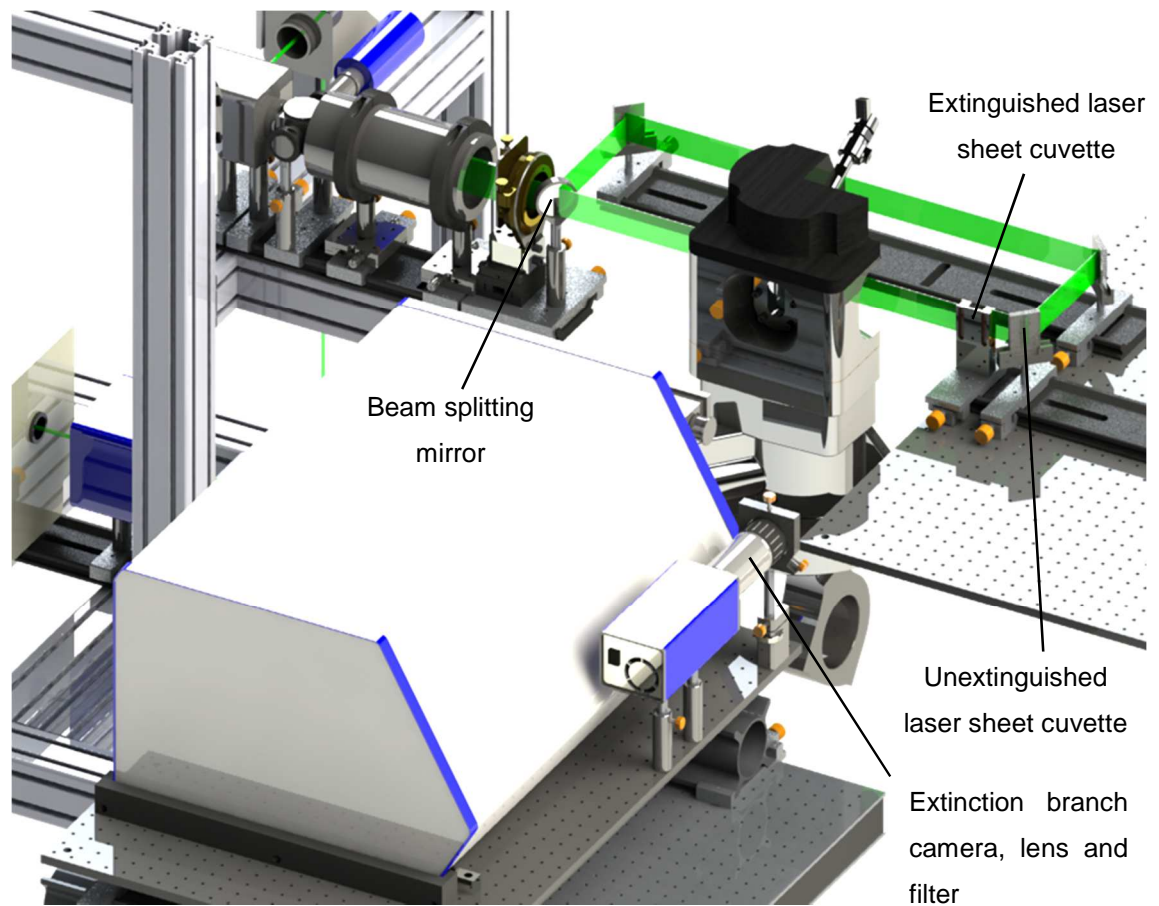


Figure 58 Experimental scheme highlighting extinction branch apparatus.

3.4.4 Control/ Procedure

3.4.4.1 Proteus

The Proteus was run at 500 rpm crankshaft speed throughout. A strategy of skip firing, where a combustion cycle (a single crankshaft rotation due to the two stroke configuration) occurs and then a number of non-fired cycles occur, was employed to purge the chamber of residual gases, aid the minimization of window fouling, and also to allow a rate of repetition of the laser that fell within the laser unit's optimum operating range.

A strategy of one fired and three skipped cycles represented a frequency of 2.08 Hz, a near integer multiple of the desired 10 Hz optimum for the laser unit.

The injection strategy was originally intended to be set at a fixed angular position, however the necessity to produce soot across a range of in-cylinder pressures (3 to 5 MPa) and for it to occur within the optical chamber field of view, meant that injection timing was extensively adjusted. The specific operating conditions employed for each data set in section 5.4 (the high pressure diesel combustion experimental results) are presented to provide a context of the thermodynamic conditions at which the data was captured.

3.4.4.2 Experiment

The laser system was externally driven by the LaVision timing hardware-equipped personal computer. The timing unit received a signal from the injector driver to trigger the acquisition chain. A calculation as to the optimum trigger point of the laser q-switch was continuously performed and output to the laser unit. A trigger pulse was sent in advance to the acquisition controlling computer.

The laser fluence was monitored and recorded throughout the experiment using the in-line energy monitor. A target (sheet cross section) average laser fluence between 180 and 190 $\text{mJ}\cdot\text{cm}^{-2}$ was used throughout (Figure 59). A laser power meter head was positioned after the optical chamber and a suitable plano-convex lens. This allowed bulk extinction measurement to be recorded for each LII event, but also provided a means of assessing the degree of window fouling by plotting the laser power data; a steady declining trend was observed and periodically the RCM operation was stopped to allow for cleaning of the optical access windows.

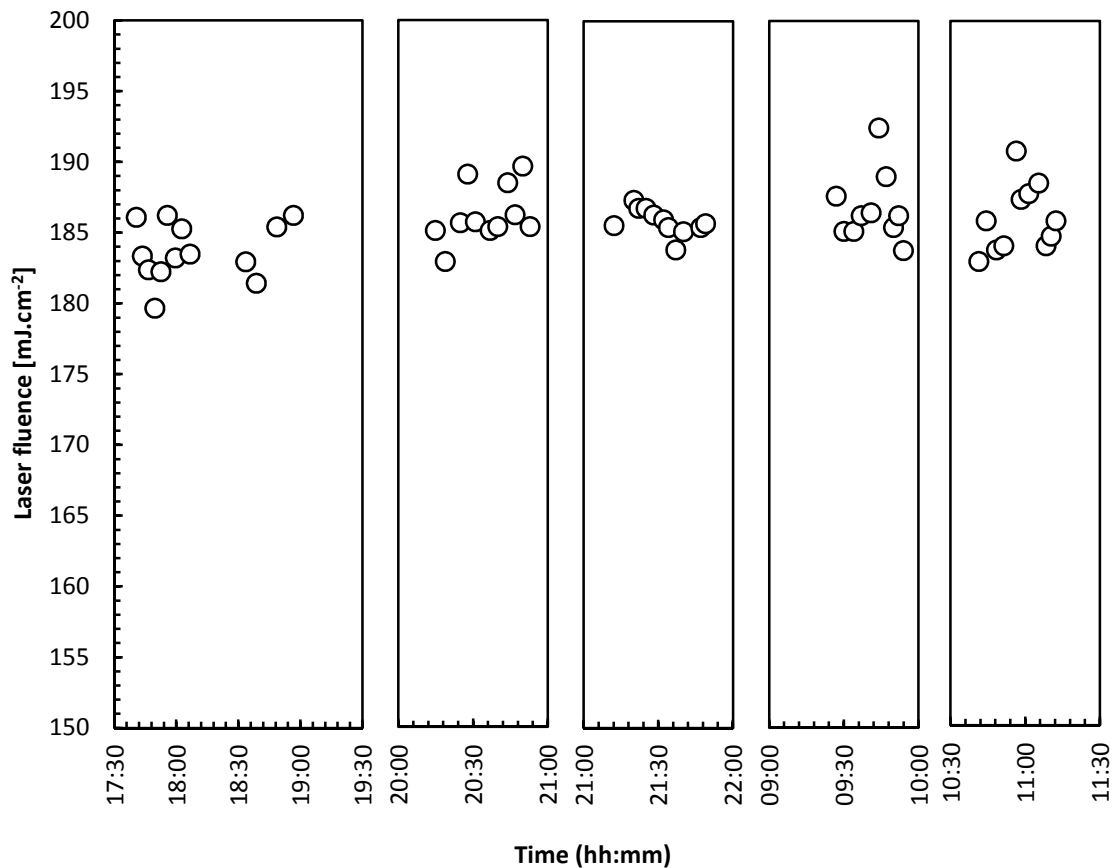


Figure 59 Laser fluence variation across ensemble average LII data sets.

The experiment was performed at constant image exposure duration of 10 ns for all frames. The scheme of timing can be visualized in Figure 60. A 5 ns exposure duration sequence would seemingly have resolved the temporally varying signal in the most fine, discrete steps, however the signal intensity was insufficient and the decision to move to a 10 ns scheme was made. The acquisition by camera was set to capture the peak incandescence signal in the third image of the sequence. The rationale for this was the same as with the atmospheric condition experiment and is addressed in 3.3.5.

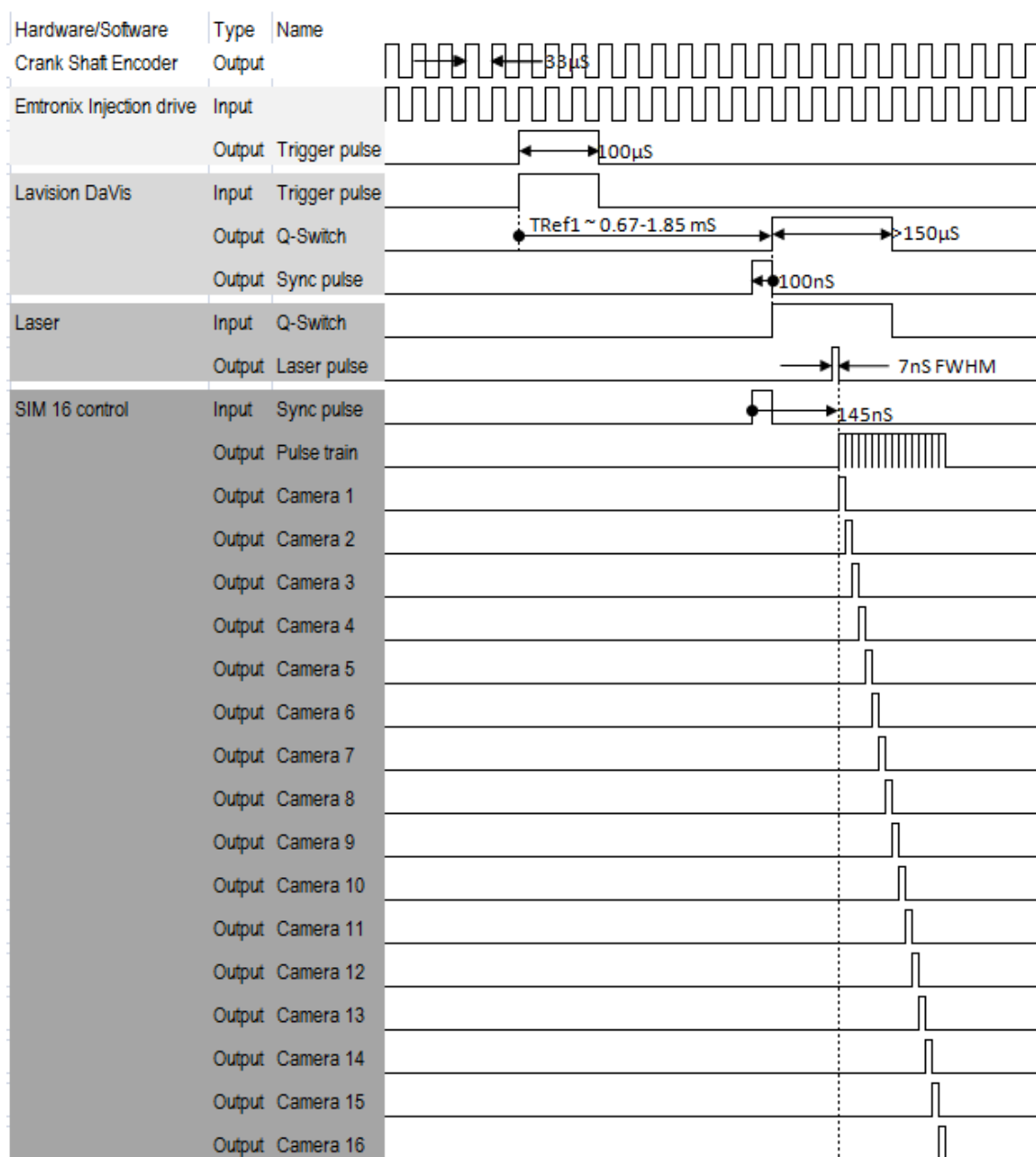


Figure 60 Timing of high pressure experiment

4 Data processing

For quantitative or qualitative measurements made using a camera, it is either desirable or necessary to extract a signal that is representative of the measured phenomenon. Typically, this comprises processing steps to remove noise and artefacts from the data produced by the camera CCD sensor and intensifier. This may be considered in terms of variation of sensitivity or quantum efficiency between pixels within a sensor array. Additionally, certain pixels may exhibit behaviour that does not relate to the quantity of incident photons, they may hold an arbitrary set value or one that is not in proportion to the incident signal. When these pixels hold a high value relative to the background average value, they appear as and are referred to as bright pixels. Where pixels take a saturated value, they are referred to as ‘hot’ pixels. It is important to characterize and remove their effect from images that are processed to yield quantitative measurements and particularly those where the measured phenomenon produces data that is visually similar with distinct high count value pixel regions set amongst low count value regions.

The captured image sets of this study each consist of a sequence of sixteen images, with individual exposure duration, intensifier gain and timing relative to a global trigger signal. The images within a set are temporally sequential with a minimum of 5ns delay between the start of numerically adjacent exposures (where the camera sensors are enumerated one to sixteen). Since the data acquired within each set originates from 16 different sensors and intensifiers, with different individual performance characteristics, care must be taken to normalize the relative sensitivity of each of the 16 image frames.

4.1 Atmospheric conditions

The laboratory burner used in this study was an open flame that burns in an ambient condition atmosphere. The oxidative species of the combustive reaction is extracted from the surrounding air. The temperature and pressure of the surrounding air was approximately 300 K and 1.01×10^5 Pa. The combustion system therefore demonstrated the ‘free molecular’ Knudsen regime.

Relative to the high pressure and temperature conditions found in a typical diesel combustion chamber, the low pressure and ambient temperatures produce a significantly

lower rate of combustion. This yields a comparatively long particle residency time within the flame structure. The formation of soot precursors and their nucleation and coalescence into primary particles that subsequently form large soot agglomerates is therefore aided. The comparatively low temperature reduces the aggressiveness of the oxidation process and thus the competitive, destructive, mechanism for soot population has minimal impact; a high soot concentration annular region within the flame structure is produced. Although the conditions of combustion and the resultant soot concentrations and primary particle diameters differ from those of a typical diesel combustion process, the resultant soot structure/population represents a favourable and largely invariant subject of study in that it is therefore convenient and repeatable as well as being well characterized elsewhere.

The effect of ambient conditions upon the laser induced incandescence signal is to slow the rate of decay of the incandescence emission significantly relative to that which occurs in a high pressure environment, by minimizing the effect of conduction with the surrounding ambient gases. The consequential persistence of a sufficiently intense radiant emission allowed several different temporal strategies of acquisition to be performed. A staggered exposure duration scheme was utilized in which the first four frames were set to 20 ns exposure, frames five to eight at 40 ns, frames nine to twelve at 80 ns and thirteen to sixteen at 160 ns exposure duration. The initial, peak intensity radiant emissions were captured by the earlier frames at an acceptable intensity level, but also with a comparatively fine temporal resolution relative to those of the subsequent frame. Progressing through the sequence of frames, the reduced intensity signal was captured in the longer duration frames, yielding similar signal levels to the earlier frames, thus aiding the signal to noise ratio of the later frame sequence data.

4.1.1 Spatial registration

The planar alignment between images within each set was necessary due to the differences in optical paths between the lens and each individual sensor within the camera assembly. Although the camera assembly undergoes an alignment process when being serviced by the manufacturer, it was evident that a pixel accurate result was not achieved and that this should be addressed at the outset of conditioning the captured data.

A series of target plate images were captured and the coordinates of marker points within each were used to produce a planar mapping of the data. This process was performed on a daily basis such that the relationship between imaging optics and subject of interest was defined even if disturbance or relative movement had occurred.

Within each target image, four marker points coordinates were extracted and used to calculate four sided polygons for each image, which in turn allowed a transformation consisting of rotation, translation and shear to be calculated such that all frames were consistent with a (most geometrically ideal) reference frame.

The resultant registration transformation of the captured data was applied as a non-interpolative, 'nearest neighbour' transform so as to maintain the quantitative integrity of the captured signal. The registration process was applied to dark field (Figure 61).and LII datasets (Figure 62).

4.1.2 Dark field/current characterization and removal

Dark current is an inherent and undesirable characteristic of CCD sensors. The magnitude at each pixel location is dependent upon the temperature of the sensor. The sensors within the camera assembly used for this study feature depressed temperature regulation through the use of peltier thermoelectric cooling devices and associated temperature control systems. Consequently the dark current addition to captured images is smaller than would be the case for ambient temperature CCD sensors, but varied slightly as the temperatures of the sensors varied within the range allowed by their control systems. It was therefore necessary to capture as many sets of dark field image sets as was practical and to characterize the dark field in a way that was most representative of the likely contribution to recorded signal.

Dark field data is typically captured by blocking incident light from entering the camera optics and capturing the resultant signal. Initially, median averaging across all the dark field data sets at each pixel location within each image was used to produce a master dark image set. This produced a dark field dataset that when applied to sample data, subtracted some amount of measured signal as well as the numerical offset due to the dark current. A routine typically used in astronomy to characterize dark current contribution in such a

way as to minimize the possibility of signal degradation is that of ‘median kappa sigma’ averaging (Lehmann 2006). This is an iterative routine that replaces the extremes of the population interval outside some factor of standard deviations from the mean of the population with the median value. With successive iterations the calculated value converges to a fixed value that overall exhibits bias toward the median value, and minimizes the contribution of the extreme values within the population.

A comparison between median and median kappa sigma dark fields demonstrated a reduction in negative calculated pixel values when applied to several sets of raw dark image sets. This indicated a more likely characterization of the dark field and was subsequently used throughout this study. The representative dark field set was subtracted from the median average LII dataset for each acquisition strategy, consistent with the steps portrayed in Figure 62.

4.1.3 Hot pixel characterization and removal

Hot or bright pixels are pixels whose values are large and persistent across image captures. They are a characteristic of the individual CCD sensors and may indicate a degradation of the functionality of the sensors. Hot pixels therefore will manifest themselves within an image without any signal due to incident light occurring. Specifically, the data captured for dark field characterization and the resultant averaged dark field set was filtered for pixels that were of greater intensity than two standard deviations from the image mean. At each qualifying hot pixel location, a nearest neighbour median value was substituted into the dark field dataset. The locations of the hot pixels were also captured in an auxiliary hot pixel map dataset (Figure 61) as a means of locating the hot pixels present amongst the LII signal data. Nearest neighbour median average values were substituted into the median average LII datasets at the hot pixel locations, prior to the dark field subtraction process (Figure 62).

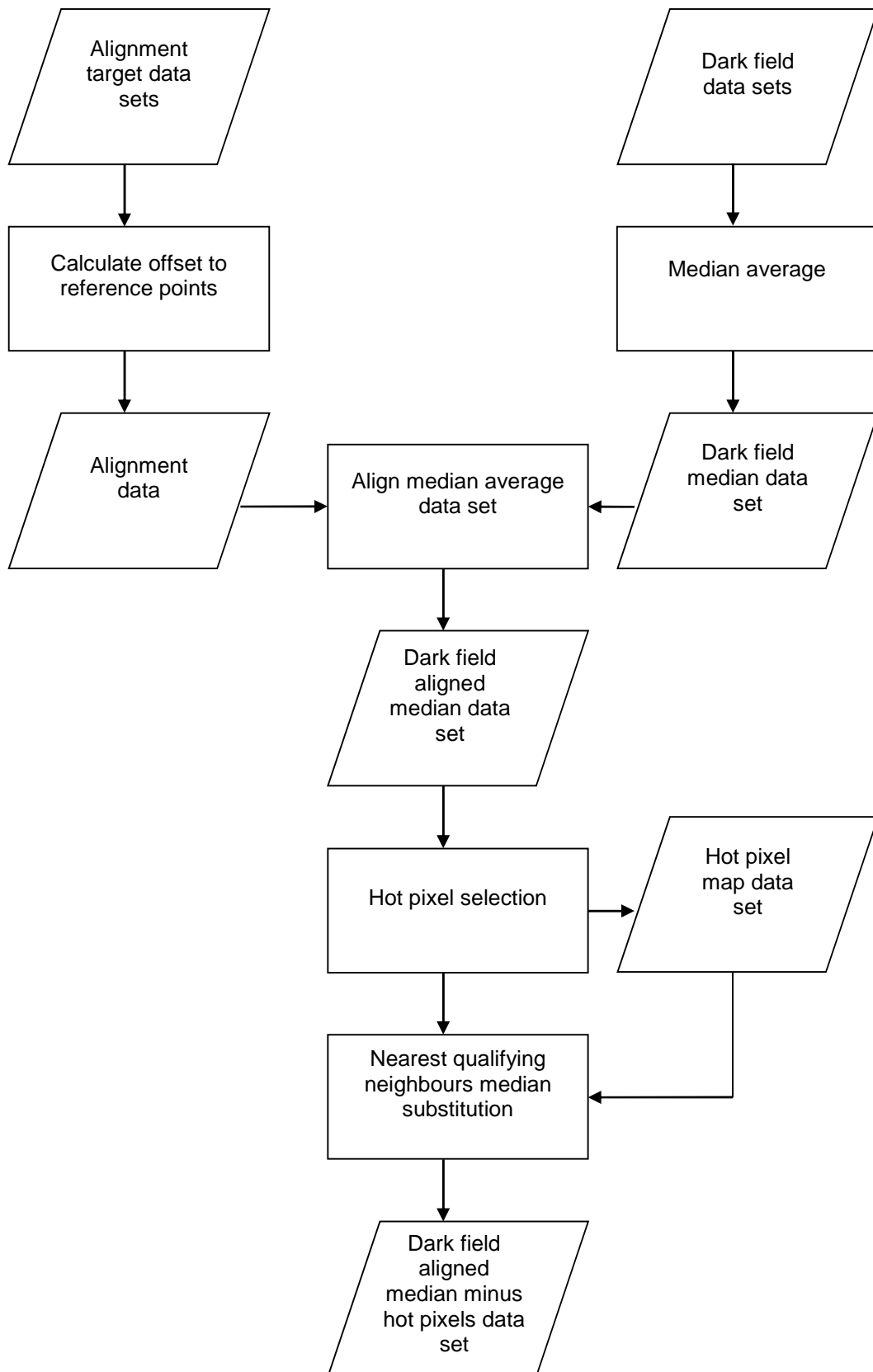


Figure 61 Flowchart of registration, dark field data averaging and hot pixel removal/hot pixel map creation.

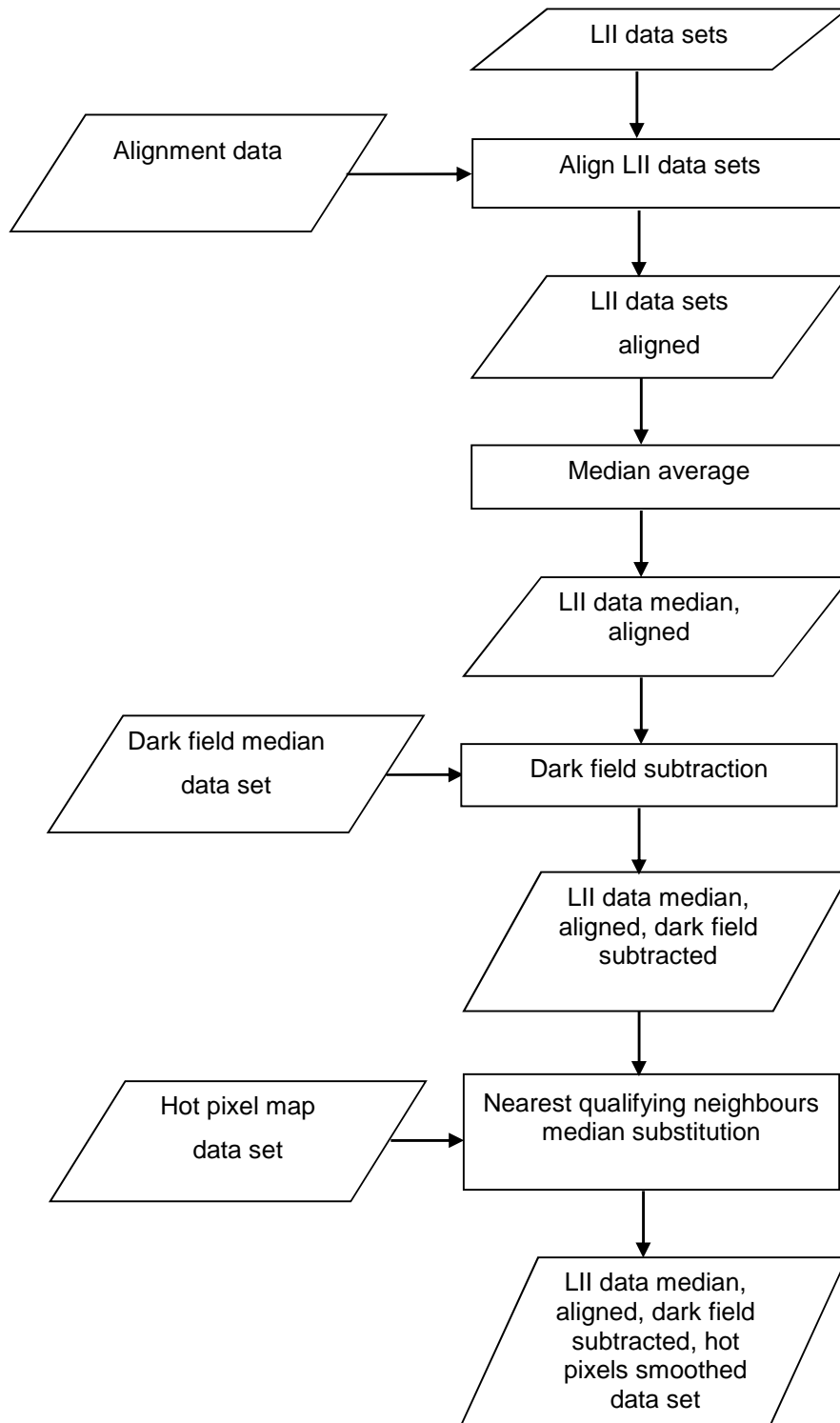


Figure 62 Flowchart of LII data averaging, alignment and hot pixel removal.

4.1.4 Binning

For the ambient condition experiment an optical acquisition scheme that yielded a raw image resolution of 36.2 pixels per millimetre and of equal horizontal and vertical extent. The specific experimental aim of this study is to measure the accumulation of incident radiant emission due to the incandescence of soot across a sequence of short camera exposure intervals; the desire to resolve as fine a temporal resolution of the signal as possible through the employment of short exposure durations whilst still yielding measurable signal intensity, meant that the experiment was performed near the cameras lower limit of exposure duration (and sensitivity) and accordingly an acceptable signal to noise ratio (SNR) was balanced against temporal resolution of the phenomenon measured.

A means of addressing these aspects is to ‘bin’ the image to a lower resolution whereby the original pixels values are summed together. As illustrated in Figure 63, the signal to noise ratio increases with binning factor.

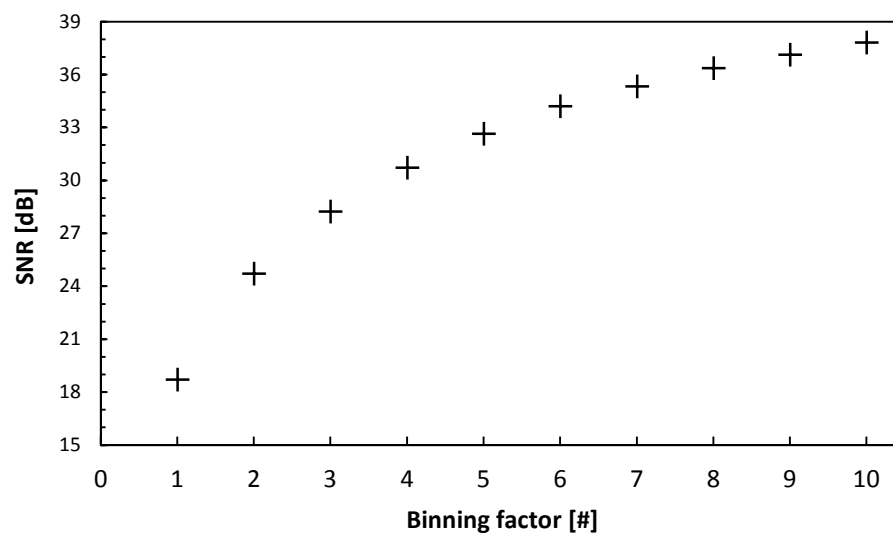


Figure 63 Typical variation of signal to noise ratio ($20\log(X/\sigma)$) with binning factor.

A balance of SNR and pixel resolution is realized. Inspection of Figure 64 suggests that a good compromise may be achieved with a binning factor $n=3$. However, the low signal count data captured due to the necessary short duration exposures, necessitated a greater bias towards SNR increase. A binning factor $n=6$ was selected for the ambient condition LII data.

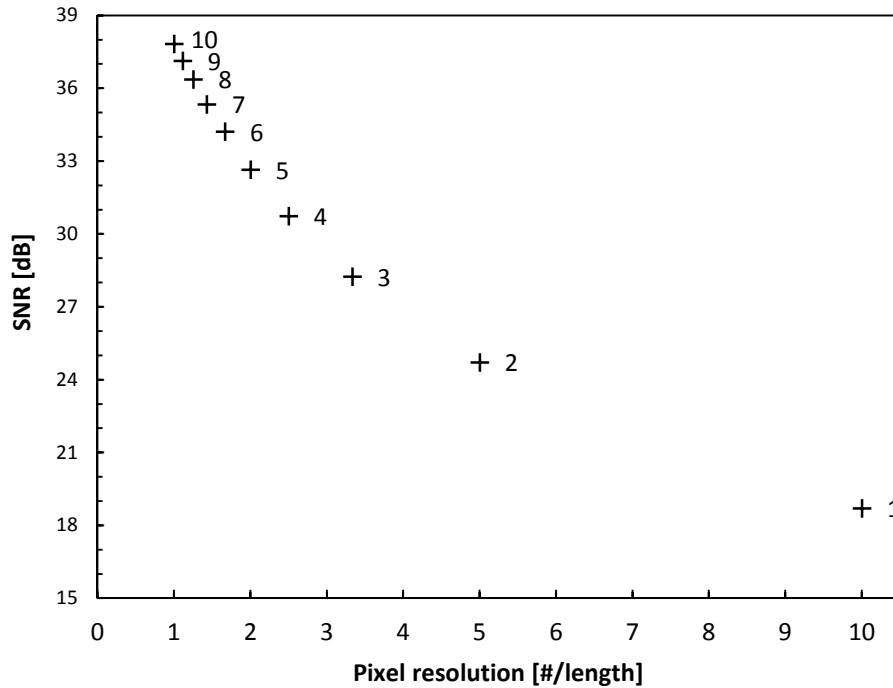


Figure 64 Typical variation of signal to noise ratio ($20\log(X/\sigma)$) with pixel resolution. Note data point enumeration indicates binning factor n , where binned ‘superpixels’ are comprised of n by n pixels.

An additional aspect to consider is that of the spatial uncertainty of the incidence of photons upon the CCD sensor individual pixel ‘potential wells’. Since the incident photons are not those emanating from the phenomenon of interest, but rather a corresponding and greater number produced by the intensifier unit, then there exists some uncertainty as to whether all the representative photons arrive at the correct CCD pixel. Therefore, as the binning factor is increased, so the effect of the photon filling the wrong (likely adjacent) potential well is reduced. The confidence of spatial accuracy of the measured signal to that of the reality of the phenomenon is therefore increased at the expense of spatial resolution.

4.1.5 Divergence from typical data preparation sequence

Typically quantitative or qualitative measurements using a CCD camera involves calibrating sensitivity across the pixel array by recording the light transmitted through a

'lambertian' characteristic diffusing plate, uniformly illuminated by a source such as a lamp, whose emission is defocused through a suitable spherical lens. The process, often referred to as 'flat-fielding', affords a consistent response to a constant intensity of incident light across all pixels in the sensor array. In conjunction with an absolute intensity calibration process comprising an emission source such as a calibrated tungsten filament lamp with a defined geometric optical scheme, the absolute intensity response for each pixel can be derived. This is however based on the assumption that the exposure duration is of sufficient length that the transient phases may be regarded as instantaneous and their effect upon the signal accumulation, trivial. It also assumes that the phenomenon of interest's rate of change of radiant emission is sufficiently low that it may be considered invariant for the duration of the exposure.

The typical LII radiant emission at ambient conditions persists at a detectable intensity above that of flame luminance for up to approximately 1 μ s, and at realistic diesel engine conditions, approximately 100 ns. Therefore a high rate of change of radiant emission intensity occurs. In particular, the initial post laser absorption time period is dominated by sublimative heat transfer. The temperature, and therefore temporal profile of radiant heat transfer, demonstrate the greatest rate of change during the initial post-laser absorption time period. The rate of change is sufficiently high that significant decrease of radiant flux occurs throughout the duration of each camera exposure event. The accumulated signal may be thought of as the convolution of a shutter event function and the LII signal, integrated across the time span of the exposure duration. It is therefore essential to characterize and functionally represent the shutter event for each of the individual intensified CCD cameras.

4.1.6 Camera shutter response

The multiple intensified CCD camera system was operated at short exposure durations, between 20 and 160 ns. Since the opening and closing of the shutter function, performed by the intensifier, is finite, a significant variation of sensitivity to incident photons occurs throughout the shutter event. The shutter's functionality as well as the amplification of the incident radiant emissions are both performed by the intensifier unit. The intensifier has a gain factor that ranges from zero to some peak amplification factor. The control system provides a square wave type signal that the physical assembly responds to,

adjusting from zero to peak gain as quickly as possible, holding at that value for the duration of the ‘high time’ of the control signal, before falling back to zero gain. The operational behaviour is dependent upon the physical construction and is therefore subject to the variations of manufacture due to tolerances of component parameter values.

Prior to further investigation and characterization, the shutter functionality of the intensifier was unknown. A crude approximation of a linear opening phase, constant peak and instant closing phase model was considered to illustrate the necessity of characterization of the operational response. Figure 65 shows that for a constant emission source, the undetected portion of the total incident signal is significant. If a negative linear trend were also used for the closing phase, the uncaptured signal proportion would be greater still.

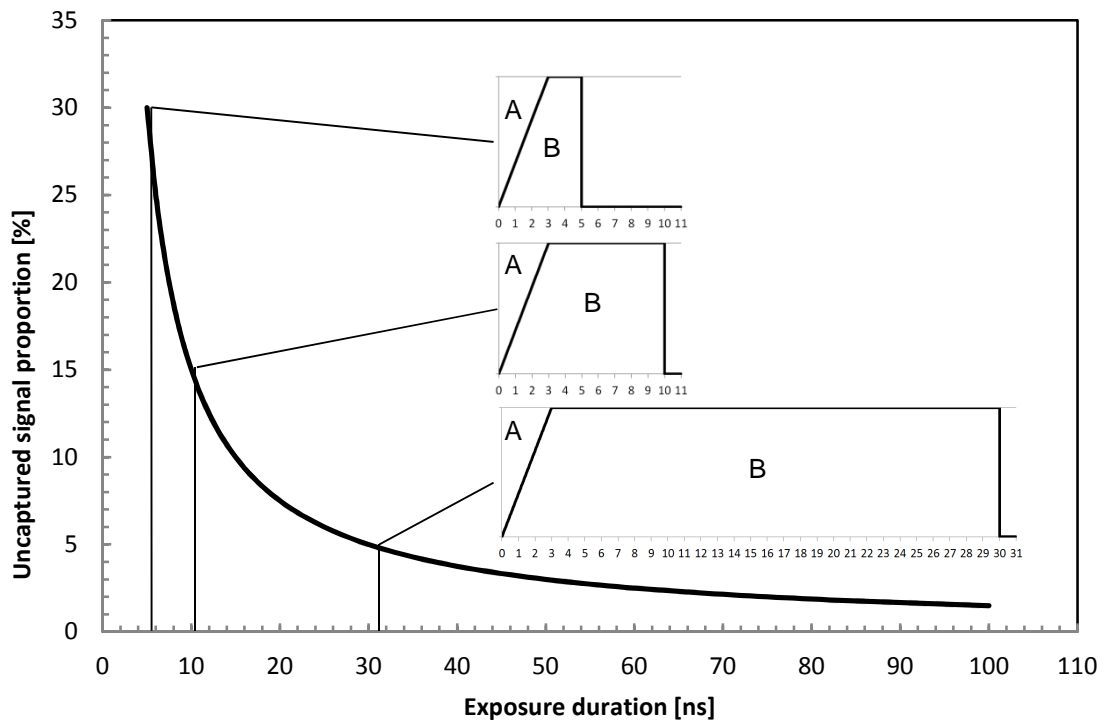


Figure 65 Uncaptured opening phase signal (the area $A/(A + B)$ in the figure), as a percentage of total incident signal for varying exposure duration, when photographing a constant emission source.

The opening and closing behaviour is a characteristic of each intensified CCD assembly within the multi-camera assembly, each may exhibit an individual response in addition to their individual susceptibility to dark current and erroneous bright pixels. The sensitivity curve for each, when driven by the same control system signal, may be significantly different. Accordingly, the measured signal for a common, invariant phenomenon will likely differ between two different intensified CCD assemblies. If the temporal variation of radiant emission typical of LII is convolved with the unknown temporally varying response behaviour of an intensified CCD assembly, then the meaningful quantification of the incident radiant emission is not attainable. A suitable characterization of the response of each intensifier to a binary state control system signal must therefore be established.

4.1.6.1 Characterization of shutter response

The luminance of a constant intensity light source was recorded for a range of exposure durations. Spectral band-pass filtering, the same as used for the main LII signal capture experiment was used since uncertainty regarding the spectral variation of temporal response could not be disregarded. The range spanned from the shortest exposure duration (5 ns) to a duration whereby the peak recorded intensity was in excess of 50 % of the cameras signal intensity range. After performing appropriate data set pre-processing, consisting of hot pixel replacement and dark field subtraction, an area median average value was calculated for each frame at each exposure duration. The values were plotted and segmentation between linear trend and transient region defined, see Figure 66. The gradient of the linear region equates to the camera frame sensitivity, and the curved transition region intercepting the origin represents the effect of the transient shutter opening event. The curved transition region can be thought of as the shortfall of captured signal when compared to a theoretical instantaneously fully open (full sensitivity) signal capture curve which would be a linear trend passing through the origin. It is therefore possible to extrapolate the linear region of response to find the ordinate value when time is zero, this equates to the undetected fraction of the signal that would be captured were the shutter response to be instantaneous. This performance data allowed a model of the shutter event to be produced that attempts to characterize the temporal shutter response. This is necessary due to the finite and temporally varying sensitivity to incident radiant

emission of the intensified CCD camera configuration and the desire to record the signal accumulation through time of the highly transient LII signal.

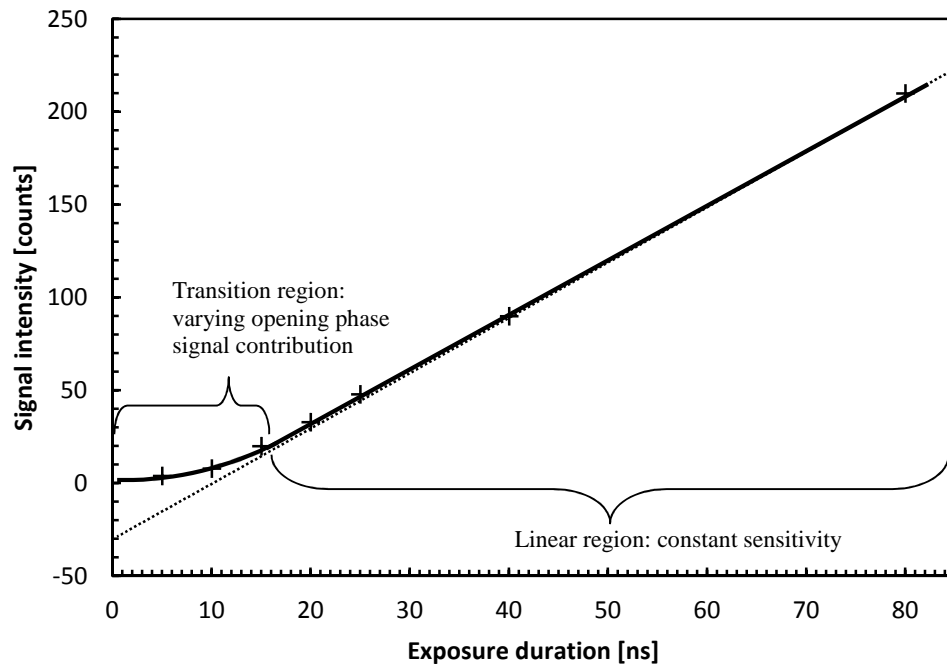


Figure 66 Scheme of distinction of transient and linear regions of response for 488nm band-pass filtered, intensified CCD to constant light source for a range of exposure durations.

The undetected signal magnitude from a constant intensity source can be equated to the magnitude of the ordinate axis intercept of the asymptotic line to which the signal intensity curve tends, as portrayed in Figure 66.

4.1.6.2 Shutter model

Consultation with the manufacturer of the camera assembly with particular reference to the shutter control system, as well as the operating principle and physical construction of the intensifier units, aided the conclusion that the opening and closing behaviour imposed by the intensifier would likely adhere to an exponential characteristic. The physical operational response of the intensifier is considered to be consistent with electromagnetic

field theory. An exponential characteristic transient response to a binary condition control signal (open/closed) in conjunction with shutter luminescence response over a range of shutter duration control signals, allows a shutter response characterization to be made, see Figure 67

In order to equate the lost portion of signal due to variation of opening phase, a standardized closing event was used. This was done out of convenience and in particular because of the decaying LII signal and the deceleration of rate of change of the signal. The opening phase variation of sensitivity and the associated discrepancy between true signal and measured signal constitutes a larger overall proportion not collected relative to that of the closing phase.

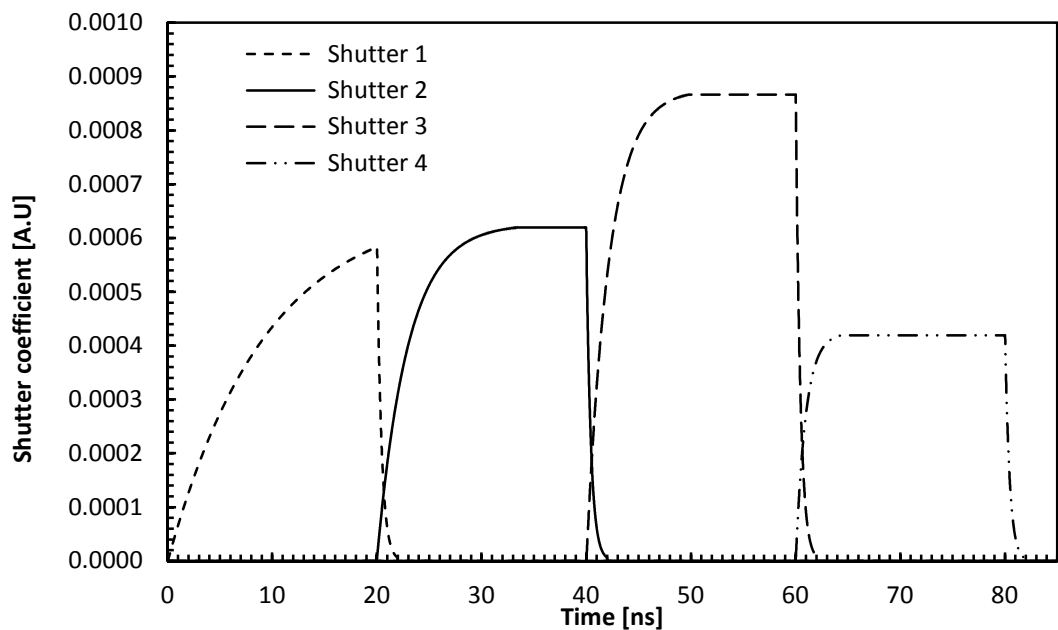


Figure 67 Example shutter response curves for 488 nm centred spectral interval model solution algorithm.

4.1.7 Laser fluence

The laser fluence magnitude at each location within the field of data was dependent upon several aspects of the experimental scheme. The fluence along a particular laser ray path was attenuated as energy was absorbed by particles with which the ray was incident.

Accordingly, the fluence value used to calculate the modelled radiant emissions must be consistent with that likely to have occurred at each location within the sooting flame structure. A model to characterize the distributed extinction contribution that occurs along the beam path was produced (Figure 68). The model provided a map of local laser fluence magnitude by calculating the attenuation due to extinction as the soot structure within the flame is traversed along the laser ray path.

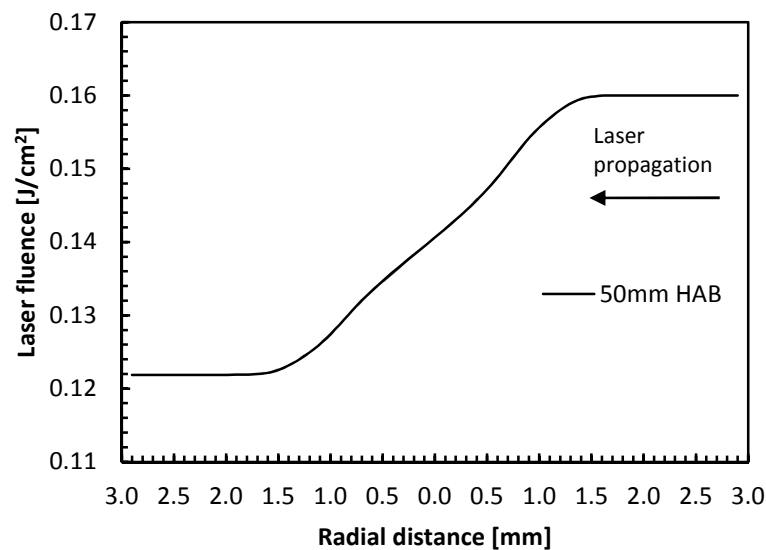


Figure 68 Laser fluence profile across flame at 50mm height above burner (HAB).

A shot to shot fluctuation of the laser fluence output from the laser head was observed. The LII data sequence associated, calibrated, online energy monitor intensity values were used to calculate the area averaged laser fluence incident upon the sooting flame structure. The overall extinction of the incident laser fluence, across the flame height span used in this study, was known to be in the order of 27% from previous in-line extinction experimentation upon the Santoro burner flame at identical operating conditions. A model of extinction factor across the flame structure was made whereby the total extinction was distributed in such proportion as to be in agreement with work elsewhere (Santoro *et al.* 1983, Oger 2013). This allowed the calculation of a local fluence map that was in turn used in the modelling of radiant emissions at each location within the sooting flame structure data field.

4.1.8 Algorithm

An indirect method was employed to solve for and find the particle population interval whose spectral emission summations, in ratio, most closely matched that of the measured data (Figure 69). A ratio of spectral intervals was used within the model for similar reasons to typical 2C-LII; an absolute intensity value calculation was undesirable due to requiring absolute intensity calibration data against which to measure the model.

Each binned pixel location within the LII data field was processed separately. The sequences of frames of pre-processed data were queried to extract thirty-two discrete data points for a specific pixel location. Two series of sixteen data points, one for each acquisition spectral interval, were realized and represented the captured proportions of the temporally changing LII radiant emission at the two acquisition spectral intervals. For each of the sixteen frame sequences, a ratio between the 488 nm and 647 nm wavelength acquisition spectral interval was calculated. The sequence of ratio values constituted the target signal ratio values for the algorithm that adjusts the particle population sizes. The summation of the contribution of all particle sizes within the guessed population interval was calculated for the two acquisition spectral intervals for each frame event. The resulting sequence of data pairs yielded ratios that would tend towards matching the measured data ratios as the guessed particle population tended towards that of the experimental subject.

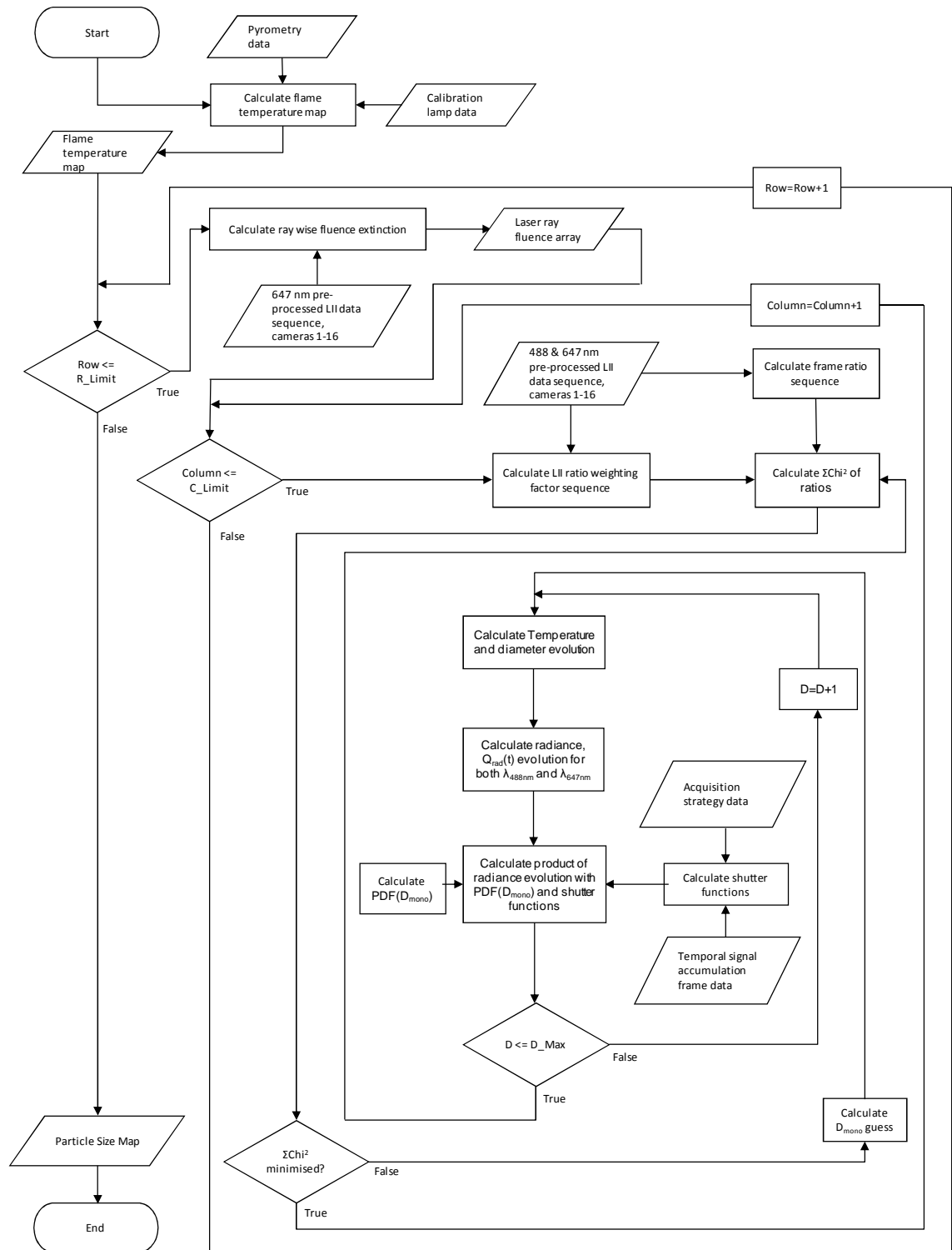


Figure 69 Solution algorithm of D_{mono} particle size map at ambient conditions.

A primary particle diameter was used to singularly parameterize the particle size distribution interval. From this value a multi-log normal size distribution interval was

calculated through the calculation of a probability density function. The temporally varying contribution of each particle size was calculated and convolved with the appropriate shutter response curve for the particular frame and the particular spectral interval. The resultant temporally varying signal was integrated across the duration of the shutter acquisition event, yielding a single value for the frame. The full sequence of frames, calculated at both acquisition spectral intervals, allowed the calculation of the modelled frame ratios to be produced. These ratios were used to compare them to the measured ratios. The difference in measured to calculated ratio values constituted the error term that the iterative algorithm attempted to minimize. The algorithm iterated through successive guessed primary particle diameter values, calculating the resultant signal ratio sequence and comparing them to the measured values. A bisection method for selecting guess value of the primary particle diameter was used. A modification of this was made to allow guess values to step outside a previously narrowed solution range. This was done to allow a more nearly globally minimized error value to be sought when local minima had been inadvertently converged upon.

4.1.8.1 Convergence criteria

The convergence criterion for the algorithm was a goodness of fit measure using a frame weighted chi squared (χ^2) value, calculated by:

$$\chi^2 = \sum_{i=2}^{12} \frac{(\Phi_{488,647,meas,i} - \Phi_{488,647,calc,i})^2}{\Phi_{488,647,meas,i}} \cdot Wf_i \quad \text{Equation 86}$$

The modification of a typical chi squared formulation was that of adding a frame specific weighting factor within the summation, calculated to reflect the magnitude of the data values, and therefore the relative degree of confidence in them. See section 4.1.8.2 for further explanation of the frame specific weighting factors.

4.1.8.2 Data ratio weighting

A method of weighting of the errors between frame ratio data points versus the ratios of modelled signal accumulation was employed such that ratio pairs with higher measured data magnitudes were weighted more heavily than those resulting from lower magnitude data. Since the solution algorithm sought a minimum of the chi-square summation value as a criteria for convergence upon a solution, a method of distinguishing between relatively high and low uncertainty data ratio values was considered appropriate.

The LII data ratio of 488 nm centred spectral interval signal intensity divided by 647 nm centred spectral interval signal intensity constitutes the target value for a specific pixel location in a specific data frame of a specific data sequence. A weighting factor inversely proportional to the variance of the data ratio is used to weight the chi-squared summation contribution for each frame ratio error, where the error is defined as the difference between the measured ratio and the calculated ratio.

$$Wf_i = \frac{1}{\sigma_{ratio488/647,i}^2} \quad \text{Equation 87}$$

Where

$\sigma_{ratio488/647,i}^2$ is the ratio variance, where $\sigma_{ratio488/647,i}$ is defined by:

$$\sigma_{ratio488/647,i} = \frac{X_{488,i}}{X_{647,i}} \cdot \sqrt{\left(\frac{\varepsilon_{488,i}}{X_{488,i}}\right)^2 + \left(\frac{\varepsilon_{647,i}}{X_{647,i}}\right)^2} \quad \text{Equation 88}$$

In which:

ε statistical variation, defined as:

$$\varepsilon = \sqrt{X_{\lambda,i}} \quad \text{Equation 89}$$

$X_{\lambda,i}$ LII data pixel value for spectral interval centre wavelength λ

i frame number

4.2 High pressure conditions

4.2.1 High pressure regime and models used

Since the ICP and temperature present prior to the onset of combustion means the heat transfer model was in the Knudsen continuum regime, the expressions used for conductive and sublimative heat transfer were changed to suitable expressions as addressed in 2.7.4.

The high pressure condition and the effect upon the heat transfer mechanisms increases the rate of decay of the LII radiant emission until the useful section of temporally resolved emission is in the order of 100 ns total duration. This meant that the minimum exposure duration of 5 ns was desirable for each of the camera exposures in the sequence of sixteen images. Upon conducting the experiment, the signal intensity was found to be very low and so the decision to move to 10 ns exposures was taken. This allowed the early frames (1 and 2) to capture prior to the LII signal, aiding certainty as to the synchronisation of the acquisition relative to the LII signal. Since the time span was increased to 160 ns the useful signal decay was still fully resolved. In common with the ambient condition experiment, the frame data ratios were weighted in significance dependent upon the magnitude of the signals from which they were composed. The consequence of this was that the later frames of the temporal sequence, when radiant emission due to LII was minimal, were weighted comparatively lightly relative to the earlier frame data.

4.2.2 Laser fluence

The high pressure conditions experiment did not lend itself to a similar modelling of local laser fluence magnitude as with the Santoro burner flame. The symmetric geometry, ambient condition diffusion flame burner allowed a simple approach to establishing a local extinction value by virtue of its symmetric and regular flame structure. The flame and associated soot structures produced within the optical access combustion chamber of the RCM demonstrated a cycle to cycle variation, deviating from a regular axis-symmetric

distribution. The precise conditions at the onset of combustion, in terms of the fuel plume structure and distribution, temperature, as well as the environmental conditions and the consequential variation flame kernel propagation meant that a different approach was necessary. An auxiliary laser extinction experiment was performed simultaneously with the LII experiment. This provided data as to the beam-wise integrated extinction of the laser sheet as it traversed the combustion chamber for the particular soot structure that occurred due to the particular combustion event, for which the LII data was the principle focus. A scheme in which two cuvettes containing a fluorescing solution were used, one with (a known proportion of) the unextinguished laser sheet incident upon it and a second with the laser sheet that had traversed the combustion chamber, incident upon it.

The fluorescent emissions from both cuvettes were captured using a PCO SensiCam CCD camera, which has a 1280x1024 pixel and a monochrome 12 bit luminosity resolution. The data captured was that of a proportion of the unattenuated laser sheet as a reference, and that of the partially extinguished laser sheet, having traversed the combustion chamber and its contents, prior to its incidence upon the second cuvette. For each captured sequence of LII images, and associated monochrome image of pair of fluorescing Rhodamine 590 solution filled cuvettes provided laser intensity data that would allow, if not an outright calculation of the extinction at each location within the chamber field of view, an inference of distribution of extinction across the intersected soot plume.

The approach of ray-wise extinction modelling through the optical access combustion chamber was undertaken. The spatial geometric relationship between cuvettes, optical chamber and laser sheet was established. A slight divergence across the long (vertical) axis of the laser sheet necessitated a ray-wise approach. The spatial path that each conceptual ray describes passing through the optical access combustion chamber was modelled. The relationship between height locations in the laser sheet prior to the first beam-splitting mirror and the height location upon the cuvette was calculated. The simultaneous height upon the second (unextinguished laser sheet) cuvette was also calculated such that a relationship between the path through the chamber and locations in both cuvette images was defined. This allowed a scheme to be established where the ray-wise integrated extinction could be calculated. At that point, a ray average approach could have been taken whereby the extinction, and therefore the fluence gradient along the path of the ray within the chamber, would be constant. This did not seem to be an acceptable

approximation of what was likely occurring within the combustion chamber and so a different approach in which an LII image was used to infer a distribution of the extinction within the field of view Figure 70 and Figure 71.

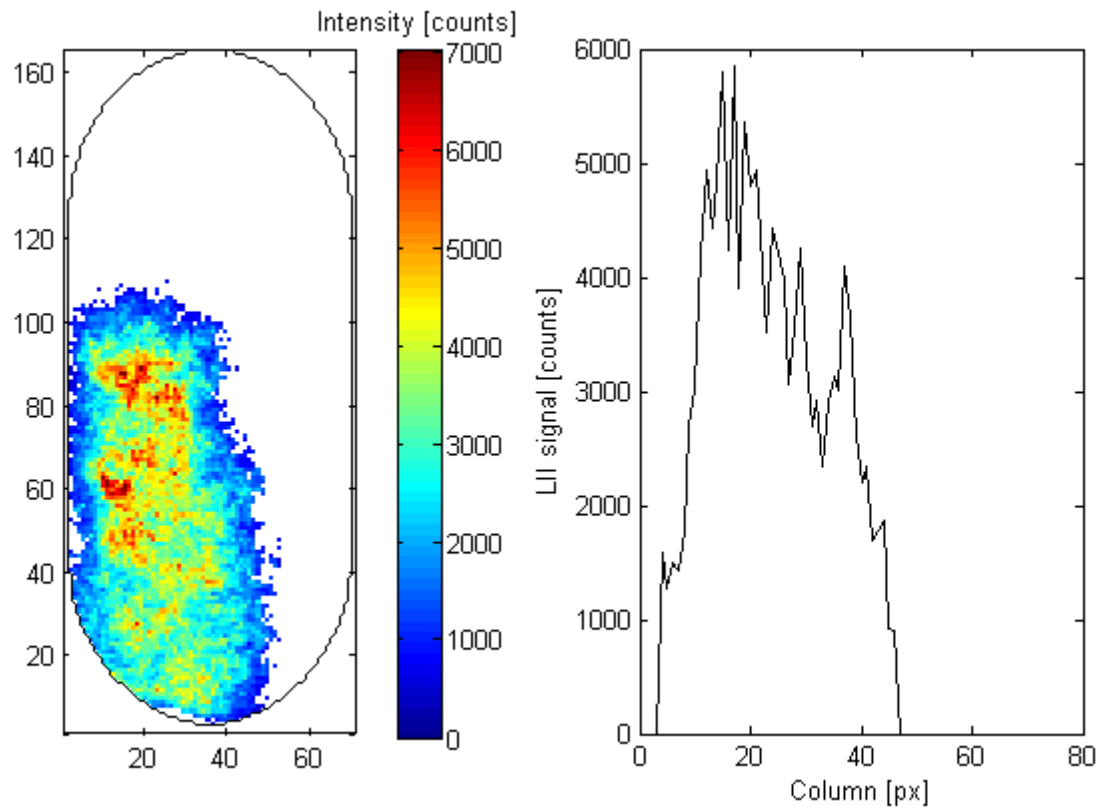


Figure 70 (left) An example data field for a 750 nm spectrally filtered peak intensity LII emission with, (right) a horizontal profile for row 55.

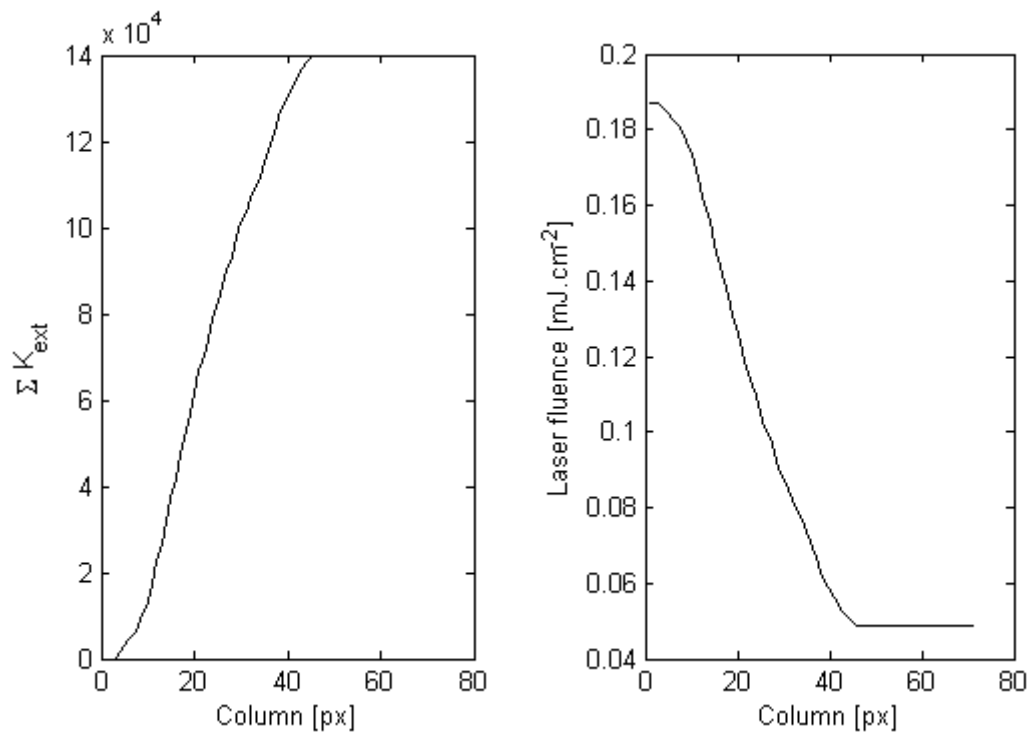


Figure 71 (left) shows the accumulation of extinction factor K_{ext} , as the soot plume is traversed, whilst (right) shows the resultant calculated distribution of laser fluence for the same path.

This yields an analytical compromise in that the entire chamber content is not portrayed within the field of view of the LII optical access window. It is reasoned however that the central, vertically orientated, injector fuel plume, injected into a near quiescent chamber, likely demonstrates a flame and soot structure where the majority of the laser extinguishing soot structure is situated within the central region of the chamber and is therefore depicted in the LII images. No corrections for contributions of soot extinction beyond the field of acquisition were performed.

4.2.3 Algorithm

The particle size map solution algorithm for the high pressure experiment is similar to the low pressure algorithm and iteratively searches for guessed particle sizes using the same Nelder-Mead simplex algorithm (Figure 72). It differs from the ambient solution algorithm with regard to the heat transfer equations due to the continuum Knudsen regime, and the method of establishing local laser fluence. Also, a temperature map within the combustion chamber data field was not measured so a global gas temperature was estimated from crank-angle resolved RCM operating data, specifically in-cylinder pressure, intake charge pressure and intake charge temperature. Notable experimental parameter changes include the acquisition spectral filter specifications, the acquisition timing strategy and therefore the acquisition shutter characterization.

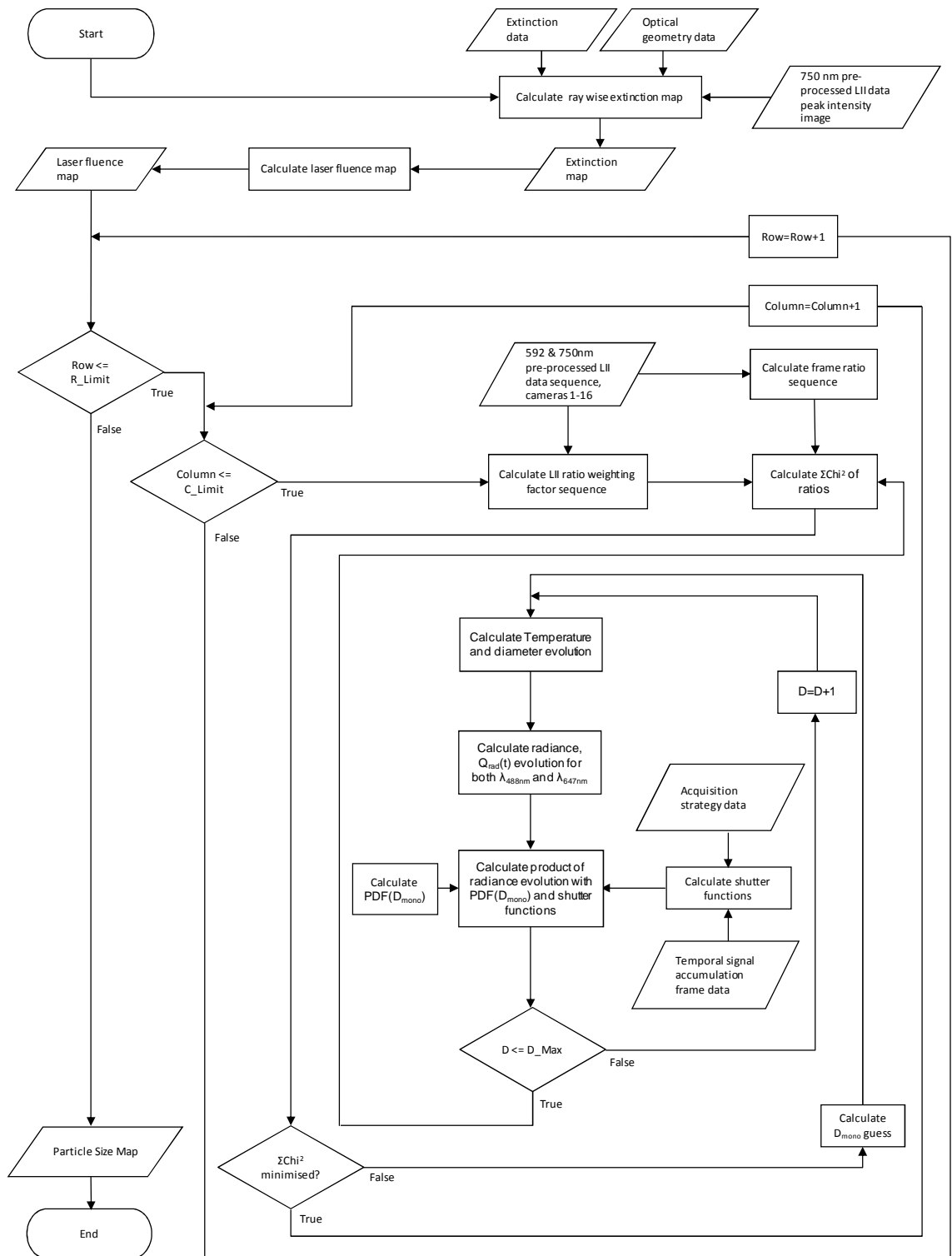


Figure 72 Solution algorithm of D_{mono} particle size map at high pressure conditions.

4.2.4 Spatial registration

As with the atmospheric condition experimental data, a spatial registration between frames within the temporal sequence and between acquisition channels was necessary to extract the temporal variation of signal intensity at each location within the spatially resolved field of view.

The RCM optical accesses are configurable in that either window holder assemblies, blanking plates or alternate use components may be fitted to the apertures leading to the narrow upper cylindrical region of the combustion chamber. An assembly was used that presented a flat target plate within the chamber, vertically disposed and collinear with the plain of laser propagation. A printed target image featuring a grid of crosses (5 mm centre to centre, 3 mm line length) was affixed to the target plate and illuminated as evenly as practicable using external light sources. Several sequences of images were captured, in turn through both optical paths from the image doubler assembly. The sets were summed together for each optical channel to yield two sets (32 images in total) of well resolved alignment grid images. Through inspection, a set of four grid marker locations, visible in all frames of both optical paths, were selected. The location coordinates were extracted and transposed into a suitable form for use in an image registration transformation calculation. The calculated transforms were applied to the alignment images and by inspection deemed to have been acceptably well registered, spatial jitter or movement between the frame images was assessed to be in the order of ± 1.5 pixels magnitude. This represented the least erroneous alignment achieved and was considered acceptable since the LII data would subsequently undergo binning by some factor, certain to be three or greater due to the necessity of enhancing the SNR. The registration transformations were then recorded for application to the LII datasets.

A mask that described the common optical access region of the images was created from a CAD geometry file. The window holder assembly was orientated such that the view was consistent with the optical path from one side of the image doubler. This was repeated for the second optical path and the two spatial models Boolean summed to provide a common optical aperture. An image was captured and a threshold routine applied to yield an optical region within an otherwise blank mask. This was then applied to the data post spatial registration in order to focus upon meaningful data sequence locations and reject

scattered light that illuminated the RCM window holder assembly within the field of view of the two acquisition paths.

5 Results and discussion

5.1 Introduction

The results from both the atmospheric condition, technique validation experiment and those from the diesel engine condition, technique application experiment, are presented herein. Discussion of uncertainties associated with aspects of the experimental scheme design and performance thereof are initially considered. Thereafter, each result is presented with brief discussion. After the complete results presentation, a section is presented in which the efficacy of the technique, its sensitivity to parametric variation of the measured entity and/or experimental conditions, is discussed.

5.2 Uncertainties

The resultant quantitative values presented are essentially without a quantified degree of uncertainty. This is principally for two reasons. The first is that the primary focus of the study has been to ascertain the viability of the technique and to highlight aspects that warrant refinement or the employment of alternative strategies. As such, the realization of a planar resolved technique that demonstrates sensitivity to particle sizes was of more concern for what must be considered, an immature technical variation of TiRe-LII. The second is a more pragmatic reason in that it became apparent the propagation of estimated measurement uncertainties through the convoluted indirect solution algorithm of coupled differential equations, would constitute a significant undertaking. It was therefore decided to set this beyond the scope of this study, recognizing the value of such an undertaking for future studies in which practical challenges do not dominate.

Sources of uncertainty of the experimental schemes used within this study might be summarized as consisting of instrument measurement uncertainty, the consequences of geometric and temporal uncertainty and the degree of deviation of optical components from their published specifications. Specific aspects of the study affected by these are addressed herein.

5.2.1 Laser fluence

Both experimental schemes employed an extinction principle derived local laser fluence value. They are therefore subject to the measurement uncertainty of the laser intensity prior to and after the soot plume. For the atmospheric condition experiment, an in-line energy monitor was used to measure the incident laser beam intensity. A calculation of the local distribution of energy within the resultant sheet-formed laser was therefore performed. Furthermore, the ray-wise distribution of extinction due to the soot plume, and the resultant ray-wise laser fluence was also subject to calculation thereafter. The potential for significant error in the local laser fluence value should therefore be acknowledged. The simultaneous extinction experiment undertaken for the high pressure diesel condition experiment introduced aspects of uncertainty regarding the spatial relationship between both cuvettes and the field of view within the optical access region of the combustion chamber. The fluorescence profiles extracted from the captured image of the cuvettes may be subject to error in that the intensity of the fluorescence, whilst demonstrating no obvious plateau of intensity, may have been wholly or partially excited to an intensity at which the Rhodamine solution demonstrated non-linear incident energy to fluorescence performance.

5.2.2 Ambient (or flame) temperature

The atmospheric pressure experiment upon the laminar burner utilized a flame temperature data field previously measured and calculated using a two colour pyrometry technique. Good agreement with values presented in the literature were achieved however, the technique is subject to uncertainty, both instrumental and conceptual, and particularly regarding the consequence of the soot emissivity value used. The temperature field therefore had an associated uncertainty of approximately ± 100 K. This uncertainty propagates through the subsequent heat transfer term calculations, the modelling of the temporal variation of the LII radiant emission, and ultimately, the calculated particle sizes.

The high pressure, diesel combustion conditions experiment utilized a global chamber temperature value, calculated from the RCM data. It seems likely therefore that the local temperature values across the chamber were subject to considerable uncertainty and were

likely to have been in excess of the value used. In retrospect it is apparent that the earlier images of the capture sequence could have been configured to perform a two colour pyrometry technique, prior to excitation by the laser sheet.

5.2.3 Acquisition sensitivity

The characterization of all aspects of the camera assembly performance that affect the captured image pixel values is of great importance and the degree of uncertainty of the measurements made in these experiments, whilst unknown, seemingly demonstrate high overall noise content. Characterization of the camera assembly performance would therefore entail characterization of the sources of noise (dark noise, shot noise, read-out error, inconsistencies of intensifier performance in a shot to shot basis), which would allow the calculation of an associated measurement uncertainty value.

5.2.4 Acquisition temporal jitter

Variation of acquisition timing, relative to that of the laser excitation event, may have been manifest and may contribute to a ‘temporal smearing’ when considering the effect upon ensemble average data. This would therefore introduce uncertainty to the subsequently calculated particle sizes. For the experimentation presented within this study, a timing uncertainty limit of 5 ns was targeted so as to minimize the consequence upon the resultant data. Future analysis of the captured data may allow quantification of temporal jitter, assessment of the impact upon calculated particle size, but also the possibility of analysing the trade-off between the number of qualifying data sets used in ensemble averaged data, to the standard deviation value of the synchronization timing.

5.2.5 High pressure effects

Radiant heat transfer, and hence LII signal, is proportional to the fourth power of temperature and third power of particle diameter. The consequence of this upon the technique for resolving particle diameters, is that the sensitivity is significantly lower for small particles relative to that of large particles. A bias of sensitivity towards large particles is inherent in the physical scheme.

The difference of peak temperature to which small and large particles are heated during laser excitation increases with ambient pressure. The intensity of the small particle signal contribution therefore is diminished relative to that of large particles with increase of ambient pressure. A further bias of sensitivity towards large particle diameter solutions is therefore manifest with increase of ambient pressure. An informative characterization of the effects of ambient conditions upon incandescence radiation is presented elsewhere (Cenker 2014). An additional consequence of this may be that some proportion of the soot population size interval may be heated to or beyond the vaporization threshold; so a perturbation of the soot population may occur in which the number of smaller particles are reduced relative to the larger particles, biasing the population sample measured.

5.3 Atmospheric condition experimental results

As described in section 3.3.3.3.5, two branches of acquisition were simultaneously performed upon the atmospheric condition experiment. The temporally staggered sequential camera exposures provided data acquisition for a planar region of radiant emission due to LII at discrete points through time. A second acquisition scheme was that of a point location or 'punctual', two colour, time resolved laser induced incandescence (2C-TiRe-LII) that utilized two photomultiplier tubes, each spectrally filtered with the same specification as those used for the camera acquisition (488 nm and 647 nm, 10 nm FWHM, 70%Tr). Through the utilization of lenses and a beam-splitting mirror, both photomultipliers were presented with the emission from the same location, chosen to be 2.4 mm radial distance from the central symmetric axis, and 50 mm height above burner (HAB). This location, although situated in a region of likely high soot size gradient, also presented a high soot volume fraction, therefore yielding a high radiant intensity from LII and minimizing the local presence of obfuscating emissions such as fluorescence from NO or OH.

The photomultiplier data was captured simultaneously with the camera data as well as the laser fluence for each LII event. An analysis of laser fluence variation was conducted, in particular to characterize any 'drift', however due to experimental operational procedure in which laser fluence was periodically checked using a laser power meter and adjusted to a target value, the drift of fluence was largely eradicated.

5.3.1 Punctual 2C-TiRe-LII

The photomultiplier data was filtered for outlier sets using a median plus or minus two standard deviations rule. Figure 73 and Figure 75 portray the photomultiplier data traces as temporally evolving data point series from left to right. Signal intensity is conveyed by false colour scale. Figure 74 and Figure 76 illustrate the bounds of qualifying data. Each data sequence was assessed at each data point as to whether it fell within acceptable bounds, defined as the mean profile ± 2 standard deviations. The summed acceptable signal data points for each profile were expressed as a proportion of a fully qualifying signal data point count. A threshold of qualification was set at 95% and data sets filtered accordingly. This method was employed since each entire profile needed to be utilized or disregarded collectively based upon qualification criteria imposed across their entire data point series span.

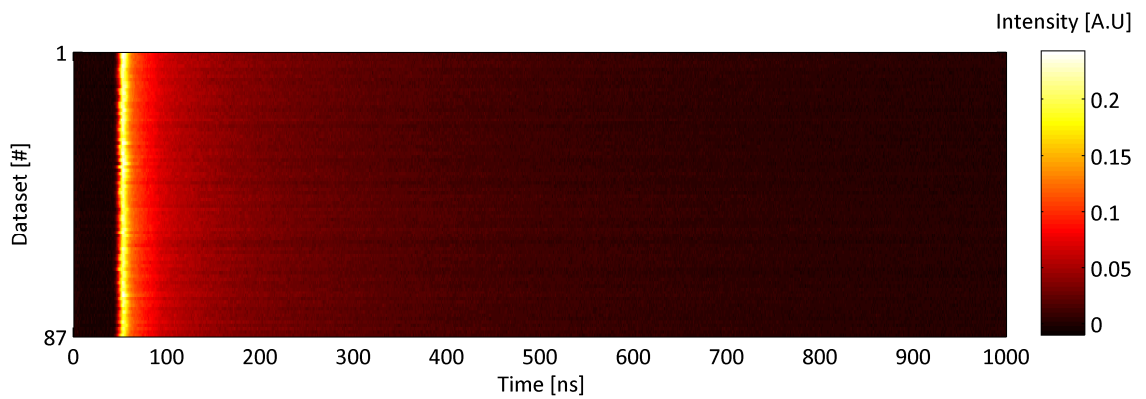


Figure 73 LII signal data, 488 nm spectrally filtered photomultiplier signals

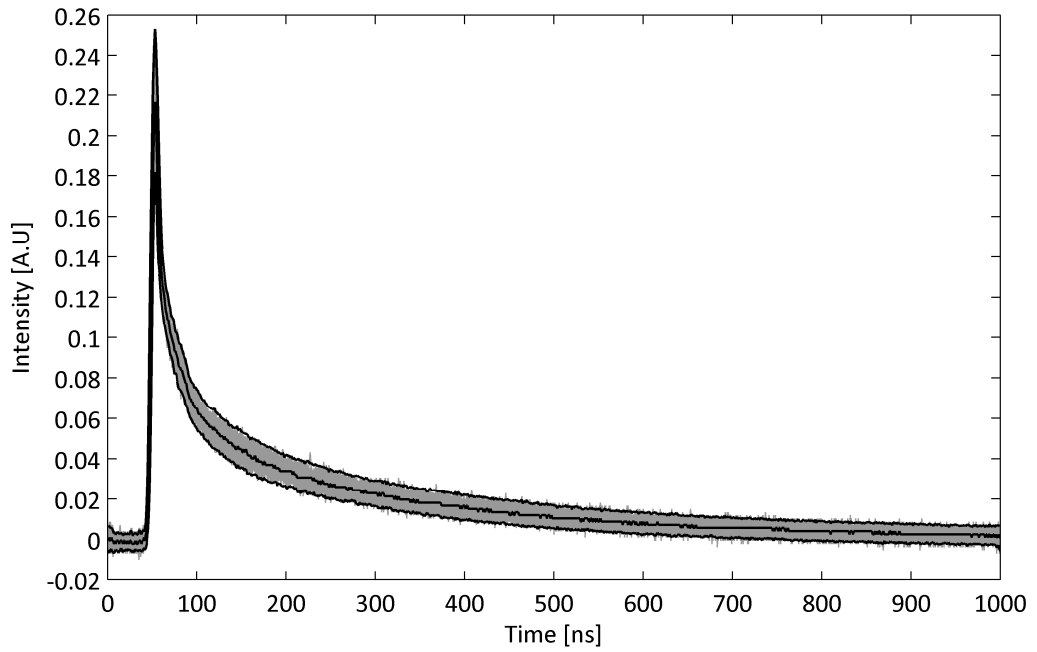


Figure 74 LII signal data and filtering profiles. Grey data: 488 nm spectrally filtered photomultiplier signal, central black line: median average, upper black line: mean plus two standard deviations, lower black line: mean minus two standard deviations.

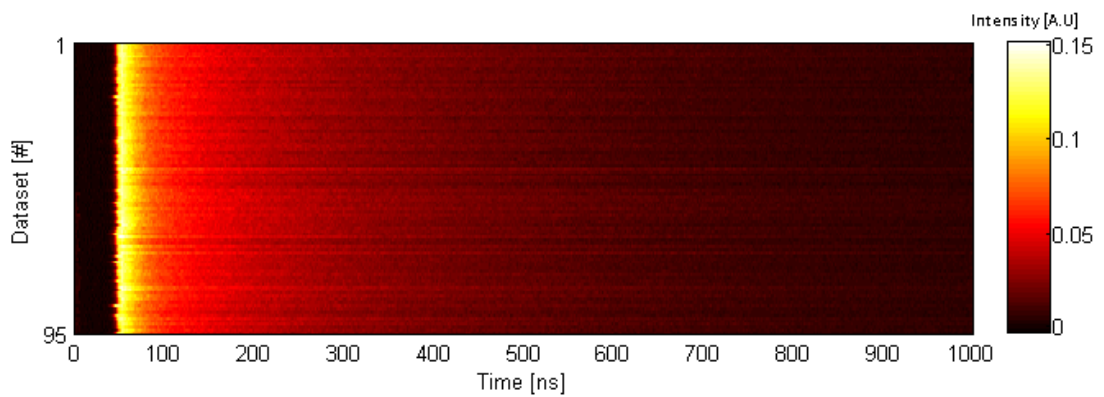


Figure 75 LII signal data, 647 nm spectrally filtered photomultiplier signals.

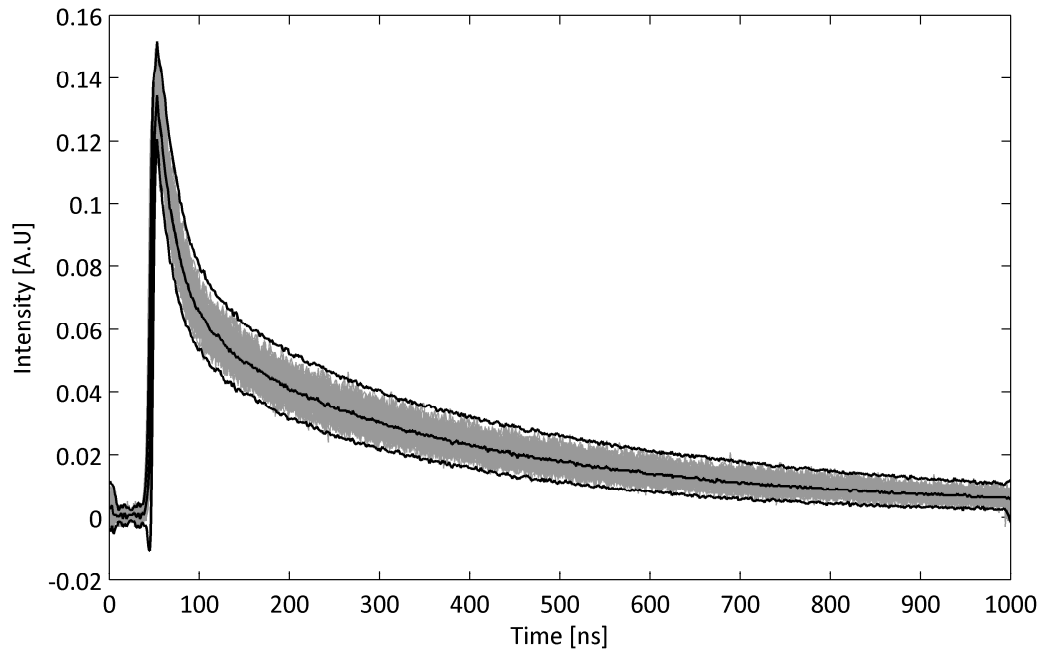


Figure 76 LII signal data and filtering profiles. Grey data: 647 nm spectrally filtered photomultiplier signal, central black line: median average, upper black line: mean plus two standard deviations, lower black line: mean minus two standard deviations.

Figure 77 presents the resultant ensemble averaged data point series of both spectrally filtered photomultiplier signals. Normalized to very nearly the same peak intensity, the more rapid decay of the 488 nm wavelength centred band-pass filtered signal is apparent, relative to that of the 647 nm wavelength centred band-pass filtered signal. Quantization error, particularly in the later part of the 488 nm signal is apparent due to the oscilloscopes analogue to digital (ADC) conversion resolution, the effect of which was manifest in the pyrometry ratio of the two signals and the subsequently calculated temporally varying temperature profile, presented in Figure 78.

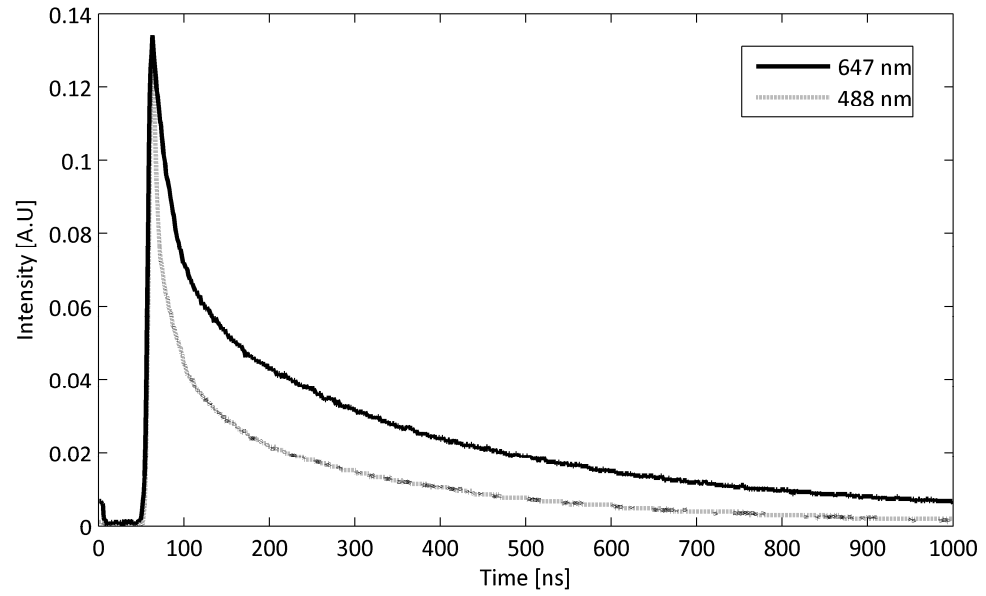


Figure 77 Normalized ensemble averaged photomultiplier signals due to LII emissions.

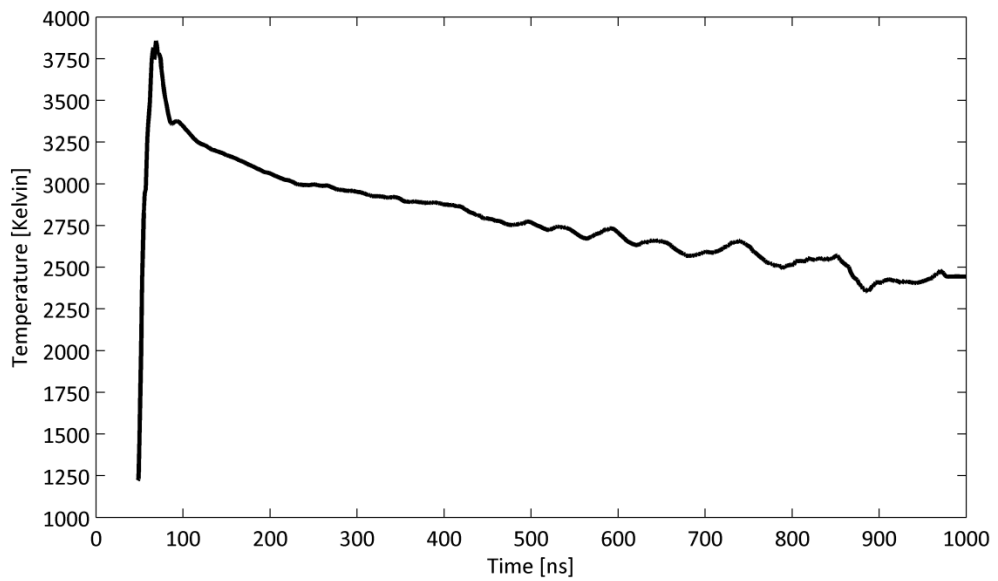


Figure 78 Calculated temperature profile of 50 mm HAB, 2.4mm radius punctual measurement location.

5.3.2 Primary Particle sizing (d_p)

The model developed in this study was applied to solve for the primary particle diameter whose temporal variation of temperature and therefore spectrally filtered radiance was consistent with that captured by the photomultipliers. A particle diameter of 33 nm was calculated for a multi-lognormal size distribution ($n=4$, $\sigma_1=0.2$ $\sigma_2=0.24$) at the punctual measurement location of 50 mm HAB, and at a radius of 2.4 mm, at the right side of the flame, upon which the laser sheet was first incident. Figure 79 illustrates the modelled fit to that of the experimentally obtained data.

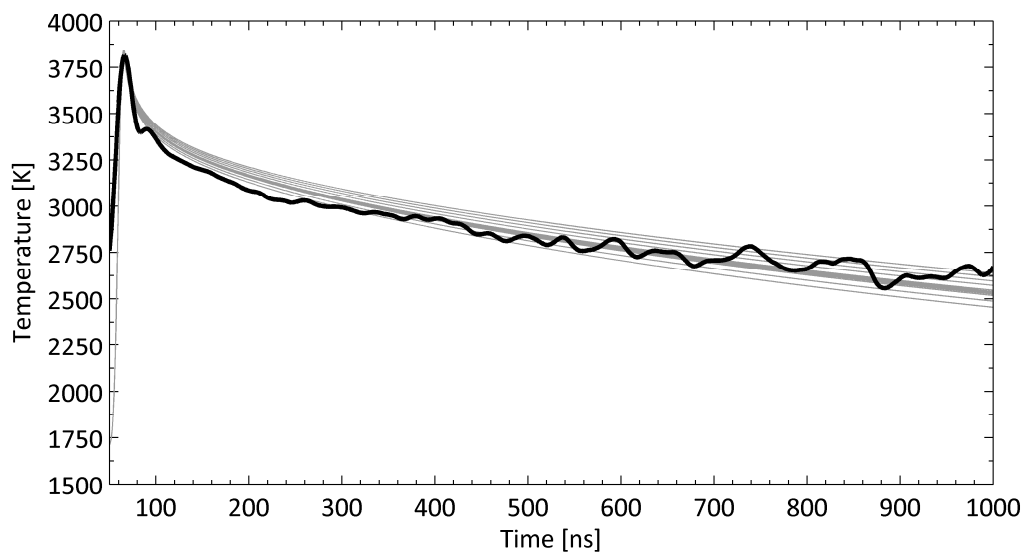


Figure 79 Fit of modelled temperature change with time (grey curves) compared to measured temperature change through time.

Successive iterations of the solution algorithm yielded a particle diameter distribution (black line) Figure 81. The range of all evaluated distributions are also shown (grey lines). The associated error term, the sum of the frame ratio weighted Chi^2 values ($\sum \chi^2$), is presented in Figure 80. A satisfactory convergence behaviour is illustrated. Figure 81 portrays the size distribution function associated with the modelled primary particle. For each modelled primary particle size, the associated particle population contributions of radiant emission are summed to calculate the total emission contribution for that particle size distribution.

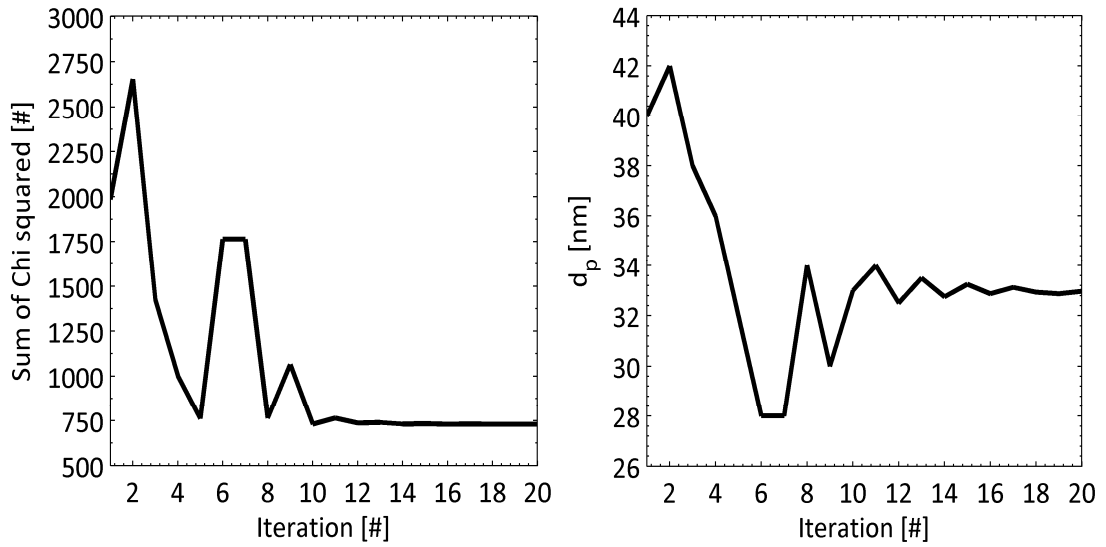


Figure 80 (Left) Variation of the sum of χ^2 ($\sum\chi^2$) with successive solution iterations. (Right) Variation of primary particle diameter (d_p) with successive solution iterations

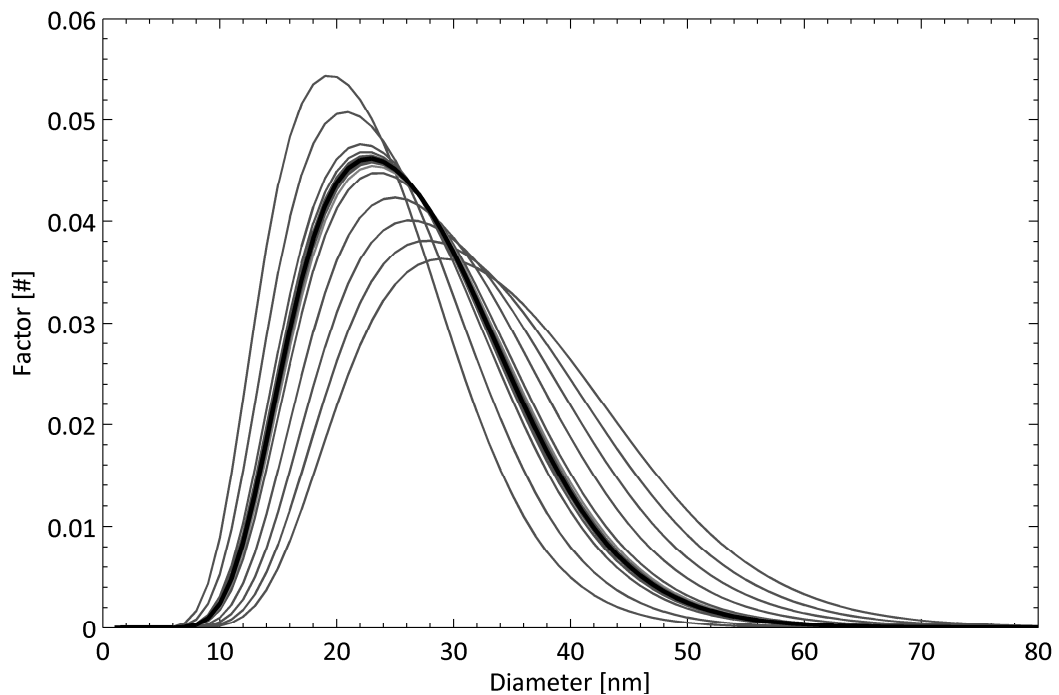


Figure 81 Variation of (area normalized) multi-log-normal particle size distribution function with successive solution iterations. Black curve denotes the final solution value ($n=4$, $\sigma_1=0.2$ $\sigma_2=0.24$, presented by (Schraml *et al.* 1999)).

5.3.3 2D-2C-TiRe-LII

The primary particle diameter (d_p) plots are presented for the staggered acquisition scheme experiment. They differ in the initial delay by 5 ns from the event trigger and thus represent differing acquisition schemes when regarding the distribution of radiation due to the LII, across the discrete exposure events. Both schemes however achieve a maximum signal in image four of sixteen and representative LII emission images for both schemes are presented first. Both schemes were performed as a means of investigating the effect of synchronization timing of the acquisition 'shutter' events relative to that of the phenomenon of interest.

5.3.3.1 LII signal

Presented herein are the resultant ensemble averaged (107 sets for the 295 ns initial delay acquisition strategy, 104 sets for the 300 ns initial delay acquisition strategy) LII images from image four of the sixteen image sequences. The first four camera exposure durations were set at 20 ns and both strategies yielded a peak of signal in the fourth image of the acquired sequences. The acquisition strategies differed by 5 ns initial delay from the experimental reference time signal. This increment of acquisition timing shift was selected because it represented both the minimum increment of adjustment, but more significantly, it ensured the resultant data from two different acquisition schemes could be compared in which the peak intensity LII radiant emission occurred in the same image of the sequence (image 4). This is significant because the variation of performance can then be attributed to the transient response of the commonly utilized, ICCD sensors.

The decay of the LII radiant emission intensity can be of sufficiently high rate of change that the intensity presented at the end of an exposure can be significantly differ from that at the start. A shift of 5 ns within a 20 ns exposure duration, in which the opening and closing phases likely deviate below the peak sensitivity, will therefore constitute differing convolution schemes of temporal variation of acquisition sensitivity and signal. Each pixel count value comprises the signal accumulation due to the convolution of the temporal variation of both the radiant emission and total detection path acquisition sensitivity for the particular ICCD sensor pixel.

The 300 ns initial delay data sets had the effect of moving the signal (relative to the 295 ns scheme) towards the start of the exposures duration of each image in the data capture sequence. This is significant because the most intense part of the radiant emission signal is therefore convolved with more of the opening phase of the camera shutter transition to fully open, peak sensitivity. Potentially, more of the signal is uncaptured and the significance of the shape of the opening phase transition has greater impact upon the captured signals, their ratio values and ultimately the point that the particle size model is driven to.

The presented images have been pre-processed to extract the signal from the total captured signal value. Typically, this comprises the signal of interest, as well as spurious elements such as 'bright' or 'hot' pixels, noise due to CCD sensor readout error, dark current and shot noise. Routines that remove spurious pixel values and replace them with nearest neighbour median values, as well as dark field characterization and subtraction, have been applied.

Ensemble median average data sets comprising 107 (295 ns) and 104 (300 ns) filtered and pre-processed data sets, are presented at 488 nm spectral band-pass interval (Figure 82 and Figure 83) and 647 nm spectral band-pass interval (Figure 84 and Figure 85). The ensemble averaged data is not entirely smooth and suggests a larger number of data sequences would have yielded data sets that were in-turn, more smoothly varying in solution values. The time required to capture and read out data from the camera assembly was significant, taking a minimum of three minutes between successive data sets. It was estimated prior to undertaking the experiment that one hundred data sets would constitute a reasonable balance between the laborious acquisition process and resultant data field quality.

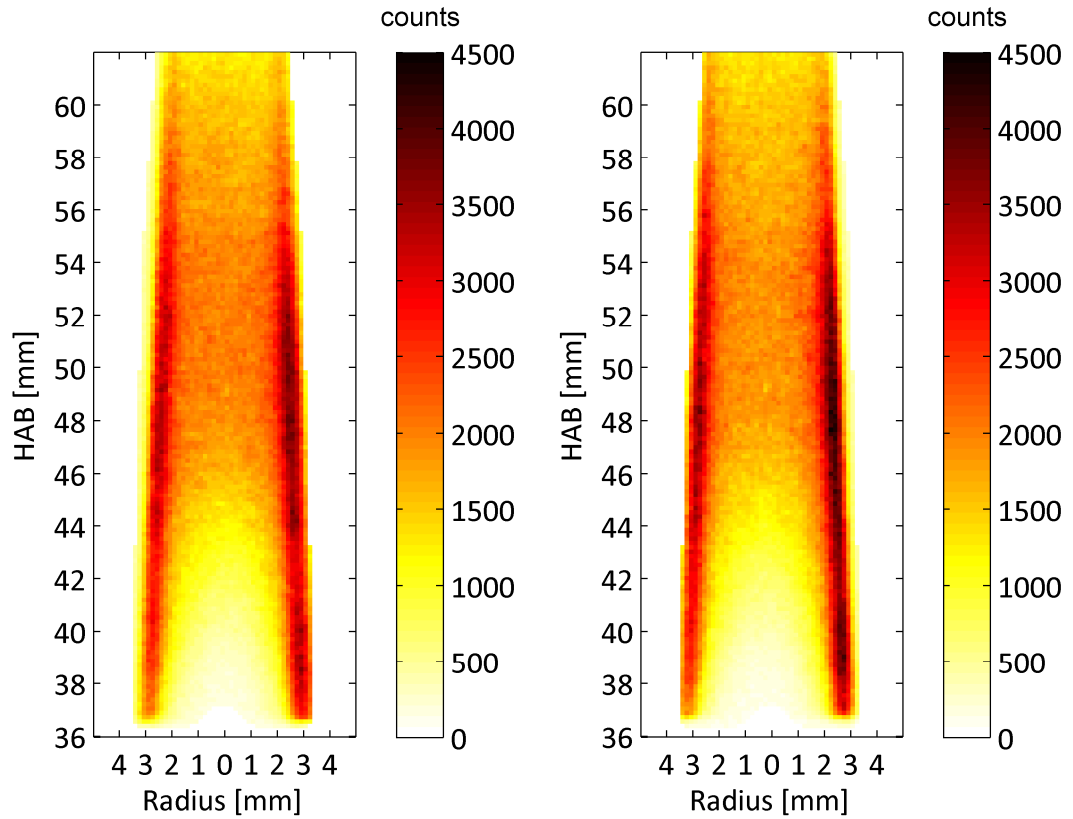


Figure 82 (Left) LII signal ensemble averaged (107 sets), through 488 nm centre wavelength spectral filter, 295 ns initial delay acquisition strategy

Figure 83 (Right) LII signal ensemble averaged (104 sets), through 488 nm centre wavelength spectral filter, 300 ns initial delay acquisition strategy

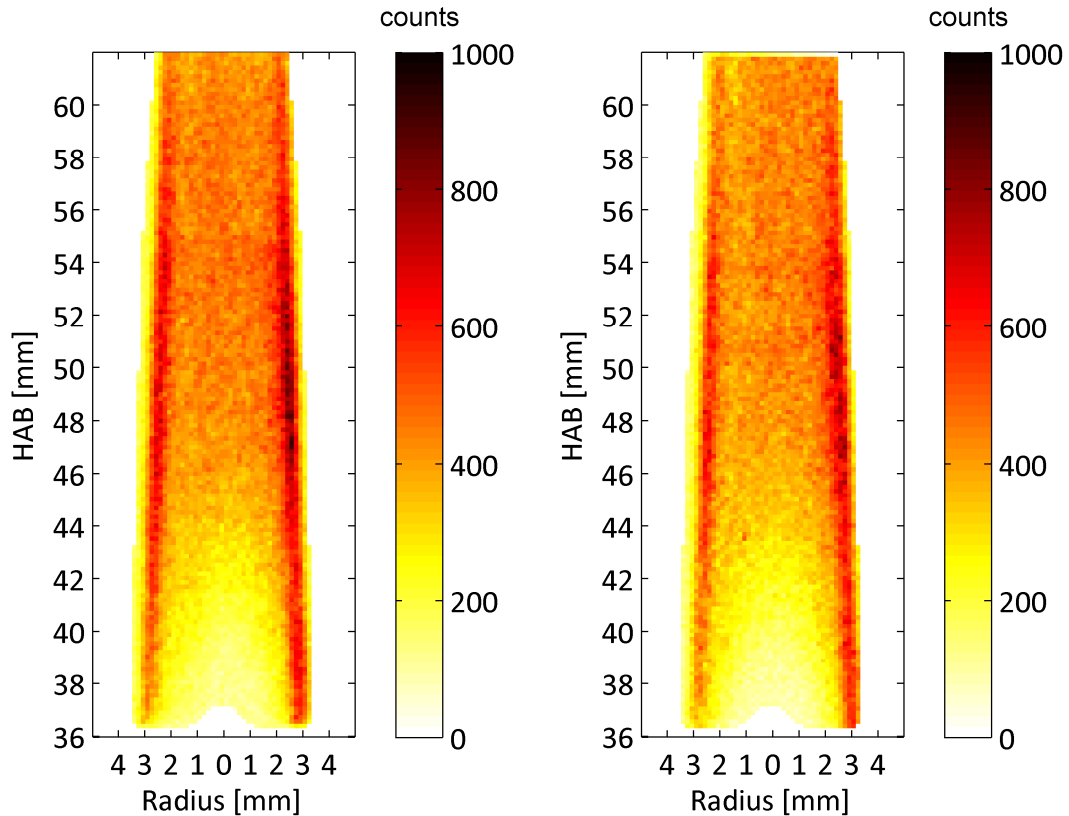


Figure 84 (Left) LII signal ensemble averaged (107 sets), through 647 nm centre wavelength spectral filter, 295 ns initial delay acquisition strategy.

Figure 85 (Right) LII signal ensemble averaged (104 sets), through 647 nm centre wavelength spectral filter, 300 ns initial delay acquisition strategy.

Figure 86 and Figure 87 present the primary particle diameters solution plots for the entire planar region of measurement. It is apparent that not all locations are resolved and in particular the upper region on the laser incidence (right) side. Peak soot diameter annular regions are apparent for both solution plots. An erroneous bias towards larger peak particles at the laser incidence side is also apparent.

Primary particle diameters for the horizontally disposed 50 mm HAB profile for 295 ns (Figure 88), and 300 ns (Figure 89) initial acquisition delay, are presented. A selection of profiles consisting of those that at an HAB of 50 mm \pm 0.5mm are presented in addition to averaged (mean and median) profiles.

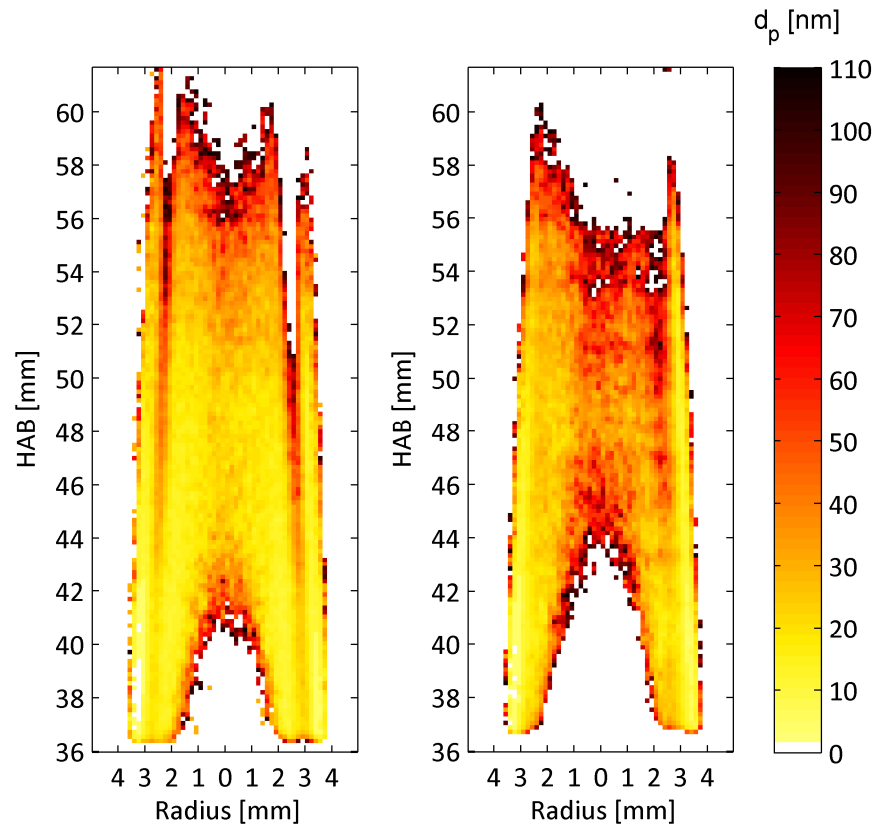


Figure 86 Primary particle diameters plot for (left) 295 ns and (right) 300 ns initial delay acquisition scheme.

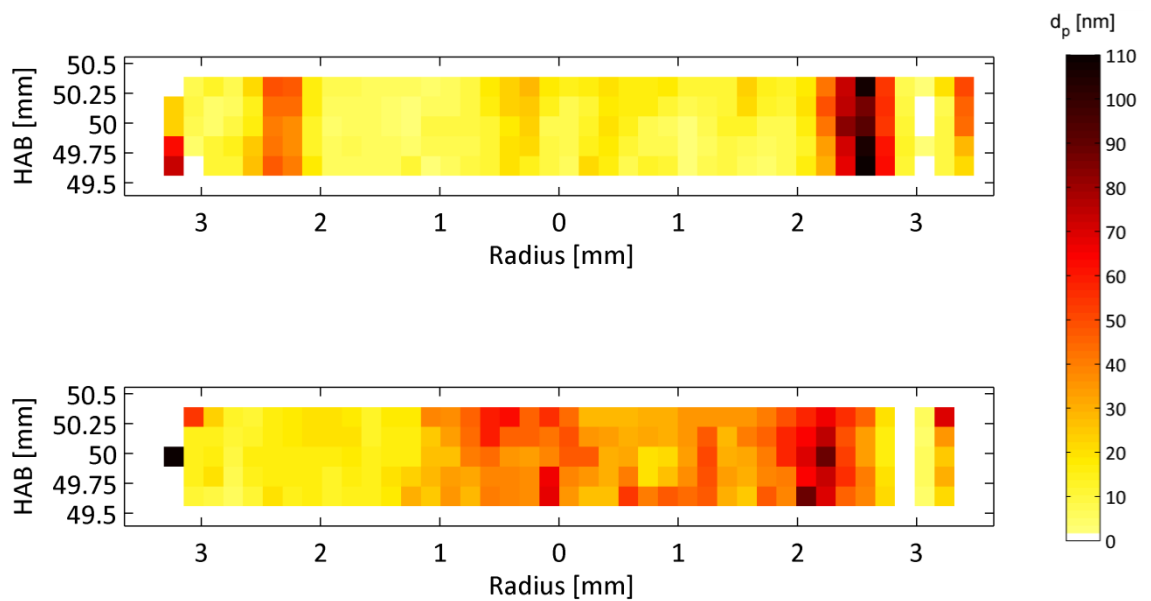


Figure 87 Primary particle diameters plot for (top) 295 ns and (bottom) 300 ns initial delay acquisition scheme data, for height span 49.67 to 50.33 mm HAB.

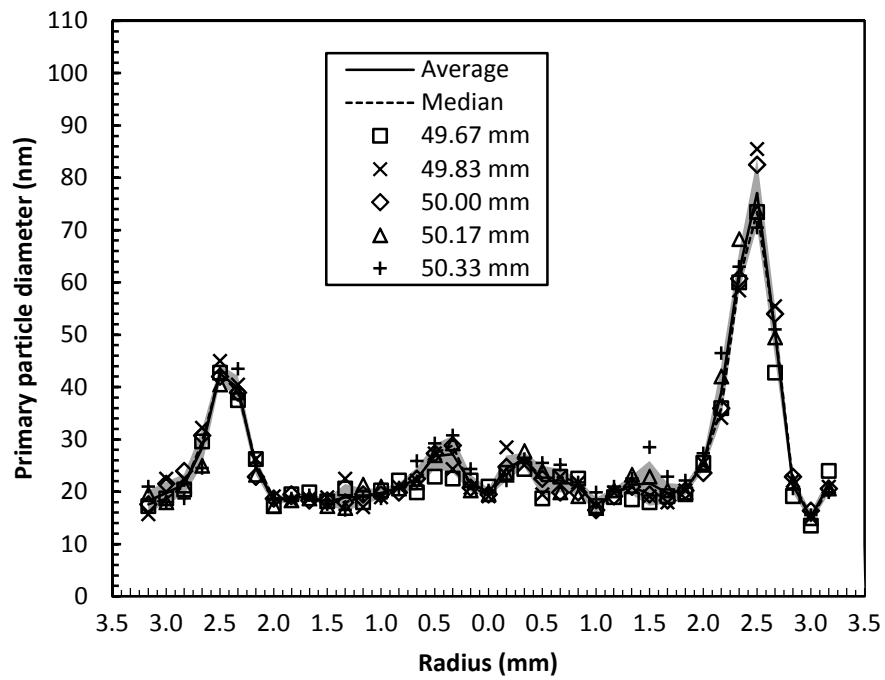


Figure 88 Calculated primary particle diameter versus radius for data centred around 50 mm HAB, captured using 295 ns initial delay acquisition scheme. The average (solid line) and median (dashed) data were calculated using a 3 column by 5 row window. The grey envelope bounds indicate the average values \pm one associated standard deviation.

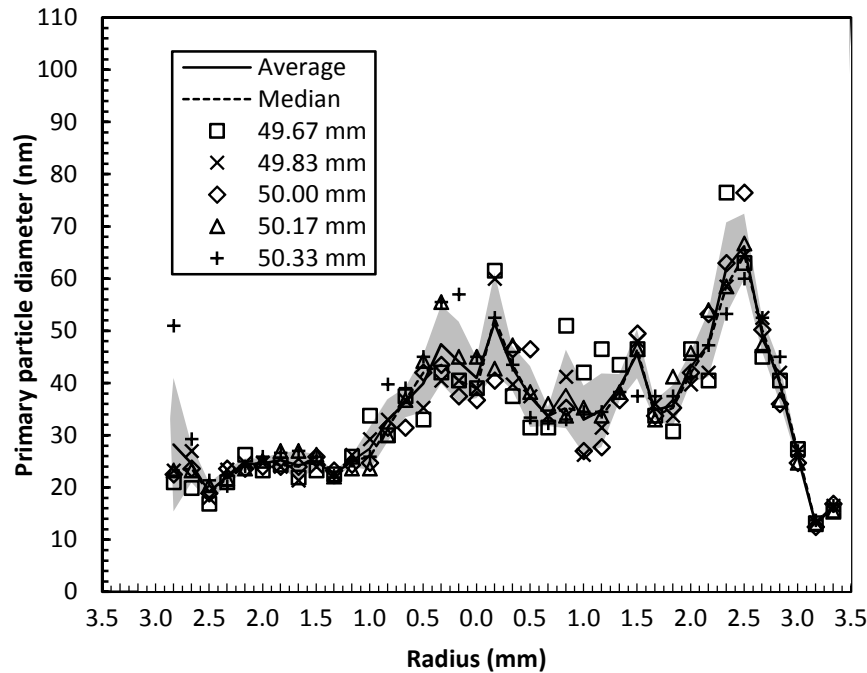


Figure 89 Calculated primary particle diameter versus radius for data centred around 50 mm HAB, captured using 300 ns initial delay acquisition scheme. The average (solid line) and median (dashed) data were calculated using a 3 column by 5 row window. The grey envelope bounds indicate the average values \pm one associated standard deviation.

It is apparent that the results produced by the technique are sensitive to the variation of acquisition synchronization. The principle consequence of which, is to vary the distribution of radiant emission between the camera images within the acquisition sequence.

The radiant emission is unchanged with change of acquisition parameters, but the distribution within the image sequence of the acquired signal does change with acquisition delay. The modelled radiant emission timing was adjusted for initial delay to match the experimental parameter and as such, the resultant calculated primary particle sizes should have demonstrated independence of acquisition scheme if the characterization of the shutter events were correct. It therefore is likely that the characterization of the camera acquisition is in error to some extent. The peak sensitivity of each frame, at each band-pass filtered spectral interval was satisfactorily characterized for long exposure durations. Uncertainty therefore remains as to the effectiveness of the

characterization of the transition from close to open and from open to close. As such, this aspect of the camera's transient response constitutes a significant parameter that warrants further work to more completely characterize its performance and therefore the impact upon its utilization for quantitative measurement.

5.3.3.2 No solution regions

Both plots exhibit regions in which the solver converged to unrealistic values (negative or very large diameter values). Consequently, and to aid clarity of interpretation of the likely valid data, the results have been filtered to reject values greater than 110 nm and less than 1 nm diameters. The values have been removed rather than replaced, and as such the blank regions of the solution plots portray the locations that the solver was unable to converge to realistic values. Although such a process could be interpreted as imposing a desired result, inspection of graphical output of solution iterations clearly illustrated the effect of spurious data ratios within a sequence of otherwise credible values, and the effect of driving the model towards a bound of the modelled solution space. As the bounds were approached, the model demonstrated an instability that resulted in an accelerated divergence away from the likely solution region. The utilized model of particle size solutions considered the particle size distribution spanning the range of 1 to 110 nm diameter. Where a presented data set comprised a sequence of data ratio values that qualitatively seemed consistent with a large particle solution, for example, 80 nm diameter, but with a seemingly spurious ratio from two significant signal intensity values (therefore the associated weighting factor would give significance to the ratio value), then the model solver would diverge off towards very large values within a few iterations. This was in part due to the bounds of modelling the contribution of the particle size interval. As the solution moved towards one extreme of the span, the multi-lognormal size distribution curve would have an increasingly significant proportion of its span outside the summed particle radiant emission contribution span. So, the effect of this was for change of the modelled ratios to plateau, stop changing with successive particle diameter guess iterations. This represents an area of the modelling that could be improved upon to eradicate solver instability.

Regions of high signal gradient across the plane of resolution were most sensitive to the spatial registration between both the two spectrally band-pass filtered image sequences

and the images within each sequence. Consequently, some regions presented ratios to the solver that were not representative of the radiant emission signal ratio emanating from a location of interest; the solver diverged to values outside of plausible solution values. Regions in which a high gradient of signal across the solution plane occur (such as the transitions either side of the 2.4mm radius location for 50mm HAB), were therefore inherently more sensitive to misalignment or erroneous registration between contributing data points.

5.3.3.3 Distribution

Both acquisition strategy solution plots exhibit a distribution of primary particle diameter that show a peak primary particle diameter at radii consistent with studies elsewhere and the theoretically defined region of laminar diffusion interface between the fuel phase and the oxidative co-flow medium. Both indicate some degree of symmetry of soot structure, although the magnitudes of primary particle diameters typically are not symmetric about the flame centre line. Considering the two peak primary particle diameter regions at 2.4mm radius of the 295 ns initial acquisition delay results data, a bias toward larger particles is demonstrated on the right side (70-80 nm at 50 mm HAB) of the soot structure relative to those calculated at the same radius on the left side (40-50 nm at 50mm HAB). Since the flame and the resultant soot structure are axially symmetric, the planar region with which the laser sheet is incident must necessarily constitute a symmetric plane of distribution of particle sizes. Errors in the calculated values are therefore certainly demonstrated in that an internal consistency of the technique is not demonstrated. The cause of the erroneous results is not conclusively defined in this study. The effect upon the calculated primary particle diameter due to any error in the calculation of local laser fluence value may be the cause. An alternative cause may be related to error in the ratio values sequence presented to the solver due to signal to noise ratio variation. The laser sheet propagates from right to left of the resolved plane, and its local fluence is progressively attenuated as energy is absorbed by the particles along the path of propagation. Accordingly, the particles on the right side absorb more energy than those at the same radius on the left side. Since an asymmetry of internal energy within the particles occurs, an associated asymmetry of radiant emission of energy also occurs. This asymmetry of signal intensity should be nullified due to the utilization of the ratio of two spectral band-pass filtered signals. The ratio of radiant emissions is independent of degree of excitation (providing no significant variation of sublimation occurs across the soot

structure). Since the calculated primary particle diameters do not demonstrate a strong symmetry about the central axis of the flame and soot structure, it is possible that the inherent trend of reduction of signal to noise ratio from right to left may have presented ratio value sequences that deviate from the reality of the ratio of spectrally filtered radiant emission. In particular, a shift towards smaller primary particle diameter solutions seems apparent in the 300 ns initial acquisition delay results data.

5.3.4 Comparison of punctual location (2C-TiRe-LII) with planar (2D-2C-TiRe-LII) results

The profiles presented in Figure 90 illustrate the comparison of the results obtained and presented by (Oger 2013) for the same burner using a calibrated LII/ELS technique, to those of this study. Both the 295 and 300 ns initial acquisition delay data show peaks radially disposed at approximately 2.4mm diameter, in agreement with the results by (Oger 2013). The 295 ns initial acquisition delay data is the most similar in terms of radial distribution characteristic, although considerable asymmetry of magnitude is apparent.

The primary particle diameters measured by the 2D-2C-TiRe-LII technique with the 295 ns delay demonstrate some aspects of concurrence with the results by Oger (2013). For small flame radiuses (less than ± 1 mm on Figure 90), an average of approximately 20 nm is presented, albeit with a globally erratic variation imposed upon it. However, significant difference is apparent at the periphery of the flame. This may be attributed to the sensitivity of the 2D-2C-TiRe-LII technique to errors in the spatial registration of each image pair. Indeed, when strong LII signal gradients occur, as is the case at the periphery of a Santoro type burner, small errors in spatial registration can lead to relatively large differences in the ratio between the two LII filtered signals. Additionally, fluorescence may be manifest towards the periphery of the flame due to the excitation of PAH's and this should be an aspect addressed in future research.

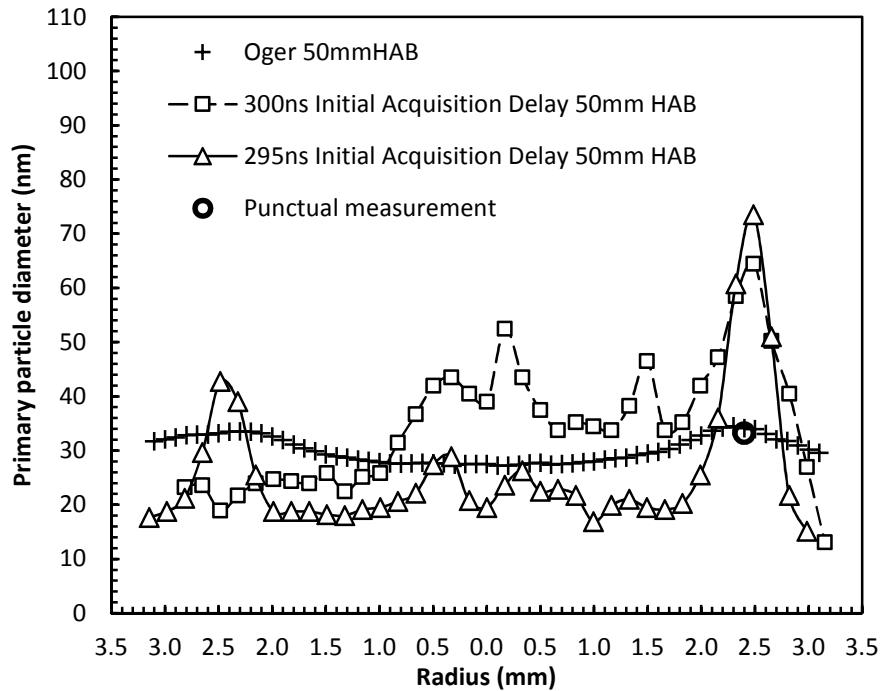


Figure 90 Comparison at 50mm height above burner (HAB) of the variation of primary particle diameter (d_p) with variation of radius from the flame centreline.

5.3.5 Discussion

Figure 90 presents the 50 mm HAB primary particle radius for both acquisition delay schemes of the 2D-2C-TiRe-LII undertaken in this study and compares them with previous results obtained (Oger 2013) in which a calibrated LII/ELS technique was employed upon the same laboratory burner. The first point of contrast is the erratic particle radius results achieved in this study when compared to the smoothly varying results of the LII/ELS technique. The harvested LII data, both before and after processing demonstrated a wide standard deviation of values when expected similar sized particle regions of the signal were compared.

A variation of particle radii between 15 and 52 nm, with an average in the order of 30 nm (across both acquisition schemes) is apparent in the central region (Radius < 2 mm) of the flame soot structure. For the 295 ns acquisition delay data, an average error magnitude of 26% relative to the previously published LII/ELS data, and 35% for the 300 ns acquisition delay data was realized. The central region contains the smallest spatial rate of change of soot volume fraction and LII signal. It therefore provides a region in which

the consequence of spatial alignment errors of registration between images, and between the two spectral filtered channels, is minimized. As such, it ought to present the most easily resolvable primary particle sizes of the data field. This was not manifest in either the recorded data or consequently, the calculated primary particle sizes.

The reasons for this are unknown and may be speculated upon. The SNR of the acquired data was unfavourably low through the central span, and the characterization and subtraction of obfuscating emissions may have been inadequate. These could include acquisition artefacts due to the ICCD, or possibly fluorescence from PAH's or radicals (OH, NO) that persisted with sufficient intensity to manifest within the sequence of data used for modelling. The latter point however, might be expected to present as obfuscating emissions predominantly in the earlier images of the selected, however inspection of the data sequences suggested that this was not the case, with the most erratically varying pixel intensity values (from one frame to the next) occurring in the later frames of the sequences. Characterization of the standard deviations of the various erroneous signal contributions would aid understanding of the seemingly erratic calculated particle sizes.

The peak signal regions and the associated high spatial gradients of signal intensity (which are not negligible compared to the camera's optical resolution) highlight the data processing sensitivity to registration errors. This, in conjunction with any signal contribution from obfuscating emissions, particularly those from constituents that likely manifest in regions of high soot concentration resulted in significant variation and overestimation of particle sizes. Relative to the previously published LII/ELS data or the punctual TiRe-LII calibration data point, the 295 ns acquisition delay data yielded an average error magnitude of 53% in the 2 mm > radius > 3 mm interval of the 50 mm HAB profile. In the same interval, the 300 ns acquisition delay data yielded an average error magnitude of 55%.

In spite of the seemingly noisy or erratic variation of particle radius, particularly relative to a more direct technique (calibrated LII/ELS, for example), the resultant particle sizes are within a size interval, that whilst not particularly encouraging, demonstrates a sensitivity to variation of particle size of the subject of measurement. Refinement of aspects of the experimental scheme to which the solution algorithm demonstrated greatest sensitivity, may likely yield more accurate and smoothly varying results.

The asymmetry of the presented particle diameter profiles in Figure 90 and the planar data of Figure 86 and Figure 87 may be attributed to several causes. Whilst the flame structure is rotationally symmetric and therefore inherently symmetric in planar section, the laser sheet traversed the flame from right to left and in doing so, presented a local laser fluence value that varied across the flame. The calculation of the localized fluence therefore represents a source of uncertainty: The bulk extinction across the soot structure was measured and a symmetric distribution of extinction contribution modelled.

The asymmetry of laser excitation was contended with by calculating a map of laser fluence that was then used in the particle heat transfer model within the solution algorithm to calculate particle diameter. An unavoidable aspect of this is the inherent asymmetry of SNR of the LII data. The soot on the more extinguished side of the flame is heated to a lower peak temperature by the lower fluence laser. This produces lower intensity value LII data that necessarily has a lower SNR value. Since the search algorithm demonstrated sensitivity to noise, the comparatively low signal intensity region of the LII data field corresponds to the least well resolved particle diameter values.

The 2D-2C-TiRe-LII technique, as implemented, is sensitive to timing errors and spatial registration uncertainties. The sensitivity to spatial registration uncertainties was unavoidable in the setup, since the image pairs could not be registered with sub-pixel accuracy across the full field of view. This aspect could be addressed by replacing the camera and image doubler with two separate ultra-fast framing cameras and a beam splitter. Such an approach was not financially viable at the time of this study.

5.4 Application to high pressure diesel combustion

The application of 2D-2C-TiRe-LII on a high pressure rapid compression machine served two distinct purposes. Firstly, it is to investigate the efficacy of the technique at realistic engine conditions, specifically in terms of elevated ambient pressure and temperature within the combustion chamber. The realistic engine conditions constitute a change of Knudsen regime from 'transition' to 'continuum'. This necessitates a change of the mathematical expressions of the heat transfer terms in which inter-molecular proximity affects the overall rate of energy transmission through or from a medium, as well as the rate of sublimative material transport. Uncertainty exists as to the degree of correctness of these alternative heat transfer expressions; in part due to the challenging experimental conditions required in which to validate them. Accordingly, comparatively few studies that rely upon these expressions have been disseminated to date. Therefore, the investigation of the efficacy of the application experiment compounds issues of the experimental technique with those of the validity of the underlying mathematical formulations used.

The second purpose of the application experiment is to ascertain whether changes to the combustion system, specifically, in-cylinder pressure (ICP), fuel injection rail pressure (P_{rail}), and acquisition timing relative to the combustion event reference (T_{Ref}), produce discernible and credible differences between the resultant data for different combustion event conditions. In this sense, the absolute values of primary particle diameters resolved are less important than demonstrating the techniques' sensitivity to variation of the evolution of incandescence radiant emission, and therefore the ability to distinguish between primary particles of different sizes.

5.4.1 Example of experimentally acquired data

Since there exists a fair degree of abstraction between the experimental data that was recorded and the resultant primary particle diameter data field plots, it is informative to review the experimentally obtained data, if only such that subsequent experimentation undertaken with the aim of validating or extending the work presented here, may be conducted with greater certainty as to the consistency of each step of the process.

5.4.1.1 LII data

An example series of LII images, captured at both 592 and 750 nm wavelength centred band-pass filters, are presented in Figure 91 and Figure 92. The images, in common with the subsequent presentation of LII data throughout this chapter, are presented as inverted 12 bit depth luminescence monochrome images. It is apparent from inspecting both Figure 91 and Figure 92 that the sequences do not adhere to an intuitive notion of decreasing intensity progressing through time, from left to right. This is due to the variation of sensitivity of the individual camera and intensifier assemblies, each of the sixteen assemblies recording a pair (one from each filtered channel) of images. Typically a luminescence calibration is performed such that the presented images appear to demonstrate the expected near exponential characteristic decay of signal intensity. As addressed previously (4.1.5 and 4.1.6), a single calibration cannot be applied since a temporally varying sensitivity of the camera and intensifier assembly is necessary in order to model the convolution of temporally varying signal with that of temporally varying acquisition sensitivity. Only then can the accumulated count values read out from the potential wells of the CCD be correctly utilized to calculate the temporally varying radiant LII emission. The first three images of each sequence are omitted since they precede the LII signal. Scales and labels are omitted to aid clarity but are consistent with all subsequent spatial scales presented herein.

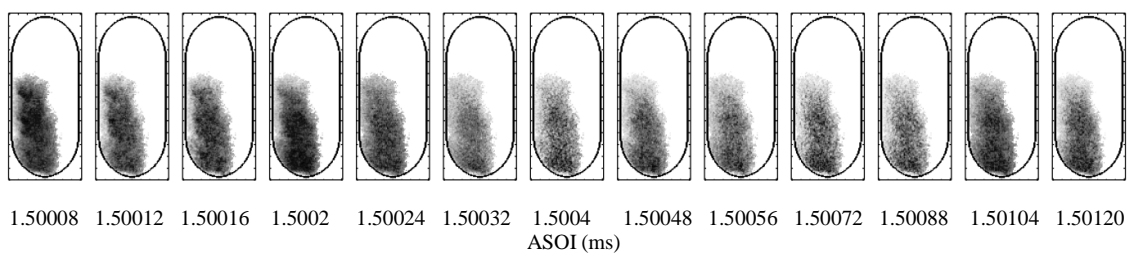


Figure 91 LII image sequence (images 4 to 16) filtered via 592 nm wavelength centred band-pass filter.

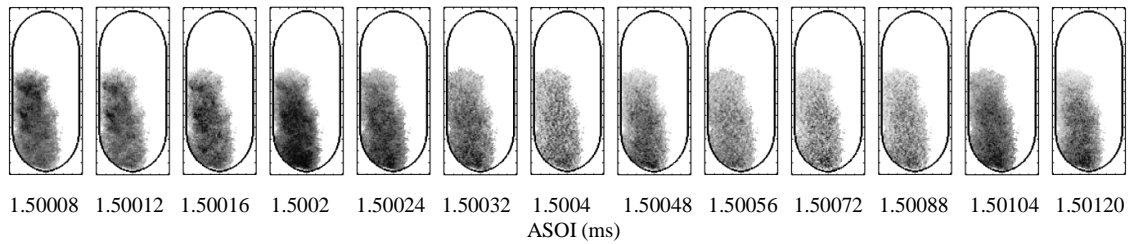


Figure 92 LII image sequence (images 4 to 16) filtered via 750 nm wavelength centred band-pass filter.

5.4.1.2 Extinction data

The algorithm used to solve for primary particle diameters across the resolved spatial plane modelled the effect of the laser fluence incident upon the particles. A laser fluence incident upon each location within the resolved spatial plane was defined through the employment of a model that characterized the ray-wise extinction of the incident laser. A laser fluence map of values was therefore produced for each soot structure of each data set sequence. To achieve this, an auxiliary branch of the experimental setup was configured such that an unextinguished intensity profile of laser fluence entering the optical access measurement chamber was captured along with the extinguished, post optical access chamber, intensity profile. The energy profiles were extracted from a simultaneously captured image (to the main LII emission capture) of two cuvettes (Figure 93, left), each containing the same concentration Rhodamine 590 fluorescent dye in solution with Ethanol. The intensity distribution of the fluorescence emissions were in proportion to the intensity distributions of the incident laser sheets, such that the unextinguished and extinguished intensity profiles were quantified from the images. (Figure 93, centre-right and right). The extracted fluorescence intensity profiles were used to calculate an extinction profile for the ray-wise integrated soot structure. An extinction distribution was calculated along each ray path and a planar resolved extinction map constructed. A resultant local laser fluence value was then calculated at each location within the planar region such that it conformed to the distribution of extinction associated with the distribution of soot concentration, as well as the fluence values prior to, and post, the soot plume (see sections 2.8 and 3.4.3.4 and 4.2.2).

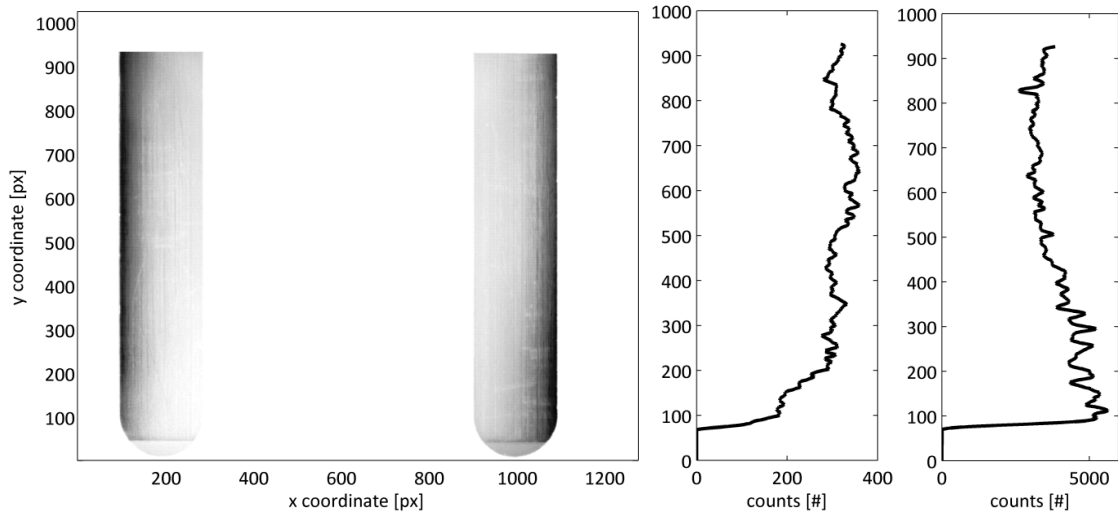


Figure 93 Example fluorescence emission of Rhodamine 590 dye contained in two mounted cuvettes (left). Example extracted profile of fluorescent intensity excited by extinguished laser sheet (centre-right), and fluorescent intensity excited by unextinguished laser sheet (right).

5.4.1.3 ICP pressure trace and capture event.

In-cylinder pressure and other key RCM operating parameters were data logged to provide thermodynamic context and timing data for the subsequent LII processing to yield particle sizing, but also to allow the effect of variation of operating parameters to be characterized. Figure 94 illustrates a typical operating condition of 40 bar in-cylinder pressure (when motored), with the typical cycle to cycle peak pressure variation illustrated (inset) for the fired condition.

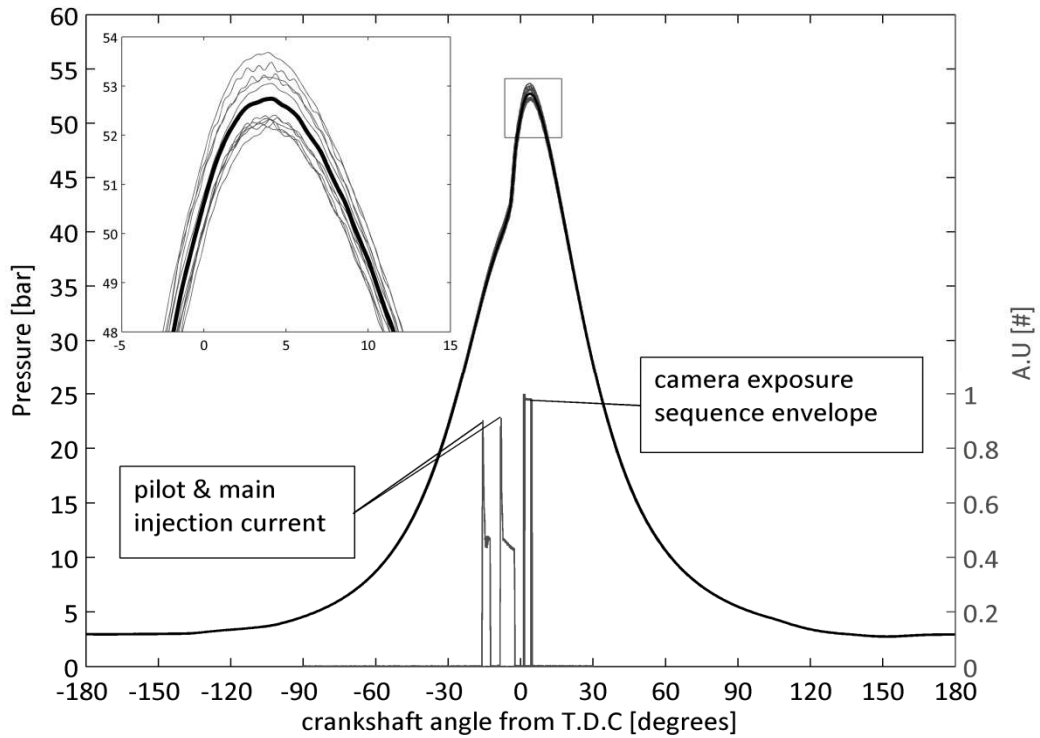


Figure 94 Example in cylinder pressure trace (ICP) resolved by crankshaft angle from TDC. Inset plot shows detail of peak pressure traces for ensemble cycles (grey) with average trace (black).

5.4.2 Ensemble average data set results

The median average of ten sets of LII radiant emission data sequences were used for each resultant primary particle diameter data field. The LII radiant emission data sequences therefore represent a spatial average of the stochastically varying combustion cycles, and resultant flame and soot structure. The meaning of such data is informative of the cycle to cycle variation in the spatial distribution of the soot structure and the distribution of primary particle sizes within it.

Presented herein are the resultant primary particle diameter false colour plots organized thematically to illustrate the effect upon the result values of the variation of the in-cylinder pressure (ICP), the fuel injection system rail pressure (P_{rail}), and the variation of the acquisition timing (T_{Ref}) relative to a fixed, common timing signal calculated from the engine crank angle and instantaneous shaft speed.

5.4.2.1 Variation of acquisition timing (T_{Ref}) for ensemble averaged data.

Variation of the T_{Ref} value and therefore the synchronisation with the combustion event (Figure 95), was investigated experimentally with the aim defining a span of T_{Ref} values in which the combustion events consistently occurred within the field of view of the acquisition optical access. It was determined that as T_{Ref} was increased, the soot structures persistence was principally toward the lower region of the optical access chamber.

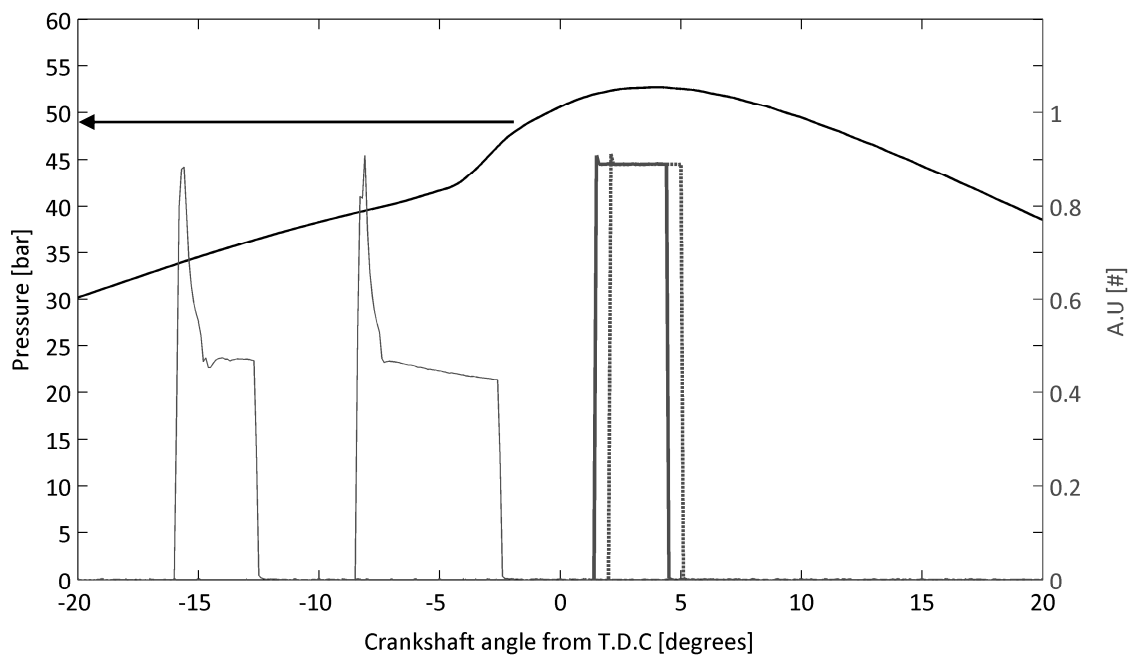


Figure 95 Combustion event and acquisition signal synchronization. Injection driver current pre and main pulses (thin lines) and the corresponding in cylinder pressure trace (smooth continuous line). The trigger pulses T_{Ref}=1.5 ms (thick black line) and T_{Ref}=1.7 ms (dotted line) respectively place the acquisitions after the diffusion flame combustion phase.

Figure 96 presents the primary particle diameter maps for the environmental conditions of ICP=40 bar, P_{rail}=1000 bar and with a variation of acquisition time of 0.2 ms. A spatial progression toward the lower region of the optical access chamber with later acquisition timing (increased T_{Ref}) is demonstrated.

The data suggests the region of maximum primary particle diameter is within the core of the fuel spray plume furthest from the injector nozzle. This is consistent with the rationale that increased residency time and relative scarcity of oxidative medium yields the most favourable conditions for soot particle inception, growth and agglomeration.

The variation of particle size across the horizontal dimension of the structure presented in Figure 96, for both conditions, suggests that the right most side of the structure has not been resolved, rather than a real structural asymmetry occurring. This is most likely due to the extinction of laser fluence such that the excitation of the right side soot particles was insufficient to demonstrate significant incandescent radiant emission, or that the sensitivity of the acquisition apparatus was insufficient to resolve it. The particle sizes of the left most region are biased towards the small sizes. If this represents real phenomena, then the right most side would also be constituted of comparatively small diameter particles. The combination of the lowest local laser fluence and the most rapidly decaying LII radiant emission signal characteristic of the smaller particles may have contributed to the insufficiently intense signal, and its occurrence not being detected.

Both solutions present an ensemble average soot particle structure and in doing so, provide a sense of the likely spatial distribution of the soot plume at that point in the combustion event. The later acquisition results ($T_{Ref}=1.7$ ms) show a rapid movement of the soot plume towards the lower edge of the field of view. This may not be attributed to the momentum of the injected fuel plume, since the injection was completed well before the LII acquisition.

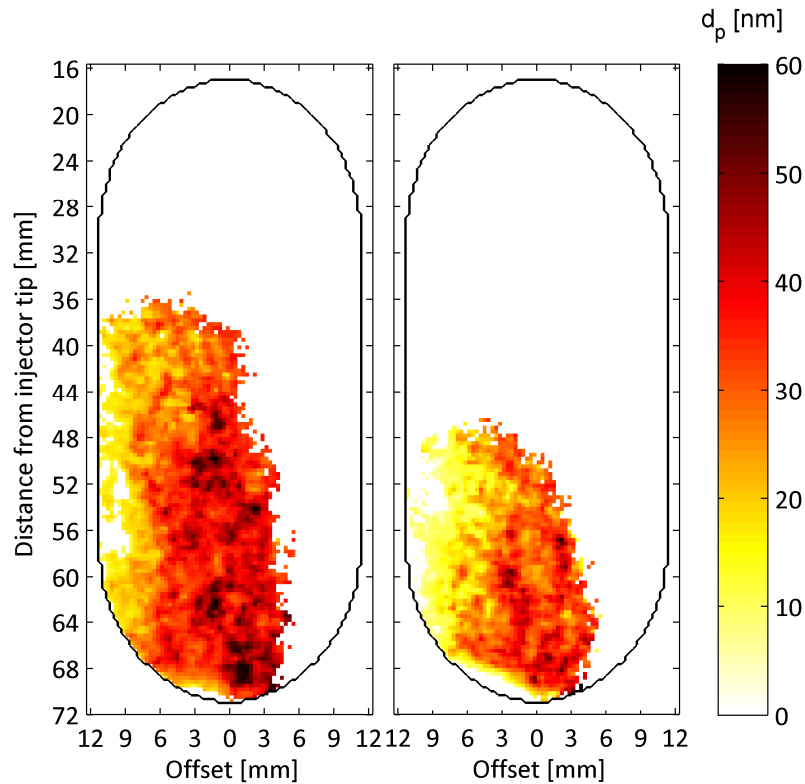


Figure 96 Primary particle diameter (d_p) false colour maps for ICP=40 bar, $P_{\text{rail}}=1000$ bar, at $T_{\text{ref}}= 1.5$ ms (left) and 1.7 ms (right).

The normalized by peak signal intensity, late image sequence images of Figure 97, represent a means of distinguishing, albeit in a crude and non-linear proportioned way, between particles that present a more or less persisting radiant emission signal and therefore between larger and smaller particle locations. The comparison with the calculated primary particle diameter map shows a broad agreement of overall structure when regarding the bias towards larger particles towards the central vertical axis. A trend from small to large particle diameter is apparent also from top to bottom for both conditions and is manifest in the calculated primary particle diameter data.

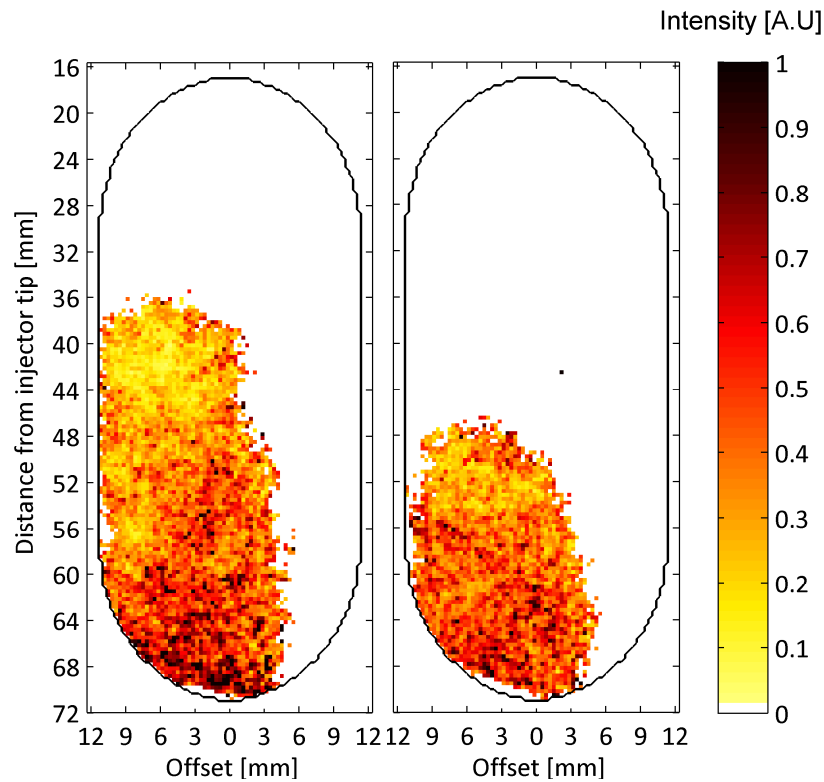


Figure 97 Peak intensity normalized late LII image. $T_{Ref}=1.5$ ms (left) and 1.7 ms (right).to characterize degree of persistence of LII radiant emission; greater intensity corresponds to larger primary particles, lesser intensity to smaller primary particles.

The comparison of histograms of primary particle sizes for both acquisition timing schemes is presented in Figure 98. A similar distribution of particle sizes is apparent with both conditions presenting a bimodal distribution, with modes of approximately 10 and 30 to 35 nm diameters. The 10 nm mode is addressed in section 5.4.4.1. The remaining likely true mode values are similar with perhaps the slightest bias for the latter acquisition ($T_{Ref}=1.7$ ms) towards 30 nm. The measurements presented in Figure 98 may indicate a rapid late-cycle oxidation process since spatial relocation of the soot plume to such an extent would seem unlikely given that momentum of the injection plume would have previously dissipated.

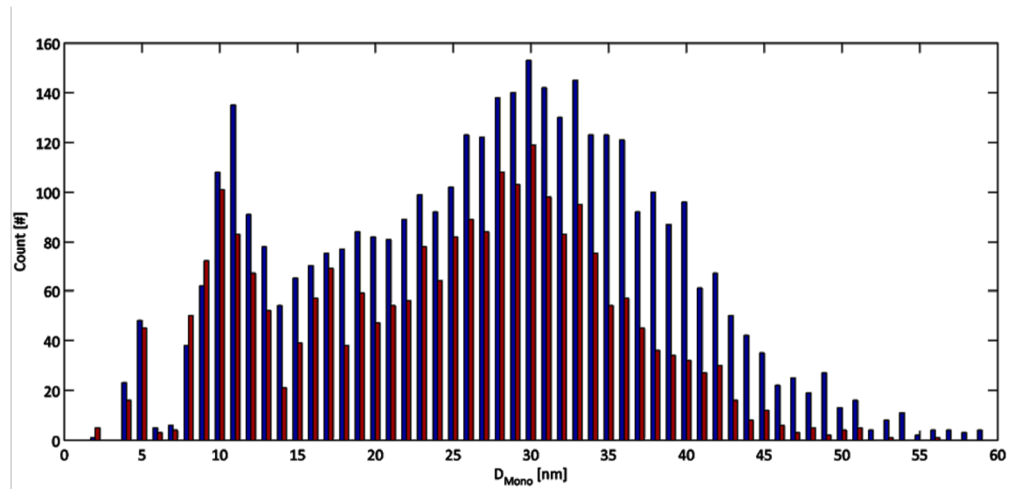


Figure 98 Histograms of primary particle diameter (D_{Mono}) for $T_{\text{Ref}}=1.5$ ms (blue) and $T_{\text{Ref}}=1.7$ ms (red).

5.4.2.2 Variation of fuel injection rail pressure (P_{rail}).

An increase of fuel injection rail pressure produces finer fuel droplet atomisation which increases homogeneity within the fuel spray plume. The increased abundance of local oxidative species is attractive because it aids more complete combustion and reduces the global soot volume fraction and particle sizes. Figure 100 presents the primary particle diameter maps for three fuel injection rail pressures and demonstrates an increasing bias toward smaller primary particle diameters with increasing pressure.

The timing of the acquisition was necessarily optimized to position the soot structure within the acquisition optical access field of view. The previously established variation of position within the combustion chamber with the variation of the synchronization was exploited to maintain the combustion and associated soot plume within the field of acquisition. This aspect represents a compromise imposed by the experimental apparatus. It is therefore unclear as to the balance of contribution to the reduction in primary particle size being from fuel injection rail pressure and earlier acquisition with the associated reduction of soot particle residency time. Figure 99 portrays the variation of injection timing duration necessary to deliver the same quantity of fuel for different injection rail pressures. Adjustment of the acquisition timing ($T_{\text{Ref}}=1.5$ ms for $P_{\text{rail}}=1000$ bar, $T_{\text{Ref}}=1$ ms for $P_{\text{rail}}=1300$ bar and $T_{\text{Ref}}=0.66$ ms for $P_{\text{rail}}=1600$ bar), all at 40 bar ICP, for the soot structure to remain within the field of view is also apparent.

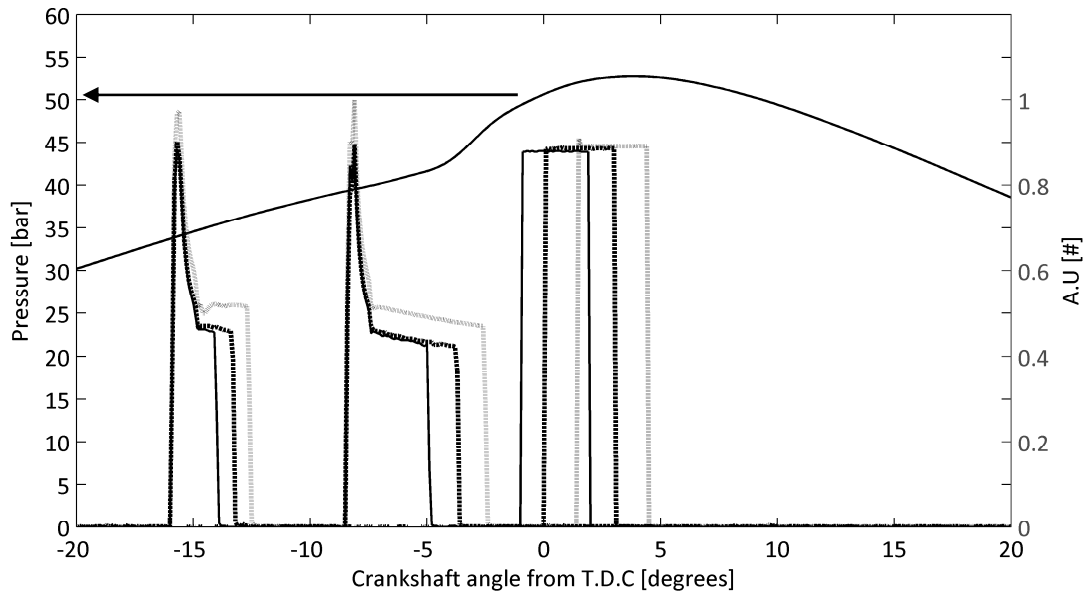


Figure 99 Combustion event and acquisition signal synchronization. $P_{\text{rail}}=1000$ bar (grey line), $P_{\text{rail}}=1300$ bar (black dotted line) and $P_{\text{rail}}=1600$ bar (black line), for both injection current driver pre and main pulses. An example fired in-cylinder pressure trace is presented although slight variation with injection timing variation is likely.

Figure 100 shows the variation of ensemble average soot structure for a variation of injection rail pressure, P_{rail} . Successively earlier acquisition timings were required as the injection rail pressure was increased. An undesirably convoluted scheme is therefore presented in which the effect of variation of injection rail pressure, is not isolated.

As fuel injection rail pressure is increased, so the duration of injection necessarily decreases in order to deliver a consistent quantity of fuel. Since the injection start point crankshaft angles are the same for each condition, the end angles are necessarily different; accordingly the end times. The adjustment of the acquisition timing (earlier with increase of fuel injection rail pressure) was necessary to maintain the soot plume location within the field of view.

Figure 101 shows the associated late LII sequence images normalized by the peak image to illustrate the relative persistence of signal and therefore the relative sizing of particles. Reasonably good agreement between the calculated results in the respective positions within Figure 100 and those in Figure 101 is shown. Specifically, the position of the

plume core of larger diameter primary particles for the right most image ($P_{\text{rail}}=1600$ bar, $T_{\text{Ref}}=0.66$ ms), is consistent, whilst the gradient towards larger particles moving away from the injector is just apparent for the centre image ($P_{\text{rail}}=1300$ bar, $T_{\text{Ref}}=1$ ms) in both the results plot and the normalized late sequence LII image. The left most image ($P_{\text{rail}}=1000$ bar, $T_{\text{Ref}}=1.7$ ms) pair of Figure 100 and Figure 101 seems to offer the least concurrence, however the location of low primary particle size region laterally spanning the soot structure at approximately 52 mm below injector tip, is apparent in both results and normalized late sequence LII image upon inspection.

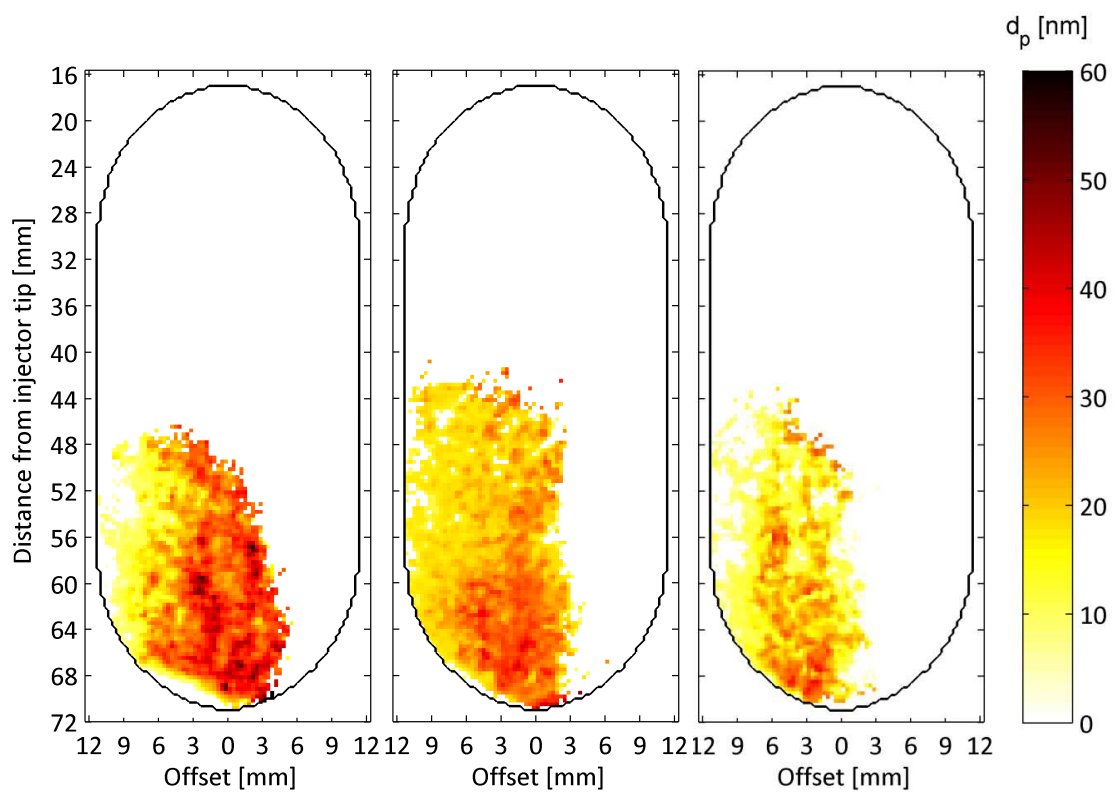


Figure 100 Primary particle diameter (d_p) false colour maps for ICP=40 bar, at $P_{\text{rail}}=1000$ bar, $T_{\text{Ref}}=1.7$ ms (left), $P_{\text{rail}}=1300$ bar, $T_{\text{Ref}}=1$ ms (centre), and $P_{\text{rail}}=1600$ bar, $T_{\text{Ref}}=0.66$ ms (right).

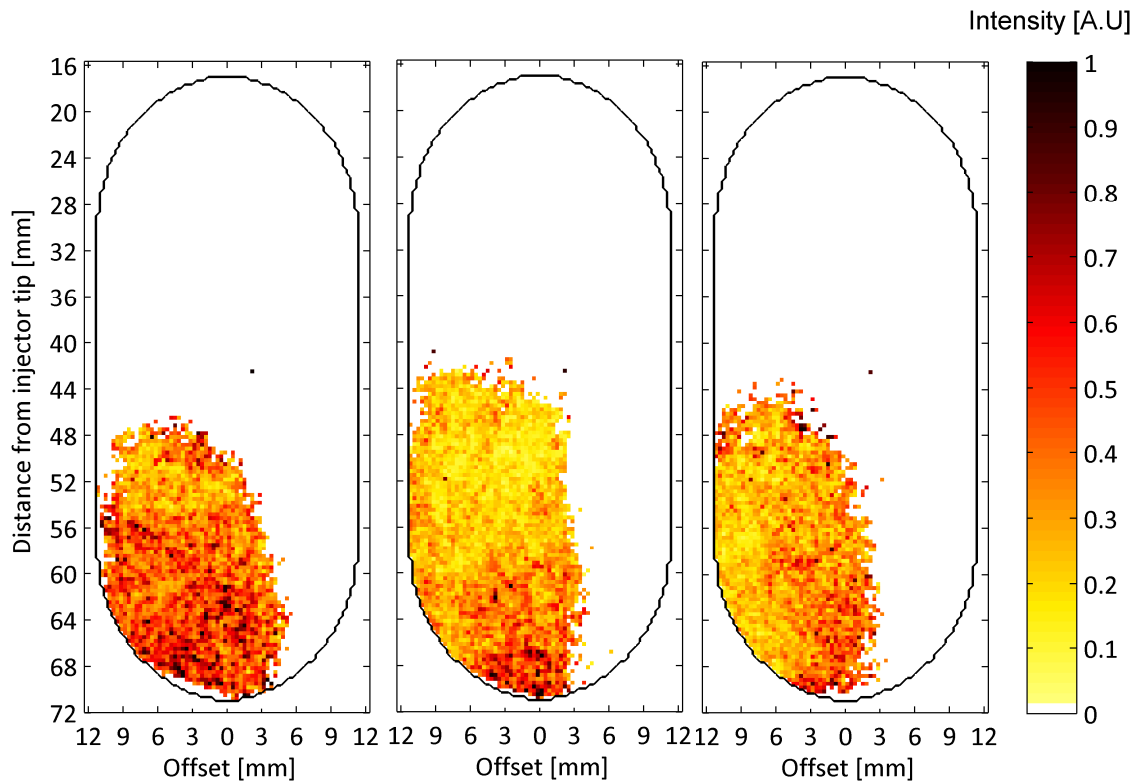


Figure 101 Late LII sequence image 11 normalized by peak LII intensity image 4 to characterize degree of persistence of LII radiant emission; greater intensity corresponds to larger primary particles. $P_{\text{rail}}=1000$ bar $T_{\text{Ref}}=1.7$ ms (left), $P_{\text{rail}}=1300$ bar $T_{\text{Ref}}=1$ ms (centre), and $P_{\text{rail}}=1600$ bar $T_{\text{Ref}}=0.66$ ms (right), all at $\text{ICP}=40$ bar.

Figure 102 shows shift towards smaller primary particle diameters across the resolved plane with increased injection rail pressure. $P_{\text{rail}}=1300$ and 1600 bar are indistinct from each other, both with a mode value of approximately 18 nm. They both therefore show a clear shift from $P_{\text{rail}}=1000$ bar, mode value of approximately 30 nm. The common 10 nm mode is discussed in section 5.4.4.1. It is likely that the effect of increasing injection rail pressure will demonstrate a diminishing return in terms of decreasing soot primary particle diameter. Whether the effect is diminished to indistinguishable levels somewhere between 1300 and 1600 bar for this combustion system, is open to question.

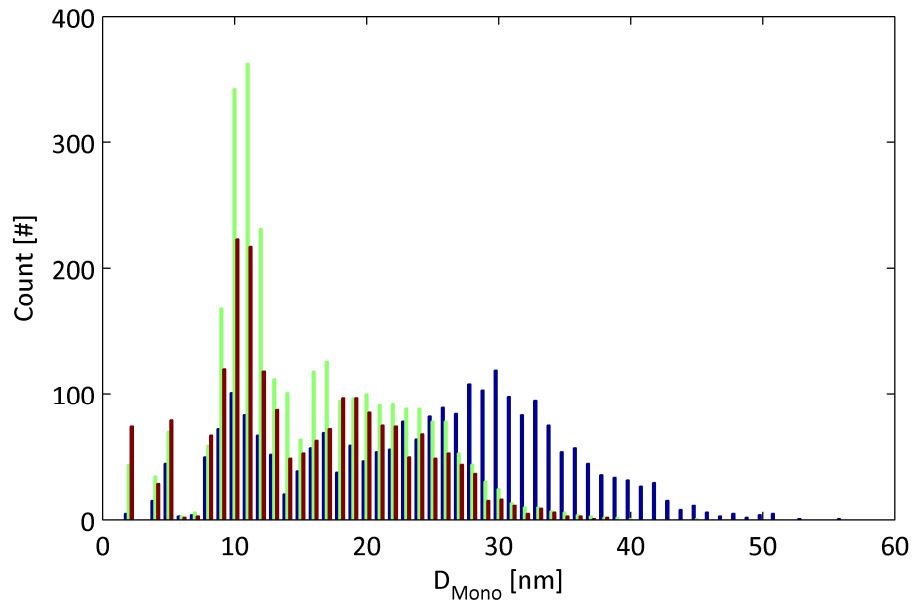


Figure 102 Histograms of primary particle diameter (D_{Mono}) for $P_{\text{rail}}=1000$ bar, $T_{\text{ref}}=1.5$ ms (blue), $P_{\text{rail}}=1300$ bar, $T_{\text{ref}}=1$ ms (green) and $P_{\text{rail}}=1600$ bar, $T_{\text{ref}}=0.66$ ms (red)

A relationship between increased fuel injection rail pressure and a shift towards smaller diameter soot population size distributions is well documented and characterized elsewhere and may be supported by these results. A diminishing reduction in soot population sizes with increase of injection rail pressure may be characterized in Figure 102

5.4.2.3 Variation of in cylinder pressure (ICP)

Figure 103 shows the primary particle diameter results for ICP=40 bar (left) and 50 bar (right). Both constitute credible results in terms of distribution of sizes laterally and axially from the injector tip. An asymmetry to the plume is apparent as with most results presented in this study, though this is likely to relate to the localized fluence variation and erroneous filtering of the employed data processing routines, used to select regions of interest.

The soot plume remains in a similar location within the field of view for both conditions but required different acquisition timing in order to achieve this. For the ICP=50 bar condition, penetration length of the fuel and soot plume was slightly reduced relative to that of the ICP=40 bar condition. The ICP=50 bar data was captured 0.1 ms later than that of the ICP=40 bar condition, yet occupies a similar spatial location, suggesting similar acquisition timing may yield a plume demonstrating significantly reduced penetration length.

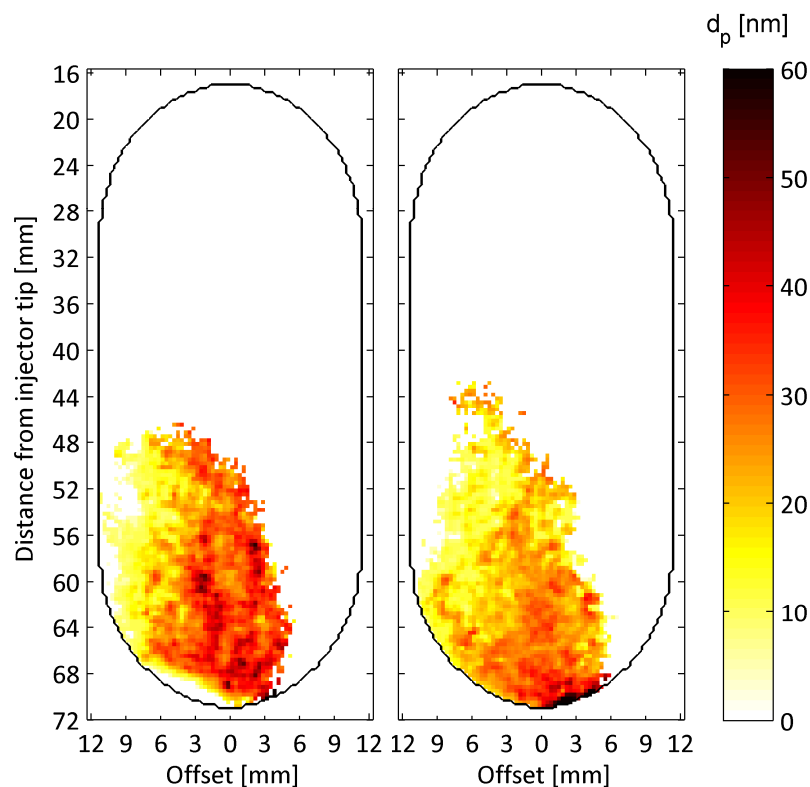


Figure 103 Primary particle diameter (d_p) false colour maps for fuel injection rail pressure $P_{\text{rail}}=1000$ bar, at ICP=40 bar at $T_{\text{Ref}}=1.7$ ms (left), and at ICP=50 bar at $T_{\text{Ref}}=1.8$ ms (right).

Figure 104 shows the normalized by peak LII intensity, late LII sequence images for both operating conditions. The spatial distribution of higher value location values (larger particles) corresponds very well with the results plots of Figure 103 for the ICP=50 bar (right) image.

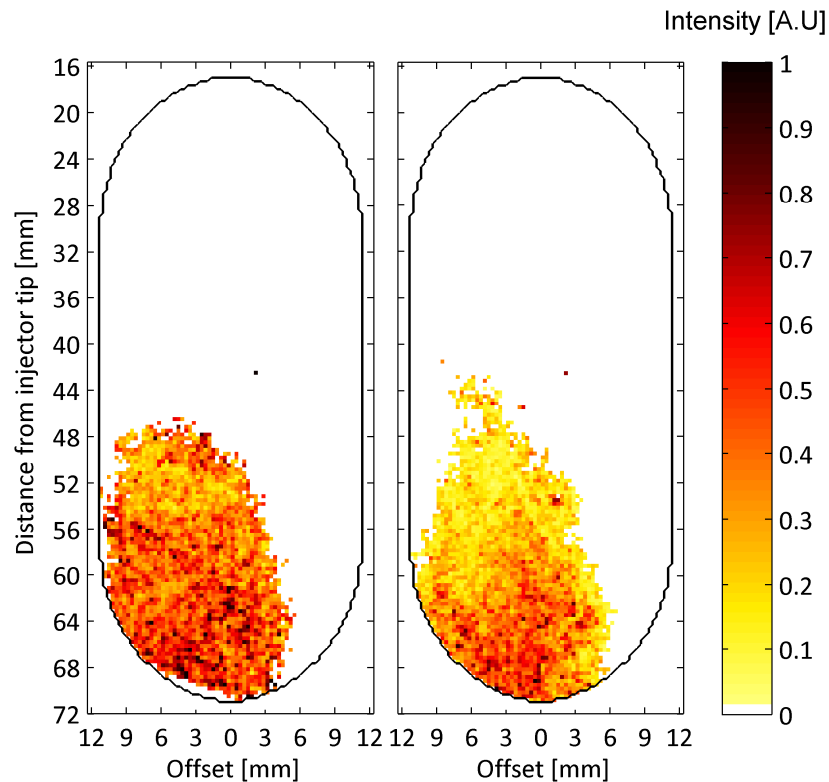


Figure 104 Late LII sequence image 11 normalized by peak LII intensity image 4 to characterize degree of persistence of LII radiant emission; greater intensity corresponds to larger primary particles. $P_{\text{rail}}=1000$ bar with ICP=40 bar, $T_{\text{Ref}}=1.7$ ms (left) and ICP=50 bar, $P_{\text{rail}}=1000$ bar $T_{\text{Ref}}=1.8$ ms (right).

Figure 105 portrays a reduction in the main mode (non-10 nm mode) primary particle diameter from approximately 28 nm to 22 nm as the ICP is increased from 40 to 50 bar. For both histogram series, the 10 nm mode is addressed in section 5.4.4.1. This perhaps constitutes the clearest concurrence of presented results with expectation of the effect of a parameter variation.

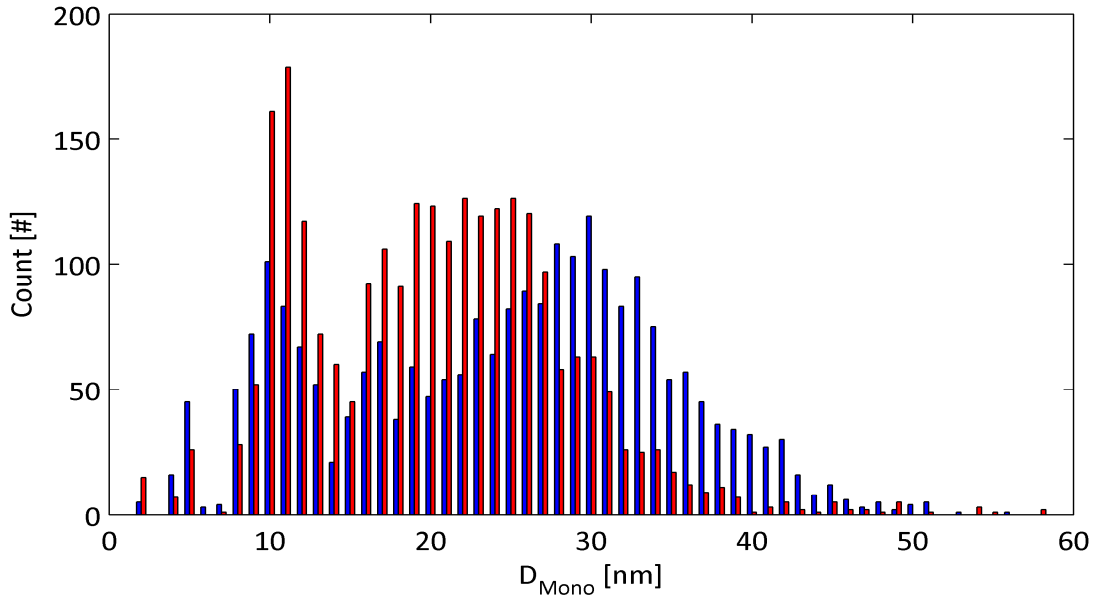


Figure 105 Histograms of primary particle diameter (D_{Mono}) for ICP=40 bar, $T_{\text{Ref}}=1.7$ ms (blue) and ICP=50 bar, $T_{\text{Ref}}=1.8$ ms (red).

5.4.3 Individual LII data sequence derived results

One of the attractive aspects of the 2D-2C-TiRe-LII technique is the possibility of capturing individual combustion events and calculating the soot primary particle size distribution within the field of measurement. Whilst ensemble averaged data provides a statistically likely distribution of soot and of the particle sizes within the resolved plane, it necessarily cannot portray small scale features within the soot structure that are smoothed by the averaging process. Individual combustion event analysis offers the opportunity to resolve details about the specific distribution of soot for a specific combustion event. This may be of interest for work that intends to experimentally study the relationship between the topology of combustion and the resultant soot size distribution.

5.4.3.1 Data set 58 (ICP=40 bar, $P_{\text{rail}}=1000$ bar, $T_{\text{Ref}}=1.7$ ms)

Figure 106 shows images of peak radiant LII emission for a specific combustion event. This set was selected since it occupies approximately the same spatial location as the ensemble data of the set from which it was taken. An interesting inhomogeneity of signal

intensity is apparent; since the signal intensity is dependent upon the local soot volume fraction, there may be no apparent relationship between LII signal distribution and spatial distribution of soot primary particle sizes.

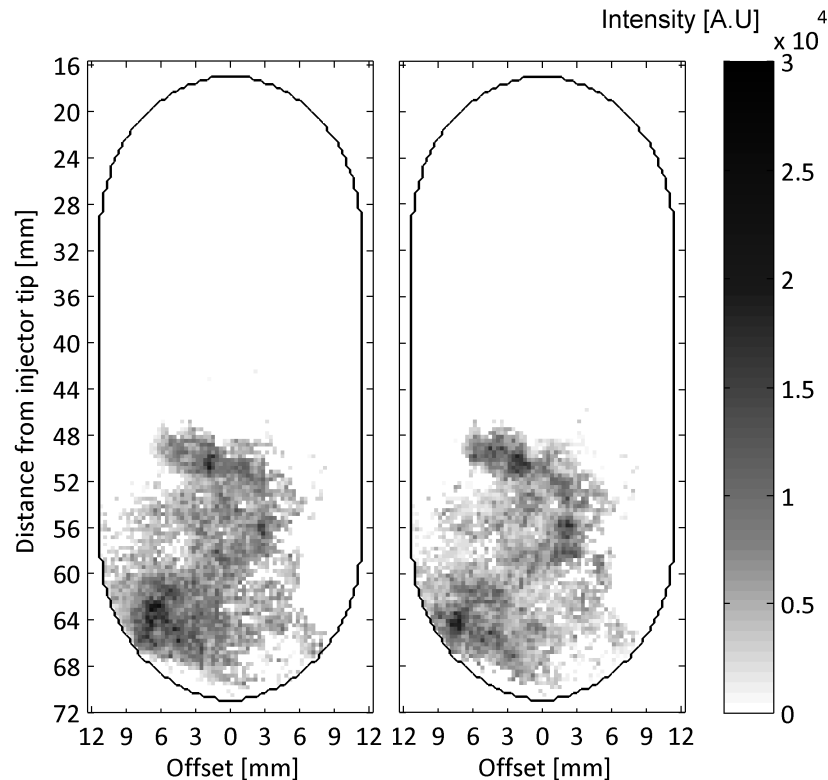


Figure 106 LII radiant emission via 592 nm centre wavelength filter (left) and 750 nm centre wavelength filter (right) for ICP=40 bar, $P_{\text{rail}}=1000$ bar, $T_{\text{Ref}}=1.7$ ms, for data set 58.

Figure 107 shows both the calculated results of primary particle size (left), and peak LII intensity normalized, late sequence LII image (right). The primary particle map shows a far more intricate distribution than is presented for the ensemble average data. The overall spatial distribution trend is similar to the ensemble average data, suggesting that the result may be credible. Comparison to the late sequence LII image, shows similarity in the spatial location of two regions of smaller particles, centred at 49 mm below injector, 4 mm left of the injector major axis, and 57 mm below injector, 3 mm right of the injector major axis.

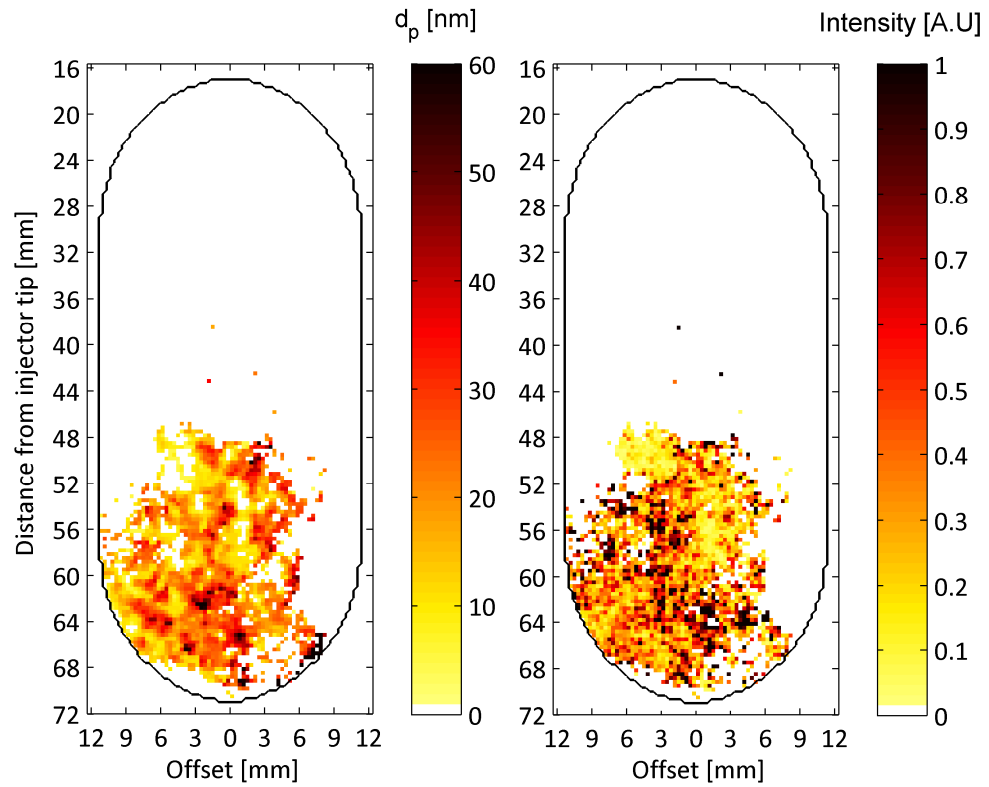


Figure 107 Primary particle diameter (d_p) false colour map for conditions of ICP=40 bar, $P_{\text{rail}}=1000$ bar, $T_{\text{ref}}=1.7$ ms for a selected data set 58 (left). Late LII image 11 normalized by image 4 (right) to characterize degree of persistence of LII radiant emission; greater intensity corresponds to larger primary particles.

Figure 108 shows the comparison of the ensemble data primary particle size distribution with that of the selected individual combustion event (set 58). A difference between their respective primary mode values is apparent, the individual combustion event data yielding a mode of approximately 23 nm versus 30 nm for the ensemble data.

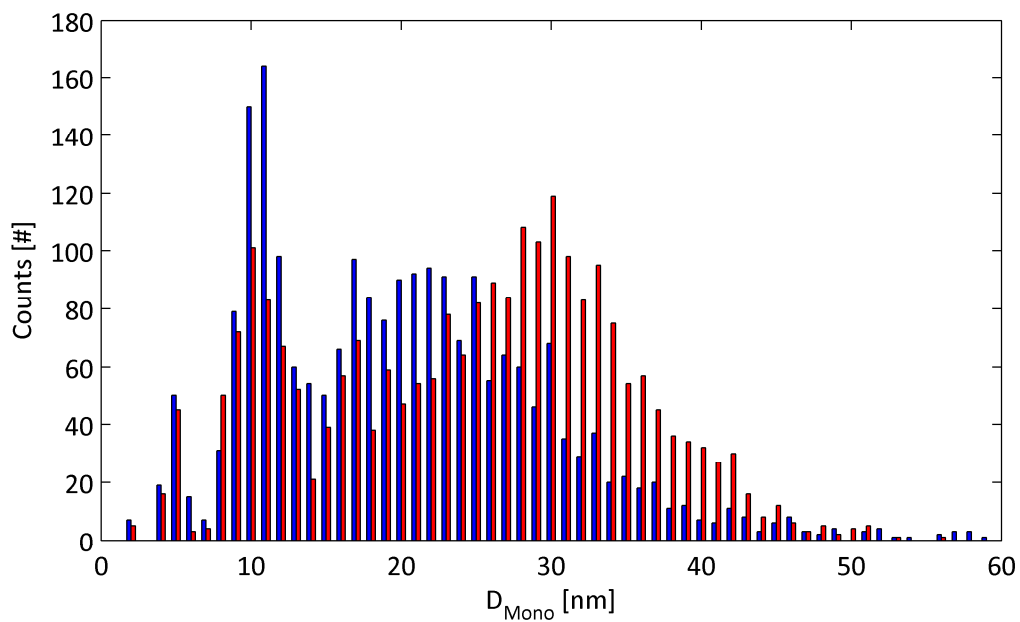


Figure 108 Histograms of primary particle diameter (D_{Mono}) for individual data set 58 (blue) versus ensemble average data (red), at ICP=40 bar, P_{rail} =1000 bar, T_{Ref} =1.7 ms.

5.4.3.2 Data set 28 (ICP=40 bar, $P_{\text{rail}}=1300$ bar, $T_{\text{ref}}=1$ ms)

Figure 109 shows images of peak radiant LII emission for a specific combustion event. This set was selected due to the interesting inhomogeneity of signal intensity, and spatial distribution. Notably the soot plume is resolved nearer to the injector tip than is apparent in the ensemble averaged data, from which it was selected.

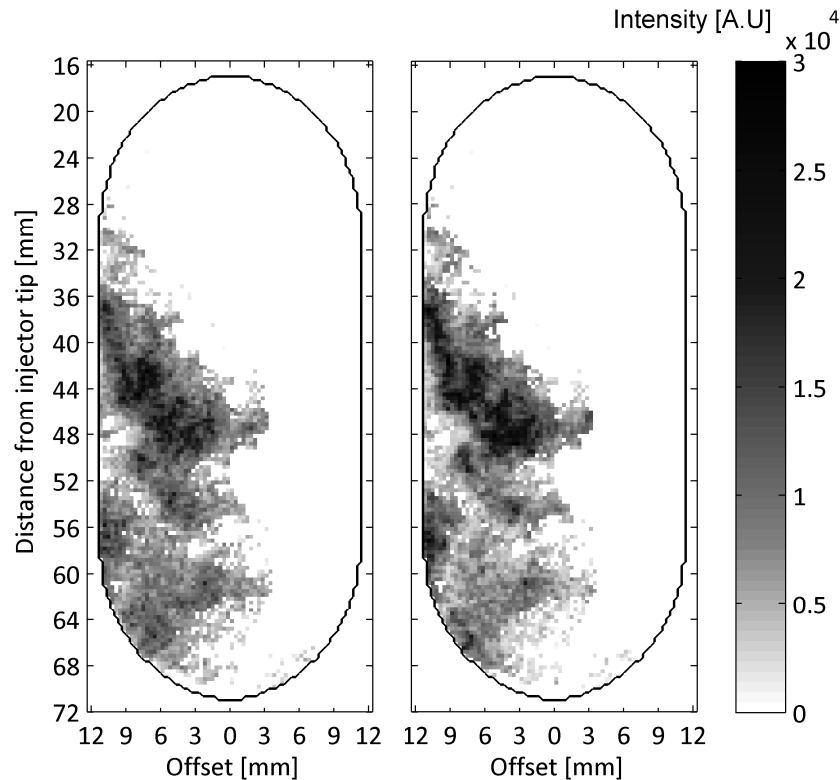


Figure 109 LII radiant emission via 592 nm centre wavelength filter (left) and 750 nm centre wavelength filter (right) for ICP=40 bar, $P_{\text{rail}}=1300$ bar, $T_{\text{ref}}=1$ ms, for data set 28.

Figure 110 shows both the calculated results of primary particle size (left), and peak LII intensity normalized, late sequence LII image (right). As it appears for all the primary particle diameter results data from individual combustion events, a far more intricate distribution than is presented for the ensemble average data is apparent. The overall spatial distribution trend is similar to the ensemble average data, in that a slight gradient of increasing primary particle diameter is apparent moving away from the injector tip. This concurrence of distribution supports the credibility of the result. Comparison to the

late sequence LII image, shows similarity in the spatial location of a region of smaller particles, at approximately 48 mm and less from the injector tip.

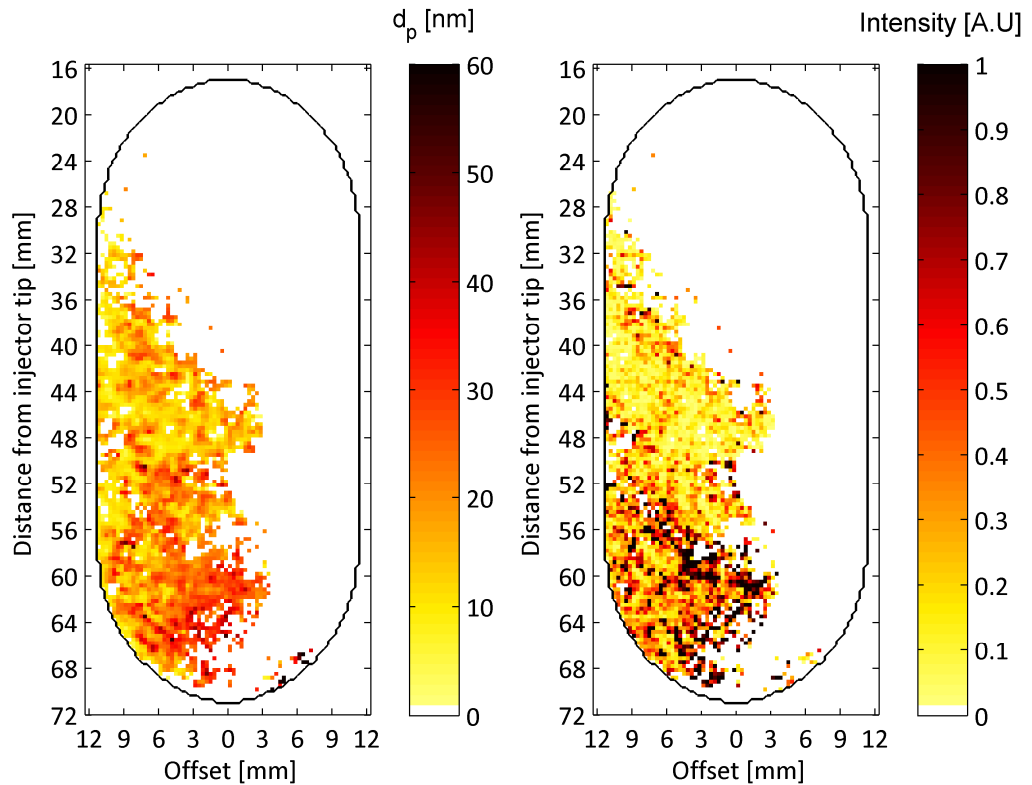


Figure 110 Primary particle diameter false colour map for conditions of ICP=40 bar, RP=1300 bar, TRef=1 ms for data set 28 (left). Late LII image 11 normalized by image 4 (right) to characterize degree of persistence of LII radiant emission; greater intensity corresponds to larger primary particles, lesser intensity to smaller primary particles.

Figure 111 shows the comparison of the ensemble data primary particle size distribution with that of the selected individual combustion event (set 28). A very similar distribution is apparent with a principal mode value of approximately 20 nm diameter.

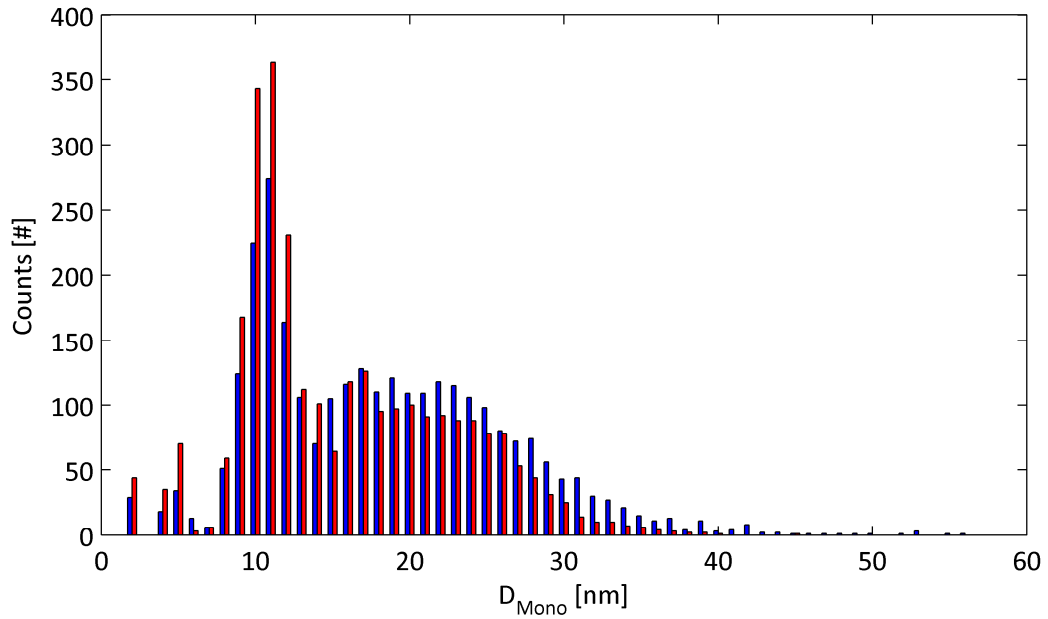


Figure 111 Histograms of primary particle diameter (D_{Mono}) for individual data set 28 (blue) versus ensemble average data (red), at ICP=40 bar, P_{rail} =1300 bar, T_{Ref} =1 ms.

5.4.3.3 Data set 1 (ICP=50 bar, P_{rail} =1000 bar, T_{Ref} =1.8 ms)

Figure 112 shows the peak LII signal images for both acquisition channels. Significant extinction due to the dense plume of soot particles suggests difficulty in resolving the local extinction and therefore error in the local laser fluence values may propagate through the calculation of primary particle size.

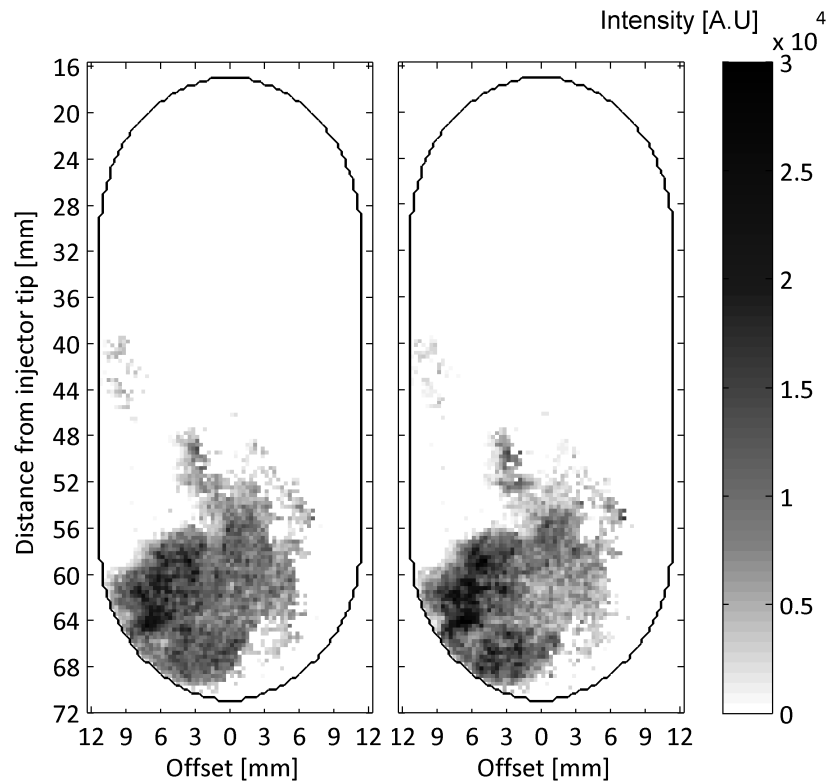


Figure 112 LII radiant emission via 592 nm centre wavelength filter (left) and 750 nm centre wavelength filter (right) for ICP=50 bar, $P_{\text{rail}}=1000$ bar, $T_{\text{Ref}}=1.8$ ms, for data set 1.

Figure 113 shows both the calculated results of primary particle size (left), and peak LII intensity normalized, late sequence LII image (right). The primary particle diameter results data presents a more smoothly varying solution value characteristic than is apparent for the other individual combustion event data. The overall spatial distribution of primary particle sizes is consistent with both the ensemble average data soot plume and the peak LII intensity normalized late sequence LII image.

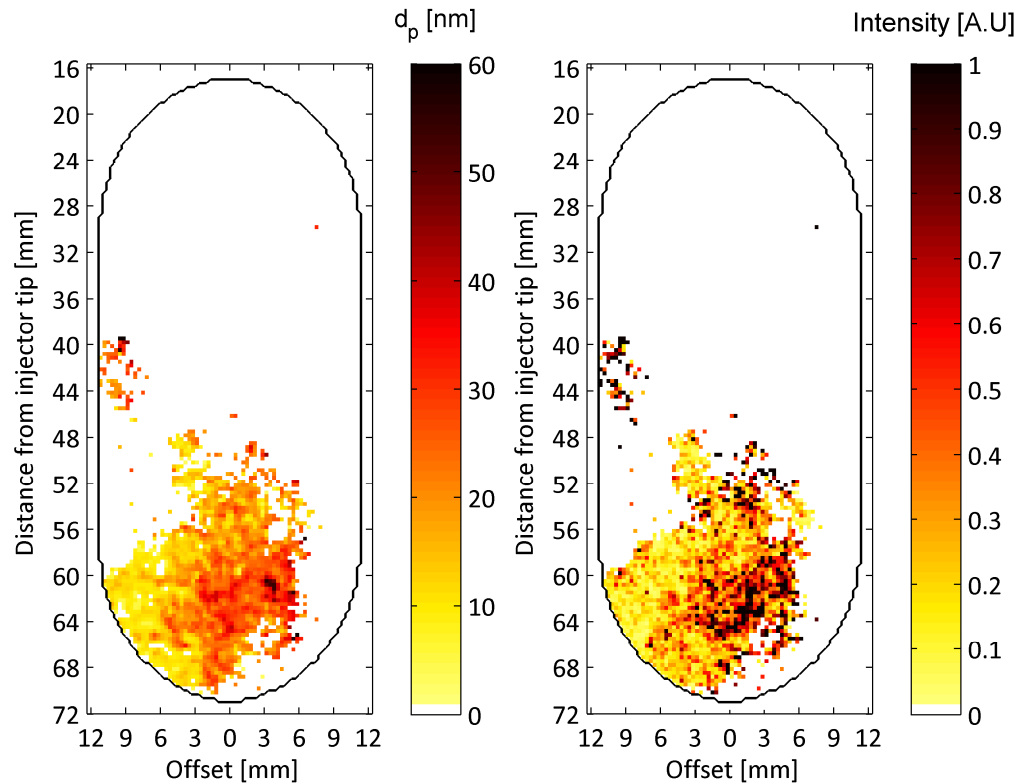


Figure 113 Primary particle diameter false colour map for conditions of ICP=50 bar, RP=1000 bar, T_{Ref}=1.8 ms for data set 1 (left). Late LII image 11 normalized by image 4 (right) to characterize degree of persistence of LII radiant emission; greater intensity corresponds to larger primary particles.

Figure 114 shows the comparison of the ensemble data primary particle size distribution with that of the selected individual combustion event (set 1). A very similar distribution is apparent with a principal mode value of approximately 22 nm diameter.

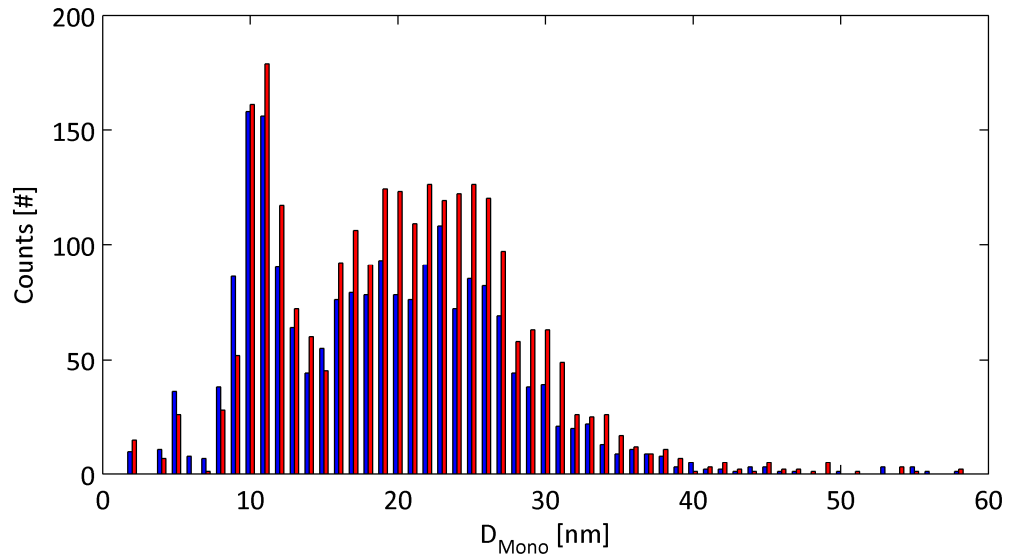


Figure 114 Histograms of primary particle diameter (D_{Mono}) for individual data set 1 (blue) versus ensemble average data (red), at ICP=50 bar, P_{rail} =1000 bar, T_{Ref} =1.8 ms.

5.4.3.4 Data set 33 (ICP=40 bar, P_{rail} =1600 bar, T_{Ref} =0.66 ms)

Figure 115 shows the peak LII signal images for both acquisition channels. A significantly inhomogeneous distribution of signal, and therefore soot particles, is apparent. The effect of such a distribution, and whether it was manifest in the particle size distribution, contributed to the selection of set 33.

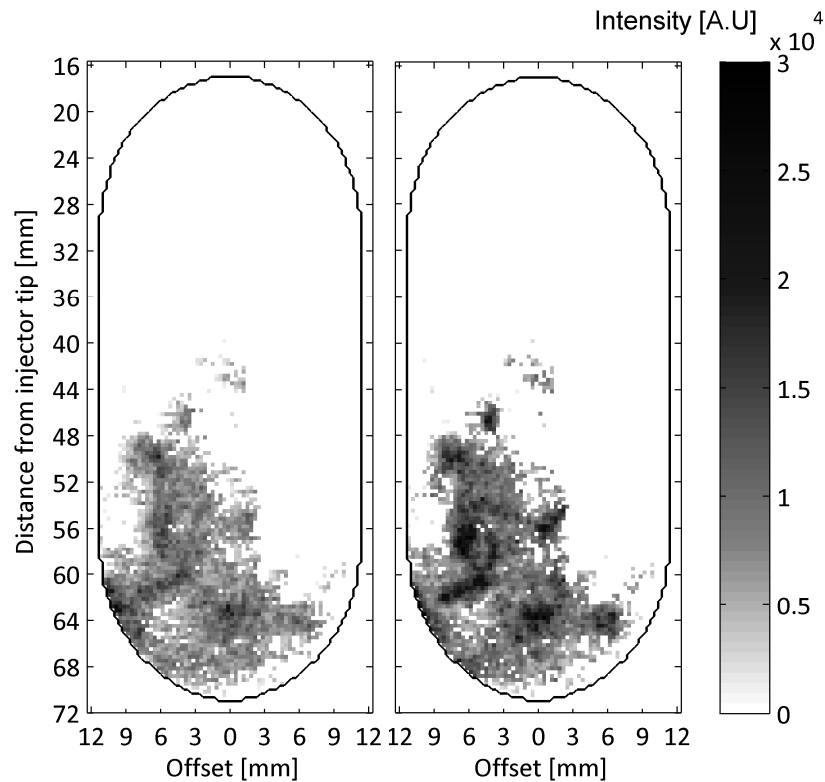


Figure 115 LII radiant emission via 592 nm centre wavelength filter (left) and 750 nm centre wavelength filter (right) for ICP=40 bar, $P_{\text{rail}}=1600$ bar, $T_{\text{Ref}}=0.66$ ms, for data set 33.

Figure 116 shows both the calculated results of primary particle size (left), and peak LII intensity normalized, late sequence LII image (right). The primary particle diameter results data is sparsely resolved and biased towards the smaller particle scale extreme. Such is the spatial distribution that it is difficult to make comparison to the characteristics of the ensemble average data from which it was selected. The lower region (furthest from the injector nozzle) demonstrates a slight bias towards larger particles and is consistent with the late frame normalized signal.

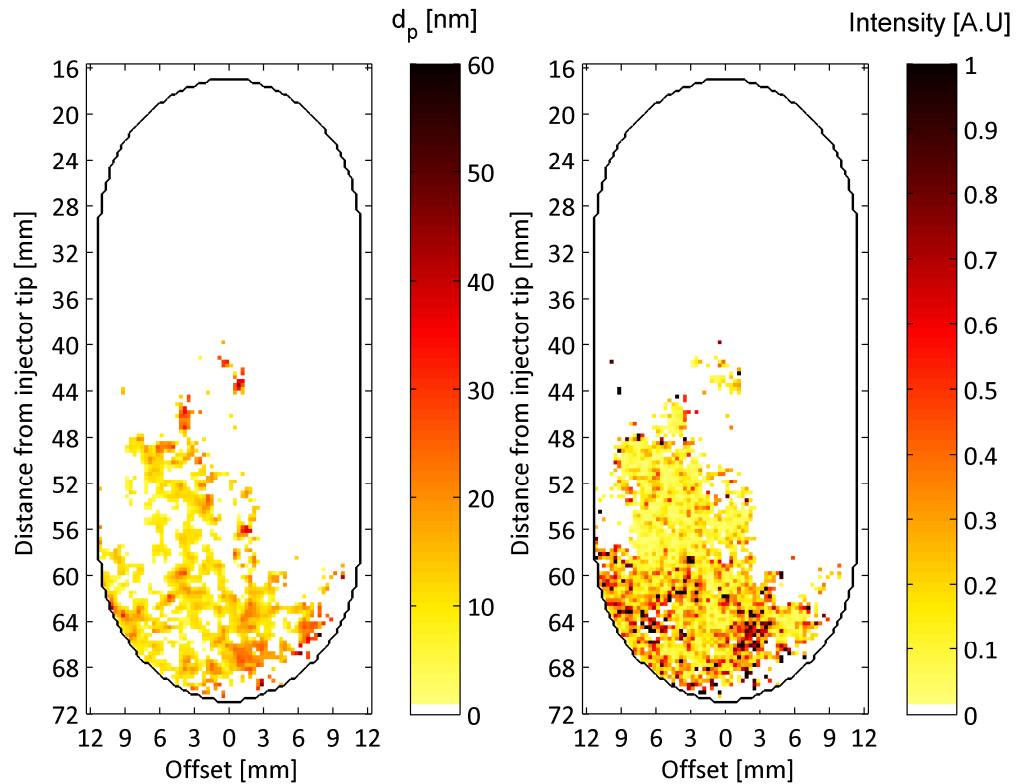


Figure 116 Primary particle diameter false colour map for conditions of ICP=40 bar, $P_{\text{rail}}=1600$ bar, $T_{\text{ref}}=0.66$ ms for data set 33 (left). Late LII image 11 normalized by image 4 (right) to characterize degree of persistence of LII radiant emission; greater intensity corresponds to larger primary particles.

Figure 117 shows the comparison of the ensemble data primary particle size distribution with that of the selected individual combustion event (set 33). A dissimilar trend is apparent with a principal mode value of approximately 15 nm for the individual combustion event data (set 33) that is partially absorbed into the anomalous 10 nm mode, compared to the ensemble data mode of approximately 20 nm.

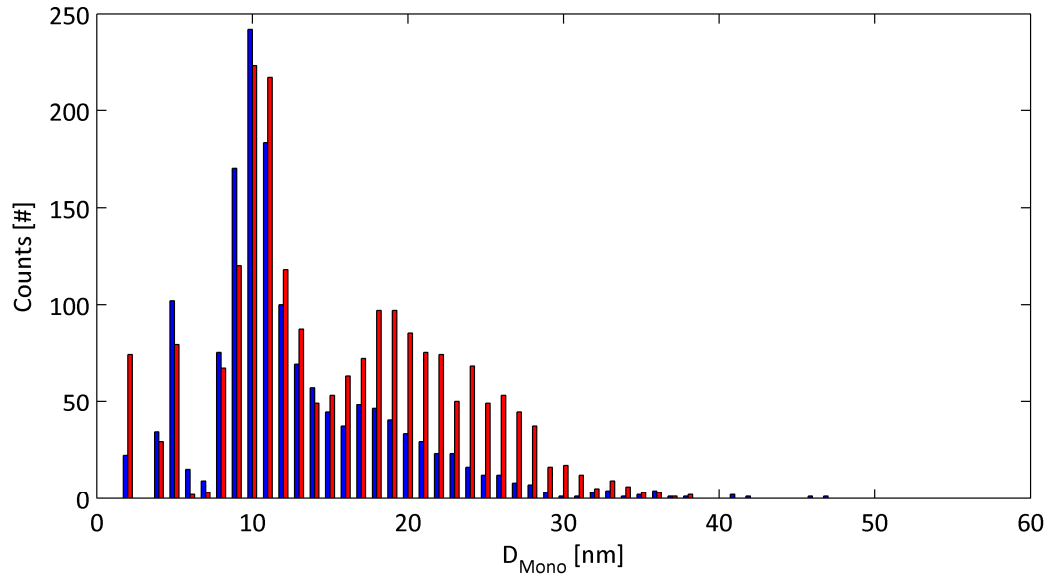


Figure 117 Histograms of primary particle diameter (D_{Mono}) for individual data set 33 (blue) versus ensemble average data (red), at ICP=40 bar, $P_{\text{rail}}=1600$ bar, $T_{\text{Ref}}=0.66$ ms.

5.4.4 Discussion

Typically, LII data captured from RCM type experimental apparatus has been quantitative in nature and ensemble averaged to aid insight into the stochastically likely structure and spatial distribution within the optical access chamber. The ensemble average data presented within this study is qualitatively consistent with that that has gone before. It is however resolved over a series of images and therefore through time, albeit in discrete steps. This represents an advance in that the ensemble averaged, stochastically likely structure may be quantified. It is unclear as to whether the median averaging across the data series appropriately represents the ensemble radiant emission at each location. A bias toward larger, dominant persisting signal emitting particles may be in evidence.

Quantification of spatially resolved individual data series represents a unique capability presented by 2D-2C-TiRe-LII. To that end, the technique has yielded data that has in part demonstrated a relationship to, and consistency with, the ensemble data sets, from which the individual sets were selected. Furthermore, soot structures that would necessarily be hidden in ensemble data may be apparent. The spatial distribution within each individual combustion event seems to be far more granular and segmented than the ensemble data has previously facilitated the resolution of. This result, if valid, is of interest to the

research community focused upon the characterization and modelling of flame and soot processes and their interaction.

5.4.4.1 10 nm mode

A distribution of primary particle size mode centred at approximately 10 nm diameter across all the presented diesel engine condition results, irrespective of operating conditions, is apparent. It is unlikely to represent a real characteristic of the combustion by products, or an artefact of the experimental method and associated data processing. It may be due to spurious radiant emission(s) (flame luminosity, fluorescence, radical emission, etc.) contribution to the overall processed signal ratio sequences from which particle size is calculated. Images prior to laser excitation do not indicate significant flame luminosity. Care was taken in selection of detection spectral intervals and acquisition timing to avoid significant contribution due to fluorescence of OH and NO radicals. Whilst it therefore remains unexplained within this study, further investigation is recommended, particularly with regard to whether PAH fluorescence may present a dominant signal contribution in the images immediately after the laser excitation, synthesizing the contribution of small particles, to which the solution algorithm duly converged.

6 Conclusion

The work undertaken in this study illustrates the working principle of an optical diagnostic technique that merges spatially-resolved LII and time-resolved LII. This novel approach presents the possibility of an absolute quantification of soot particle size, resolved across a planar measurement volume. The technique was first undertaken upon a laminar diffusion flame, on a Santoro type burner, that is quantitatively well characterized by previous researchers both at the University of Brighton and in the open literature. Simultaneous measurement using a punctual 2C-TiRe-LII technique demonstrated excellent agreement with values presented in the literature and in doing so, validated the flame characteristics as consistent with those of Santoro burners utilized in other studies. By contrast, the deviation from that value of the associated location within primary particle sizes data field for the 2D-2C-TiRe-LII experiment, illustrates that the technique requires significant refinement and development. In particular, the adoption of 532 nm for the principle laser excitation wavelength rather than 1064 nm may have stimulated fluorescence and perturbed, to some unquantified extent, the measured emissions and therefore the calculated primary particle sizes.

The 2D-2C-TiRe-LII technique was adapted and applied to an RCM in which realistic diesel engine combustion conditions were manifest. A simultaneous laser extinction experimental branch was developed in order to provide partnering data for calculation of localized laser fluence.

The experimental technique and associated data processing demonstrated a high degree of sensitivity to the accuracy of the spatial registration between all the data contributing images for each particle size calculation. In particular, where spatial signal gradients are greatest, typically adjacent to peak LII signal regions, the sensitivity of the solution algorithm to erroneous data spatial registration is greatest. Low intensity value contributory data values also affected results; Low signal values tended to correspond to low SNR data that in-turn produce erratically varying ratio sequences in which the propagation of error was significant. Consequently, the solution algorithm was presented with awkward datasets, producing erratically varying results, with significant associated uncertainty.

Highly extinguished local laser fluence reduced LII signal intensity in downstream regions of the respective soot structures for both experimental schemes. Calculation of local laser fluence value is likely a significant source of uncertainty in particle diameter calculation.

This work has presented the rationale for the necessity of utilizing a characterization of the acquisition temporal response that encompasses the transient response of the system. Significant errors in the computed primary particle diameter values were apparent when a binary state shutter response was initially used. Hence, a novel acquisition calibration rationale and camera shutter event characterization has been presented and utilized in a temporally integrated LII radiation model of the signal captured by each camera exposure.

A fundamental issue of utilizing an indirect solution method through the application of a search algorithm is that it does not readily provide insight into the shape of the solution space. The nature of the solution (e.g. finding a global or local minimum/maximum) cannot be conveniently assessed and so there is a reluctance to add further parameter dimensions to the solution space. Of the original aims of this work, the last was to introduce a size distribution function shape parameter variable. The technique in the configurations used in this study did not permit this due to their insufficient sensitivity and contention with rudimentary issues of low signal-to-noise ratio and spatial registration uncertainty between images captured with different ICCD assemblies.

6.1 Validation of the technique at atmospheric conditions

The working principle of the 2D-2C-Tire-LII technique has been demonstrated upon a well characterized laboratory burner. High spatial gradients of signal variation, in conjunction with the necessity of registering/aligning images captured by different ICCD cameras, (and between two different acquisition channel images due to the use of an image doubler), provided uncertainty as to the inter-frame alignment and consequently the set of pixels attributed to each binned pixel location and therefore pixel sequence values. This contributed to the uncertainty of the resultant particle diameter solution at each location.

6.2 Application of 2D-2C-Tire-LII at high ambient pressures

Application of the 2D-2C-Tire-LII technique to an optical RCM at realistic diesel engine combustion chamber conditions has also been demonstrated. A simultaneous laser extinction experimental branch was incorporated to characterize the local laser fluence.

The inhomogeneous and irregular spatial distribution of soot plumes produced within the RCM confirmed the necessity of characterizing the spatially irregular extinction of the laser sheet as it traversed the soot plumes. The significant laser fluence attenuation demonstrated across the soot plume structure confirmed that a global laser fluence approximation would not be an approximation that fell within the bounds of acceptability.

The necessity of characterizing the localized laser fluence by an appropriate means such as on-line extinction characterization has been demonstrated. In particular, the necessity of the employment of a method to successfully characterize the spatially variant laser fluence through the inhomogeneous soot plume (such as those produced within the RCM combustion chamber), was addressed.

The application of the technique to a combustion system as presented in the optically accessible RCM seemingly demonstrated several phenomena, potentially of interest to the light duty diesel (LDD) combustion research community. However, due to the uncertainty of the results achieved in such challenging conditions, only the rapid displacement of the soot plume can be credibly be asserted at this time.

The single combustion event (non-ensemble average) results illustrate the possibility of realizing a spatial distribution of quantified soot sizes of a specific combustion event. The study of in-cylinder soot formation and oxidation may be aided by the enhanced detail thereafter realizable. For example, the effects of interaction of incident or adjacent flame kernels upon the local distribution of constituents, temperature and pressure; parameters that may affect the resultant soot population contribution.

The presented results, in particular the characterization of combustion phenomena, should be viewed with the understanding that they are included to principally illustrate that the technique seems to demonstrate sensitivity to variation of that to which it is applied.

Considerable development and refinement, both experimentally and conceptually, is required to ascertain the limitations of the technique and whether an absolutely quantified, spatially resolved technique constitutes a reasonable aspiration.

6.3 Future work

The work conducted and presented within this study illustrates several aspects that ought, in retrospect, to be more thoroughly addressed. Therefore, several recommendations for future work pertaining to the experimental configuration, the data processing and the characterization of the acquisition performance of the 2D-2C-TiRe-LII technique are proposed herein:

- Characterization of camera performance. To include resolution spectrally, temporally, for linearity of measurement versus intensity of irradiance, and for variation of intensifier gain.
- Experimental configuration in which greater radiant flux is incident with ICCD sensors, achievable through less stages of optical path splitting (four stages for the SIM 16 design)
- Utilization of 1064 nm wavelength laser excitation and suitable spectral performance laser path optical components, in order to avoid the stimulation of fluorescence and the resultant obfuscation of LII radiation.
- Improved laser fluence characterization, through a more optimal geometrically configured extinction profile experimental branch.
- Improvement to spatial registration of LII data, between images within a temporal sequence, and between the two spectral filtered channels.
- Filtering of data for jitter of the acquisition to laser synchronization timing, when producing ensemble averaged data.
- Extension of the particle size distribution heat transfer model to encompass shape parameters (σ).
- Utilization of pre-laser pulse acquisition images to perform a comparatively long exposure duration (\sim ms) two-channel pyrometry upon the soot plume. This would produce more precise local temperature distributions which can be used as input for the 2D-2C-TiRe-LII processing.

- Resolution of the source of signal contribution yielding a primary particle diameter population distribution mode at approximately 10 nm diameter.

References

- Anonymous. (2005). Ambient Air Quality and Cleaner Air for Europe. Brussels.
- Akihama, K., Y. Takatori, et al. (2001). "Mechanism of the smokeless rich diesel combustion by reducing temperature." Training **2011**: 03-15.
- Al-Qurashi, K., A. D. Lueking, et al. (2011). "The deconvolution of the thermal, dilution, and chemical effects of exhaust gas recirculation (EGR) on the reactivity of engine and flame soot." Combustion and Flame **158**(9): 1696-1704.
- Alatas, B., J. A. Pinson, et al. (1993). A study of NO and soot evolution in a DI diesel engine via planar imaging, Society of Automotive Engineers, 400 Commonwealth Dr, Warrendale, PA, 15096, USA.
- Allouis, C., A. D'Alessio, et al. (2000). "Time resolved laser induced incandescence for soot and cenospheres measurements in oil flames." Combustion science and technology **153**(1-6): 51-64.
- Alriksson, M., T. Rente, et al. (2005). "Low soot, low NOx in a heavy duty diesel engine using high levels of EGR." SAE paper(2005-01): 3836.
- Amann, C. A. and D. C. Siegl (1981). "Diesel Particulates—What They Are and Why." Aerosol Science and Technology **1**(1): 73 - 101.
- Appel, J., B. Jungfleisch, et al. (1996). Assessment of soot volume fractions from laser-induced incandescence by comparison with extinction measurements in laminar, premixed, flat flames, COMBUSTION INSTITUTE.
- Arnold, A., H. Becker, et al. (1990). "Laser in situ monitoring of combustion processes." Applied Optics **29**(33): 4860-4872.
- Axelsson, B., R. Collin, et al. (2000). "Laser-Induced Incandescence for Soot Particle Size Measurements in Premixed Flat Flames." Applied Optics **39**(21): 3683-3690.
- Axelsson, B., R. Collin, et al. (2001). "Laser-induced incandescence for soot particle size and volume fraction measurements using on-line extinction calibration." Applied Physics B: Lasers and Optics **72**(3): 367-372.
- Baker, H. D., E. A. Ryder, et al. (1961). "Temperature measurement in engineering, vol. II. John Wiley & Sons." Materials and Corrosion.
- Baker, H. D., E. A. Ryder, et al. (1961). "Temperature measurement in engineering. Vol. 2." Stamford: Omega Press, 1953.
- Bartok, W. and A. F. Sarofim (1991). "Fossil fuel combustion." John Wiley and Sons Inc, New York.
- Beatrice, C., C. Bertoli, et al. (1995). "Two-colour pyrometry measurements of soot loading in a diesel engine burning model fuels of varying quality." Combustion science and technology **110**: 321-340.
- Beyer, V. and D. A. Greenhalgh (2006). "Laser induced incandescence under high vacuum conditions." Applied Physics B: Lasers and Optics **83**(3): 455-467.
- Birch, K. P. and M. J. Downs (1993). "An updated Edlén equation for the refractive index of air." Metrologia **30**(3): 155-162.
- Bladh, H. and P. E. Bengtsson (2004). "Characteristics of laser-induced incandescence from soot in studies of a time-dependent heat-and mass-transfer model." Applied Physics B: Lasers and Optics **78**(2): 241-248.
- Bladh, H., P. E. Bengtsson, et al. (2006). "Experimental and theoretical comparison of spatially resolved laser-induced incandescence (LII) signals of soot in backward and right-angle configuration." Applied Physics B: Lasers and Optics **83**(3): 423-433.

- Bladh, H., J. Delhay, et al. "Experimental and theoretical comparison of spatially resolved laser-induced incandescence signals in a sooting flame."
- Blanquart, G., P. Pepiot-Desjardins, et al. (2009). "Chemical mechanism for high temperature combustion of engine relevant fuels with emphasis on soot precursors." Combustion and Flame **156**(3): 588-607.
- Blevin, W. R. (1972). "Corrections in optical pyrometry and photometry for the refractive index of air." Metrologia **8**(4): 146-147.
- Böhm, H., D. Hesse, et al. (1989). The influence of pressure and temperature on soot formation in premixed flames. Symposium (International) on Combustion, Elsevier.
- Boiarciuc, A., F. Foucher, et al. (2006). "Soot volume fractions and primary particle size estimate by means of the simultaneous two-color-time-resolved and 2D laser-induced incandescence." Applied Physics B: Lasers and Optics **83**(3): 413-421.
- Boiarciuc, A., F. Foucher, et al. (2005). "Laser-Induced Incandescence to study the soot formation inside the combustion chamber of a Diesel engine."
- Bruce, C. W., T. F. Stromberg, et al. (1991). "Trans-spectral absorption and scattering of electromagnetic radiation by diesel soot." Applied Optics **30**(12): 1537-1546.
- Castaldi, M. J., N. M. Marinov, et al. (1996). "Experimental and modeling investigation of aromatic and polycyclic aromatic hydrocarbon formation in a premixed ethylene flame." Symposium (International) on Combustion **26**(1): 693-702.
- Cenker, E. (2014). Imaging measurements of soot particle size and soot volume fraction with laser-induced incandescence at Diesel engine conditions, Châtenay-Malabry, Ecole centrale de Paris.
- Chapman, S. and T. G. Cowling (1970). "The Mathematical Theory of Non-Uniform Gases." Cambridge: Cambridge University.
- Choi, M. Y., A. Hamins, et al. (1994). "Simultaneous optical measurement of soot volume fraction and temperature in premixed flames." Combustion and Flame **99**(1): 174-186.
- Clague, A. D. H., J. B. Donnet, et al. (1999). "A comparison of diesel engine soot with carbon black." Carbon **37**(10): 1553-1565.
- Colket, M. B. and D. J. Seery (1994). "Reaction mechanisms for toluene pyrolysis." Symposium (International) on Combustion **25**(1): 883-891.
- D'anna, A. and A. D'Alessio (2000). "Modeling the rich combustion of aliphatic hydrocarbons." Combustion and Flame **121**(3): 418-429.
- Dankers, S. and A. Leipertz (2004). "Determination of primary particle size distributions from time-resolved laser-induced incandescence measurements." Applied Optics **43**(18): 3726-3731.
- De Iuliis, S., M. Barbini, et al. (1998). "Determination of the soot volume fraction in an ethylene diffusion flame by multiwavelength analysis of soot radiation." Combustion and Flame **115**(1-2): 253-261.
- Dec, J. E. (1992). "Soot distribution in a DI diesel engine using 2-D imaging of laser-induced incandescence, elastic scattering, and flame luminosity."
- Dec, J. E. (1997). "A Conceptual Model Of DI Diesel Combustion Based On Laser-Sheet Imaging." SAE TRANSACTIONS **106**(3): 1319-1348.
- Dec, J. E., A. O. zur Loye, et al. (1991). "Soot distribution in a DI diesel engine using 2-D laser-induced incandescence imaging."
- Demory, R. (2007). Optical Measurement of Nitric Oxide and Hydroxyl Radicals Distributions in Combusting Diesel Sprays, University of Brighton: 207.

- Desantes, J. M., V. Bermúdez, et al. (2005). "Effects of current engine strategies on the exhaust aerosol particle size distribution from a Heavy-Duty Diesel Engine " Journal of Aerosol Science **36**(10): 1251-1276.
- Edlen, B. (1966). "The refractive index of air." Metrologia **2**: 71-80.
- Fann, N., A. D. Lamson, et al. (2012). "Estimating the national public health burden associated with exposure to ambient PM_{2.5} and ozone." Risk Analysis **32**(1): 81-95.
- Fiala, J., B. Denby, et al. (2009). Spatial assessment of PM₁₀ and ozone concentrations in Europe (2005), EEA Technical report.
- Filippov, A. V. and D. E. Rosner (2000). "Energy transfer between an aerosol particle and gas at high temperature ratios in the Knudsen transition regime." International journal of heat and mass transfer **43**(1): 127-138.
- Flower, W. L. (1985). "Laser diagnostic techniques used to measure soot formation." Appl Opt **24**(8): 1101.
- Flower, W. L. (1989). An investigation of soot formation in axisymmetric turbulent diffusion flames at elevated pressure. Symposium (International) on Combustion, Elsevier.
- Gao, Z. and W. Schreiber (2001). "The effects of EGR and split fuel injection on diesel engine emission." International Journal of Automotive Technology **2**(4): 123-133.
- Gaydon, A. G. (1957). "The spectroscopy of flames." The spectroscopy of flames. By Gaydon, Alfred Gordon. New York, Wiley, 1957.
- Glassman, I. (1989). Soot formation in combustion processes, Elsevier.
- Glassman, I. (1996). Combustion, Academic Press.
- Glassman, I. (1998). "Soot formation in combustion processes." Symposium (International) on Combustion, 22nd, Seattle, WA; UNITED STATES: 295-311.
- Gray, W. A. and R. Müller (1974). Engineering calculations in radiative heat transfer, Pergamon.
- Habib, Z. G. and P. Vervisch (1988). "On the refractive index of soot at flame temperature." Combustion science and technology **59**(4): 261-274.
- Haynes, B. S. and H. G. Wagner (1981). "Soot formation." Name: Prog. Energy Combust. Sci.
- Henle, A., G. Bittlinger, et al. (2005). "Homogeneous operating strategies in a DI diesel engine with pent-roof combustion chamber and tumble charge motion: studies on a single-cylinder test-engine and an optical access engine." Lubricating Oil **2013**: 09-06.
- Higgins, B. and D. L. Siebers (2001). "Measurement of the flame lift-off location on DI diesel sprays using OH chemiluminescence." SAE paper(2001): 01.
- Higgins, B. S., D. L. Siebers, et al. (2000). "Diesel-spray ignition and premixed-burn behavior." Development **2012**: 04-13.
- Hofmann, M., W. G. Bessler, et al. (2003). "Laser-induced incandescence for soot diagnostics at high pressures." Applied Optics **42**(12): 2052-2062.
- Hottel, H. C. and F. P. Broughton (1932). "Determination of true temperature and total radiation from luminous gas flames."
- ICRP, I. C. o. R. P. (1994). Human respiratory tract model for radiological protection: A report of a task group of the International Commission on Radiological Protection, Elsevier Health Sciences.
- Idicheria, C. A. and L. M. Pickett (2005). "Soot formation in diesel combustion under high-EGR conditions." SAE TRANSACTIONS **114**(4): 1559-1574.
- Idicheria, C. A. and L. M. Pickett (2007). "Effect of EGR on diesel premixed-burn equivalence ratio." Proceedings of the Combustion Institute **31**(2): 2931-2938.

- Inagaki, K., S. Miura, et al. (1998). "Quantitative Soot Concentration Measurement with the Correction of Attenuated Signal Intensity Using Laser-Induced Incandescence." pulse **532**: 1D64nm.
- International Commission on Radiological, P. (1994). Human respiratory tract model for radiological protection: A report of a task group of the International Commission on Radiological Protection, Elsevier Health Sciences.
- Janssen, N. A. H., G. Hoek, et al. (2011). "Black carbon as an additional indicator of the adverse health effects of airborne particles compared with PM10 and PM2. 5." Environmental Health Perspectives **119**(12): 1691.
- Jenkins, T. P. and R. K. Hanson (2001). "Soot pyrometry using modulated absorption/emission." Combustion and Flame **126**(3): 1669-1679.
- Kamimoto, T. and M.-h. Bae (1989). "High combustion temperature for the reduction of particulate in diesel engines." SAE TRANSACTIONS **97**: 692-701.
- Ketterle, W., M. Schäfer, et al. (1992). "2D single-shot imaging of OH radicals using tunable excimer lasers." Applied Physics B **54**(2): 109-112.
- Kock, B. F., T. Eckhardt, et al. (2002). "In-cylinder sizing of Diesel particles by time-resolved laser-induced incandescence (TR-LII)." Proceedings of the Combustion Institute **29**(2): 2775-2782.
- Kock, B. F., C. Kayan, et al. (2005). "Comparison of LII and TEM sizing during synthesis of iron particle chains." Proceedings of the Combustion Institute **30**(1): 1689-1697.
- Kock, B. F. and P. Roth (2003). Two-color TR-LII applied to in-cylinder diesel particle sizing.
- Kosaka, H., T. Aizawa, et al. (2005). "Two-dimensional imaging of ignition and soot formation processes in a diesel flame." International Journal of Engine Research **6**(1): 21-42.
- Koylu, U. O., G. M. Faeth, et al. (1995). "Fractal and projected structure properties of soot aggregates." Combustion and Flame **100**(4): 621-633.
- Koylu, U. O., C. S. McEnally, et al. (1997). "Simultaneous measurements of soot volume fraction and particle size / microstructure in flames using a thermophoretic sampling technique." Combustion and Flame **110**(4): 494-507.
- Koylu, U. O., C. S. McEnally, et al. (1997). "Simultaneous measurements of soot volume fraction and particle size/microstructure in flames using a thermophoretic sampling technique." Combustion and Flame **110**(4): 494-507.
- Kreyling, W. G., M. Semmler-Behnke, et al. (2006). "Health implications of nanoparticles." Journal of Nanoparticle Research **8**(5): 543-562.
- Ladommatos, N., P. Rubenstein, et al. (1996). "Some effects of molecular structure of single hydrocarbons on sooting tendency." Fuel **75**(2): 114-124.
- Ladommatos, N. and H. Zhao (1994). "A Guide to Measurement of Flame Temperature and Soot Concentration in Diesel Engines Using Two-Color Method - Part 1: Principles." SAE Paper 941956.
- Lee, K.-O., C. M. Megaridis, et al. (2000). "Soot formation effects of oxygen concentration in the oxidizer stream of laminar coannular nonpremixed methane/air flames." Combustion and Flame **121**(1-2): 323-333.
- Lee, K. O., R. Cole, et al. (2001). "Detailed Characterization of Morphology and Dimensions of Diesel Particulates Via Thermophoretic Sampling." SAE Paper 2001-01-3572: September 2001.
- Lee, S. C. and C. L. Tien (1981). Optical constants of soot in hydrocarbon flames.
- Lehmann, G. (2006). "Kappa Sigma Clipping." Insight J.

- Limbach, L. K., P. Wick, et al. (2007). "Exposure of engineered nanoparticles to human lung epithelial cells: influence of chemical composition and catalytic activity on oxidative stress." Environmental Science & Technology **41**(11): 4158-4163.
- Liu, F., K. J. Daun, et al. (2007). "Some theoretical considerations in modeling laser-induced incandescence at low-pressures." Applied Physics B **87**(1): 179-191.
- Liu, F., G. J. Smallwood, et al. (2005). "Effects of primary particle diameter and aggregate size distribution on the temperature of soot particles heated by pulsed lasers." Journal of Quantitative Spectroscopy and Radiative Transfer **93**(1-3): 301-312.
- Mansurov, Z. A. (2005). "Soot formation in combustion processes (review)." Combustion, Explosion and Shock Waves **41**(6): 727-744.
- Marinov, N. M., W. J. Pitz, et al. (1999). The formation of aromatics and PAHs in laminar flames. Joint meeting of the British, German and French sections.
- Matsui, Y., K. Kamimoto, et al. (1980). "SAE Paper 800970 A Study on the Application of the Two-Color Method to the Measurement of Flame Temperature and Soot Concentration in Diesel Engines." Society of Automotive Engineering, Warrendale, PA.
- Melton, L. A. (1984). "Soot diagnostics based on laser heating." Applied Optics **23**(13): 2201-2208.
- Michelsen, H. A. (2003). "Understanding and predicting the temporal response of laser-induced incandescence from carbonaceous particles." The Journal of Chemical Physics **118**(15): 7012-7045.
- Michelsen, H. A., F. Liu, et al. (2007). "Modeling laser-induced incandescence of soot: a summary and comparison of LII models." Applied Physics B: Lasers and Optics **87**(3): 503-521.
- Michelsen, H. A., P. O. Witze, et al. (2003). "Time-resolved laser-induced incandescence of soot: the influence of experimental factors and microphysical mechanisms." Applied Optics **42**(27): 5577-5590.
- Miles, P. C., R. Collin, et al. (2007). "Combined measurements of flow structure, partially oxidized fuel, and soot in a high-speed, direct-injection diesel engine." Proceedings of the Combustion Institute **31**(2): 2963-2970.
- Oberdörster, G. (2000). "Pulmonary effects of inhaled ultrafine particles." International archives of occupational and environmental health **74**(1): 1-8.
- Oger, B. (2013). Soot Characterisation In Diesel Engines Using Laser-Induced Incandescence, Brighton. **Ph.D**: 223.
- Payri, F., J. V. Pastor, et al. (2007). "Contribution to the application of two-colour imaging to diesel combustion." Measurement Science and Technology **18**: 2579-2598.
- Pickett, L. M. and D. L. Siebers (2006). "Soot formation in diesel fuel jets near the lift-off length." International Journal of Engine Research **7**(2): 103-130.
- Pinson, J. A., T. Ni, et al. (1994). "Quantitative Imaging Study of the Effects of Intake Air Temperature on Soot Evolution in An Optically-Accessible D.I. Diesel Engine." SAE Paper 942044.
- Politis, M., C. Pilinis, et al. (2008). "Ultrafine particles (UFP) and health effects. Dangerous. Like no other PM? Review and analysis." Global NEST Journal **10**(3): 439-452.
- Price, O. T., B. Asgharian, et al. (2002). "Multiple Path Particle Dosimetry model (MPPD v1. 0): A model for human and rat airway particle dosimetry." RIVM rapport 650010030.

- Ryser, R., T. Gerber, et al. (2009). "Soot particle sizing during high-pressure Diesel spray combustion via time-resolved laser-induced incandescence." Combustion and Flame **156**(1): 120-129.
- Santoro, R. J., H. G. Semerjian, et al. (1983). "Soot particle measurements in diffusion flames." Combustion and Flame **51**: 203-218.
- Sato, H., D. Tree, et al. (1990). A study on the effect of temperature on soot formation in a jet stirred reactor. Proceedings of the 23rd international symposium on combustion. The Combustion Institute.
- Schack, A. (1925). "Strahlung von leuchtenden Flammen." Z. tech. Physik **6**: 530-540.
- Schraml, S., S. Dankers, et al. (2000). "Soot temperature measurements and implications for time-resolved laser-induced incandescence (TIRE-LII)." Combustion and Flame **120**(4): 439-450.
- Schraml, S., S. Will, et al. (1999). "Simultaneous measurement of soot mass concentration and primary particle size in the exhaust of a DI diesel engine by time-resolved laser-induced incandescence (TIRE-LII)."
- Schulz, C., B. F. Kock, et al. (2006). "Laser-induced incandescence: recent trends and current questions." Applied Physics B: Lasers and Optics **83**(3): 333-354.
- Schwarzwald, R., P. Monkhouse, et al. (1987). "Picosecond fluorescence lifetime measurement of the OH radical in an atmospheric pressure flame." Chemical physics letters **142**(1): 15-18.
- Siddal, R. G. and I. A. McGrath (1962). "Ninth Symposium (International) on Combustion: The Emissivity of Luminous Flames." The Combustion Institute, Pittsburgh: 102-110.
- Siebers, D. and B. Higgins (2001). "Flame lift-off on direct-injection diesel sprays under quiescent conditions." SAE paper(2001): 01.
- Siebers, D. L. (1999). "Liquid-Phase Fuel Penetration in Diesel Sprays." Development **2013**: 01-09.
- Smallwood, G. J., D. Clavel, et al. (2002). "Concurrent Quantitative Laser-Induced Incandescence and SMPS Measurements of EGR Effects on Particulate Emissions from a TDI Diesel Engine." SAE TECHNICAL PAPER SERIES **2002-01-2715**.
- Smith, O. I. (1981). "Fundamentals of soot formation in flames with application to diesel engine particulate emissions." Name: Prog. Energy Combust. Sci.
- Smyth, K. C. and C. R. Shaddix (1996). "The elusive history of $m = 1.57-0.56 i$ for the refractive index of soot." Combustion and Flame **107**(3): 314-320.
- Snelling, D. R., G. J. Smallwood, et al. (2005). "A calibration-independent laser-induced incandescence technique for soot measurement by detecting absolute light intensity." Applied Optics **44**(31): 6773-6785.
- Snelling, D. R., G. J. Smallwood, et al. (2000). "In-situ real-time characterization of particulate emissions from a diesel engine exhaust by laser-induced incandescence." SAE TRANSACTIONS **109**(4): 1914-1925.
- Snelling, D. R., K. A. Thomson, et al. (2002). "Spectrally resolved measurement of flame radiation to determine soot temperature and concentration." AIAA Journal **40**(9): 1789-1795.
- Stagg, B. J. and T. T. Charalampopoulos (1993). "Refractive indices of pyrolytic graphite, amorphous carbon, and flame soot in the temperature range 25° to 600°C." Combustion and Flame **94**(4): 381-396.
- Svensson, K. I. (2005). Effects of Fuel Molecular Structure and Composition on Soot Formation in Direct-Injection Spray Flames, Brigham Young University.

- Therssen, E., Y. Bouvier, et al. (2007). "Determination of the ratio of soot refractive index function $E(m)$ at the two wavelengths 532 and 1064 nm by laser induced incandescence." Applied Physics B: Lasers and Optics **89**(2): 417-427.
- Tree, D. R. and D. E. Foster (1994). "Optical Measurements of Soot Particle Size, Number Density, and Temperature in a Direct Injection Diesel Engine as a Function of Speed and Load." SAE Paper 940270.
- Tree, D. R. and K. I. Svensson (2007). "Soot processes in compression ignition engines." Progress in Energy and Combustion Science **33**(3): 272-309.
- Vander Wal, R. L., T. M. Ticich, et al. (1999). "Can soot primary particle size be determined using laser-induced incandescence?" Combustion and Flame **116**(1-2): 291-296.
- Wahiduzzaman, S., T. Morel, et al. (1987). Experimental and analytical study of heat radiation in a diesel engine.
- Wang, H. (2011). "Formation of nascent soot and other condensed-phase materials in flames." Proceedings of the Combustion Institute **33**(1): 41-67.
- Wang, H. and M. Frenklach (1997). "A detailed kinetic modeling study of aromatics formation in laminar premixed acetylene and ethylene flames." Combustion and Flame **110**(1): 173-221.
- Watson, A. Y. and P. A. Valberg (2001). "Carbon black and soot: two different substances." AIHAJ-American Industrial Hygiene Association **62**(2): 218-228.
- Will, S., S. Schraml, et al. (1998). "Performance characteristics of soot primary particle size measurements by time-resolved laser-induced incandescence." Applied Optics **37**: 5647-5658.
- Will, S., S. Schraml, et al. (1995). "Two-dimensional soot-particle sizing by time-resolved laser-induced incandescence." Optics Letters **20**(22): 2342.
- Williams, M. M. R. and S. K. Loyalka (1991). Aerosol science: theory and practice: with special applications to the nuclear industry, Pergamon Pr.
- Xu, F. and G. M. Faeth (2001). "Soot formation in laminar acetylene/air diffusion flames at atmospheric pressure." Combustion and Flame **125**(1-2): 804-819.
- Yan, J. and G. L. Borman (1988). Analysis and in-cylinder measurement of particulate radiant emissions and temperature in a direct-injection diesel engine, AD-A-204522/7/XAB, Wisconsin Univ., Madison, WI (USA). Engine Research Center.
- Zhao, H. and N. Ladommatos (1998). "Optical diagnostics for soot and temperature measurement in diesel engines." Progress in Energy and Combustion Science **24**(3): 221-255.

Appendix A: High pressure condition, peak intensity LII data

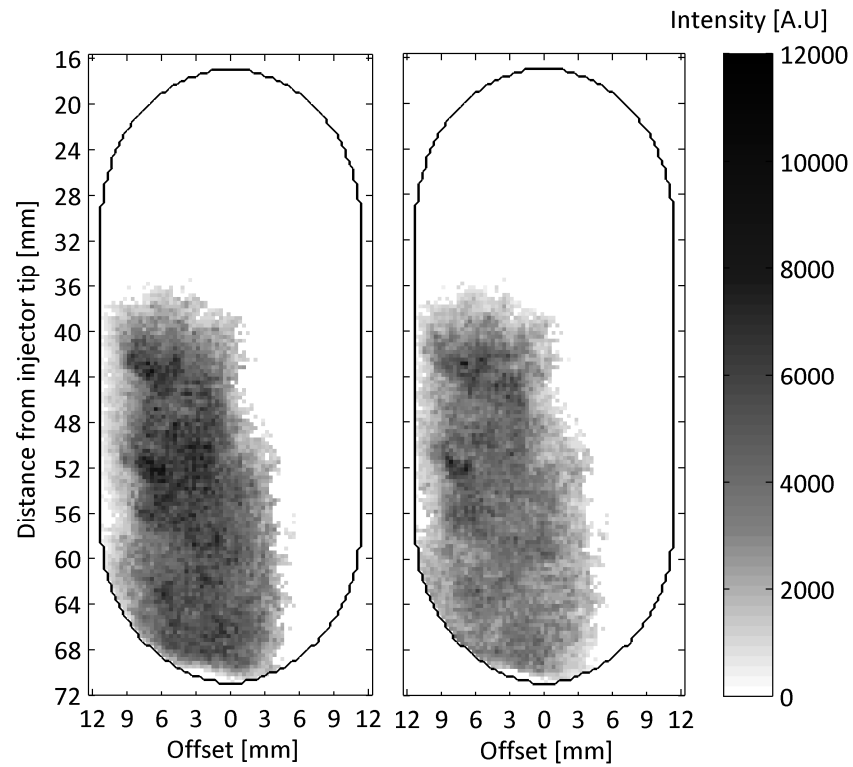


Figure 118 LII radiant emission via 592 nm (left) and 750 nm (right) filter for $T_{\text{Ref}}=1.5$ ms acquisition trigger signal timing ($P_{\text{ICP}}=40$ bar, $P_{\text{rail}}=1000$ bar).

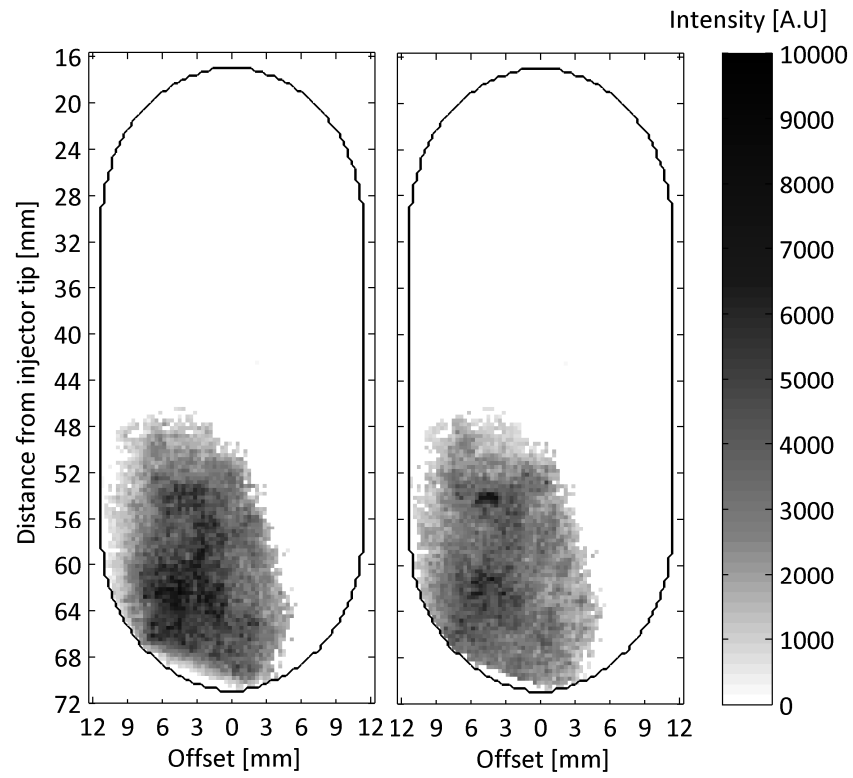


Figure 119 LII radiant emission via 592 nm (left) and 750 nm (right) filter for $T_{\text{Ref}}=1.7$ ms acquisition trigger signal timing ($ICP=40$ bar, $P_{\text{rail}}=1000$ bar).

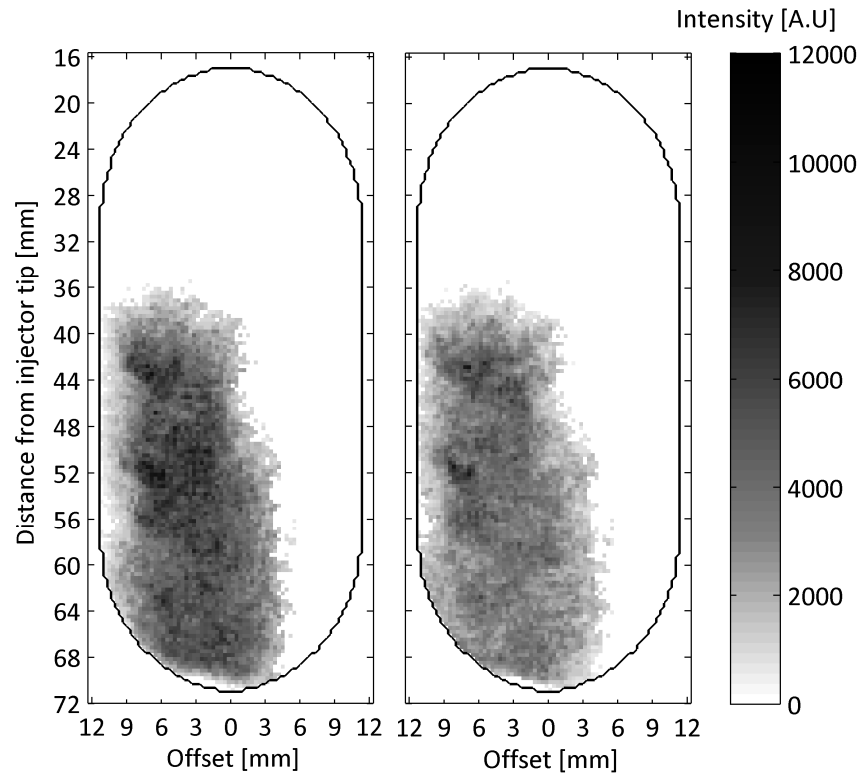


Figure 120 LII radiant emission via 592 nm centre wavelength filter (left) and 750 nm centre wavelength filter (right) for $P_{\text{rail}}=1000$ bar, $T_{\text{Ref}}=1.5$ ms.

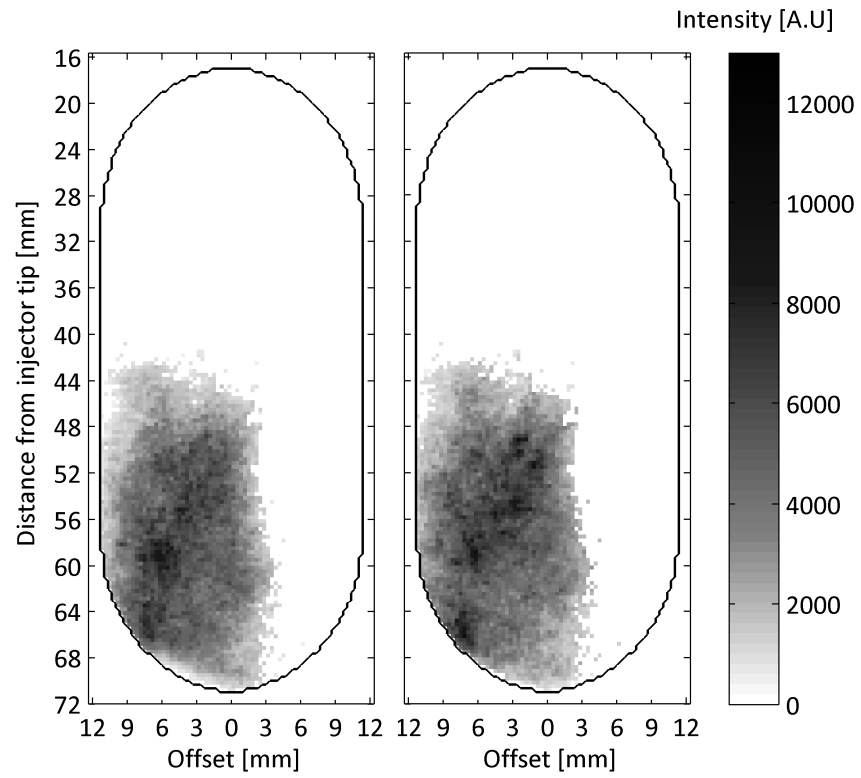


Figure 121 LII radiant emission via 592 nm centre wavelength filter (left) and 750 nm centre wavelength filter (right) for $P_{\text{rail}}=1300$ bar, $T_{\text{Ref}}=1$ ms, $\text{ICP}=40$ bar.

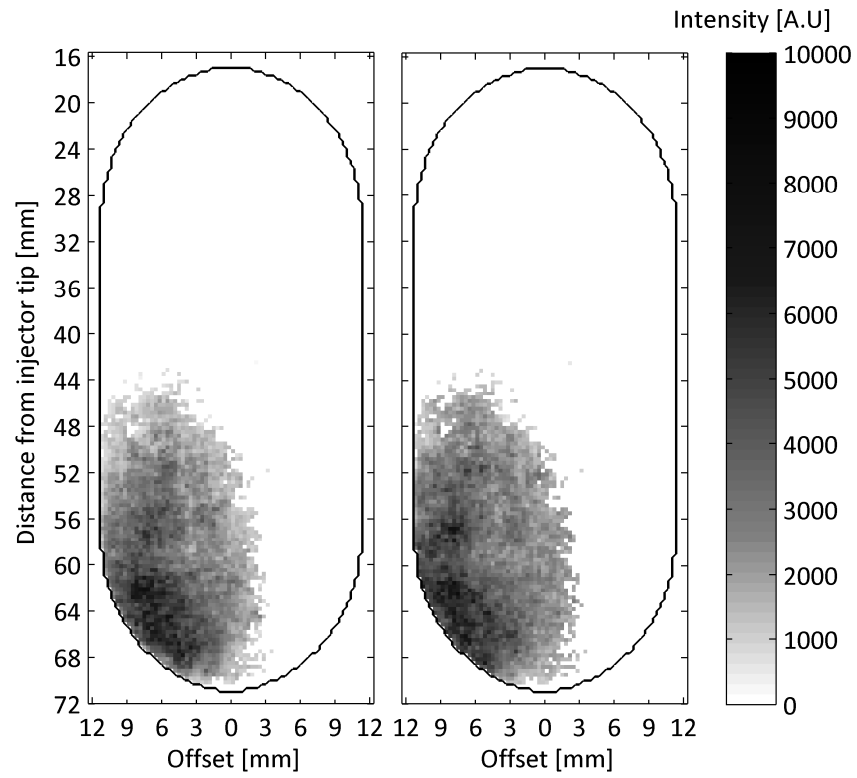


Figure 122 LII radiant emission via 592 nm centre wavelength filter (left) and 750 nm centre wavelength filter (right) for $P_{\text{rail}}=1600$ bar, $T_{\text{Ref}}=0.66$ ms.

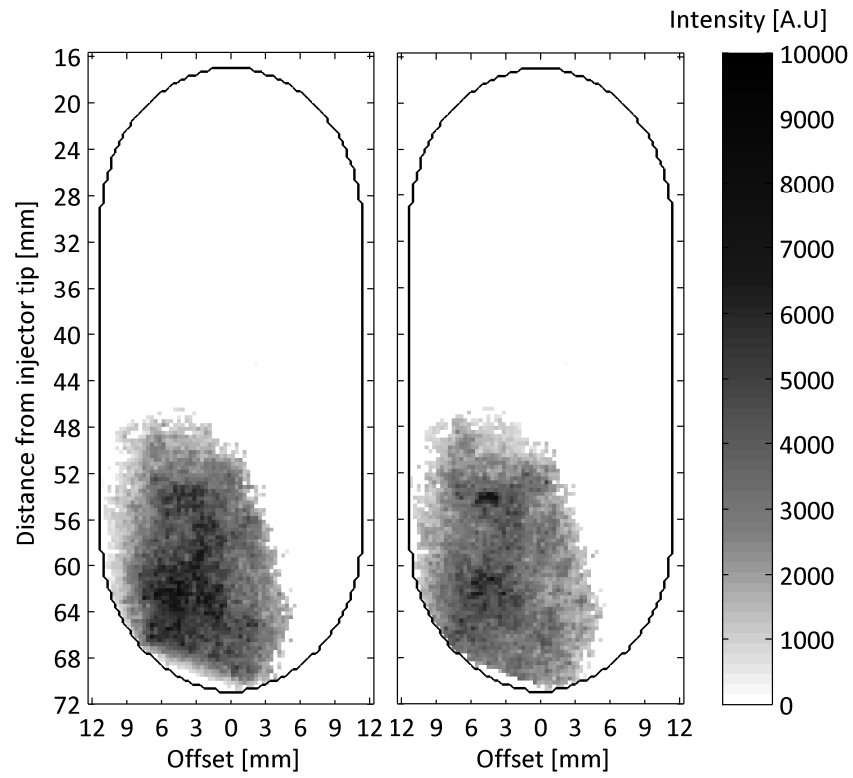


Figure 123 LII radiant emission via 592 nm centre wavelength filter (left) and 750 nm centre wavelength filter (right) for ICP=40 bar, $P_{\text{rail}}=1000$ bar, $T_{\text{Ref}}=1.7$ ms, ICP=40 bar.

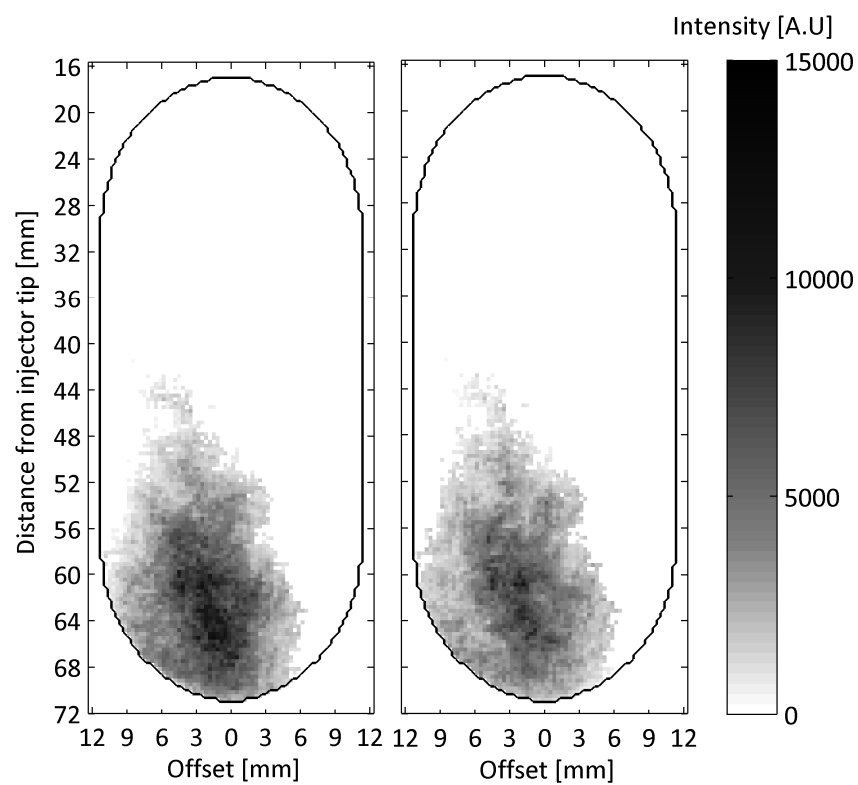


Figure 124 LII radiant emission via 592 nm centre wavelength filter (left) and 750 nm centre wavelength filter (right) for ICP=50 bar, $P_{\text{rail}}=1000$ bar, $T_{\text{Ref}}=1.8$ ms.